

PALACKÝ UNIVERSITY IN OLOMOUC

Faculty of Science

Department of Physical Chemistry



**Study of Fluorinated Graphene Reactivity Using
Quantum Chemistry Methods**

Doctoral Thesis

Author:	Mgr. Dagmar Zaoralová
Supervisor:	doc. RNDr. Miroslav Medved', Ph. D.
Study programme:	Chemistry
Study field:	Physical Chemistry
Study form:	Daily
Date of submission:	August 2021

Olomouc 2021

Bibliographical identification:

Author's first name and surname	Mgr. Dagmar Zaoralová (birth name Matochová)
Title	Study of Fluorinated Graphene Reactivity Using Quantum Chemistry Methods
Type of thesis	Doctoral
Department	Department of Physical Chemistry
Supervisor	doc. RNDr. Miroslav Medved', Ph. D.
The year of presentation	2021
Keywords	Fluorographene reactivity, cyanographene, graphene acid, graphene derivatization, substitution reactions, heteroatom doping, (de)fluorination, C–F bond, single atom catalysis, transition metals, hydrazine oxidation reaction, density functional theory
Number of pages	77
Number of appendices	7
Language	English

Declaration of the author

I declare that I have worked out this thesis by myself using the cited sources. Neither the thesis nor any of its parts was previously used for obtaining any academic degree.

Olomouc 2021

Dagmar Zaoralová

Acknowledgement

Firstly, I would like to express my sincere gratitude to my supervisor doc. Medved' for his excellent advices and endless patience and kindness. I also thank prof. Otyepka for the opportunity to join his research group. It was an honour to work with you.

I am also grateful to my husband and family for supporting me for all these years. The latest thanks goes to both my dogs for cheering me up whenever needed.

Outline

List of Abbreviations	vii
Abstract.....	1
Preface and Thesis Aims	2
1. Chemistry of Fluorographene	3
1.1. Properties and Applications of Fluorographene.....	3
1.2. Thermal Stability and Reactivity of Fluorinated Graphene	6
1.3. The Nature of C-F Bonds.....	11
1.4. Structural Motifs in Fluorinated Graphene	14
1.5. Graphene Derivatives Derived from Fluorographene.....	18
2. Methods	21
2.1. Density Functional Theory.....	21
PBE functional.....	22
PBE0 functional.....	23
ω B97X-D functional	23
2.2. Finite-size versus Periodic Systems.....	24
Solution for molecules.....	24
Solution for periodic systems	24
2.3. Solvent Models	25
3. On Track to Explore the Chemistry of Fluorographene	27
3.1. Variability of the C–F Bond Nature Influences the Formation of Specific Structural Motifs in Fluorinated Graphene	27
3.2. Point Defects Enhance the Reactivity of Fluorographene	34
3.3. The Reaction Mechanism of Fluorographene Nucleophilic Substitution.....	39
3.4. The Role of Vacancies in Nitrogen Doping of Fluorographene	43
3.5. Covalent Functionalization of Partially Fluorinated Graphene by Polysulfide Chains	49

4. Graphene Derivatives Derived from Fluorographene as Supporting Materials for Single Atom Catalysts.....	51
4.1. Cyanographene and Graphene Acid as Supporting Materials for Anchoring of a Series of Late <i>3d</i> and <i>4d</i> Elements	51
4.2. The Mechanism of Hydrazine Oxidation Reaction Catalysed by Co^{2+} Cations Anchored to Cyanographene	57
5. Conclusions.....	61
6. References.....	64
Appendices.....	77

List of Abbreviations

ACN	acetonitrile
AcOH	acetic acid
AEA	adiabatic electron affinity
BDE	bond dissociation energy
BDG	bond dissociation Gibbs energy
c2	<i>trans</i> -decafluoronaphthalene
c3	<i>trans</i> -tridecafluorophenylene
c7	<i>trans</i> -tetracosafuorocoronene
c10	<i>trans</i> -dotriacontafuoroovalene
CG	cyanographene
CPCM	conductor-like polarizable continuum model
CVD	chemical vapor deposition
DFT	density functional theory
DMA	dimethylamine
DMAACN	dimethylaminoacetonitrile
DMAc	<i>N,N</i> -dimethylacetamide
DMF	<i>N,N</i> -dimethylformamide
<i>dp</i> -GA	deprotonated graphene acid
DV	double vacancy
EA	electron affinity
EDD	electron density difference
EPR	electron paramagnetic resonance
F-DMF	<i>N,N'</i> -dimethylcarbamoyl fluoride
F_{cis}	number of adjoining fluorine ad-atoms in <i>cis</i> positions

F_{cis}	number of adjoining fluorine ad-atoms in <i>cis</i> positions
F_{trans}	number of adjoining fluorine ad-atoms in <i>trans</i> positions
FG	fluorographene (C_1F_1)
FT-IR	Fourier transform infrared spectroscopy
GA	graphene acid
GC-MS	gass chromatography mass spectroscopy
GGA	generalized gradient approximation
GS	structure of the lowest energy, ground-state structure
HOMO	highest occupied molecular orbital
HzOR	hydrazine oxidation reaction
IMS	intermediate state
IP	ionization potential
LDA	local density approximation
LUMO	lowest unoccupied molecular orbital
MAS NMR	magic angle spinning nuclear magnetic resonance
NBO	natural bond orbital analysis
NMP	<i>N</i> -methyl-2-pyrrolidone
NMR	nuclear magnetic resonance
N_π	the number of C–C bonds that enter the π -conjugation after dissociation of given C–F bond
P	final state, product
PBC	periodic boundary conditions
pFG	partially fluorinated graphene (C_1F_x , $0 < x < 1$)
(p)FGs	partially fluorinated graphenes and fluorographene (C_1F_x , $0 < x \leq 1$)
PS	polysulfide
R	initial state, reactants

SAC	single atom catalyst
SASA	solvent-accessible surface area
SCRF	self-consistent reaction field
SET	single electron transfer
SMD	universal solvation model based on electron density
S _N 1	monomolecular nucleophilic substitution
S _N 2	bimolecular nucleophilic substitution
SOMO	singly occupied molecular orbital
SV	single vacancy
SW(55-77)	Stone-Wales vacancy
THF	tetrahydrofuran
TPD	temperature-programmed desorption
TS	transition state
TV	triple vacancy
VASP	Vienna Ab-initio Simulation Package
VEA	vertical electron affinity
vdW	van der Waals
XANES	X-ray absorption near edge structure
XPS	X-ray photoelectron spectroscopy
XRD	X-ray diffraction

Abstract

The unexpected reactivity of fluorographene (FG) has attracted growing attention since it allows the enrichment of the palette of graphene-based materials by derivatives such as cyanographene (CG), graphene acid (GA), alkyl-, hydroxyl-, and amino-derivatives and heteroatom-doped graphenes. In real-life applications, it is of utmost importance to precisely control the final structure and composition of the products which can hardly be achieved without understanding related reaction pathways. However, only few studies have been focused on the mechanisms of covalent functionalization and heteroatom doping of FG. The susceptibility of the material to nucleophilic substitution is rather staggering because the C–F bond is commonly viewed as the strongest bond in organic chemistry. However, density functional theory (DFT) calculations revealed that the bond dissociation energy of C–F bonds in partially fluorinated graphenes varies from 25.6 to 118.2 kcal·mol⁻¹ and depends on the local configuration of fluorine ad-atoms. The variable nature of C–F bonds is mirrored in the formation of specific structural motifs of fluorine ad-atoms during (de)fluorination of the material. Moreover, electron paramagnetic resonance (EPR) measurements revealed a distribution of point defects (radical centres) in the structure of FG that play a key role in FG's chemistry. The radical centres can act as electrophilic sites and cause a homolytic cleavage of bonds. Using DFT methods, we have proposed a new radical mechanism of FG defluorination in the environment of *N,N'*-dimethylformamide (DMF) consistent with the experimental data. In addition, we have investigated the reaction mechanism of the nucleophilic attack of NH₂⁻, OH⁻, CN⁻, and S_n²⁻ on single atom radical sites and larger defluorinated areas in the structure of FG. Interestingly, the radical centres may also occur at the edges of vacancies in FG and may play a vital role in the mechanism of nitrogen incorporation into the FG lattice. We believe that our findings substantially contribute to the understanding of FG's unique chemistry.

New graphene derivatives derived from FG represent a promising class of substrate materials which can be utilized to anchor metal atoms for single-atom catalysis. To derive rules that influence the bond strength between the metal atoms and CG/GA, we have investigated a group of late *3d* and *4d* elements including the iron triad, light platinum group, and coinage metals in different oxidation states (from 0 to +III) anchored to either CG or GA. The unprecedented catalytic properties of single-atom catalysts (SACs) were demonstrated by the hydrazine oxidation reaction (HzOR) catalysed by Co²⁺ cations immobilized on CG. Our findings on the electronic structure of SACs based on CG/GA rationalizing their catalytic activity can help design new materials for heterogeneous catalysis, spintronics, and electrochemical applications.

Preface and Thesis Aims

The intriguing 2D world of graphene chemistry has significantly expanded in the last decade thanks to the successful synthesis of FG. The surprising reactivity of FG has enabled covalent grafting of various functional groups and incorporation of heteroatoms into the graphene lattice which would be demanding or nearly impossible using pristine graphene. To promote applicability of new graphene derivatives in both industrial and scientific fields, it is essential to gain control over the processes related to chemical transformations of FG.

There is still a significant gap in the understanding of FG's chemistry. Up to these days, only few studies have been published that discuss reaction mechanisms and processes accompanying cleavage of C–F bonds and substitutions of carbon atoms in the structure of FG. So far known results are not sufficient to satisfactorily explain the experimental observations. By using DFT methods, we aimed to clarify the processes that influence the reactivity of FG and to propose probable reaction mechanisms that lead to formation of new graphene derivatives.

Recently synthesized new graphene derivatives have significantly enlarged the applicability of graphene-based materials. For instance, CG and GA may be utilized in single atom catalysis owing to the ability to immobilize metal atoms and cations and efficiently transfer the charge from/to the metal. The outstanding performance of SACs is based on the maximally reduced size of the metal particles. Therefore, a strong interaction between the metal and substrate is crucial since it prevents unwanted processes such as aggregation into bigger particles and consequent decrease of catalytic performance of the material.

To broaden the knowledge about the stability of single atoms immobilized by either CG or GA, we have applied DFT methods to collect data about a group of the late *3d* and *4d* elements in different oxidation states anchored to CG or GA. We aimed to derive rules that would help to predict the stability of these complexes. In addition, we have investigated the influence of Co²⁺ cations anchored to CG on the thermodynamics of the HzOR.

1. Chemistry of Fluorographene

1.1. Properties and Applications of Fluorographene

After its discovery in 2010,¹⁻³ FG became a celebrity among graphene derivatives as the only stable stoichiometric halogen derivative with composition C_1F_1 that can exist in four conformations – chair, armchair, boat, and zigzag (stirrup) (Figure 1).⁴⁻⁶ There are two main approaches how to prepare fluorinated graphene: (i) top-down methods including sonochemical, thermal, microwave-assisted, and modified Hummer's exfoliation of graphite fluoride^{1, 2, 7, 8} and (ii) bottom-up methods relying typically on direct gas fluorination of graphene by XeF_2 , F_2 , SF_6 , and MoF_6 gas,^{1, 3, 9-11} plasma fluorination of graphene by fluorine radicals using SF_6 , CF_4 , or F_2 as plasma sources,¹²⁻¹⁶ solvothermal and hydrothermal fluorination of graphene,^{17, 18} and photochemical fluorination by laser irradiation of fluoropolymer-covered graphene.^{19, 20} The diverse synthetic procedures provide fluorinated graphenes with different amount and topology of fluorine ad-atoms as well as a different number and types of defects, thus leading to materials with varied properties which can be exploited in a wide range of applications.

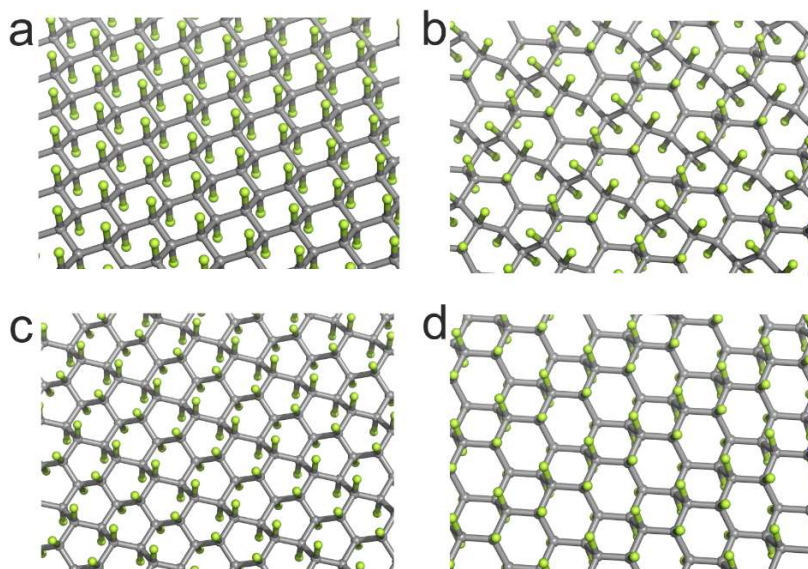


Figure 1: Conformations of FG: a) chair (the most stable), b) armchair, c) boat, and d) zigzag (stirrup). Carbon atoms are grey, fluorine green.

Fluorination of graphene is accompanied by a transformation of the delocalized π -conjugated network of sp^2 C–C bonds into newly created $C(sp^3)$ –F bonds. Therefore, a zero-bandgap semiconductor (graphene) turns gradually -with an increasing level of fluorination- into a wide-bandgap insulator (FG).^{2, 4, 9, 21, 22} Kumar *et al.*²² studied thoroughly the band structure of partially and fully fluorinated graphenes ((p)FGs) with the stoichiometry

ranging from $C_{18}F_1$ to $C_{18}F_{18}$ using DFT methods (Figure 2). The formation of C–F bonds creates new bonding states in the valence band maximum and antibonding states in the conduction band minimum. The band structures of pFGs with odd number of fluorine ad-atoms indicate that these materials are good conductors. On the other hand, pFGs with even numbers of fluorine ad-atoms are semiconductors with the band gap ranging from 0.12 eV to 3.64 eV. This led to the idea that the electronic properties of pFGs could be tuned by the amount of fluorine ad-atoms, which was supported by the results showing that pFGs of different stoichiometry are nonmagnetic semimetals, nonmagnetic or magnetic metals, and nonmagnetic or magnetic semiconductors.^{3, 22-28} Compared to graphene, (p)FGs also show higher optical transparency confirming the bandgap opening.^{1, 12, 29} Interestingly, the fluorination of graphene can also enhance the photoluminescent properties of the material.³⁰

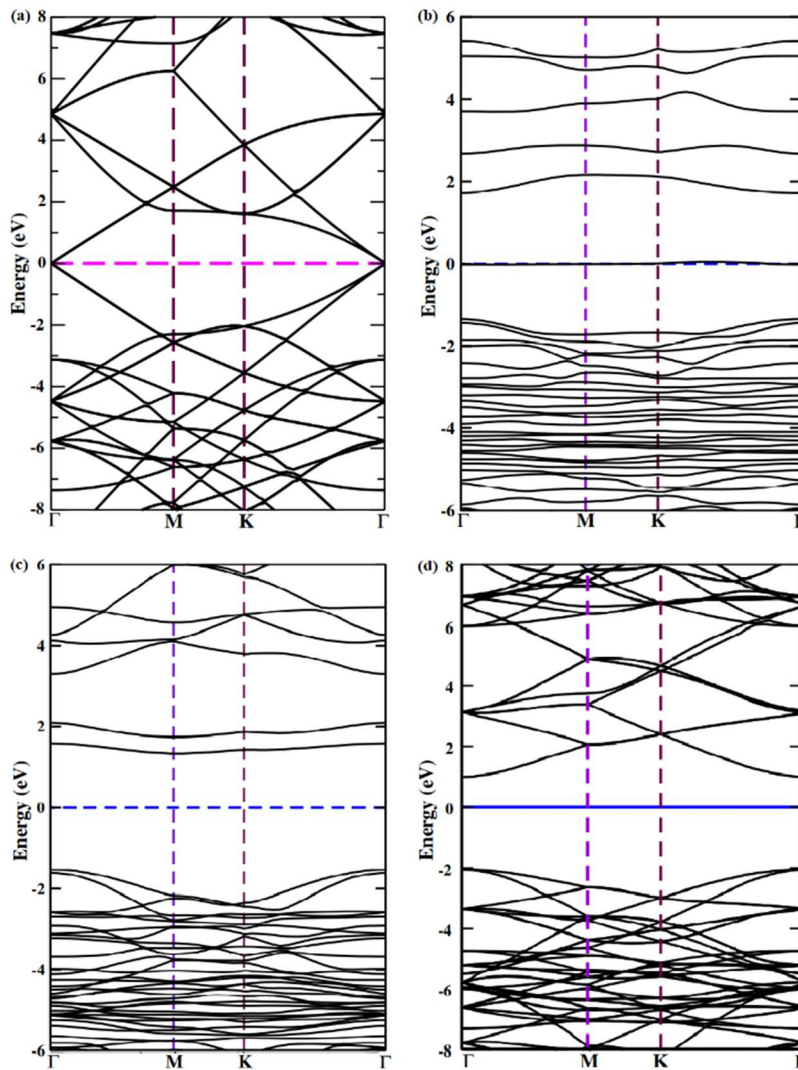


Figure 2: Band structure of a) pristine graphene and of (p)FGs with b) 50%, c) 78%, and 100% coverage of fluorine ad-atoms. Fermi energy is set to zero of the energy. Figures are from ref. 22.

It is worth noting that there is still a discrepancy between the experimentally and computationally obtained values of FG's bandgap.^{21, 31-34} Karlický *et al.*^{21, 34} calculated the bandgap of pristine FG in chair conformation using the many-body GW theory. The estimated value of FG's bandgap (from ~ 7.0 to ~ 8.0 eV) was much higher than that obtained experimentally (from ~ 3.0 to ~ 5.0 eV).^{1,9,35} This large difference may be partly caused by high exciton binding energy (~ 2.0 eV, BSE-GW level of theory).^{21, 32, 34} Therefore, the theoretical value of the optical bandgap of pristine FG appears to be in a range from ~ 5.0 to ~ 6.0 eV which is still larger than the experimental data. Recently, Dubecký *et al.*³³ used highly accurate many-body GW and fixed-node diffusion Monte Carlo calculations to obtain a benchmark value of the fundamental bandgap 7.1 ± 0.1 eV which -in combination with the exciton binding energy of 1.92 eV calculated using the Bethe-Salpeter equation- gives a theoretical (gas-phase) optical gap estimate of 5.2 ± 0.1 eV.

The presence of C-F bonds makes (p)FGs highly hydrophobic, which is an obstacle in their application as precursors for electrodes and composites.³⁶⁻³⁸ On the other hand, (p)FGs can be dispersed in organic solvents such as phenylethylene, tetrahydrofuran (THF) and *N*-methyl-2-pyrrolidone (NMP).³⁷ Fluorine ad-atoms also enhance tribological properties of graphene. Owing to its low friction coefficient, FG is considered as important ultrathin lubricant and is used, e.g., as an additive for lubricating oils.³⁹ Thermal conductivity of (p)FGs is less sensitive to strain than that of graphene. Moreover, it is tunable since it decreases during fluorination and then increases again when the C/F ratio approaches 1.0. Therefore, (p)FGs are interesting materials combining hydrophobic and lubricating properties with heat dissipation.^{40, 41}

Owing to their remarkable properties, (p)FGs offer fascinating opportunities for many applications. They can be used as the cathode material in lithium primary batteries thanks to their ultrathin 2D structure, tunable amount of fluorine ad-atoms, favourable diffusion kinetics, and large specific surface area.⁴²⁻⁴⁴ The unique electronic properties controlled by the degree of fluorination open road for applications in electronics (transistors, supercapacitors, ...) and electrochemistry.⁴⁵⁻⁴⁷ Biological applications of (p)FGs such as drug delivery and therapy, biosensing, bio-imaging, tissue engineering, and cell growth have also attracted a considerable interest.^{29, 48, 49} To achieve a better control over the stoichiometry, structure, and topology of the material with desired properties, a deeper understanding of the fluorination process and related structure property relationships at the atomistic level is of paramount importance.

1.2. Thermal Stability and Reactivity of Fluorinated Graphene

Perfluorinated hydrocarbons are very stable compounds thanks to the very strong C–F bonds which can be utilized in many practical applications.⁵⁰⁻⁵² For example, polytetrafluoroethylene (Teflon) as a thermally stable and chemically inert material can be used instead of glass in chemical labs, as insulation of wiring in aerospace, or as a weather-resistant material in construction.⁵⁰ The high stability of perfluorinated groups is also employed for stabilization of unusual molecules in organic chemistry.⁵¹ Originally, FG was also anticipated to be thermally stable and chemically inert.⁵² However, many studies showed that the thermal stability can be decreased in presence of some solvents,^{53, 54} and that (p)FGs are unexpectedly reactive.^{2, 3, 55}

The thermal stability of (p)FGs is highly dependent on several factors such as the time of fluorination, fluorinating agent, supporting material, and storage conditions. For example, graphene fluorinated for a few hours can be restored to its pristine state by short annealing in a mixture of Ar and H₂. However, a longer fluorination results in a more stable material which could not be completely defluorinated even at 700 K.⁵² Raman and X-ray photoelectron spectra (XPS) of pFG (with the stoichiometry C₂F) that was heated up to 400 K showed no significant decrease of fluorine content. Higher temperatures caused gradual defluorination, but 0.5% of fluorine ad-atoms remained in the material up to 1073 K (Figure 3).^{56, 57} Temperature-programmed desorption (TPD) revealed that defluorination of pFG was associated with the desorption of HF and CO molecules.⁵⁷

Fluorination of graphene prepared by chemical vapor deposition (CVD) on different substrate materials by XeF₂ resulted in different amounts of fluorine ad-atoms (Figure 4). Graphene on the SiO₂ substrate was fluorinated to a higher degree in comparison to metal substrates (i.e., Cu, Au) at the same conditions because SiO₂ substrate allowed fluorination on both sides of a graphene plane.^{3, 58} However, the level of fluorination declined in a few days after fluorination and then reached a stable stoichiometry. The highest fluorine loss of 70% was observed in samples stored under ambient conditions for a few days due to air humidity that caused substitution of fluorine ad-atoms by functionalities containing oxygen. On the other hand, the fluorine loss was also observed in samples stored in nitrogen atmosphere and in vacuum, suggesting that another mechanism of fluorine desorption must have occurred. The observed recovery of C=C double bonds with the decrease of fluorine content over time proposes that in some cases expelling of fluorine ad-atoms and enlargement of the π -conjugated area of C–C bonds is thermodynamically preferred.⁵⁸

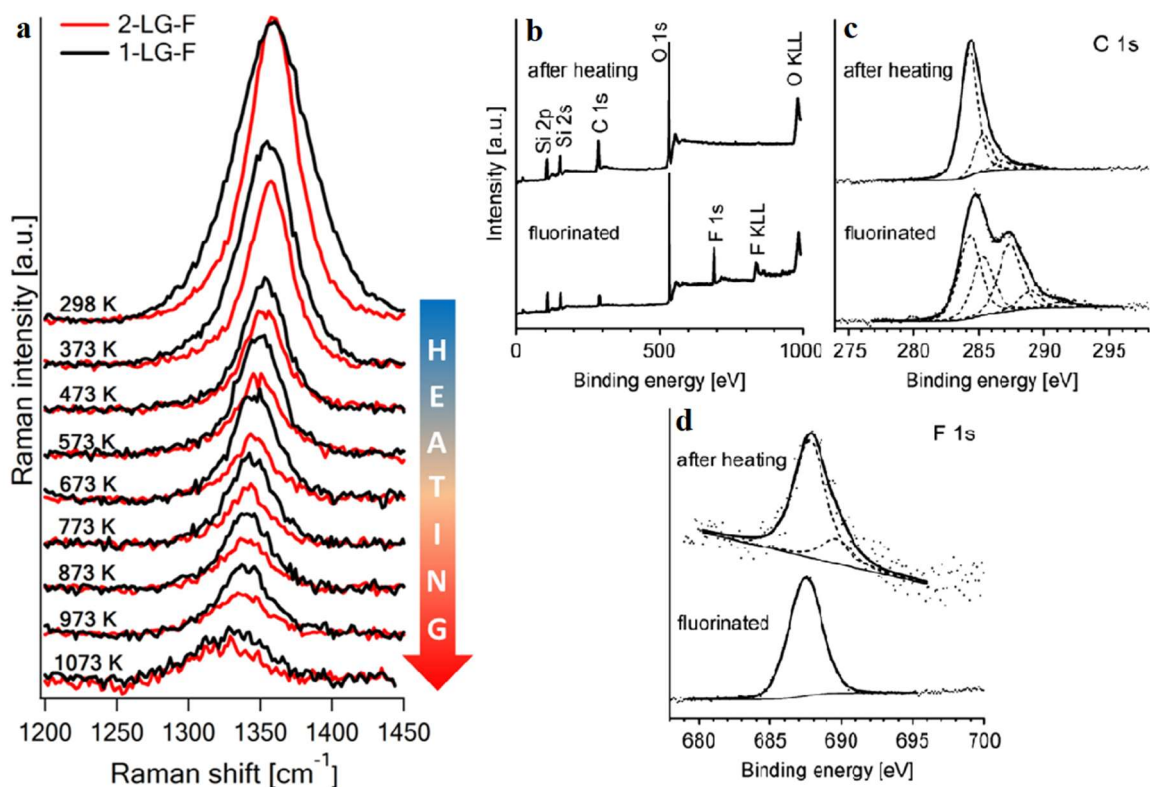


Figure 3: a) Temperature dependence of the D-band in Raman spectra of one-layered (1-LG-F) and two-layered (2-LG-F) pFG (with the starting stoichiometry C_2F), b) XPS survey spectrum, c) C 1s XPS spectrum and d) F 1s XPS spectrum of 1-LG-F before (bottom) and after heating (top). Figures are from ref. 56.

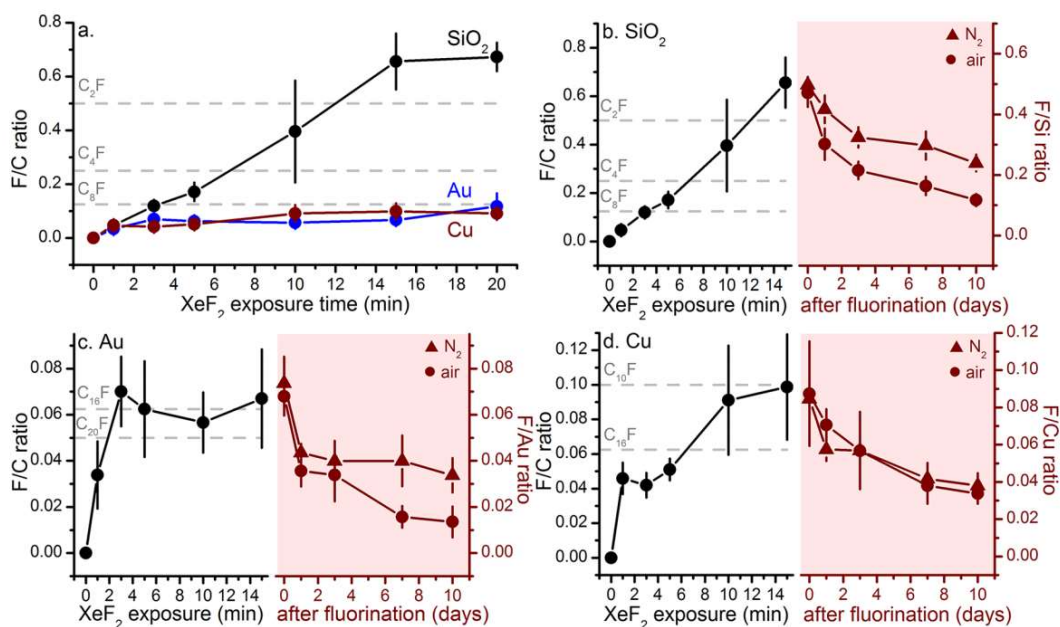


Figure 4: a) Relative degree of fluorination of graphene samples on SiO_2 , Cu, and Au substrates by XeF_2 . Subsequent decline of the amount of fluorine ad-atoms over several days in N_2 and air atmosphere for the samples on b) SiO_2 , c) Au, and d) Cu substrates. Figure is from ref. 58.

FGs can be reduced in the presence of some dipolar solvents at room temperature. Wang *et al.*⁵³ studied the influence of chloroform, methanol, ethanol, DMF, *N,N*-dimethylacetamide (DMAc), and NMP on the properties of FG. While FG treated in chloroform, methanol, and ethanol remained unaffected, DMF, DMAc, and NMP caused reduction of the material and decrease of its thermal stability. Chloroform-FG, methanol-FG, and ethanol-FG samples decomposed mainly around 545 °C in contrast to DMF-FG, DMAc-FG, and NMP-FG samples which decomposed at temperatures below 400 °C indicating the presence of weaker C–F bonds in the structure. Partial defluorination of FG and subsequent elongation and weakening of remaining C–F bonds of FG in DMF, DMAc, and NMP were confirmed by X-ray diffraction (XRD), XPS, Raman, and Fourier transform infrared spectroscopy (FT-IR) analyses. The authors attributed the ability of DMF, DMAc, and NMP to defluorinate FG to their highly nucleophilic (dipolar) character. In our study (Appendix B and section 3.2)⁵⁹ we have revealed a plausible reaction mechanism of FG defluorination in DMF which is initiated by hydrogen transfer from DMF to a radical site in FG structure.

Surprising reactivity of FG was observed after addition of potassium iodide into a dispersion of FG in sulfolane and subsequent heating that caused transformation of FG into metastable graphene iodide followed by the restoration of pristine graphene and I₂.² FG also undergoes reduction by hydrazine vapor, triethylsilane, or Zn particles.^{3,55} Reaction of FG with NaOH in acetone with the activation barrier of ca. 14 ± 5 kcal·mol⁻¹ causes the loss of fluorine ad-atoms and transformation into graphene oxide at ambient temperature.^{55, 60} Alkyl lithium reagents induce defluorination and alkylation of FG.⁶¹ In addition, fluorine ad-atoms of FG can be substituted with diamines.⁶²

Dubecký *et al.*⁶⁰ pursued several reaction mechanisms of FG reduction and nucleophilic substitution. In particular, radical decomposition, S_N1, S_N2, and elimination on the surface and edges of FG were studied using DFT methods. The homolytic cleavage of a C–F bond in a fully fluorinated area on the surface was found to be energetically very demanding with the bond dissociation energy (BDE) of 104.7 and 105.5 kcal·mol⁻¹ in the gas phase and the aqueous environment, respectively. A following dissociation of the neighbouring C–F bond appeared to be much easier (BDE = 53 kcal·mol⁻¹). BDEs of second-neighbour C–F bonds were not significantly affected. The corresponding bond dissociation Gibbs energies (BDGs) were about 14 kcal·mol⁻¹ lower because entropy favoured the dissociated state.

The heterolytic cleavage of C–F bonds was found to be even more energetically demanding than the radical dissociation. In the gas phase, this first step of the S_N1 mechanism cost twice as much and in water it was by 40% higher than the homolytic cleavage. On the other hand,

the heterolytic cleavage on edge sites was about $12 \text{ kcal}\cdot\text{mol}^{-1}$ more favourable than on surface sites, albeit still less probable than the radical dissociation. The $\text{S}_{\text{N}}2$ mechanism was presented as the most plausible, although the Gibbs activation energy barrier of $48.1 \text{ kcal}\cdot\text{mol}^{-1}$ in the aqueous environment ($21.5 \text{ kcal}\cdot\text{mol}^{-1}$ in the gas phase, Figure 5) was rather high and the reaction product was disfavoured by ca. $56 \text{ kcal}\cdot\text{mol}^{-1}$ in both environments due to a crooked resulting structure. Importantly, it was found that the lower coverage of fluorine ad-atoms makes the material more susceptible for the $\text{S}_{\text{N}}2$ reaction.⁶⁰

		R(vdW)	TS	P(vdW)	P
<i>water</i>	ΔE	-0.9	40.0	25.4	56.6
	ΔG	5.9	48.1	34.0	56.3
<i>vacuum</i>	ΔE	-14.9	3.1	-21.8	57.0
	ΔG	-11.1	10.4	-13.7	56.8

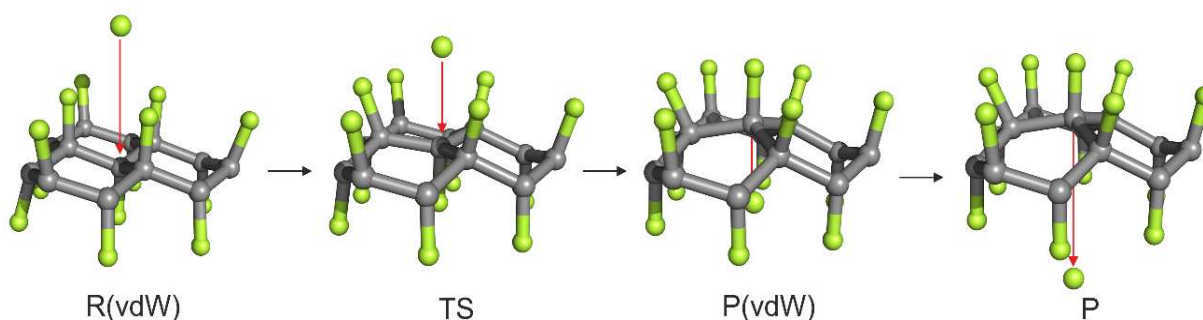


Figure 5: Top: relative energies (ΔE) and Gibbs energies (ΔG) with respect to reactants (isolated FG and a fluoride anion) in water and vacuum calculated at the $\omega\text{B97X-D}/6\text{-311G(d,p)}/\text{CPCM}$ level of theory. Bottom: Scheme of the $\text{S}_{\text{N}}2$ reaction. All values are in $\text{kcal}\cdot\text{mol}^{-1}$. Fluorine atoms are green, carbon grey. Results are from ref. 60.

Lai *et al.*⁶³ predicted a radical mechanism of pristine FG reduction using DFT methods in combination with EPR. It was assumed that the radical defluorination starts with a single electron transfer (SET) to C–F bond and proceeds via detachment of fluoride anion from the surface and formation of a spin centre in FG structure. In addition, $\text{S}_{\text{N}}1$ and $\text{S}_{\text{N}}2$ mechanisms were found to be hindered by both kinetics and thermodynamics. The nucleophilic substitution mechanism initiated by the SET step was demonstrated by the reaction of triethylamine with FG.

Electron transfer from metal surfaces and electron-rich organic donors to fluorocarbons is possible owing to the relatively low energy of the C–F bond σ^* orbital.⁶⁴ The σ^* orbital can also be employed in a so-called negative hyperconjugation with p orbitals of the neighbouring atom or π orbitals of the neighbouring bonds. In the reduction process, a metastable anion radical can be created, and a fluoride anion is subsequently released. The newly created radical centre on the carbon atom can be attacked by a nucleophile or can bring further defluorination. It is worth noting that the electron is preferentially donated into the σ^* orbitals of the tertiary C–F bonds. Thus, the tertiary C–F bonds are sometimes called as the ‘Achilles heel’ of perfluorinated hydrocarbons.⁶⁵

Nevertheless, the high values of FG electron affinity calculated in our work (Appendix B, section 3.2)⁵⁹ pointed out that the SET to FG can occur only if strong reducing agents are used, and thus this mechanism cannot fully explain the rich chemistry of FG. Interestingly, by combining the in-house EPR measurements with theoretical calculations we have shown that point defects (i.e., carbon sites with a missing fluorine ad-atom) in FG samples could explain the susceptibility of FG for nucleophilic substitution even without the assistance of strong reducing agents. This observation was also supported by the work of Liu *et al.*⁶⁶ about successful reductive defluorination of FG in a solution of aniline that is a weak non-nucleophilic agent. The important role of radical sites was very recently also discussed in the study by Siedle *et al.*⁶⁷ on successful grafting of nitrogen-containing moieties to graphite fluoride and concurrent defluorination of the material using benzylamine and tetramethylethylenediamine. The authors predicted that the defluorination proceeds through so-called proton coupled electron transfer which starts with SET from the amine molecule to the radical site in the structure of graphite fluoride. Simultaneously, fluoride anion is released from the graphite fluoride, reacts with the radical cation created from the amino molecule and forms HF. Attachment of a small amount of nitrogen moieties to the graphite fluoride was explained in terms of the reaction of ionic and radical intermediates produced by the oxidation of amines and C=C bonds in graphite fluoride.

To deeper analyze the reaction mechanisms of FG reduction and nucleophilic substitution, we have investigated the reaction of FG with three nucleophilic species (NH_2^- , OH^- , and CN^-) in four different solvents (THF, acetone, methanol, and DMF) and in the gas phase (Appendix C, section 3.3).⁶⁸ The reaction energy profiles of $\text{S}_{\text{N}}2$ mechanism showed a high reaction barrier in solvents ($\sim 50 \text{ kcal}\cdot\text{mol}^{-1}$) and a moderately high barrier in the gas phase ($\sim 20\text{-}37 \text{ kcal}\cdot\text{mol}^{-1}$), which was inconsistent with the experimentally determined activation energy ($14 \pm 5 \text{ kcal}\cdot\text{mol}^{-1}$) in methanol.⁶⁰ Consequently, the $\text{S}_{\text{N}}2$ reaction pathway of pristine

FG was not a plausible explanation of the high reactivity of FG. Therefore, we have also considered a nucleophilic attack on the radical sites. Indeed, this reaction mechanism was found to be energetically favourable for all three considered nucleophilic species in all environments. Moreover, the attack on FG radical site can cause further defluorination because the nucleophilic species contribute a negative charge to the material, and the C–F bonds in the vicinity become susceptible to heterolytic cleavage.

1.3. The Nature of C-F Bonds

The C–F bond characteristics of (p)FGs have attracted attention since they may help to explain the unexpected reactivity of the material. Experimentally, FT-IR and XPS revealed that the C–F bonds exhibit different polarity in FGs exfoliated in acetonitrile (ACN) and chloroform from graphite fluoride (Figure 6).⁴² The peak at 1216 cm^{-1} and the shoulder at 1312 cm^{-1} in the FT-IR spectra of FG exfoliated in ACN (FG-1) were attributed to the covalent C–F and C–F₂ bonds. However, in the FT-IR spectrum of FG exfoliated in chloroform (FG-2), there was an additional peak at 1143 cm^{-1} attributed to semi-ionic C–F bond, and the peaks of covalent C–F bonds were smaller. These observations were supported by the C 1s XPS spectrum of FG-1 with peaks at 290.02, 291.01, and 292.01 eV of covalent C–F, C–F₂, and C–F₃ bonds and the XPS spectrum of FG-2 with one additional peak at 288.44 eV of semi-ionic C–F bond (Figure 7). The corresponding F 1s XPS spectra confirmed these findings.

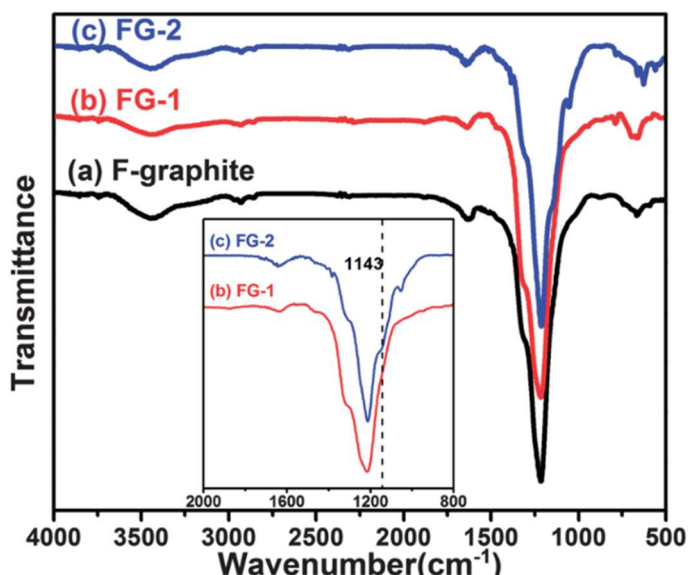


Figure 6: FT-IR spectra of a) fluorinated graphite, b) FG exfoliated in ACN, and c) FG exfoliated in chloroform. Figure is from ref. 42.

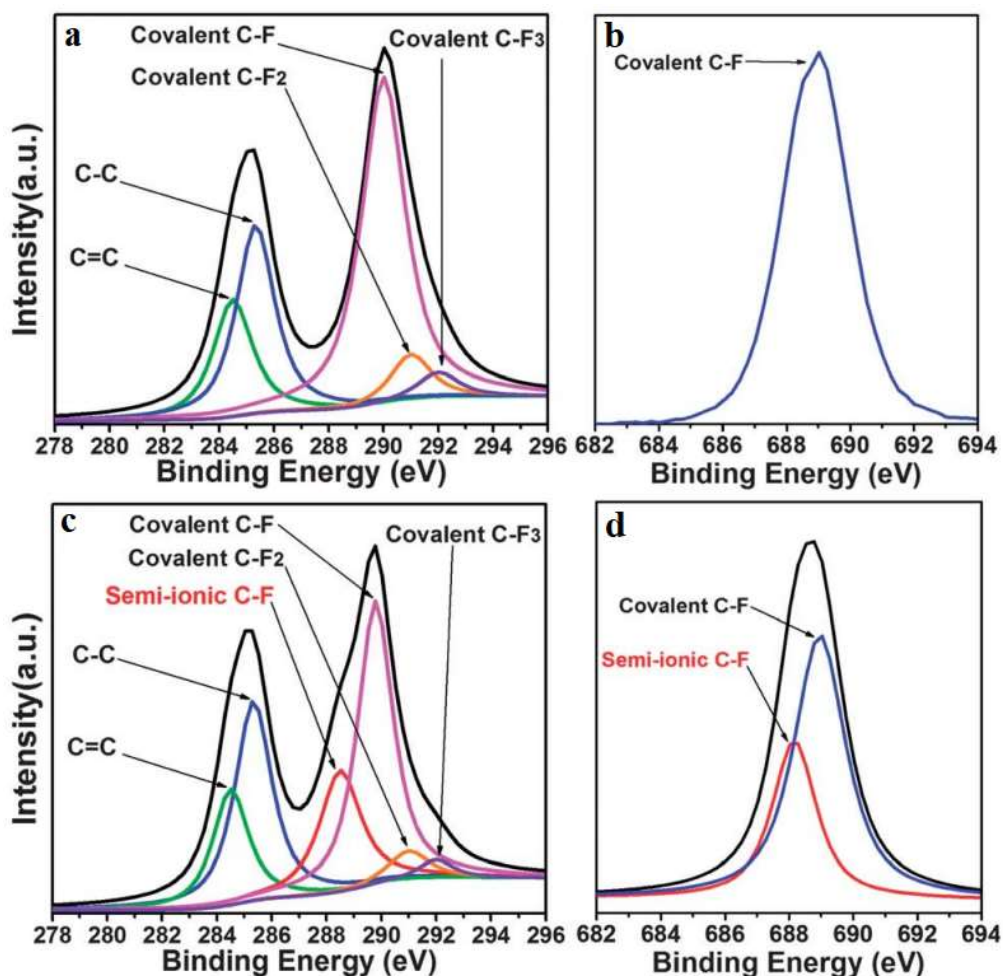


Figure 7: High resolution XPS spectra of a) C 1s and b) F 1s of FG exfoliated in ACN, and c) C 1s and d) F 1s of FG exfoliated in chloroform. Figure is from ref. 42.

The polarity of C–F bond changes during fluorination and depends on the level of fluorination. The XPS and FT-IR spectra of (p)FGs in samples fluorinated by XeF₂ for different times demonstrated the variability of C–F bonds (Figure 8).⁶⁹ With the increasing fluorination time, an absorption band at 1112 cm⁻¹ that was attributed to semi-ionic C–F bonds appeared and gradually changed into a band at 1211 cm⁻¹ that indicated the presence of covalent C–F bonds. The same trend was confirmed by the C 1s and F 1s spectra. The peak at 284.6 eV in C 1s spectrum of pristine graphene gradually shifted to 287.5 eV. From the F 1s spectra, the peak of semi-ionic C–F bonds at 685.5 eV was shifted to 687.5 eV that was attributed to covalent C–F bonds.

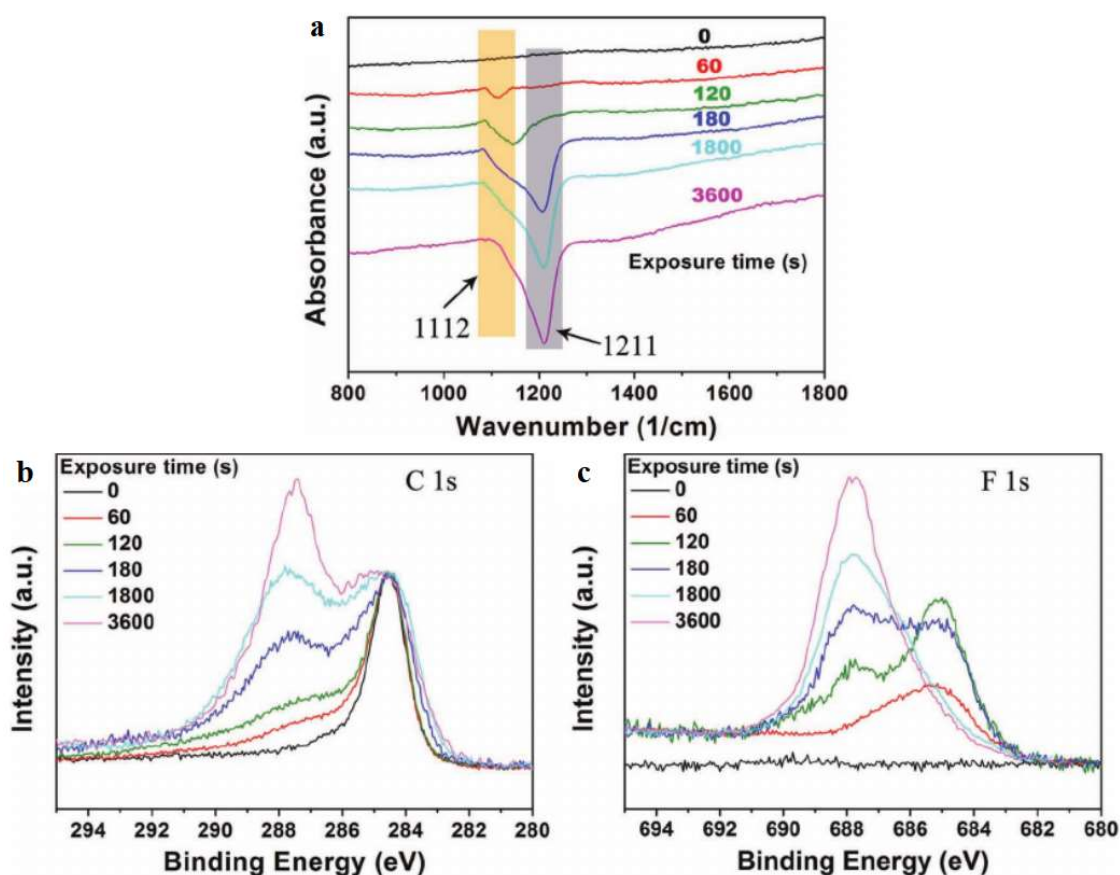


Figure 8: Evolution of a) FT-IR, b) C 1s XPS, and c) F 1s XPS spectra of graphene fluorinated by XeF₂. Figures are from ref. 69.

DFT calculations showed that BDE of C–F bond varies with the level of fluorination from ca. 110 kcal·mol⁻¹ in the case of C–F bonds in fluorinated areas to 50 kcal·mol⁻¹ for an isolated C–F bond. The C–F bonds are elongated with a decreasing number of fluorine ad-atoms from ca. 1.4 Å to 1.6 Å.^{22, 28, 60, 70, 71} Current explanations of these concentration-dependent properties of C–F bonds can be divided into two groups. First, the nature of C–F bonds depends on the concentration of fluorine ad-atoms and varies from semi-ionic to covalent.^{45, 72} Second, the C–F bonds are always covalent, and the variability of the properties of (p)FGs is caused by differences in π -conjugation of C–C bonds,⁷³ deformation of the graphene plane due to the change of hybridization of carbon atoms,⁷⁴ or by different local conformations of C–F bonds.⁶

Zhou *et al.*⁷² investigated in detail the nature of C–F bonds by using DFT methods in calculations of core-level XPS binding energies of C and F atoms in different bonding states. In particular, a physisorbed fluoride anion, isolated C–F bonds, C–F bonds on the edge and in the centre of a fluorinated area, and C–F bonds on the edge of a graphene sheet were considered (Figure 9). The value of 1s core-level binding energy of the fluorine ad-atom in the isolated C–F bond (light green abscissa in Figure 9) was predicted to be in between the values of the

physisorbed fluoride anion (dashed black abscissa) and the covalent C–F bond on the edge (orange abscissa). Therefore, the nature of an isolated C–F bond is halfway between ionic and covalent and can be regarded as semi-ionic. The XPS binding energies of C–F bonds in the centre of the fluorinated area (cyan abscissa) differed only by 0.4 eV from those on the edges of the graphene sheet which confirmed their strong covalent character. It is also worth noting that the C–F bond shortens with the increasing covalency.

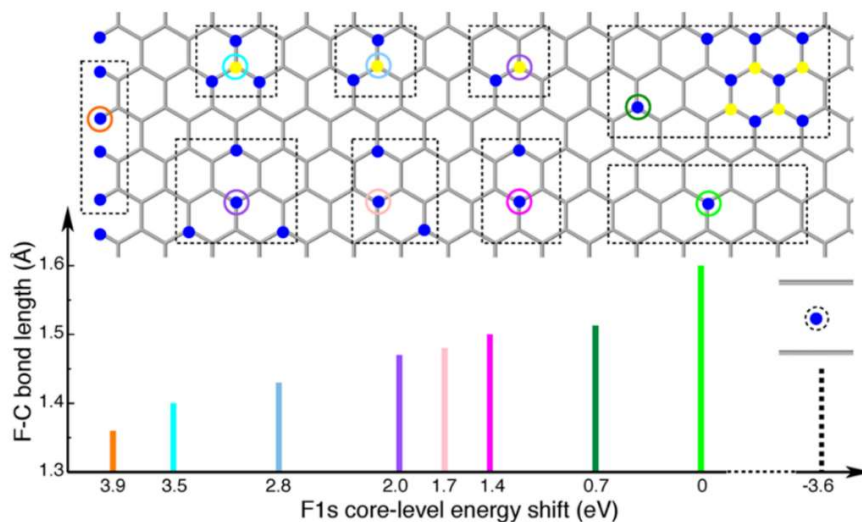


Figure 9: XPS F 1s core-level energy shifts (x-coordinates) and length of C–F bonds (y-coordinates) in different bonding environments. Figure is from ref. 72.

1.4. Structural Motifs in Fluorinated Graphene

In the structure of low-fluorinated graphene, fluorine ad-atoms preferentially bind to the *ortho trans* or *para trans* positions of the carbon hexagons to minimize the repulsion between their negative partial charges and maximize the size of the π -conjugated network. On the other hand, the *meta cis* position is the least favourable due to the high repulsion between close fluorine ad-atoms, consequent deformation of the graphene plane, and disruption of the π -conjugation. If the fluorination occurs only on one side of the graphene plane, fluorine ad-atoms preferentially arrange in *para cis* positions. A highly electronegative fluorine atom creates partial positive charges on neighbouring carbon atoms. Therefore, further fluorination preferentially leads to structures with fluorine ad-atoms arranged in short chains and/or in perfluorinated domains separated by π -conjugated graphene-like areas.^{72, 75-80}

Lee *et al.*⁸⁰ described in detail the mechanism of graphene fluorination by XeF₂ using periodic DFT. In the case of one-side fluorination, the first two fluorine ad-atoms were attached on carbons that were not members of the same hexagonal ring (Figure 10b). Since the activation barriers ($E_a \cong 21 \text{ kcal}\cdot\text{mol}^{-1}$) and reaction energies (E_R from -1.1 to $4.9 \text{ kcal}\cdot\text{mol}^{-1}$) were

comparable for all resultant configurations of fluorine ad-atoms, the position of ad-atoms was mainly given by the initial orientation of the XeF_2 molecule above the graphene plane (Figure 10a). A perpendicular position of XeF_2 (Pre-1) did not lead to fluorination. Further fluorination preferably led to the formation of fluorine ad-atoms in *para cis* positions separated by conjugated hexagonal rings. The situation was different during the fluorination on both sides of the graphene plane. In the first reaction step, the system had to overcome a similar reaction barrier as in the case of one-side fluorination ($E_a = 21.7 \text{ kcal}\cdot\text{mol}^{-1}$, TS-1 in Figure 11a) and reached an intermediate state in which one XeF_2 molecule had already reacted with graphene while the second XeF_2 molecule was ready to react on the other side of the graphene plane (INTER). The second reaction step with the reaction barrier of $E_a = 12.7 \text{ kcal}\cdot\text{mol}^{-1}$ (TS-2) resulted in an energetically favourable product, i.e., graphene with two pairs of fluorine ad-atoms in *ortho trans* positions ($E_R = -44.7 \text{ kcal}\cdot\text{mol}^{-1}$, POST). Consequently, only 25% coverage by fluorine ad-atoms was obtainable by fluorination of one side of the graphene plane, while 100% coverage was achievable by fluorination of both sides of the graphene plane. The fluorination of defective graphene was also considered. The reaction profile of XeF_2 bonding on defective graphene with one carbon atom missing (Figure 11b) clearly showed that fluorination preferably takes place on sites with dangling bonds such as vacancies and edges.

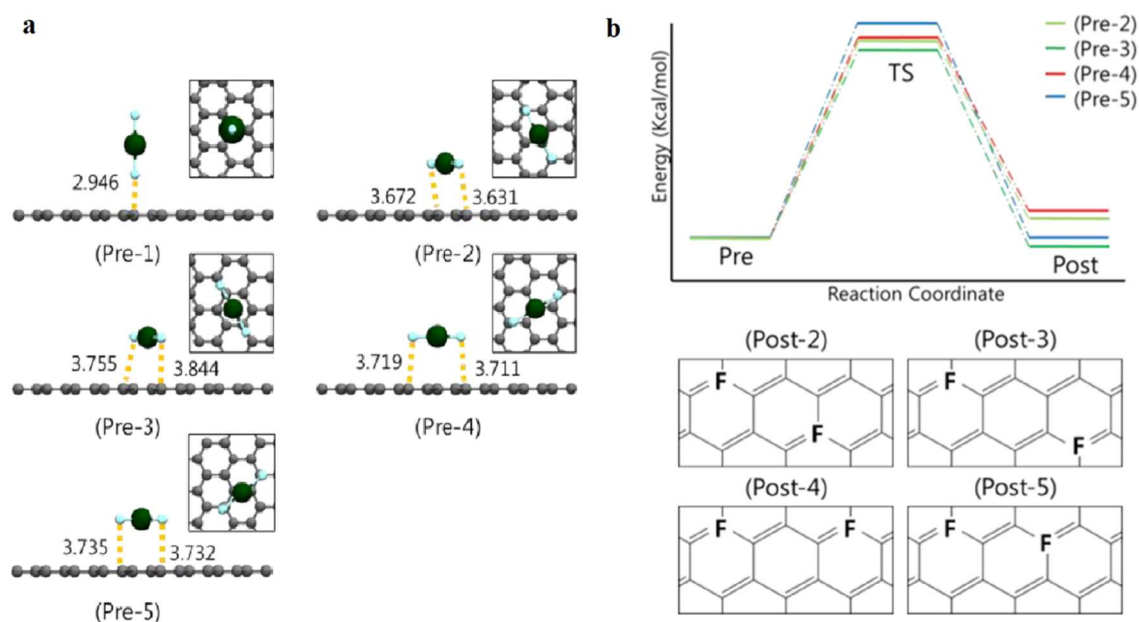


Figure 10: a) Initial orientation of an XeF_2 molecule above the graphene plane and b) top: comparison of reaction profiles of attachment of the first two fluorine ad-atoms starting from different initial orientations of the XeF_2 molecule, and bottom: resultant positions of the fluorine ad-atoms. Xenon atoms are green, fluorine blue, and carbon grey. Bond lengths are in Å, energies are in $\text{kcal}\cdot\text{mol}^{-1}$. Figures are from ref. 80.

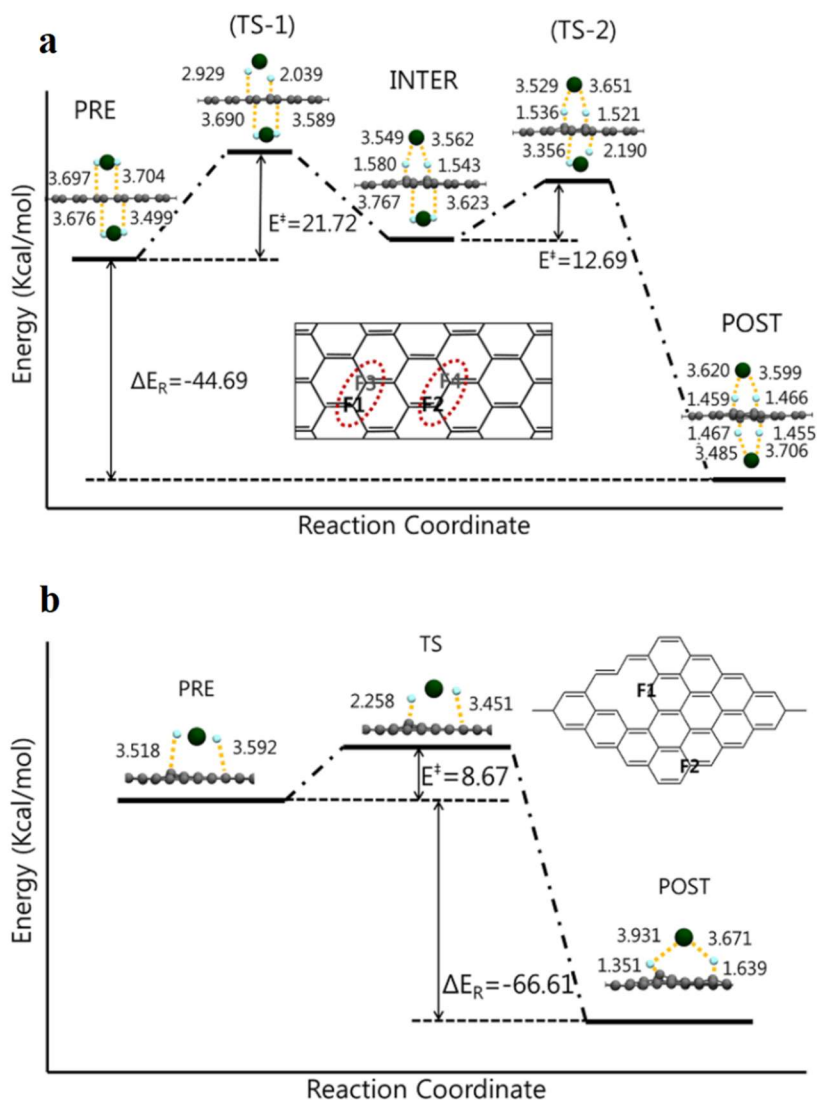


Figure 11: a) Reaction profile of first two reaction steps of both-side fluorination by XeF_2 molecule and b) reaction profile of the first reaction step of fluorination XeF_2 molecule on a single vacancy in the graphene plane. Xenon atoms are green, fluorine blue, and carbon grey. Bond lengths are in \AA , energies are in $\text{kcal}\cdot\text{mol}^{-1}$. Figures are from ref. 80.

Step-by-step modelling of graphene fluorination using DFT methods by Boukhvalov⁷⁵ confirmed the tendency to form fluorinated chains along armchair directions due to lower deformation of the graphene plane than in the case of zigzag chains. The lowest formation energy corresponded to a structure with the $\text{CF}_{0.935}$ stoichiometry, where only one chain of carbon atoms remained conjugated while the rest was fully fluorinated. This explains the difficulty to experimentally obtain 100% fluorinated material. Since freshly fluorinated (p)FGs obtain a distribution of different fluorination motifs and in time these motifs can relax to the energetically preferable configuration,^{71, 81} rearrangement of ribbon-like structure of fluorinated and nonfluorinated areas into the structure of alternating fluorinated and

nonfluorinated chains was also studied.⁷⁵ The first step of two fluorine ad-atoms moving from fluorinated area into pristine area was found to be the most energetically demanding ($\Delta E = 0.53$ eV) because the uniform structure of the pattern was disrupted (Figure 12). Every next step appeared to be less endothermic, and some were found even exothermic. In addition, the energy barrier of fluorine ad-atoms migration decreased with the increasing level of fluorination from ca. 1.3 to 0.4 eV and then again increased when fluorination reached 93.5% that corresponded to the most stable stoichiometry of $\text{CF}_{0.935}$. Therefore, it was concluded that rearrangements of fluorine ad-atoms might occur even at room temperature.

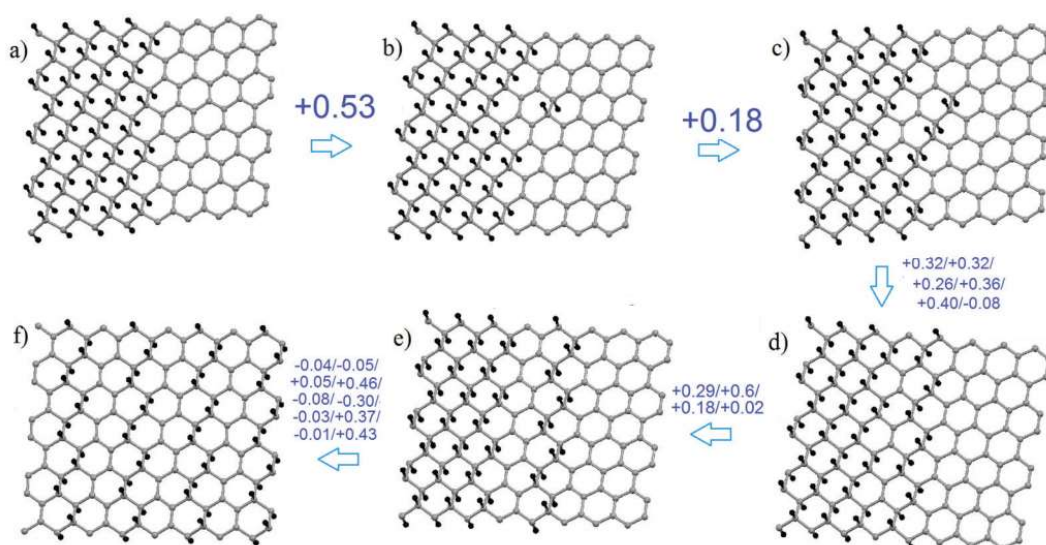


Figure 12: The total energy differences of structures along the way of rearrangement of ribbon-like structure of fluorinated and nonfluorinated areas into the structure of alternating fluorinated and nonfluorinated chains. Values are in eV. Carbon atoms are grey, fluorine black. Figure is from ref. 75.

Magic angle spinning nuclear magnetic resonance (MAS NMR) in combination with DFT calculations revealed that various structural motives (isolated fluorine ad-atoms, chains of zigzag and armchair configuration, and fluorinated cyclohexane rings) might be present in (p)FGs of different stoichiometry (Figure 13).^{71, 81} X-ray absorption near edge structure (XANES) and Raman spectra confirmed that fluorinated chains and islands separated by π -conjugated areas occur in the structure of (p)FGs.⁸¹ These areas could be responsible for a narrower bandgap of (p)FGs compared to FG. Therefore, it can be concluded that fluorination is not led only by thermodynamics but also by stochasticity. That means that a degree of randomness during fluorination influences the distribution of fluorinated sites over the graphene plane. Let us recall that the stability of (p)FGs may be affected by the presence of stronger and weaker C–F bonds and by various structure defects like grain boundaries, vacancies, and dislocations.

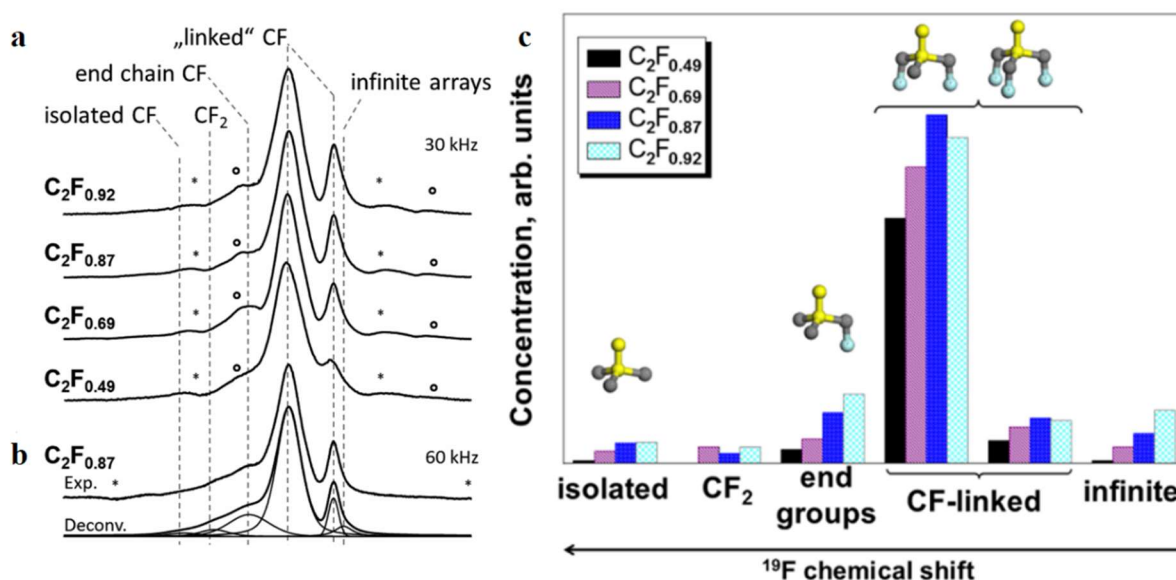


Figure 13: a) ^{19}F MAS NMR spectra at 30 kHz of pFGs of different stoichiometry, b) top: ^{19}F MAS NMR spectrum at 60 kHz of pFG of stoichiometry $\text{C}_2\text{F}_{0.87}$ and bottom: its deconvolution, c) quantification diagram obtained by integration of the ^{19}F MAS NMR spectra weighted by fluorine content. Figures are from ref. 71.

All these findings are discussed in our study about the intriguing variability of C–F bonds (Appendix A, section 3.1)⁸² in which we demonstrate that the strength of C–F bonds strongly depends on the local arrangement of fluorine ad-atoms and the level of fluorination, and thus -unlike in molecular organic chemistry- it cannot be viewed as the strongest chemical bond in 2D chemistry. As a result, the properties of (p)FGs may be influenced by the method of fluorination and may evolve in time as the material relaxes into the thermodynamically most favourable configuration. Moreover, the reactivity of (p)FGs changes during chemical reactions in very complex ways, demonstrating that the chemistry of (p)FGs cannot be compared with molecular chemistry in one-to-one fashion.

1.5. Graphene Derivatives Derived from Fluorographene

FGs attract attention as promising precursors for other graphene derivatives due to their (i) high thermal stability, (ii) cheap synthesis from graphite fluoride that is available in a large scale as an industrial lubricant, (iii) well-defined structure that is guaranteed by the adsorption of monovalent fluorine atoms which prevents the formation of non-stoichiometric structures, and (iv) susceptibility to reductive defluorination and nucleophilic substitution. FG chemistry opens a road to a plethora of new graphene derivatives such as amino,⁸³⁻⁸⁵ hydroxyl,^{86, 87} and

sulfur-linked derivatives,^{88, 89} alkylated graphene,^{90, 91} CG, and GA.⁹² They can be utilized in a wide portfolio of applications including (bio)sensing, bioimaging, medicine, water purification, chemical catalysis, electronics, photonics, spintronics, and energy storage.^{93, 94}

Synthetic procedures of covalent functionalization take advantage of the electrophilic character of FG defects and are mostly based on simultaneous nucleophilic substitution and defluorination of the material.⁵⁹ For example, graphene functionalized by –CN groups (CG) can be prepared by a reaction of FG with NaCN in DMF.⁹² The reaction leads effectively to total defluorination (less than 1% of fluorine content remains) which is associated with a partial replacement of fluorine ad-atoms by nitrile groups. The π -conjugation of graphene sheets is in part restored, and the conductivity of the material is recovered. The resultant material contains 11.4 at. % of N homogenously distributed over the graphene plane. By addition of 20% HNO₃, the –CN functionalities are oxidized into –COOH groups, and a new graphene derivative called graphene acid (GA) is obtained. The nitrile and carboxylic groups of CG and GA can be utilized for anchoring single metal atoms and cations which offer a great potential as SACs (Appendix E, section 4.1).⁹⁵⁻⁹⁷ For example, Co²⁺ cations immobilized on CG have an outstanding performance in electrocatalytic hydrazine oxidation reaction as reported in our work (Appendix F, section 4.2).⁹⁸ On the other hand, the total defluorination can be undesirable in some applications, and thus alternative approaches for (p)FGs functionalization are explored. Recently, a novel method for covalent functionalization through activation of dormant radicals was used to graft acrylic acid and styrene on the pFG surface without the loss of fluorine ad-atoms.⁹⁹

New graphene derivatives are also accessible via the replacement of carbon atoms with other elements such as boron, nitrogen, sulfur, phosphorus, and silicon. Among others, boron and nitrogen are the best dopants, since they do not differ significantly from carbon in size. Incorporation of boron and nitrogen into the hexagonal lattice of graphene alters its band structure and results in n-type and p-type materials with unique properties which can be used in supercapacitors, batteries, fuel cells, catalysis, and water splitting.^{100, 101} However, the methods of graphene doping with nitrogen require high temperatures (usually ≥ 800 °C) or solvothermal treatment and annealing which makes them rather energy-demanding and cost-ineffective.¹⁰² Recently, FG was studied as a promising precursor also for heteroatom-doping.¹⁰³⁻¹⁰⁵

Like the covalent functionalization of (p)FGs, heteroatom doping is also accompanied by extensive defluorination. For instance, Li *et al.*¹⁰⁶ proposed that N-doping of FG is accessible via direct doping by ammonia gas that is accompanied by defluorination. Experimental data in

combination with DFT calculations revealed that ammonia molecules could substitute C–F bonds and create C–NH₂ groups. The reaction then proceeded via defluorination and deprotonation of C–NH₂ groups that was accompanied with releasing of HF molecules. Consequently, nitrogen was cyclized into aziridinic groups and rearrangement of atoms that led to the incorporation of nitrogen was anticipated. However, in our work (Appendix D, section 3.4)¹⁰⁷ about the reaction mechanism of FG N-doping by NaNH₂ was demonstrated that the rearrangement of aziridinic groups and consequent incorporation of nitrogen into the unperturbed structure of FG is improbable. More likely, the NH₂[−] anion is bounded into vacancies in FG lattice. This nucleophilic attack is followed by expansion or healing of the vacancy.

In general, the mechanisms of both covalent functionalization and heteroatom doping are rather unexplored. The knowledge of possible reaction mechanisms may offer new routes to graphene materials applicable in many interesting fields of science. The ability to precisely control the derivatization process is essential to sensitively alter the properties of the obtained material. In this work, we have significantly contributed to the understanding of FG's unique chemistry.

2. Methods

Computational methods are nowadays increasingly used as indispensable complementary tools for experimental research. A rich palette of theoretical approaches can be applied to explain and predict various experimentally observed phenomena. To investigate the chemistry of FG and its derivatives, either electronic structure methods -explicitly describing the electronic structure of the material- or methods of molecular mechanics -simplifying the studied system as a set of van der Waals spheres and thus not dealing with individual electrons- can be employed. The choice of a computational method depends on the size of the system and the properties of interest. In this work, DFT methods were mostly applied.

2.1. Density Functional Theory

The popularity of DFT has been rapidly increasing during the last three decades thanks to its relatively low computational costs and good results.¹⁰⁸ The central quantity of DFT is the electron density $\rho(\vec{r})$ defined as a multiple integral over the spin coordinates of all electrons and over all except one spatial coordinate.

$$\rho(\vec{r}) = N \int \dots \int |\Psi(\vec{x}_1, \vec{x}_2, \dots, \vec{x}_N)|^2 ds_1 d\vec{x}_2 \dots d\vec{x}_N \quad (1)$$

The electron density determines the probability of finding one electron in the spatial volume $d\vec{r}$ with arbitrary spin while the other $N-1$ electrons are in arbitrary positions having arbitrary spins (\vec{x}_N), if the system is in a state Ψ . Electron density is thus a non-negative function of three spatial variables that integrates to the total number of electrons. One important property of $\rho(\vec{r})$ is that it reaches finite maxima at the positions of nuclei. The electron density is also observable experimentally by XRD.

The major theoretical pillars of DFT are Hohenberg-Kohn theorems. The first Hohenberg-Kohn theorem says that the electron density uniquely determines the Hamilton operator and thus all properties of the system. The second Hohenberg-Kohn theorem is speaking about an energy functional for the system and demonstrates that the exact $\rho(\vec{r})$ of the ground state minimizes the energy functional. Using the Born-Oppenheimer approximation, the electronic energy functional can be written as

$$E_e[\rho(\vec{r})] = T[\rho(\vec{r})] + V_{en}[\rho(\vec{r})] + J[\rho(\vec{r})] + Q[\rho(\vec{r})] \quad (2)$$

where $T[\rho(\vec{r})]$ is the kinetic energy of all electrons, $V_{en}[\rho(\vec{r})]$ is the interaction energy of electrons and nuclei, $J[\rho(\vec{r})]$ includes the classical Coulombic repulsion between electrons,

and $Q[\rho(\vec{r})]$ is the non-classical interaction energy between electrons. While the terms $V_{en}[\rho(\vec{r})]$ and $J[\rho(\vec{r})]$ are known and can be computed, the exact form of $T[\rho(\vec{r})]$ and $Q[\rho(\vec{r})]$ terms is still unknown.

The simplest approximation of $T[\rho(\vec{r})]$ is the Thomas-Fermi model that was derived for an imaginary system of uniform electron gas. This approximation is applicable only to systems with nearly uniform densities (such as some semiconductors and alloys) and is not appropriate for most systems in which chemists are interested. This inconvenience can be circumvented by Kohn-Sham's methodology, in which a Slater determinant is used as an exact solution for the system of non-interacting electrons. The part of $T[\rho(\vec{r})]$ that is not described by the Kohn-Sham's approach and $Q[\rho(\vec{r})]$ are then combined into a so-called exchange-correlation energy term, $E_{XC}[\rho(\vec{r})]$. This exchange-correlation functional is not known and needs to be approximated.

DFT functionals can be generally divided according to the level of approximation applied. The local density approximation (LDA) provides the simplest functionals that depend only on the density at the point in space where the functional is evaluated. An improvement offers the general gradient approximation (GGA) which implements the gradient of the electron density. In other words, GGA functionals use LDA as the first term in Taylor expansion and calculate also the second term. By adding the second derivative of the electron density (sometimes called the density of kinetic energy), we obtain meta-GGA functionals. A real boom of DFT was achieved thanks to hybrid functionals that combine the exact exchange energy from the Hartree-Fock method with approximative DFT functionals. The family of DFT functionals is still expanding. So far, hundreds of DFT functionals have been developed. A proper choice of the approximative exchange-correlation functional is a crucial step in every DFT calculation.^{109, 110} In the following, we only focus on the functionals that have been employed in this work.

PBE functional

The PBE (Perdew, Burke, Ernzerhof) functional¹¹¹ belongs to the class of parameter-free GGA functionals, i.e., it does not contain experimentally fitted parameters as many other functionals do. Instead, it is solely based on fundamental constants and physical arguments. It is based on the general features of the Perdew-Wang 1991 (PW91) functional and includes an improved description of the exchange-correlation term. The PBE functional is often used for its efficiency and relatively good results in a wide range of systems. It is worth noting that PBE does not include dispersion interactions. If such interactions are expected to be important, it is

possible to add them as an empirical correction. In this work, we have employed the PBE-D2 method with Grimme's correction to the total energy

$$E_{disp} = -s_6 \sum_{i=1}^{N_{at}-1} \sum_{j=i+1}^{N_{at}} \frac{C_6^{ij}}{R_{ij}^6} f_{dmp}(R_{ij}) \quad (3)$$

where N_{at} is the number of atoms, C_6^{ij} is the dispersion coefficient for a pair of atoms i and j , s_6 is the scaling factor, R_{ij} is the distance between two atoms, and f_{dmp} is a dumping function to suppress the dispersion interaction on small distances between the atoms.¹¹²

PBE0 functional

The PBE0 functional^{113, 114} mixes the PBE and Hartree-Fock exchange energy terms and thus belongs to hybrid functionals. The correlation energy is calculated in the same manner as in PBE. The form of this exchange-correlation functional is:

$$E_{XC}^{PBE0} = \frac{1}{4} E_X^{HF} + \frac{3}{4} E_X^{PBE} + E_C^{PBE} \quad (4)$$

E_X^{HF} is the Hartree-Fock exchange energy, E_X^{PBE} is PBE exchange energy, and E_C^{PBE} is PBE correlation energy. The PBE0 functional is applicable in a wide range of calculations including structural, thermodynamic, and kinetic properties. Moreover, it usually gives reasonable results for time-dependent calculations of excitation energies, although its performance depends on the type of transition.¹¹⁴

ω B97X-D functional

The ω B97X-D functional¹¹⁵ is a long-range corrected hybrid functional. That means that it includes a correction for long-range exchange interactions. It is based on the ω B97X functional¹¹⁶ that works with exchange-correlation functional defined as

$$E_{XC}^{\omega B97X} = E_X^{LR-HF} + aE_X^{SR-HF} + bE_X^{SR-B97} + E_C^{B97} \quad (5)$$

where E_X^{LR-HF} is the long-range Hartree-Fock exchange energy, E_X^{SR-HF} is the short-range Hartree-Fock exchange energy, E_X^{SR-B97} is the short-range exchange energy from B97 functional, and E_C^{B97} is the correlation energy from B97 functional. Hundred percent of the exact Hartree-Fock exchange energy in the long-range limit eliminates the long-range self-interaction error. In the short-range limit, a part of the exchange energy is calculated using the Hartree-Fock method and a part using the B97 functional. The ratio of Hartree-Fock and B97 exchange energy contributions in the short range is determined by a splitting operator that

depends on the variable ω parametrized on a diverse training set. To include dispersion interactions, it uses an empirical correction similarly as PBE-D2 (Eq. 3). This makes ω B97X-D applicable in calculations of atomization energies, barrier heights, atomic energies, and intermolecular interactions.

2.2. Finite-size versus Periodic Systems

Depending on the property or process of interest, FG being 2D material can be modelled as either a finite-size system (flake) or a 2D-periodic structure (slab). While in the former case a full armoury of molecular quantum chemistry methods available in computational chemistry can be employed, in the latter case, approaches taking advantage of periodic boundary conditions (PBC) can be applied.

Solution for molecules

In molecular quantum chemistry, it is convenient to use atomic orbitals as building blocks for constructing the wave function or electron density of a system. For example, in orbital-based DFT, one-electron Kohn-Sham orbitals composing the Slater determinant are expanded as a linear combination of atomic basis functions $\{\eta_\mu\}$:

$$\varphi_i = \sum_{\mu=1}^L c_{\mu i} \eta_\mu \quad (6)$$

If a complete basis set is used ($L = \infty$), an exact solution is obtained. However, in practice, a finite basis set must be used, and it is important to choose a suitable basis set for the studied problem. If not stated otherwise, the Pople's double-zeta 6-31++G(d,p) basis set¹¹⁷ containing both polarization and diffusion functions was employed in mechanistic studies of reactions involving (p)FG and other graphene derivatives. In the case of systems involving transition metals, the def2-SVPP and def2-TZVP basis sets^{118, 119} from the Ahlrichs def2 basis set family reasonably describing electronic structure of molecules consisting of transition metals and main group elements were employed.¹²⁰

Solution for periodic systems

In crystalline structures is every electron influenced by an average potential $U(\vec{r})$ that includes the interaction with nuclei and with all other electrons. Since the structure of a crystalline material can be constructed as a periodic repetition of an elementary cell, $U(\vec{r})$ is also periodic and invariant to the operation of translation by an arbitrary vector of the Bravais cell. Bloch's theorem states that in the periodic potential the solution of Schrödinger equation $\psi_{\vec{k}}(\vec{r})$ is

in a form of plane waves multiplied by a periodic function $u_{\vec{k}}(\vec{r})$ that has the same periodicity as the structure of the crystal:

$$\psi_{\vec{k}}(\vec{r}) = e^{i\vec{k}\cdot\vec{r}} u_{\vec{k}}(\vec{r}) \quad (7)$$

\vec{r} defines position and \vec{k} is the wave vector. To find a solution of the Schrödinger equation in the periodic potential, it is convenient to transform from the real space into the reciprocal space (k -space) using the Fourier transformation. The periodic potential can then be expanded in terms of a set of plane waves.

$$U(\vec{r}) = \sum_{\vec{G}} U_{\vec{G}} e^{i\vec{G}\cdot\vec{r}} \quad (8)$$

\vec{G} are reciprocal lattice vectors. The wave function must also fulfil the Born-von Karman boundary conditions. The resultant form of the wave function is the following:

$$\psi_{\vec{k}}(\vec{r}) = \sum_{\vec{G}} C_{\vec{k}+\vec{G}} e^{i(\vec{k}+\vec{G})\cdot\vec{r}} \quad (9)$$

Since evaluation of $\psi_{\vec{k}}(\vec{r})$ would involve a summation over an infinite number of possible values of the vector \vec{G} , in practice we take advantage of the interpretation of $\psi_{\vec{k}}(\vec{r})$ as a solution of the Schrödinger equation with kinetic energy $E = \frac{\hbar^2}{2m} |\vec{k} + \vec{G}|^2$. Then it is possible to truncate the infinite sum by considering only functions with a kinetic energy lower than the so-called cut-off energy. Therefore, the commonly used approach in PBC calculations is to define the number of plane waves used as the basis set by setting the maximum value of their kinetic energy.^{121, 122} To investigate the nature of C–F bond in (p)FGs and to assess the most stable vacancies in FG lattice a minimum cut-off energy of 400 eV was employed.

2.3. Solvent Models

Since most of the experiments are performed in the liquid environment, the possibility to run calculations that account for solvent effects is vital. There are three types of solvation models that can be utilized. First, explicit solvent models are based on considering explicit solvent molecules in the model system. As the system size increases rapidly with the number of solvent molecules, this approach becomes computationally very demanding for physically relevant systems and is used mostly in molecular mechanics, molecular dynamics, and Monte Carlo simulations. Second, implicit solvent models replace the solvent by a homogeneous polarizable medium that is characterized by the dielectric constant and other parameters, for example, molecular surface area or solute atomic radii. The calculation with implicit solvent starts with

encapsulating the solute molecule into a cavity created in the solvent continuum. The charge distribution of the solute molecule is changed due to the solvent. In return, the surrounding medium is also polarized, which causes additional polarization of the solute charge distribution. This response to the change of polarization is called a reaction field and must be iterated to self-consistency. Third, hybrid solvent models combine both previous approaches, i.e., a few molecules are added explicitly, and the rest of the solvent is included implicitly. This method is important in systems in which specific interactions such as hydrogen bonds play an important role or if the solvent molecule enters the studied reaction mechanism.¹⁰⁹ In all calculations of this thesis, the *universal continuum solvation model based on density* (SMD) was applied.¹²³

The SMD model is based on the full electron density of a solute molecule that interacts with solvent described as a continuum parametrized using a few descriptors: dielectric constant, bulk surface tension, refractive index, acidity, and basicity parameters. The term ‘universal’ in its name denotes the applicability for any solute-solvent system. In SMD, the Gibbs solvation energy, i.e., the energy needed to transfer the solute molecule from the gas phase into the solvent, is evaluated as

$$\Delta G_S^0 = \Delta G_{ENP} + G_{CDS} \quad (10)$$

where ΔG_{ENP} is the electronic, nuclear and polarization component, and G_{CDS} includes energy changes in the cavitation and dispersion energy and possible changes in local solvent structure. The first component is calculated by self-consistent reaction field (SCRF) treatment including solution of the non-homogeneous Poisson equation for electrostatics. The second component involves the contribution of short-range interactions between the solute molecule and solvent molecules in the first solvation shell. The solvation energy is also dependent on the construction of the cavity. The cavity in SMD model is created using the solvent-accessible surface area (SASA) of the solute molecule which depends on the atomic van der Waals radii.¹²³

3. On Track to Explore the Chemistry of Fluorographene

As already mentioned, FG is a promising precursor for the synthesis of new graphene derivatives such as CG, GA, sulfurhydryl derivatives, aminographenes, etc.^{83-85, 88, 89, 92} The susceptibility of FG to reductive substitution can be utilized for grafting various functional groups to the graphene lattice. To control the composition and topology of the new graphene-based 2D materials, and thus their properties, it is essential to understand the reaction mechanisms and processes that accompany the chemical transformations of FG.

3.1. Variability of the C–F Bond Nature Influences the Formation of Specific Structural Motifs in Fluorinated Graphene

Previous studies demonstrated that the nature of C–F bonds in (p)FGs is complex and is dependent on the topology and fluorination level of the material.^{22, 28, 42, 60, 69-72} With the increasing amount of fluorine ad-atoms the C–F bonds shorten and change from semi-ionic to covalent.^{22, 72, 78} In low-fluorinated graphene, the F ad-atoms preferentially bind to *ortho trans* positions to minimize the repulsion between negative partial charges on fluorine ad-atoms and to minimize the disruption of C–C bonds π -conjugation.^{72, 75, 78, 80} As the level of fluorine content increases, the structure adopts configuration with ribbons, islands, and chains of ad-atoms separated by π -conjugated areas.⁸¹ By controlling the level of fluorination and geometric structure, we can obtain materials with different conductivity (the bandgap ranges from 0 to 3.1 eV) and magnetic properties.^{24, 26, 86} Therefore, a deep understanding of the nature of C–F bonds and the rules that govern the formation of specific structural motifs in (p)FGs is needed. The comprehension of the C–F bonding can also offer new knowledge about chemical bonding in general, especially in the 2D materials world.

Despite the C–F bond is commonly considered as the strongest in organic chemistry,¹²⁴ in (p)FGs its strength and length vary considerably. Our calculations revealed (Appendix A)⁸² that the BDE of C–F bond ranges from 27.1 to 106.7 kcal·mol⁻¹ and its length ranges from 1.38 to 1.59 Å. In comparison to the average C–F bond strength in common organic molecules (105.4 kcal·mol⁻¹), most of the calculated BDEs is significantly lower. In addition, the C–F bonds in (p)FGs are longer than typical C–F bonds in aromatic organic compounds by ca. 0.1-0.2 Å.¹²⁴ Surprisingly, a common rule -the longer bond, the weaker bond- is not generally applicable in (p)FGs (Figure 14). The correlation between the C–F bond length and BDE is not at all simple. For instance, both the lowest and highest BDE values belong to the bond lengths of ca. 1.43 Å. These results are in agreement with the average C–F bond length in (p)FGs reported by Vyalikh *et al.*⁷¹

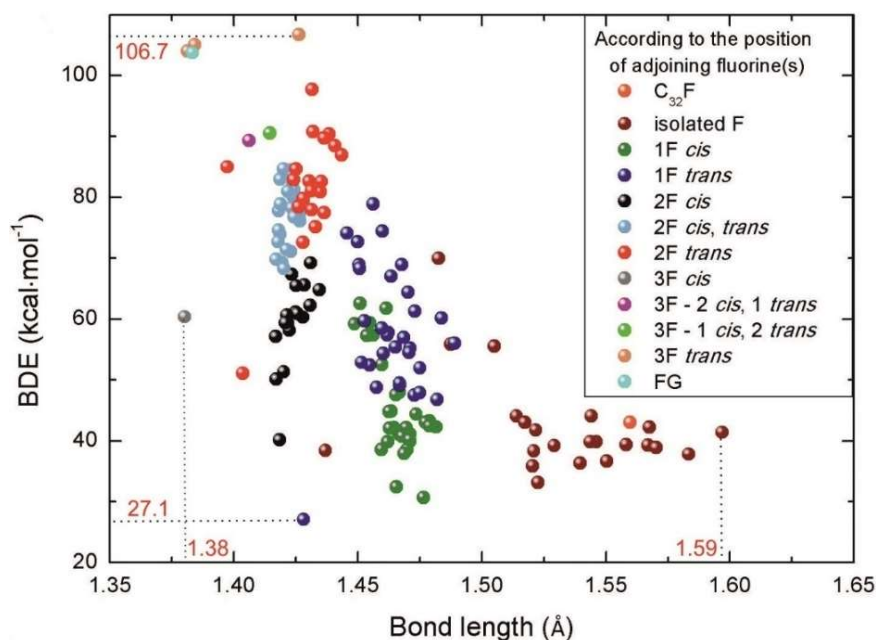


Figure 14: Bond lengths and BDEs of C–F bonds in (p)FGs of various configurations. Data are divided into groups according to the number and position of neighbouring F ad-atoms.

To find other factors that affect the BDEs of C–F bonds, we have considered their additional characteristics. Statistical analysis showed significant pair correlations of BDE with four factors: the C–F bond length (the square of the correlation coefficient, $R^2 = 0.55$), the number of adjacent fluorine ad-atoms in *trans* position (F_{trans} , $R^2 = 0.55$, Figure 15a), the number of C–C bonds that enter the π -conjugation after dissociation of given C–F bond (N_π , $R^2 = 0.53$, Figure 15c), and partly also the polarity of C–F bond ($R^2 = 0.33$, Figure 15d). Clearly, the C–F bonds that cause bigger disruption of the π -conjugation of C–C bonds are weaker (Figure 16). Therefore, the formation of fluorinated islands and ribbons is more favourable than the homogenous distribution of fluorine ad-atoms on the graphene plane as was also observed in other studies.^{72, 75-80}

As mentioned earlier, previous studies proposed that C–F bonds change from semi-ionic to covalent with increasing number of F ad-atoms.^{22, 72} Generally, with decreasing polarity the C–F bond shortens and becomes stronger. Our results follow the same trend, but the pair correlation of C–F bond polarity and length ($R^2 = 0.55$, Figure 17a) shows a weaker correlation than in the study by Zhou *et al.*⁷² However, it should be noted that we have also considered less favourable geometries with C–F bonds in *cis* positions that were not included in ref. 72. To support this explanation, we have selected the most stable configuration for each stoichiometry and carried out again the pair correlation showing much stronger correlation ($R^2 = 0.93$, Figure 17b).

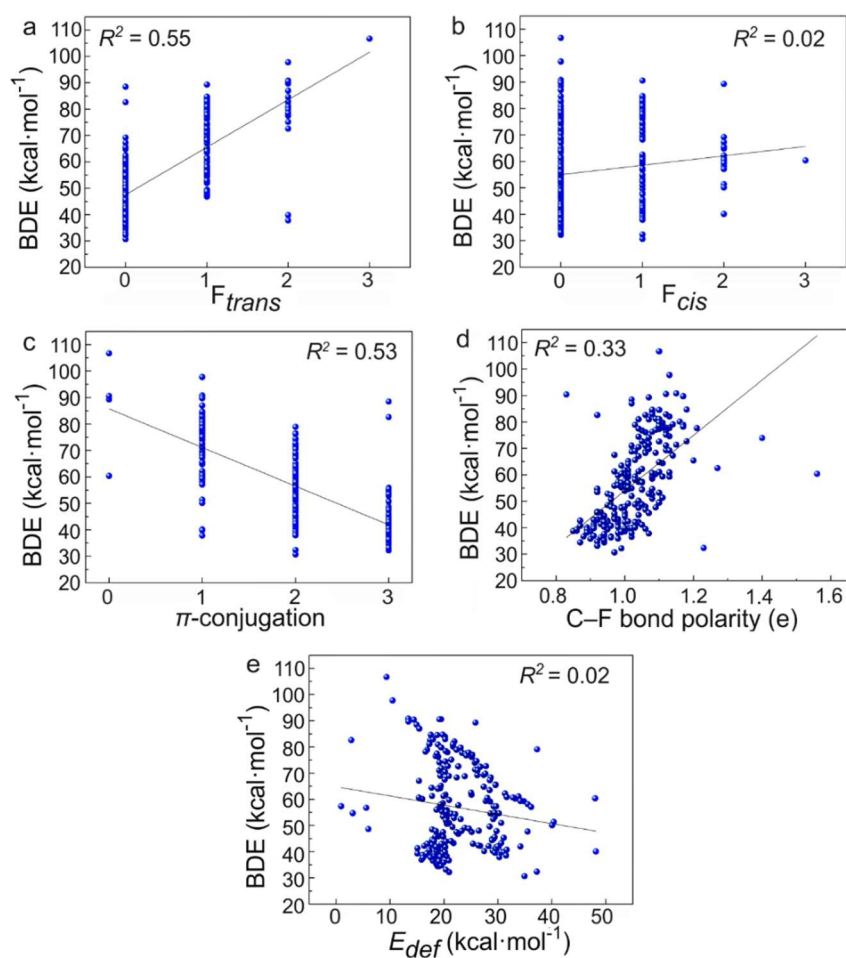


Figure 15: Pair correlations of a) BDE and F_{trans} , b) BDE and the number of adjacent fluorine ad-atoms in *cis* position (F_{cis}), c) BDE and N_{π} , d) BDE and C–F bond polarity, and e) BDE and deformation energy (E_{def}).

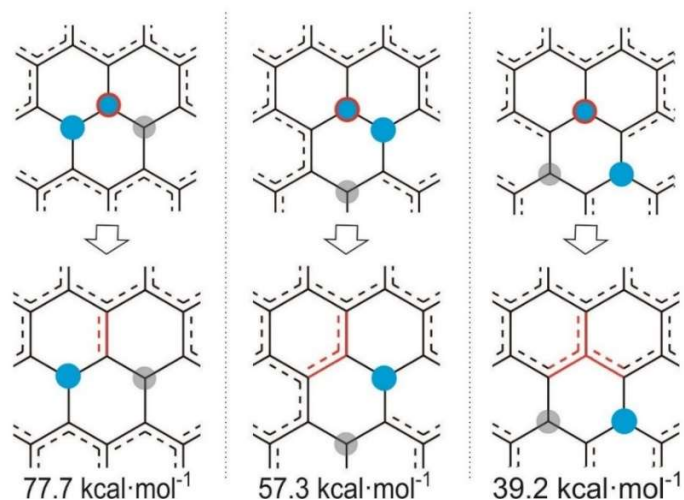


Figure 16: Example of the influence of N_{π} on BDE using 3 configurations of the same stoichiometry in which dissociation of the red-marked C–F bonds leads to the same structure. The BDE values correspond to the red marked C–F bonds. F ad-atoms are illustrated as blue and grey circles to distinguish ad-atoms on different sides of (p)FGs.

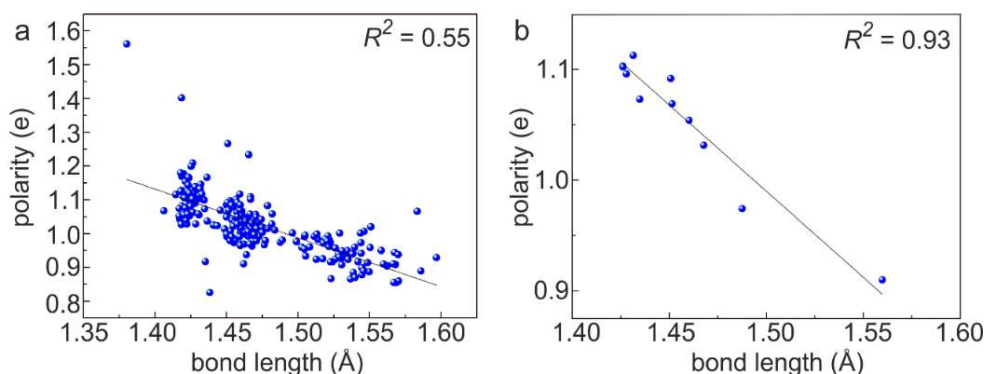


Figure 17: Pair correlation of C–F bond polarity and length of a) all calculated configurations and b) the most stable configurations.

Importantly, all considered properties of C–F bonds correlate not only with BDE but also with each other. Therefore, we have also performed a multiparametric analysis starting with the C–F bond length as the most relevant parameter for the correlation with BDE (coefficient of determination, $r^2 = 0.53$). Taking the C–F bond polarity as an additional parameter did not lead to the improvement of the correlation ($r^2 = 0.53$). On the other hand, the N_π had a more significant impact ($r^2 = 0.58$), and the most significant was found to be the parameter F_{trans} ($r^2 = 0.72$). The standard error of the BDE estimate demonstrated that 95% of all observations was in the interval of $\pm 9 \text{ kcal}\cdot\text{mol}^{-1}$. Nevertheless, it is not very practical to predict BDE from the C–F bond length since it would also require quantum chemistry calculations. Keeping this in mind, we carried out a two-parametric regression with purely topological parameters (N_π and F_{trans}), which resulted in the coefficient of determination $r^2 = 0.67$. The standard error of the estimate showed that 95% of the observations was in the interval $\pm 10 \text{ kcal}\cdot\text{mol}^{-1}$. It was found that BDE depends on these two topological parameters according to equation:

$$BDE = (68.640 \pm 5.016) - (8.873 \pm 2.005) * N_\pi + (10.925 \pm 2.307) * F_{trans} \quad (11)$$

The ability to estimate BDEs of C–F bonds in (p)FGs that is only based on a few purely topological parameters may be used for large-scale pre-screening of configurations to model real (p)FGs samples with different levels of fluorination.

The nature of C–F bonds deeply affects the reactivity and stability of (p)FGs. Thermodynamic stability is influenced by the arrangement of F ad-atoms on the lattice. To identify the most probable configurations that may be present in real samples, we have calculated Boltzmann distributions of binding energies (E_{bind}) of various structural motifs at different temperatures (293, 400, and 600 K). Generally speaking, structures with an even number of F ad-atoms that are evenly distributed on the two graphene sublattices are more stable than those with odd numbers of F ad-atoms. Also, the stability of the structures increases with the increasing

amount of F ad-atoms, and structures with homogenous distribution of F ad-atoms on the graphene plane are less favourable than those with compact fluorinated and defluorinated domains. It is worth noting that similar trends were also observed in previous studies.^{72, 75-80}

The experimental NMR and XPS spectra of graphene samples that were fluorinated by BrF_3 indicated the presence of different structural motifs such as armchair and zigzag chains, cyclohexane rings, and isolated pairs of C–F bonds randomly distributed on the graphene plane.^{62, 72} The samples were then stored under room temperature for several months, and the NMR and XPS spectra were measured again to show that the various motifs of C–F bonds relaxed to the most stable configuration.^{71, 81} Therefore, it can be deduced that the fluorination process is driven not only by thermodynamics but also by stochasticity. That means that the formation of C–F bond patterns during fluorination is to some extent random.

To model the evolution of motifs of fluorine ad-atoms during graphene fluorination, we have considered various configurations of F ad-atoms in stoichiometry ranging from low fluorine content to complete fluorination. By systematic increasing of the number of F ad-atoms and comparing E_{bind} , we have selected the most stable structures and favourable pathways of fluorination (Figure 18). The E_{bind} values decreased as the level of fluorination increased, demonstrating that the initial phase of fluorination can proceed spontaneously up to the most stable stoichiometry C_{18}F_6 that is presented by fluorinated hexagonal rings (Figure 18a, structure O) or zigzag chains (Figure 18a, structure N). These motifs were also observed experimentally by Makarova *et al.*²⁴ Despite that less stable structures can be formed by further fluorination, the increasing of F content may continue up to fully fluorinated FG (Figure 18). Interestingly, the fluorination pathway cannot fully follow the “lowest energy pathway” because the GS (ground-state structure, i. e., structure of the lowest energy) of the system with a given stoichiometry cannot always be created by adding an ad-atom to the GS of the system with lower F content. For example, the GS of C_{18}F_6 stoichiometry is created from the third most favourable structure of C_{18}F_5 stoichiometry (Figure 18a, pathway from structure J to structure O or N). Therefore, we have also calculated the energy barriers of the migration (Figure 18c) that show that the transformation of less stable configurations into GS structures is feasible, which agrees with the experimental evidence.²⁴

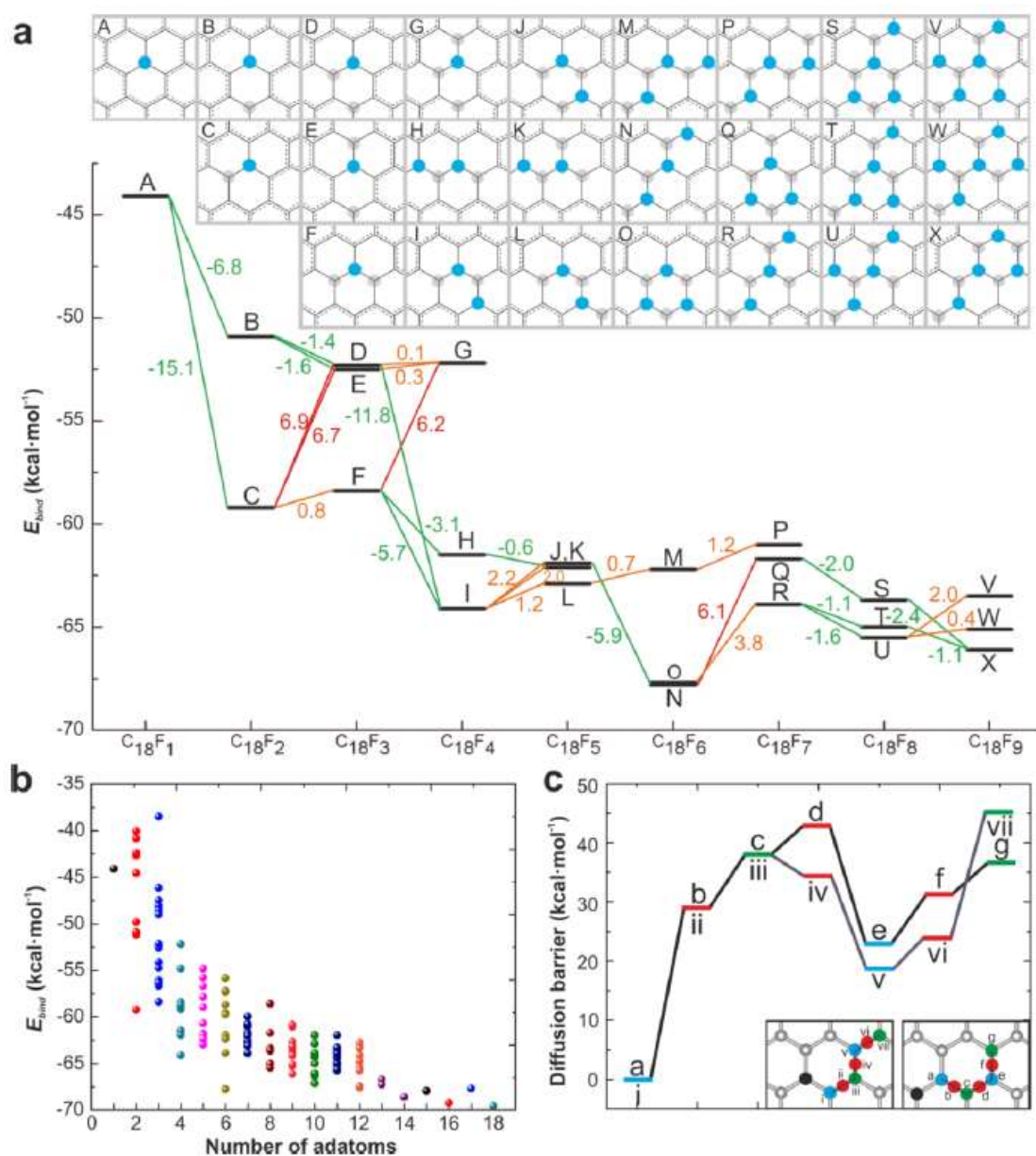


Figure 18: a) E_{bind} of the most stable configurations of C₁₈F_x (x = 1-9) demonstrating the evolution of possible patterns of fluorine ad-atoms during fluorination. Green, orange, and red lines mark energetically favourable, slightly unfavourable, and strongly unfavourable fluorination pathways, respectively. b) E_{bind} of low-energy configurations of (p)FGs with stoichiometry C₁₈F_x (x = 1-18). c) Energy barriers of the migration of two fluorine ad-atoms chemisorbed on different sides of the graphene plane. The pathways of migration are depicted in the inset. Blue, red, and green bars in c) mark non-magnetic structures, structures with fluorine ad-atom in the bridge position, and magnetic structure, respectively. F ad-atoms are illustrated as blue and grey circles to distinguish ad-atoms on different sides of (p)FGs.

From another point of view, it is reasonable to assume that defluorination, that represents processes such as thermal annealing and chemical reduction of (p)FGs, will follow the path of the weakest bonds. Therefore, we have also studied the process of defluorination by reversing

the fluorination process. The first step, i.e., detachment of the fluorine ad-atom from the unperturbed FG structure, is the most energetically demanding (BDE = 118.2 kcal·mol⁻¹, Figure 19a). However, it should be noted that radical defects are naturally present in the structure of FG as will be discussed later (Appendix B, section 3.2)⁵⁹ allowing to avoid this demanding first step. Since the detachment of the fluorine ad-atom near radical defect leads to the creation of C=C double bond, the next step is energetically much less demanding (BDE = 50.9 kcal·mol⁻¹, Figure 19b). Removal of more distant fluorine ad-atom from position *meta* or *para* to the radical defect is similarly demanding as the first step (BDE > 100 kcal·mol⁻¹). As the reaction proceeds, less and more demanding steps alternate. More precisely, it is more difficult to dissociate C–F bond neighbouring to the defluorinated chain with even number of carbon atoms than C–F bond neighbouring to the defluorinated chain with odd number of carbon atoms. It is caused by the formation of a magnetic (i. e., radical) structure in the former case. This observation is in agreement with Lieb’s theorem.¹²⁵ Generally, the detachment of the fluorine ad-atom near the defluorinated carbon is always more favourable than the dissociation of more distant C–F bonds which leads to the formation of defluorinated hexagons, zigzag and armchair chains.

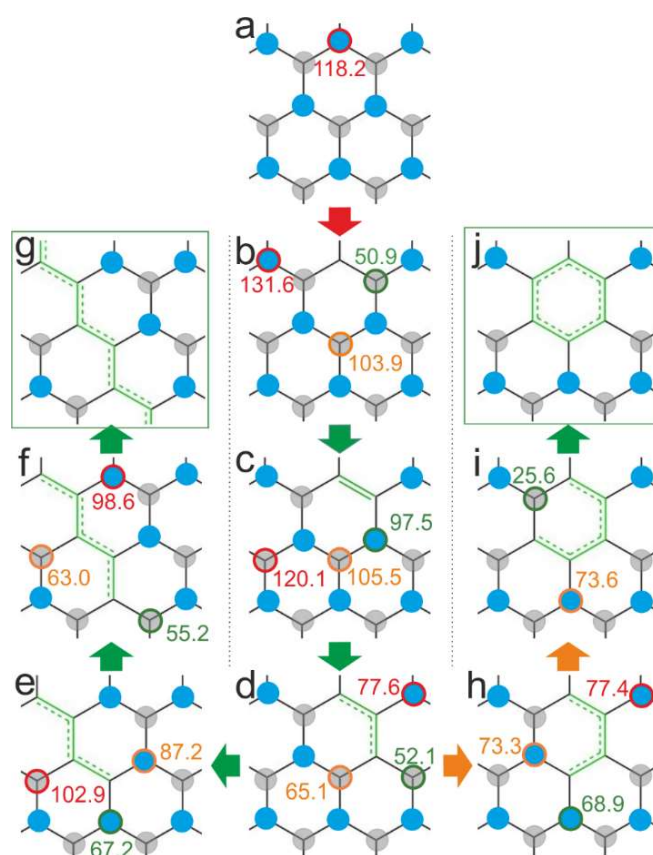


Figure 19: Gradual defluorination of FG. The values are BDE in kcal·mol⁻¹. Colours highlight the feasibility of the considered fluorine ad-atom detachment. F ad-atoms are illustrated as blue and grey circles to distinguish ad-atoms on different sides of (p)FGs.

The presented results can help to elucidate the experimental observation of processes such as fluorination, chemical reduction, and thermal annealing of (p)FGs. The knowledge of the processes that occur during (de)fluorination of fluorinated derivatives of graphene may thus be valuable in the design of new 2D materials with controllable properties and structure.

3.2. Point Defects Enhance the Reactivity of Fluorographene

Despite the C–F bond is considered one of the strongest in organic chemistry,^{64, 65, 124} tertiary C–F bonds in perfluorocarbons are sometimes called ‘the Achilles heel’ thanks to their ability to accept electrons into the σ^* orbital.⁶⁵ Lai *et al.*⁶³ assumed that FG reduction can be initiated by SET to C–F bond and followed by detachment of a fluoride anion. To support this hypothesis, we have computed the vertical (VEA), adiabatic (AEA) electron affinities, and the HOMO-LUMO gap of three model molecules representing FG: *trans*-decafluoronaphthalene (**c2**), *trans*-tridecafluorophenylene (**c3**), and *trans*-tetracosafuorocoronene (**c7**). We have found that VEA values were negative and AEA values were rather small, demonstrating the low stability of the negatively charged model molecules (Table 1). It is worth noting that our DFT results correspond very well with those obtained by MP2 method using the same basis set. Even though the VEA values increased with the size of the model molecule thanks to bigger delocalization of the charge, it can be anticipated that even for larger structures of FG the value would be small. This is also supported by the positive LUMO energies and a rather large HOMO-LUMO gap demonstrating a low tendency to accept an electron, which agrees with the large theoretically predicted bandgap of FG (from 3.1 to 7.5 eV, depending on the used method).^{21, 126} These results pointed out that the SET to FG is possible only by using strong reducing agents and thus cannot explain the lower thermal stability of (p)FGs and promoted defluorination in presence of solvents such as NMP, dimethylamine (DMA), DMF, and acetone.^{53, 54} Therefore, in our work (Appendix B)⁵⁹ we have focused on the reactivity of FG in DMF which is a commonly used solvent in FG exfoliation.

Table 1: VEA and AEA of fluorinated polycyclic hydrocarbons as FG models and corresponding radical species (one fluorine ad-atom missing) at the ω B97X-D/6-31++G(d,p) level of theory. The values in parentheses are obtained at the MP2/6-31++G(d,p) level of theory. HOMO-LUMO gaps are derived from the energies of Kohn-Sham orbitals.

	VEA (kcal·mol ⁻¹)	AEA (kcal·mol ⁻¹)	HOMO (eV)	LUMO (eV)	HOMO- LUMO gap (eV)
c2	-21.0 (-20.7)	7.1	-11.08	0.97	12.05
c3	-16.0 (-17.1)	12.0	-11.07	0.75	11.82
c7	-3.3	4.0	-10.85	0.30	11.15
c2 radical	53.5 (55.3)	67.2	-10.09	-2.15	7.94
c3 radical	60.6 (63.0)	74.4	-10.34	-2.35	7.99
c7 radical	66.8	80.6	-10.54	-2.46	8.07

^a In the case of radical species, the HOMO and LUMO energies correspond to the lowest β (unoccupied) and highest α (occupied) orbitals.

EPR measurements proved the presence of radical centres in the FG sample that could be the key to explain the enhanced reactivity of FG. The concentration of these point defects is highly influenced by the method of preparation. For example, fluorination by CF₄ plasma results in highly disordered inhomogeneously fluorinated graphene, while the usage of XeF₂ as a fluorinating agent leads to a highly ordered structure. Moreover, carbon atoms on grain boundaries, in folds or ripples may remain unfluorinated or may lead to less stable configurations of neighbouring fluorine ad-atoms in *cis* positions which make the emergence of radical centres more probable.^{127, 128} Accordingly, we have considered VEA and AEA of radical species derived from **c2**, **c3**, and **c7** model molecules (Table 1). Their very high values of both VEA and AEA clearly demonstrate that radical point defects can accept an electron into SOMO orbital and initiate the defluorination process. For example, AEA of **c7** model molecule (80.6 kcal·mol⁻¹) is higher even than that of fluorine atom (78.4 kcal·mol⁻¹). The

synergized electron-withdrawing effect of highly electronegative fluorine ad-atoms bounded on neighbouring carbon atoms around the radical centre is one of the main factors stabilizing charged structures. In addition, both VEA and AEA values increase with the system size similarly as in the case of unperturbed structures thanks to higher delocalization of the charge in bigger systems. This strong oxidizing character of radical centres in FG structure can start the defluorination process even in the presence of mild reducing agents.

Therefore, we have investigated a possible scenario of the defluorination mechanism that starts with electron transfer to the radical centre and proceeds by detachment of neighbouring fluorine ad-atoms (Figure 20). In general, the reduction steps are favourable both in the gas phase and DMF. The polar solvent stabilizes the charged structures making the reduction steps even more favourable. As expected, the closed-shell systems occurring in the reduction process have lower oxidizing power than radical species. Nevertheless, even the **1-XI** structure, that is fully π -conjugated, can be easily reduced thanks to the electron-withdrawing effect of the surrounding C–F bonds. However, it is worth noting that the electron affinity (EA) of the **1-XI** structure is lower than that of other considered structures. It is therefore reasonable to assume that defluorination in the presence of mild reducing agents may stop after the formation of bigger π -conjugated domains. The steps involving detachment of fluoride anion in DMF are in most cases exothermic thanks to the stabilization of fluoride anion by the polar solvent.

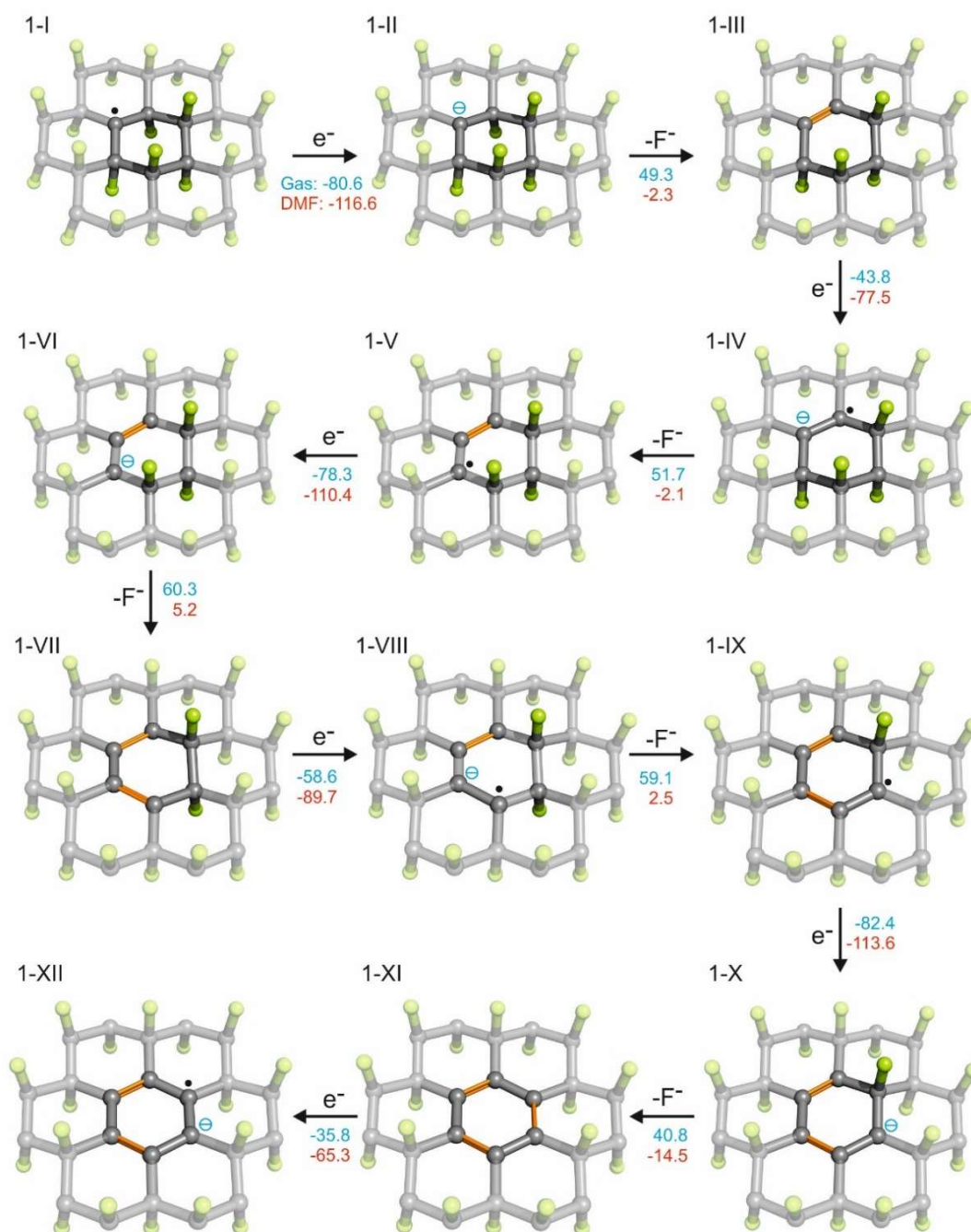


Figure 20: Initial steps of a possible cascade mechanism of FG defluorination that is initiated by electron transfer to the radical centre. Blue values are the reaction energies (in $\text{kcal}\cdot\text{mol}^{-1}$) in the gas phase, red values in DMF. Carbon atoms are grey and fluorine green. The C=C double bonds are orange.

The cascade mechanism of FG defluorination initiated by electron transfer to the radical centre is not a sufficient explanation of the defluorination mechanism that was observed in solvents with higher ionization potential (IP) than EA of FG point defects. For example, IP of DMF is $149 \text{ kcal}\cdot\text{mol}^{-1}$ which is higher than EA of FG radical centre that is $117 \text{ kcal}\cdot\text{mol}^{-1}$ (structure **1-I**, Figure 20). Evidently, direct electron transfer from DMF to FG is improbable. Therefore,

we have suggested a mechanism that starts with hydrogen atom transfer from a molecule of DMF to the radical centre of FG which is thermodynamically favourable (Figure 21, step 1a). The reaction may proceed via releasing of HF molecule, but this reaction step is energetically slightly unfavourable (step 2b). More probable next step is the attack of a DMF• radical, detachment of another F ad-atom and creation of *N,N'*-dimethylcarbamoyl fluoride (F-DMF) (step 2a). In addition, the structure **2-I** can be attacked by another DMF• that may lead either to the recombination of DMF• radical and radical centre in FG (step 1c) or to the formation of F-DMF and C=C double bond in FG structure (step 1b). The defluorination may then proceed from the structure **2-V** via further attack of DMF• radical that leads to the detachment of the fluorine ad-atom and creation of F-DMF molecule (step 3). This mechanism was also supported by spin-trap experiments and ^{19}F NMR measurements that confirmed the formation of DMF• and F-DMF.

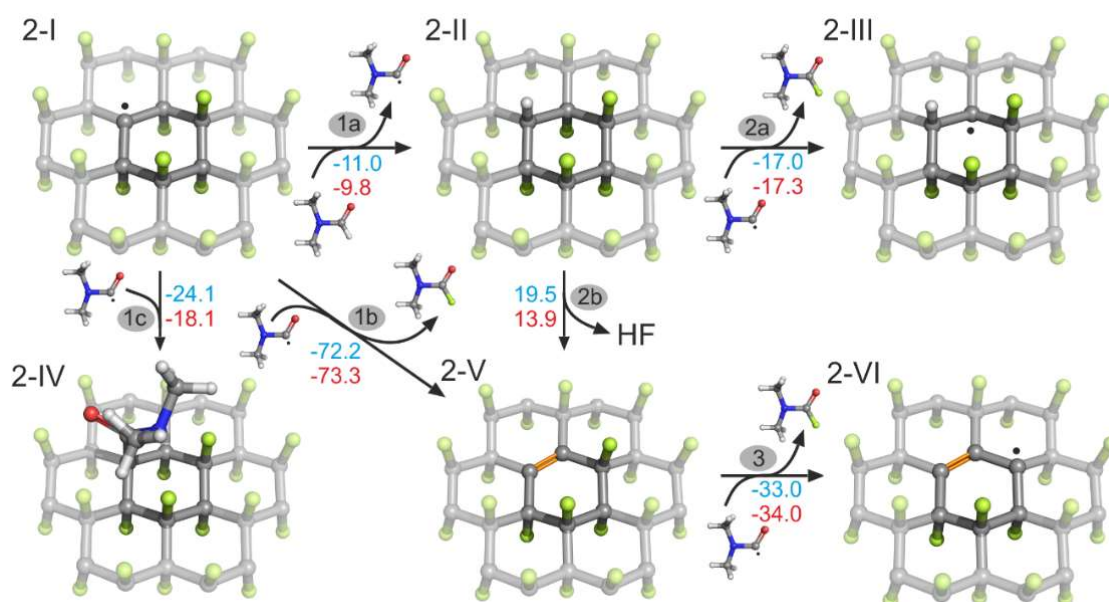


Figure 21: Radical mechanism of FG defluorination in DMF. Blue values are the reaction energies (in $\text{kcal}\cdot\text{mol}^{-1}$) in the gas phase, red values in DMF. Carbon atoms are grey, fluorine green, nitrogen blue, oxygen red, and hydrogen white. The C=C double bonds are orange.

All in all, the presence of radical centres may trigger two important processes. First, the electron transfer to the radical centre and formation of anionic centre can initiate defluorination in the presence of mild reducing agents. Second, in the presence of species sensitive to homolytic R–H bond dissociation, a hydrogen transfer to the radical centre may occur. Both reaction mechanisms lead to cascade defluorination that cause the formation of compact motifs that are stabilized by π -conjugation of C=C double bonds. It can be anticipated that these motifs will be highly susceptible to nucleophilic substitution thanks to the electron-withdrawing effect

of highly electronegative fluorine ad-atoms in the vicinity. Actually, the idea of nucleophilic substitution and reductive defluorination has already been employed using CN^- ,⁹² OH^- ,⁶⁰ NH_2^- ,⁸⁴ and Grignard reagents⁹⁰ to synthesize new graphene derivatives.

3.3. The Reaction Mechanism of Fluorographene Nucleophilic Substitution

To continue with the idea that the defluorinated carbon sites and chains are highly sensitive to nucleophilic attack, we have investigated an attack of OH^- , CN^- , and NH_2^- anion on a radical centre in FG considering various solvents (Appendix C).⁶⁸ These negatively charged species differ in nucleophilicity, the ability to form hydrogen bonds, and in the strength of the C–Nu bond. We have considered four different solvents: THF which is the least polar of considered solvents, acetone which can elevate the reduction of FG⁵⁴ and was utilized in the reaction of FG with NaOH,⁶⁰ methanol as polar protic solvent that can form hydrogen bonds and thus stabilizes the C–F bonds, and finally DMF which causes defluorination as was discussed earlier.⁵³

Reaction energies in Figure 22a demonstrate that the nucleophilic attack on the radical centre of FG is energetically favourable in all environments. The NH_2^- anion shows the highest affinity ($\Delta E_R \cong -60 \text{ kcal}\cdot\text{mol}^{-1}$) to FG thanks to its higher nucleophilicity and ability to form hydrogen bonds with the released F^- anion. On the other hand, the reaction energy of CN^- attack is only ca. $-10 \text{ kcal}\cdot\text{mol}^{-1}$. Generally, polar solvents stabilize the negatively charged species and thus impede the nucleophilic attack. Let us note that the nucleophilic attack of OH^- in methanol was less favourable than in other solvents due to the formation of strong hydrogen bonds and higher solvation energy of OH^- ($92.8 \text{ kcal}\cdot\text{mol}^{-1}$) than those of NH_2^- ($78.0 \text{ kcal}\cdot\text{mol}^{-1}$) and CN^- ($63.1 \text{ kcal}\cdot\text{mol}^{-1}$). Consequently, F^- can be released due to the negative charge that is brought to the system by Nu^- , and a new carbon radical site can be created (Figure 22b). In all cases, the heterolytic cleavage of a C–F bond in the ortho position is preferred (Figure 23). Despite the unfavorability of this step in the gas phase, the stabilization of F^- in solvents makes the process favourable in the case of OH^- and CN^- . Even in the case of NH_2^- the solvation effects make the release of F^- achievable at room temperature. Nucleophilic attack on the newly created radical site is also favourable in all environments (Figure 22c) in the similar way as the first attack. Let us note that we have also considered the reaction mechanism in which the attached $-\text{NH}_2$ group is attacked by another NH_2^- anion. This leads to dehydrogenation of the $-\text{NH}_2$ group on FG and the formation of NH_3 . The negative charge of the attacking NH_2^- anion is transferred to FG, which causes the detachment of F^- and subsequent transformation of the $-\text{NH}-$ group into a three-membered aziridinic ring (Appendix D and section 3.4, Figure 26).¹⁰⁷

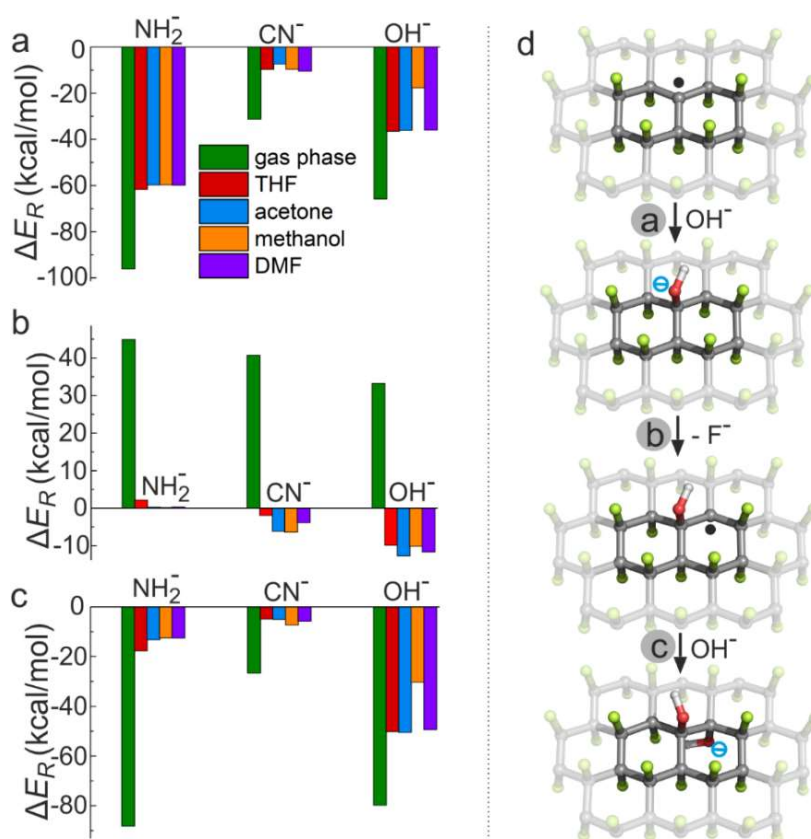


Figure 22: a) Reaction energies (ΔE_R) of the nucleophilic attack of NH_2^- , CN^- , and OH^- on a radical site of FG in various solvents, b) ΔE_R of the consequent heterolytic dissociation of C-F bond, c) ΔE_R of the nucleophilic attack on the newly created radical centre of FG, and d) reaction scheme. Carbon atoms are grey, fluorine green, oxygen red, and hydrogen white.

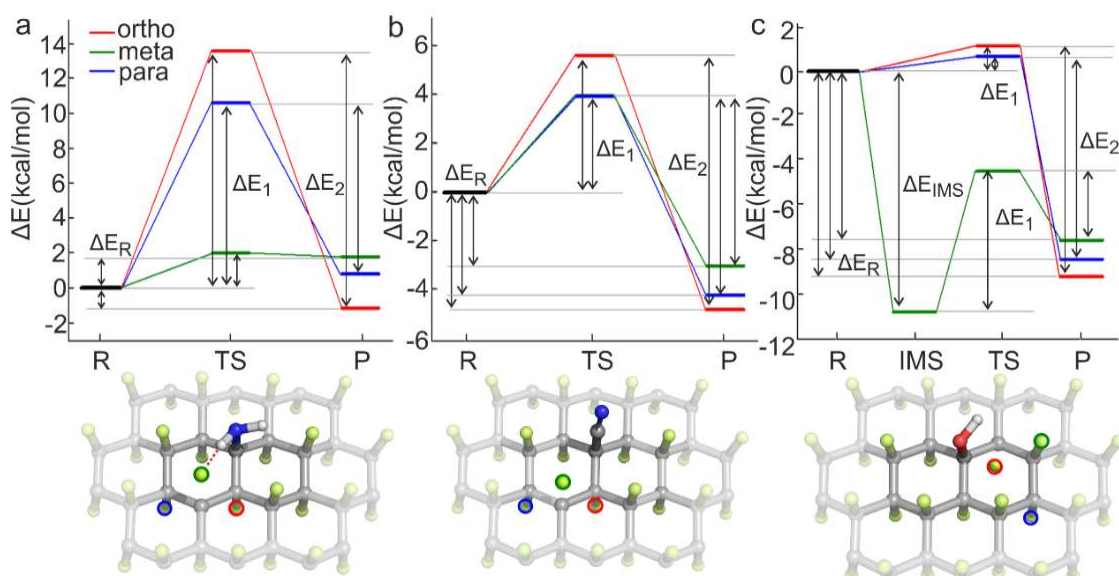


Figure 23: Energy profiles of detachment of fluoride anion after nucleophilic attack of a) NH_2^- , b) CN^- , and c) OH^- in DMF. The presence of IMS in c) is caused by the formation of a hydrogen bond between F^- and $-\text{OH}$ group. Carbon atoms are grey, fluorine green, nitrogen blue, oxygen red, and hydrogen white.

Since the C–F bond cleavage could be kinetically hampered, we have also calculated the reaction profile of the first Nu⁻ attack and F⁻ detachment in the gas phase and DMF (Figure 24). Although the high energy barrier makes the detachment of F⁻ unfavourable in the gas phase (ΔE_4 in Figure 24), the solvation of F⁻ in DMF decreases the activation energy and makes the reaction favourable, particularly in the case of CN⁻ and OH⁻. Even in the case of NH₂⁻ the activation energy is low, and the detachment of fluoride anion can occur at room temperature.

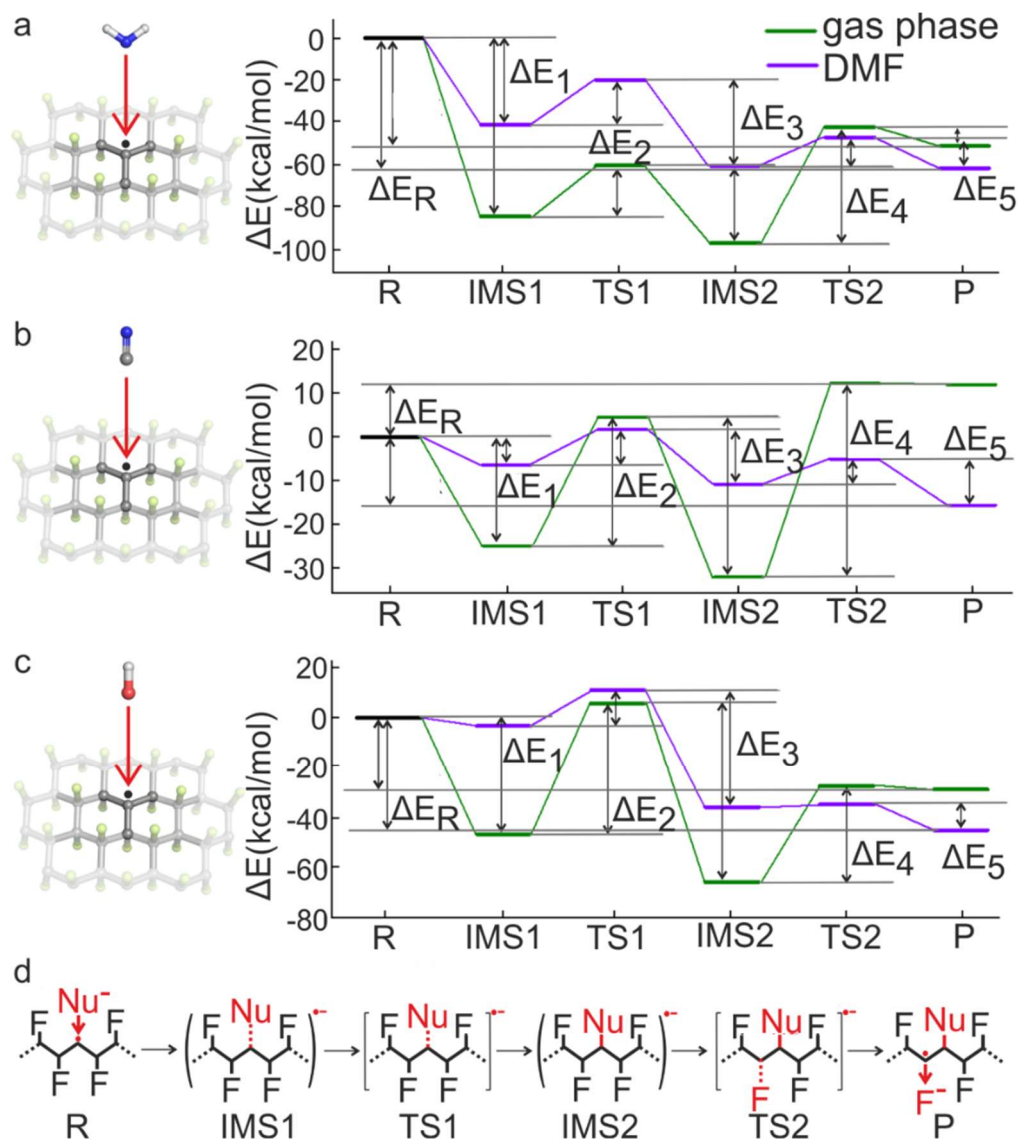


Figure 24: Energy profile of the nucleophilic attack of a) NH₂⁻, b) CN⁻, and c) OH⁻ anion on a radical centre of FG and the consequent release of fluoride anion, d) reaction scheme. Carbon atoms are grey, fluorine green, nitrogen blue, oxygen red, and hydrogen white.

It is worth noting that the product of the CN⁻ attack on the radical site of FG is thermodynamically the least favourable among the considered nucleophiles due to the smaller nucleophilicity of CN⁻ anion (Figure 24). Natural bond orbital (NBO) analysis¹²⁹⁻¹³⁴ assigned

a partial charge of $-0.2 e$ to the carbon atom of CN^- , whereas the charges on nitrogen and oxygen in NH_2^- and OH^- are $-1.4 e$ and $-1.6 e$, respectively. Moreover, the ability of NH_2^- and OH^- to form hydrogen bonds with close fluorine ad-atoms further stabilizes the products.

All in all, the radical centres of FG play multiple roles in the material's reactivity. First, they can accept an electron from a sufficiently strong reducing agent (Figure 25, path A). Second, they can initiate radical defluorination if sufficiently stable radicals are formed (Figure 25, path B). Third, they can be attacked by nucleophilic species (Figure 25, path C). Although all these three pathways can occur at the same time, the different kinetics and thermodynamics of individual steps and their dependence on the choice of solvent allow to control the processes of substitution and defluorination. For example, the reaction of FG with a nucleophilic agent (e. g., NaCN) in an inert solvent such as methanol should preferentially proceed through path C under mild conditions. The resultant material would contain a high amount of sp^3 hybridized carbon atoms. The degree of substitution (CN/F ratio) could be managed by the reaction time. Topology of functionalization can be controlled, too. For instance, the functionalization can start with the reducing phase (path A) that causes the formation of sp^2 carbon domains and afterwards the nucleophile can be added.

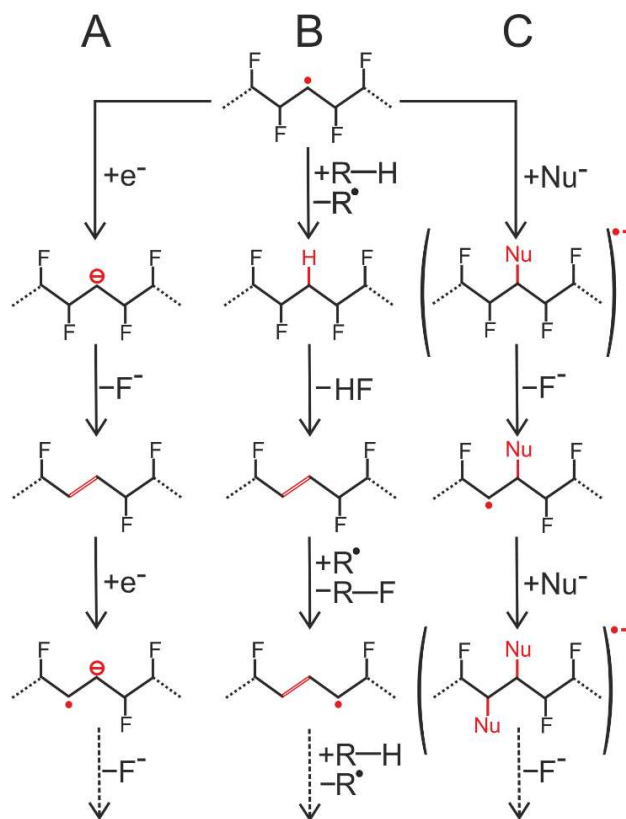


Figure 25: Possible reaction pathways of FG defluorination and nucleophilic substitution that start at radical site of FG. A) Electron transfer, B) hydrogen transfer, and C) nucleophilic attack.

3.4. The Role of Vacancies in Nitrogen Doping of Fluorographene

Doping of graphene with heteroatoms opens a road to a new group of 2D materials usable in catalysis, spintronics, and electrochemical applications.^{100, 101} To find a cheap and eco-friendly method of synthesis that leads to a homogenous distribution of heteroatoms in the graphene plane is of great importance since so far known methods usually require temperatures over 800 °C.¹⁰² In our work we have employed wet chemistry of FG for nitrogen doping by NaNH₂ at mild temperatures as low as 70 °C. Interestingly, the level of doping was controllable by the reaction time, choice of solvent, and temperature. The obtained maximum amount of nitrogen in the resultant material was estimated to be 18.2 at. %. For further experimental details, see Appendix D.¹⁰⁷

To theoretically elucidate the high-yield incorporation of nitrogen atoms into FG plane, we have studied several reaction scenarios. First, we have considered a nucleophilic attack of NH₂⁻ on a point defect in FG that is accompanied by fluoride anion releasing as was discussed earlier (Figure 22 and 24). In the next step, instead of attacking the newly created radical centre, NH₂⁻ anion may cause dehydrogenation of the bounded -NH₂ group and formation of NH₃ molecule (Figure 26, steps 2a,b). The negative charge of NH₂⁻ is then transferred to FG and F⁻ can be released. Subsequently, the -NH- group can be cyclized into an aziridinic ring ($\Delta E_R = -47.2 \text{ kcal}\cdot\text{mol}^{-1}$, step 2a), as also predicted by Li *et al.*¹⁰⁶ for the attack of ammonia molecule on FG, or the material can undergo further dehydrogenation and defluorination accompanied by releasing an HF molecule ($\Delta E_R = -63.2 \text{ kcal}\cdot\text{mol}^{-1}$, steps 2b and 3). The dissociation of the C-F bond and the release of F⁻ and HF were also supported by the experimental observation of NaF in XRD spectra. Furthermore, a DMA• radical, being a by-product of the reaction in FG + NaNH₂ + DMF mixture (Scheme 1), can bind to the C atom near the aziridinic ring ($\Delta E_R = -36.3 \text{ kcal}\cdot\text{mol}^{-1}$, step 4). In the next step, NH₂⁻ can bind to the carbon atom neighbouring to the newly created C-N bond between FG and the dimethylamino group ($\Delta E_R = -30.3 \text{ kcal}\cdot\text{mol}^{-1}$, step 5) causing a strong deformation of the FG plane that allows the releasing of *N,N'*-dimethylethyne-1,2-diamine and rearrangement of aziridinic nitrogen into pyridinic nitrogen in a newly created vacancy in the FG plane ($\Delta E_R = 7.8 \text{ kcal}\cdot\text{mol}^{-1}$, steps 6 and 7a). *N,N'*- dimethylethyne-1,2-diamine further rearranges into dimethylaminoacetonitrile (DMAACN) ($\Delta E_R = -35.8 \text{ kcal}\cdot\text{mol}^{-1}$, step 7b) - a by-product of the reaction (Scheme 1). However, the high activation barrier (> 100 kcal·mol⁻¹) of *N,N'*-dimethylethyne-1,2-diamine separation indicates that this reaction mechanism is

improbable and cannot fully explain the high amount of incorporated nitrogen. Therefore, we have considered vacancies present in the FG plane that could facilitate the insertion of N atoms under mild conditions.

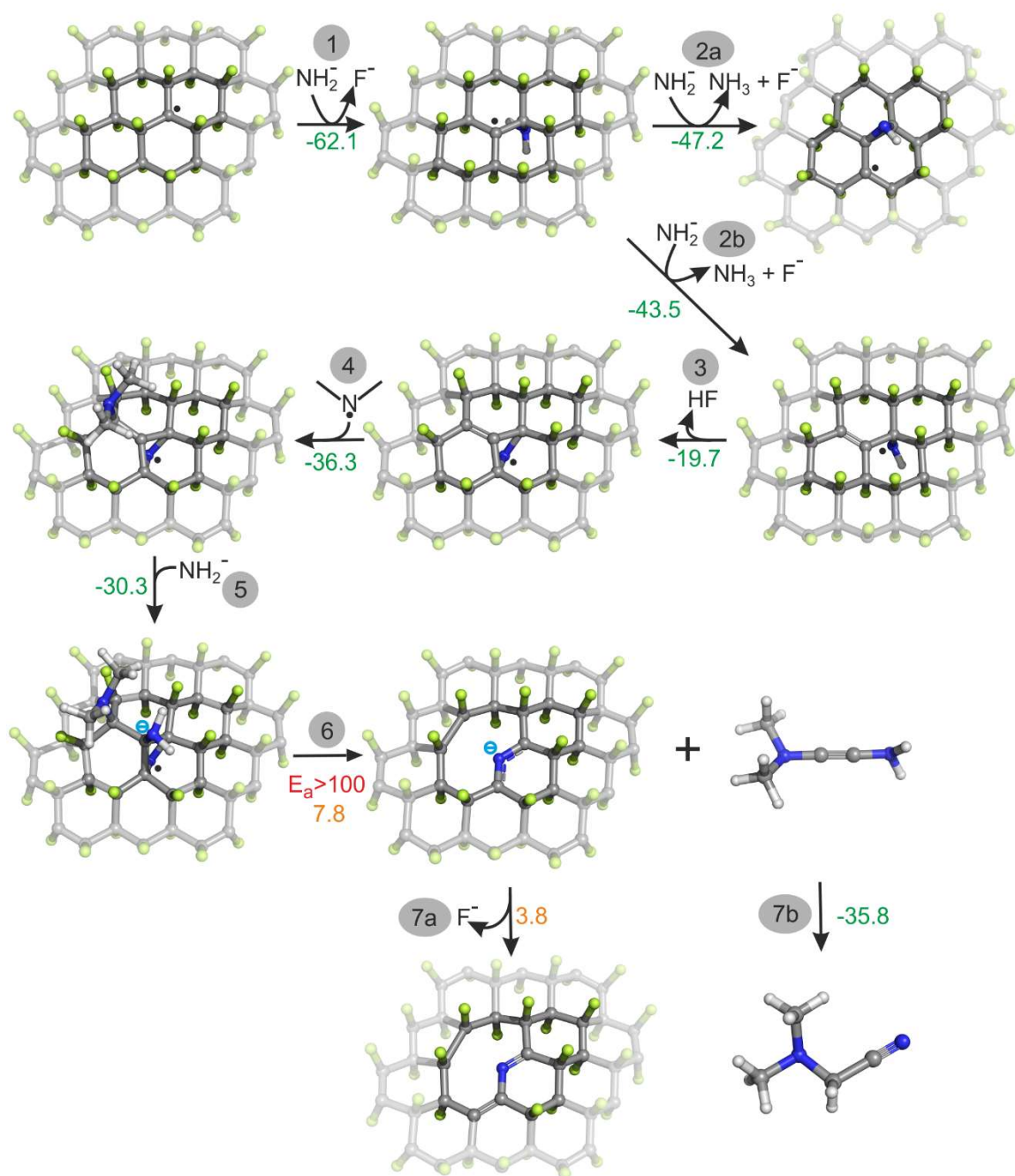


Figure 26: The reaction mechanism (in DMF) of pyridinic nitrogen formation in the FG plane that starts by NH_2^- nucleophilic attack on the point defect of FG, proceeds through the formation of aziridinic nitrogen and ends with the creation of a vacancy in FG plane with pyridinic nitrogen. Reaction energies are in $\text{kcal}\cdot\text{mol}^{-1}$. Carbon atoms are grey, fluorine green, nitrogen blue, and hydrogen white.

To investigate the role of vacancies in FG plane that may occur in the starting material, we have constructed and optimized several types of vacancies under PBCs: point defects (e.g., Stone-Wales vacancy, (SW(55-77)), single vacancies (SV), double vacancies (DV), triple vacancies (TV), and some others. We have also assumed that radical centres and biradical sites may be present in vacancies. The radical sites on the edges of vacancies were separated by 2.9-7.3 Å, in line with experimentally estimated values using EPR method.⁵⁹ Comparison of cohesion energies (E_{coh}) showed that SW(55-77) and DV(555-777) were the most stable vacancies (Figure 27a,b). However, the presence of a radical site near the vacancy was required to enable the NH_2^- nucleophilic attack. The combination of the radical site and these vacancies is improbable due to the high BDE of C-F bonds ($\sim 100 \text{ kcal}\cdot\text{mol}^{-1}$) which is almost the same as in unperturbed FG. Therefore, we have investigated the nucleophilic attack on the third and fourth most stable vacancies, i.e., SV and DV(14) (Figure 27c,d).

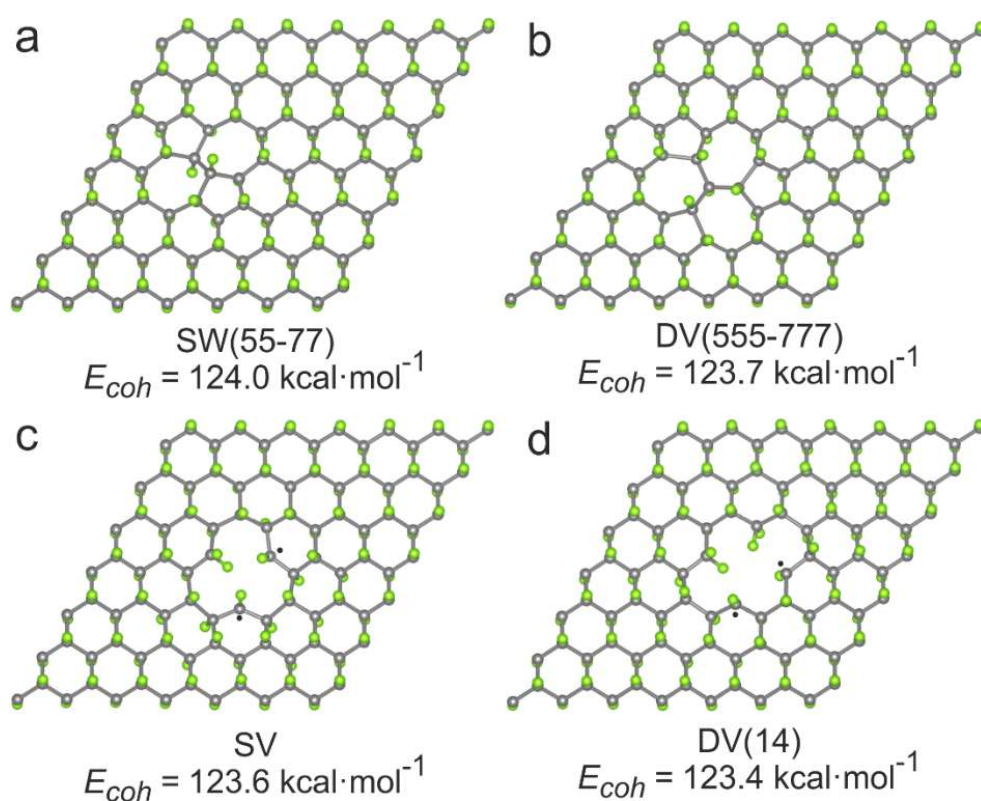


Figure 27: Supercells and cohesion energies (E_{coh}) of the four most stable vacancies that may occur in FG structure: a) SW(55-77), b) DV(555-777), c) SV, and d) DV(14). Carbon atoms are grey and fluorine green.

The first reaction step, i.e., the NH_2^- nucleophilic attack followed by the release of F^- , was found more favourable for DV(14) ($\Delta E_R = -65.1 \text{ kcal}\cdot\text{mol}^{-1}$, Figure 28a) than for SV ($\Delta E_R = 3.8 \text{ kcal}\cdot\text{mol}^{-1}$, Figure 28b). Then, the reaction can proceed via dehydrogenation and defluorination and lead to the formation of either pyrrolic or pyridinic nitrogen in the case of

DV(14) and graphitic nitrogen in the case of SV. Formation of graphitic nitrogen is energetically the most favourable ($\Delta E_R = -255.5 \text{ kcal}\cdot\text{mol}^{-1}$) followed by pyridinic nitrogen ($\Delta E_R = -72.3 \text{ kcal}\cdot\text{mol}^{-1}$), and the formation of pyrrolic nitrogen is the least favourable albeit still feasible ($\Delta E_R = -32.6 \text{ kcal}\cdot\text{mol}^{-1}$). These results demonstrate that the incorporation of nitrogen into FG plane occurs predominantly in vacancies.

a. DV(14)

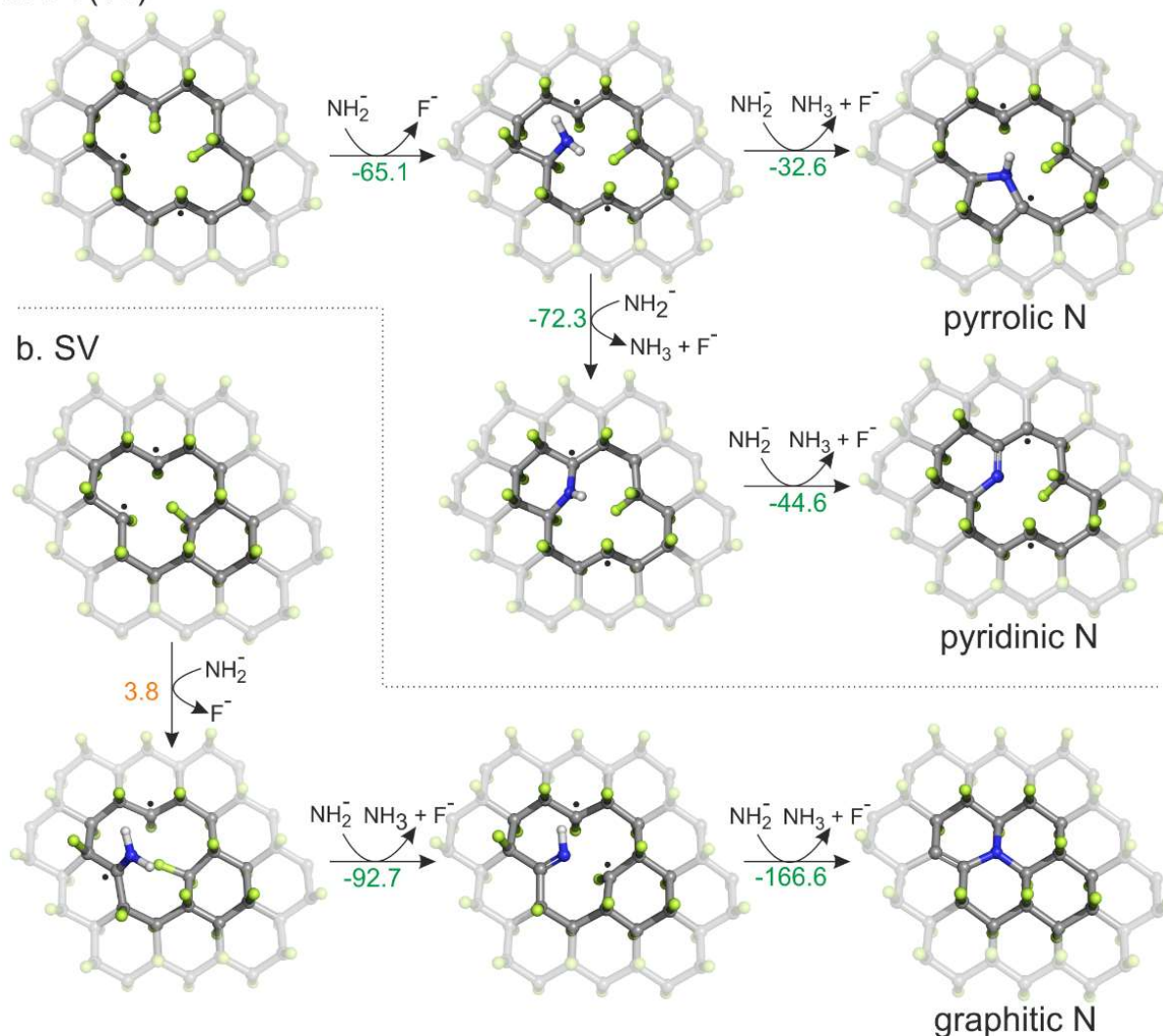


Figure 28: Mechanism of nitrogen incorporation into a) DV(14) and b) SV that leads to the formation of pyrrolic, pyridinic, and graphitic nitrogen in FG plane. Reaction energies are in $\text{kcal}\cdot\text{mol}^{-1}$. Carbon atoms are grey, fluorine green, nitrogen blue, and hydrogen white.

It is worth noting that the nucleophilic attack can also lead to an extension of the vacancy, which was also supported by the pore size analysis. As in previous cases, the reaction starts with the NH_2^- nucleophilic attack on the edge of vacancy followed by the release of F^- ($\Delta E_R = -38.8 \text{ kcal}\cdot\text{mol}^{-1}$, Figure 29, step 1). The neighbouring C atom to the newly created C–N bond may be attacked by dimethylamide anion ($\Delta E_R = 2.4 \text{ kcal}\cdot\text{mol}^{-1}$, step 2), which is one of the by-products of the reaction (Scheme 1) causing the detachment of another F^- .

Finally, the vacancy can be expanded by the release of *N,N*-dimethylethyne-1,2-diamine which can be rearranged into DMAACN molecule ($\Delta E_R = -27.7 \text{ kcal}\cdot\text{mol}^{-1}$, step 3) which was observed by the gas chromatography – mass spectroscopy (GC-MS).

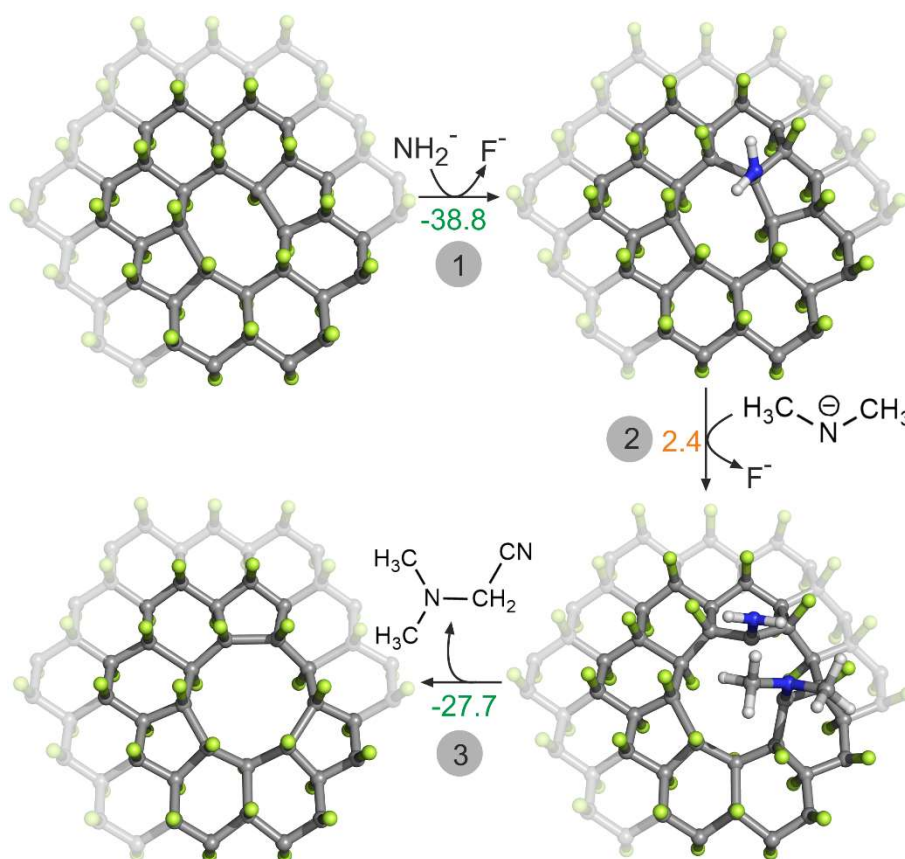
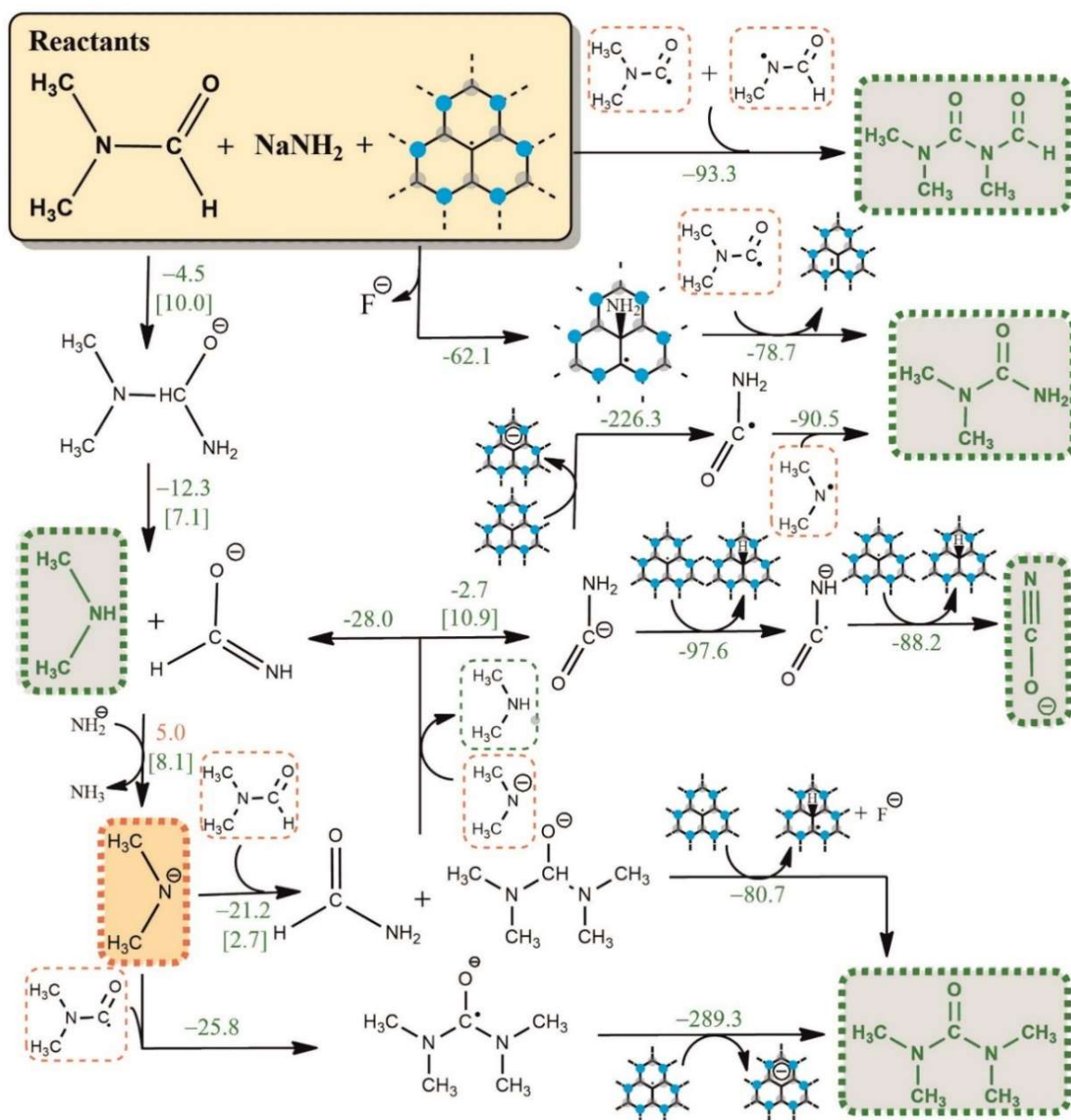


Figure 29: Reaction mechanism of an expansion of DV(5-8-5) that is caused by NH_2^- nucleophilic attack followed by dimethylamide anion attachment and consequent release of DMAACN. Reaction energies are given in $\text{kcal}\cdot\text{mol}^{-1}$. Carbon atoms are grey, fluorine green, nitrogen blue, and hydrogen white.

The experimental results of GC-MS revealed many by-products of the reaction of FG with NaNH_2 in DMF. Therefore, we have conducted a thorough theoretical exploration of possible reaction pathways that may occur in the system and lead to main by-products, i.e., DMA, DMAACN, tetramethylurea, dimethylurea, and formyltrimethylurea (Scheme 1). Orange frames indicate by-products important for other reactions; some of them were formed in the absence of FG and/or NaNH_2 (for further information see Appendix D). It is important to point out that the radical centres of FG enrich the number of possible reaction pathways and thus the number of by-products. Analysis of by-products that were observed in the supernatant from the reaction in ACN was also investigated. In comparison to the reactions in DMF, the reaction in ACN ended in a lower number of by-products, confirming the lower reactivity of ACN environment.



Scheme 1: Possible side reactions in the reaction mixture of FG with NaNH_2 in DMF. Products in green frames were observed experimentally, products in orange frames play further roles in other reactions in the mixture. Reaction energies and activation barriers -that are reported in brackets for endothermic and least exothermic processes- are in kcal·mol⁻¹

3.5. Covalent Functionalization of Partially Fluorinated Graphene by Polysulfide Chains

The ever-growing demand for portable power sources for mobile devices, electric cars, unmanned vehicles, etc. calls for cheaper batteries with higher performance.¹³⁵ Lithium-sulfur batteries are an interesting alternative thanks to their high theoretical capacity and specific energy.^{136, 137} In addition, sulfur is low-cost, abundant, environmentally friendly material, and important by-product of the petroleum industry.¹³⁸ Unfortunately, lithium-sulfur batteries suffer from several issues such as large volume change and poor conductivity of sulfur and the shuttling-effect of lithium polysulfides that are formed during the charge/discharge cycle.¹³⁹

In our work (Appendix E),¹⁴⁰ we tackle the challenge of development of a new cathode material that would restrain the shuttling effect and offer a high full-cathode-mass capacity and rate capability. Carbon-based materials are intensively studied as sulfur hosts because of their good electrical conductivity, large surface area, and good mechanical properties.¹⁴¹⁻¹⁴³ However, weak interactions between polysulfide (PS) chains and carbon-based hosts cause poor cycling stability.¹⁴⁴ Therefore, a strong covalent bond between sulfur and conductive hosting material is necessary. We report a successful synthesis of graphene-sulfur cathode material with very high sulfur loading (80 mass%) that increased the full-cell specific capacity and limited the shuttling effect.¹⁴⁰ These outstanding results were obtained via the reaction of FG with sodium polysulfide (NaPS) in NMP solvent. For further experimental details see Appendix E.

To elucidate the reaction mechanism of PS chains grafting to carbon atoms in FG plane, we have studied the nucleophilic attack of S_n^{2-} ($n=2, 4, 6$) on a radical centre of FG. Interestingly, unlike the previously considered nucleophiles (section 3.3), a direct attack of S_n^{2-} on the FG radical site was found energetically unfavourable due to sterical hindrance by surrounding F ad-atoms carrying negative partial charges. Since NMP is known to be one of the defluorinating solvents,⁵³ it was anticipated that in the first part of the reaction FG was partly defluorinated. Moreover, the low IP of PS chains (66.6 - 82.1 kcal·mol⁻¹ depending on the length of sulfur chain) and the high EA of FG (EA of the *trans*-dotriacontafluoroovalene (**c10**) model molecule is 119.5 kcal·mol⁻¹) confirm the probability of an electron transfer from PS chains to FG radical centre which may trigger further defluorination. Considering the defluorination of the material, we have studied the S_n^{2-} nucleophilic attack on partly defluorinated model molecules. Indeed, the nucleophilic attack became more feasible with the decreasing number of F ad-atoms (Figure 30). As in the case of other nucleophiles, the formation of C–S bonds and charge transfer from

the PS chain to FG caused spontaneous defluorination of the substrate. It is worth noting that the free end of a PS chain can also act as a nucleophile and can cause either cross-linking of graphene sheets or can bond to the same graphene sheet and form a cyclized structure.

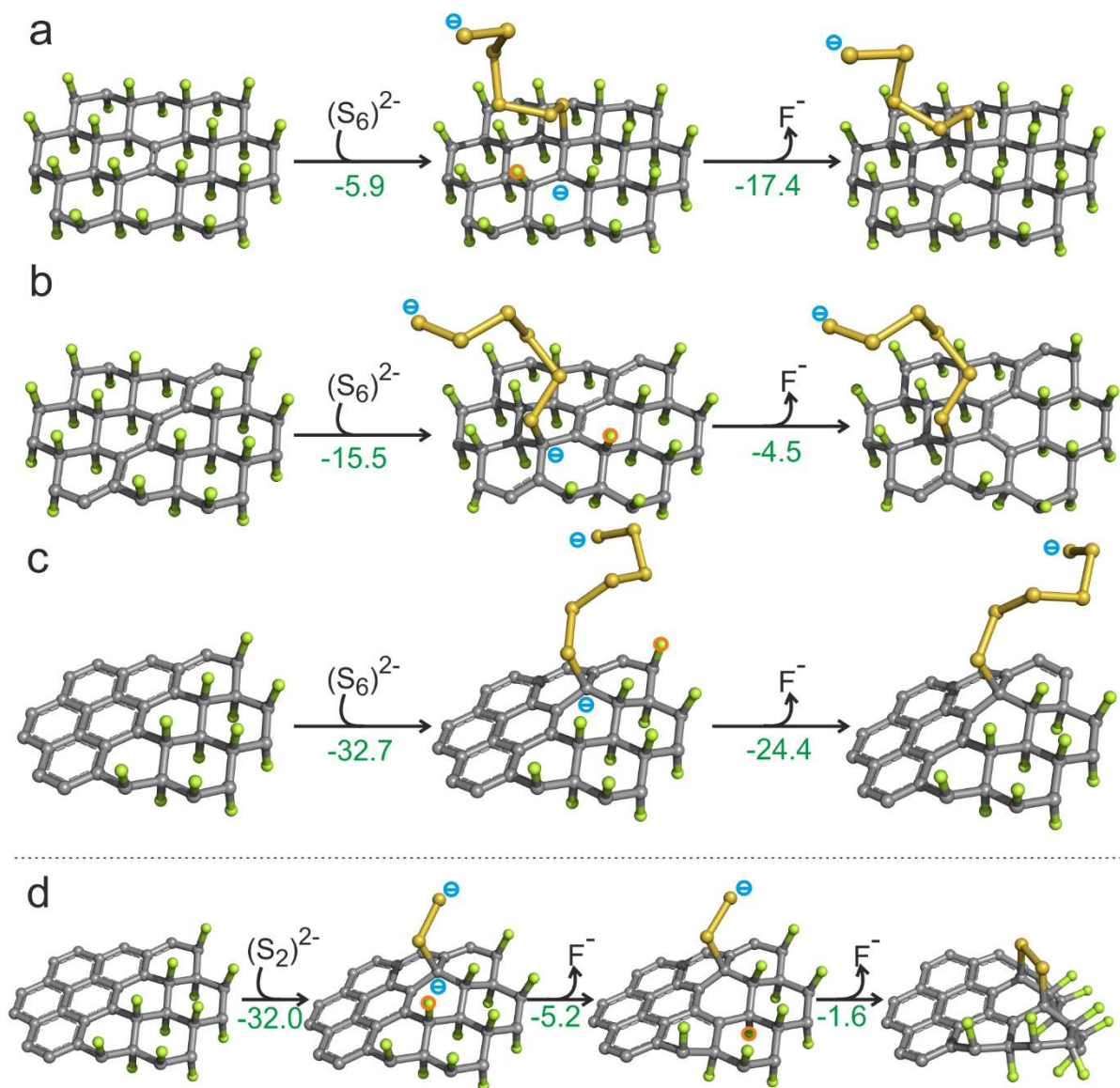


Figure 30: a-c) S_6^{2-} nucleophilic attack on (p)FG with different levels of fluorination, d) S_2^{2-} nucleophilic attack on the edge of the fluorinated and defluorinated area that leads to a cyclized structure of PS chain. Fluorine ad-atoms that are released in the next reaction step are marked by a red circle. Reaction energies are in kcal·mol⁻¹. Carbon atoms are grey, fluorine green, and sulfur yellow.

4. Graphene Derivatives Derived from Fluorographene as Supporting Materials for Single Atom Catalysts

Graphene derivatives are a promising class of 2D materials that can be used as supporting materials for so-called SACs.¹⁴⁵⁻¹⁴⁸ Owing to the maximally reduced size of metal particles that allows full exposure of active sites, SACs exhibit extraordinary catalytic performance. Immobilization of single metal atoms on supporting material offers a way to protect SACs from undesirable processes such as aggregation into larger clusters and leaching during reactions that would decrease their catalytic activity. Functional groups such as –CN and –COOH homogeneously distributed on the graphene plane offer an attractive possibility for robust binding of single metal atoms and cations. For instance, CG was used for anchoring of Cu(II)/Cu(I) ions. Resultant mixed-valence catalyst performed as a highly active catalyst for the oxidation of benzylic C–H bonds and oxidative coupling of amines.⁹⁵ GA-Pd nanohybrids can flawlessly catalyse the Suzuki-Miyaura cross-coupling reaction.⁹⁶ The coordination of metal atoms and cations on CG and GA can also be utilized in graphene-based supercapacitors relying on the charge transfer between the metal and the substrate.¹⁴⁹⁻¹⁵¹

4.1. Cyanographene and Graphene Acid as Supporting Materials for Anchoring of a Series of Late 3*d* and 4*d* Elements

To gain a general picture of the nature of the chemical binding and oxidation states of metal atoms and cations anchored to CG and GA, we have optimized an extensive series of model molecules with anchored atoms and cations of late 3*d* and 4*d* elements (Appendix F).⁹⁷ Namely, the iron triad (Fe, Co, Ni), light platinum group (Ru, Rh, Pd), and coinage metals (Cu, Ag, Au) in oxidation states ranging from 0 to +III were considered. The BDE values for the metal atoms and cations ($\text{Me}^{0/x+}$) in the gas phase indicated that the energetics is more influenced by the initial oxidation state of $\text{Me}^{0/x+}$ than by the chemical nature of the element (Figure 31). The BDEs varied considerably; from ca. 880 to 600 kcal·mol⁻¹ in the case of Me^{3+} (Figure 31b and g, orange columns), from ca. 370 to 240 kcal·mol⁻¹ in the case of Me^{2+} (Figure 31b and g, blue columns), from ca. 80 to 50 kcal·mol⁻¹ in case of Me^{+} (Figure 31b and g, green columns), and from ca. 50 to 5 kcal·mol⁻¹ (Figure 31b and g, red columns) in case of Me^0 . Interestingly, the BDE values of a particular metal atom/cation on CG and protonated GA were comparable (the maximum difference was ca. 15 kcal·mol⁻¹). The aqueous environment significantly lowered the BDE values and narrowed their range; from 329 kcal·mol⁻¹ in the case of Au^{3+} on deprotonated GA (*dp*-GA) to 1 kcal·mol⁻¹ in the case of Au^0 on CG (Figure 31d and i). Moreover, the differences between oxidation states were less regular indicating a

high influence of the polar solvent on the stability of CG/GA \cdots Me complexes. As we have considered deprotonated form of GA in water, BDEs of metal cations on *dp*-GA were higher than those on CG by 31-41 kcal \cdot mol $^{-1}$ in the case of Me $^{3+}$, by 19-24 kcal \cdot mol $^{-1}$ in the case of Me $^{2+}$, and by 2-7 kcal \cdot mol $^{-1}$ in the case of Me $^{+}$ due to the stronger electrostatic interaction between the carboxylate group and metal cation.

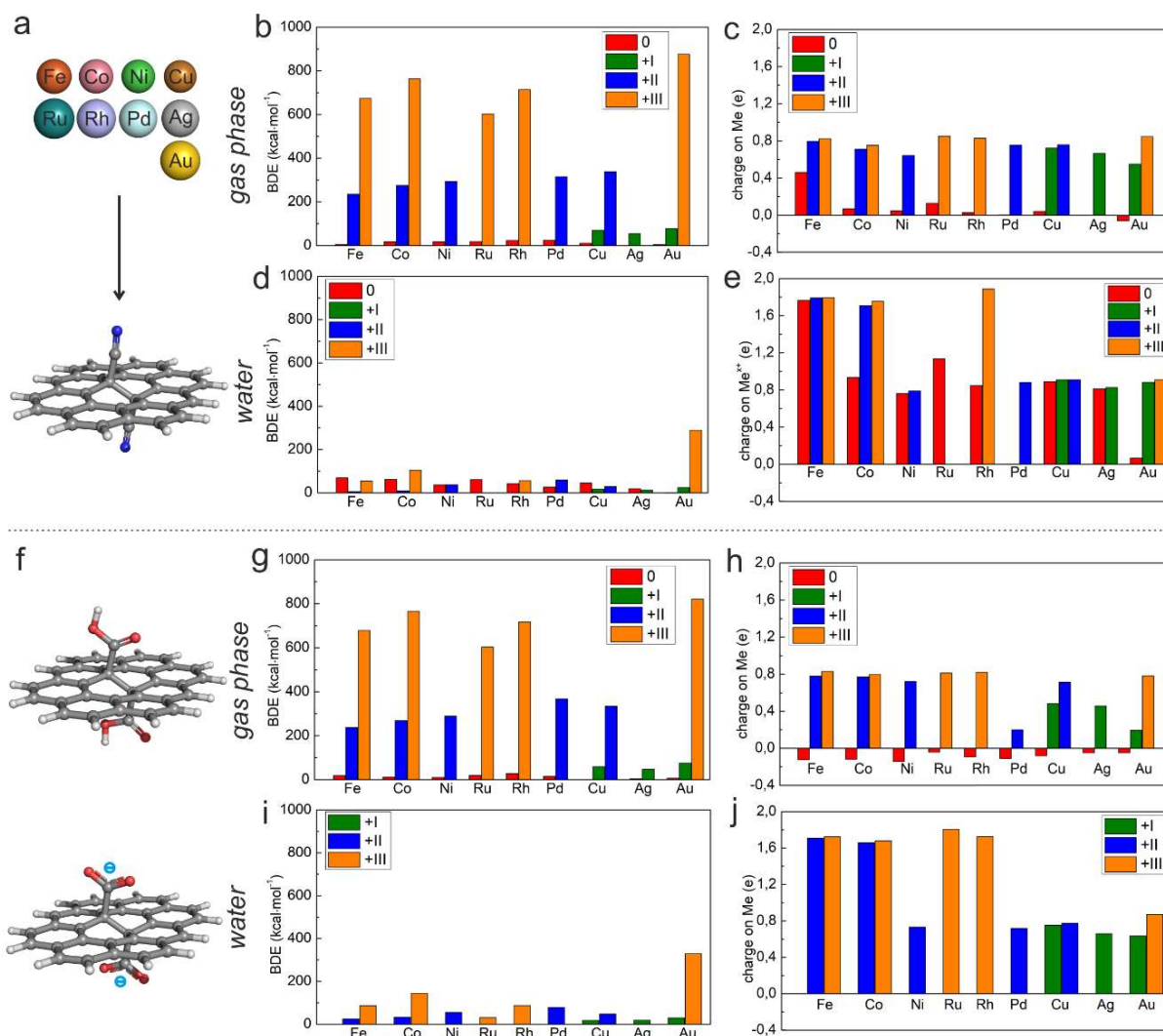


Figure 31: a, f) Schematic illustration of the considered metal elements and model molecules representing CG (top), GA (middle), and deprotonated GA (*dp*-GA, bottom). b, d) BDE of metals bonded to CG in the gas phase and water, c, e) Mulliken charges on the metal bonded to CG in the gas phase and water g, i) BDE of metals bonded to GA in the gas phase and to *dp*-GA in water, h, j) Mulliken charges on the metal bonded to GA in the gas phase and to *dp*-GA in water. Colours of columns indicate the initial charge of the metal atom/cation. Carbon atoms are grey, nitrogen blue, oxygen red, and hydrogen white.

It is worth noting that the BDEs of Me^0 and Me^+ is not sufficiently large to prevent aggregation into larger clusters. The cohesive energy of the investigated metals ranges from 160 to 60 $\text{kcal}\cdot\text{mol}^{-1}$.^{152, 153} Moreover, since the adsorption energies of Me^0 and Me^+ on the graphene plane or into vacancies are in the range from ca. 60 to 1 $\text{kcal}\cdot\text{mol}^{-1}$, adsorption may also occur on these sites.¹⁵⁴⁻¹⁶¹ On the other hand, the BDEs of metal cations with oxidation number +II or +III are much higher implying better stability of SACs.

Owing to the aptitude of CG and GA to donate electrons,^{95, 96} the anchoring of $\text{Me}^{0/x+}$ is accompanied with their reduction (Figure 31c, e, h, and j). The amount of charge transferred between $\text{Me}^{0/x+}$ and the substrate is strongly influenced by the initial charge of $\text{Me}^{0/x+}$. Indeed, the most significant decrease of the initial charge was observed in the case of Me^{3+} in the gas phase (Figure 31c, h, orange columns) and the lowest in the case of Me^0 (Figure 31c and h, red columns). The electron donor strength of CG and GA is comparable. This indicates that the reduction strength of these graphene-based substrates is associated with the π -conjugated carbon network rather than with the functional groups. The aqueous environment significantly lowers the amount of transferred charge (Figure 31e and j). Surprisingly, despite the negative charge of the carboxylate group of *dp*-GA, the reduction strength of CG was only slightly smaller than that of *dp*-GA (the difference was in the range of 0.0-0.3 e).

Whereas the metal cations were reduced, most of the investigated zero-valent metals (besides Pd and Au) anchored to CG were oxidized. Moreover, the level of oxidation was higher in the aqueous environment than in the gas phase (Figure 31c and e, red columns). On the other hand, zero-valent metals were negligibly reduced by GA (Figure 31h, red columns). This observation was explained in terms of frontier orbital analysis of the $\text{Me}^{0/x+}$ and the substrate. For instance, the HOMO energy of Fe^0 in water ($3d(\text{beta})$: -2.2 eV, $4s(\text{alpha})$: -3.2 eV, Figure 32b) was higher than the LUMO energy of CG (-3.3 eV) allowing charge transfer of ($\Delta q = -1.8$ e) from $4s$, $3d_{z^2}$, and $3d_{x^2-y^2}$ orbitals of Fe^0 (according to the NBO analysis)¹²⁹⁻¹³⁴ to CG, i. e., oxidation of Fe^0 . However, the HOMO energy of Fe^0 in the gas phase ($3d(\text{beta})$: -4.2 eV, $4s(\text{alpha})$: -5.1 eV, Figure 32a) laid between the HOMO and LUMO energy of CG (-5.2 and -3.4 eV, respectively) causing only delocalization of the charge ($\Delta q = -0.5$ e). Accordingly, the BDE of $\text{CG}\cdots\text{Fe}^0$ bond was lower in the gas phase (5.1 $\text{kcal}\cdot\text{mol}^{-1}$) than in water (69.4 $\text{kcal}\cdot\text{mol}^{-1}$).

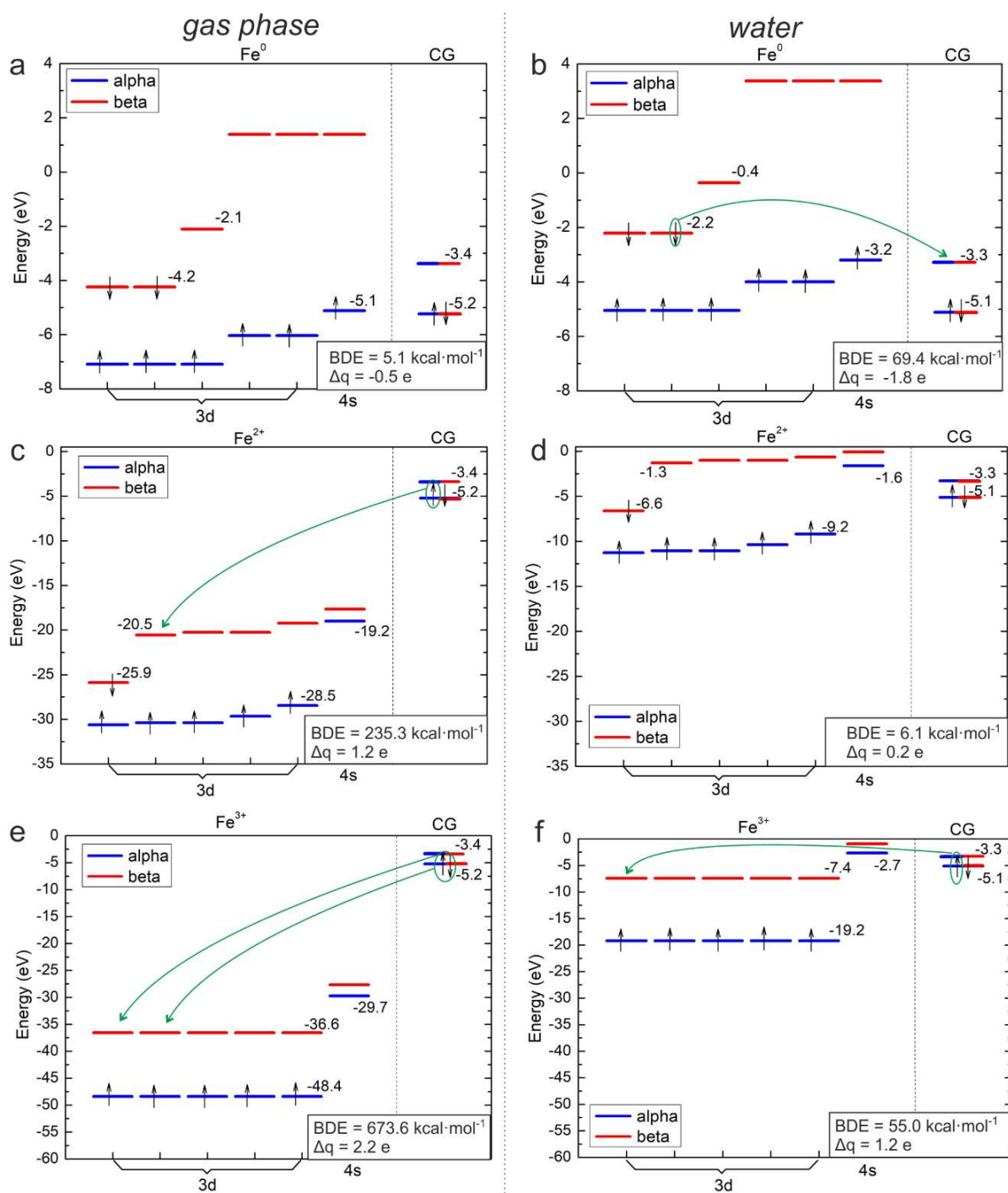


Figure 32: Comparison of HOMO/LUMO energies of CG and a) Fe⁰ in the gas phase, b) Fe⁰ in water, c) Fe²⁺ in the gas phase, d) Fe²⁺ in water, e) Fe³⁺ in the gas phase, and f) Fe³⁺ in water. Green arrows mark the charge transfer between CG and the metal according to the NBO analysis.

The metal cations were reduced more by CG and GA in the gas phase than in the aqueous environment. According to the frontier orbital analysis, the solvent effects increased the LUMO energy of Me^{x+}. For instance, the LUMO energy of Fe²⁺ was increased from -20.5 eV in the gas phase to -1.6 eV in water (Figure 32c and d), and the LUMO energy of Fe³⁺ was

increased from -36.6 eV in the gas phase to -7.4 eV in water (Figure 32e and f). Since the HOMO energy of CG was almost unaffected by the solvent (-5.2 and -5.1 eV in the gas phase and water, respectively), the reduction of Fe^{2+} was more prominent in the gas phase ($\Delta q = 1.2 e$) than in water ($\Delta q = 0.2e$). The charge transfer from the HOMO of CG and thus the creation of CG cation lowered the HOMO energy to -9.6 eV in the gas phase, allowing acceptance of two electrons by Fe^{3+} ($\Delta q = 2.2 eV$, Figure 32e).

To assess the role of π -conjugation of the graphene-based substrate and the influence of different functional groups anchoring metals, we have also investigated ACN and acetic acid (AcOH/AcO^-) as substrates analogous to CG and $\text{GA}/dp\text{-GA}$. We have chosen Pd^0 and Pd^{2+} as examples and compared the level of reduction after anchoring to different substrates. The amount of transferred charge is clearly related to the HOMO/LUMO energy of the substrate (Figure 33a-d). As was discussed earlier, the HOMO/LUMO energies of CG and $\text{GA}/dp\text{-GA}$ were comparable, causing similar Δq . Nevertheless, let us remind that this small difference of HOMO/LUMO energy led to dissimilarity in the case of Me^0 that are oxidized by CG (with two exceptions of Pd^0 and Au^0) but slightly reduced by GA in the gas phase (Figure 31). On the other hand, ACN and AcOH/AcO^- HOMO energies were significantly lower (-9.5 in the case of ACN both in the gas phase and water, -8.1 eV in the case of AcOH in the gas phase and -6.8 eV in the case of AcO^- in water) causing the charge transfer from the substrate to $\text{Me}^{0/x+}$ less efficient (Figure 33a-d). Comparably, the LUMO energies of ACN (0.9 eV in the gas phase and 1.0 eV in water) and AcOH/AcO^- (0.3 eV in the gas phase and 1.6 eV in water) were higher than those of CG and $\text{GA}/dp\text{-GA}$ causing the charge transfer in reverse direction less favourable, too.

Electron density difference (EDD) plots of Pd^{2+} bound to different substrates in the aqueous environment (Figure 33e-h) demonstrate that the π -conjugated network of CG participated more in the charge transfer than the $-\text{CN}$ group as in the case of ACN. In general, the ability of the $-\text{CN}$ group to facilitate the charge transfer between the bonded metal cation and the conductive graphene-based substrate offers a great potential for electrochemistry and electrocatalysis. Nevertheless, in the case of negatively charged carboxylate groups in $dp\text{-GA}$ and AcO^- the charge can be transferred also from the lone pair orbitals of oxygen.

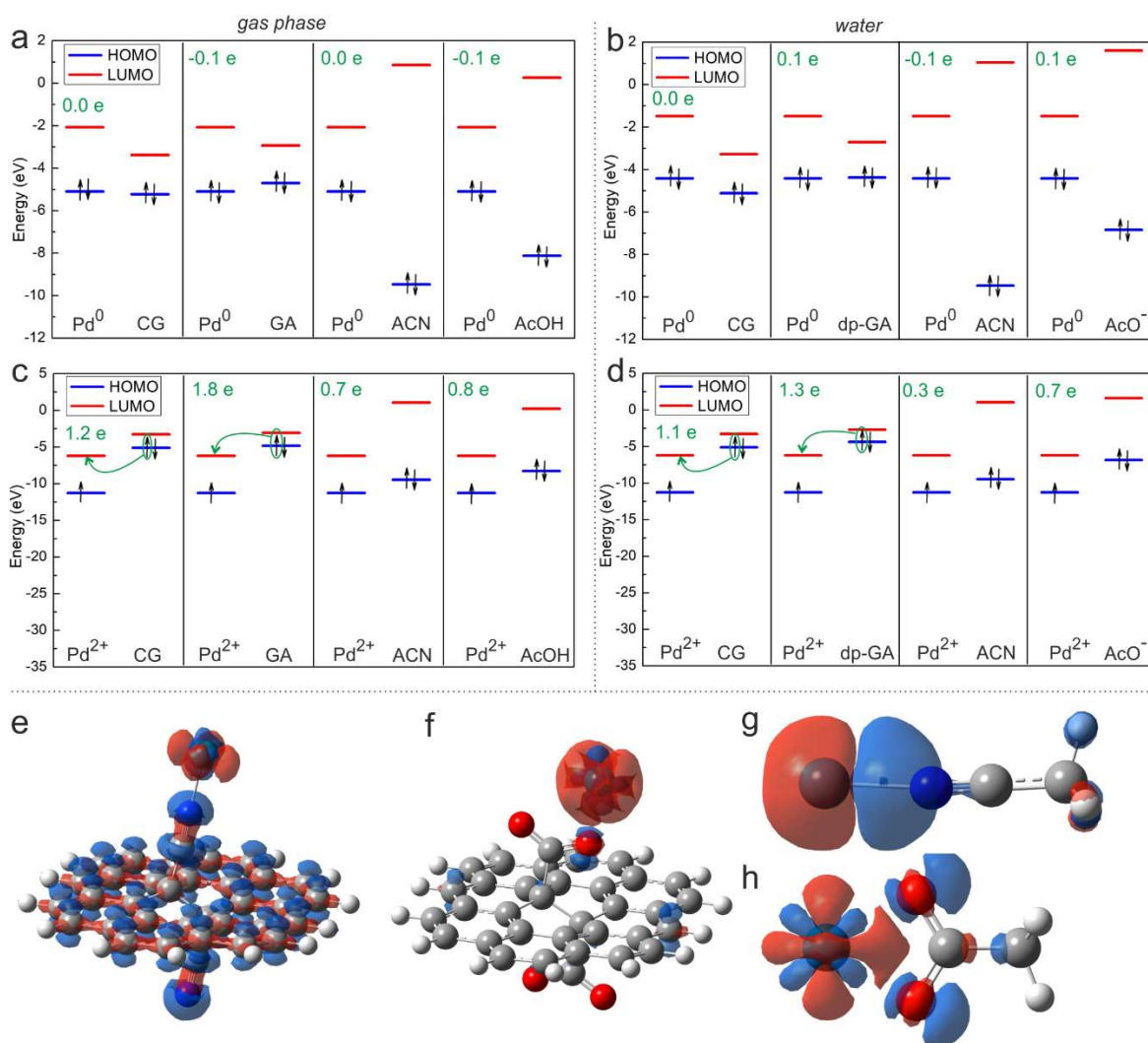


Figure 33: Top: Comparison of HOMO (blue) and LUMO (red) energies of different substrates and a) free Pd⁰ atom in the gas phase, b) free Pd⁰ atom in water, c) free Pd²⁺ cation in the gas phase, and d) free Pd²⁺ cation in water. Green arrows mark the charge transfer between the metal and substrate. Green numbers are the differences in Mulliken charges of the free metal and metal bound to substrate. Bottom: EDD plots of Pd²⁺ bound to e) CG, f) dp-GA, g) ACN, and h) AcO⁻ in water. The isosurface value is e, g) 0.015 a. u. and f, h) 0.003 a. u. Blue isosurface marks the decrease of electron density, red the increase of electron density. Carbon atoms are grey, nitrogen blue, hydrogen white, palladium cyan, and oxygen red.

The anchoring of Me^{0/x+} to CG/(dp-)GA accompanied with a charge transfer between the metal and the substrate led to either complete (for example in the case of Cu²⁺) or partial spin quenching (for example M = 6 of free Fe³⁺ cations was decreased to M = 4 in the gas phase) which opens the possibility of monitoring the entrapment of metal species by EPR. Since the oxidation states cannot be directly derived from the resultant charge on Me^{0/x+} because of their poor correlation,^{162, 163} we have estimated the formal oxidation state from the spin population on Me^{0/x+} according to ref. 164. Surprisingly, the spin populations of anchored Me^{0/x+} were

often the same regardless the initial charge of $\text{Me}^{0/x+}$. This feature of the pairs of cations $\text{Fe}^{2+}/\text{Fe}^{3+}$, $\text{Co}^{2+}/\text{Co}^{3+}$, and $\text{Cu}^+/\text{Cu}^{2+}$ can be used for designing new efficient mixed-valence SACs as was already discussed in ref. 95.

Calculated XPS energies indicate that the recognition of various oxidation states by experimental techniques is possible. For example, the XPS binding energies of the oxidation states of Fe^0 , Fe^{2+} , and Fe^{3+} were 705.7, 715.6, and 718.2 eV, respectively. Let us note that the $2p_{3/2}$ binding energies of Cu^0 , Cu^+ , and Cu^{2+} (926.5, 931.7, and 934.3 eV, respectively) are in agreement with the experimental values of 932.6 and 934.9 eV measured by high-resolution XPS.⁹⁵ This excellent agreement of theoretical and experimental XPS binding energies supports the reliability of our theoretical approach and possibility of identification of synthesized $\text{CG/GA}\cdots\text{Me}^{0/x+}$ complexes.

4.2. The Mechanism of Hydrazine Oxidation Reaction Catalysed by Co^{2+} Cations Anchored to Cyanographene

The cost-effective and sustainable alternatives of fossil fuels have attracted a large interest in the past years because the ever-growing demand of energy causes several environmental issues.^{165, 166} Conversion of chemical energy using fuels such as hydrogen, organic acids, alcohols, and hydrazine in fuel cells is a promising way to produce energy with high efficiency and minimal greenhouse gas emissions. In our study (Appendix G),⁹⁸ we have investigated the electrocatalytic oxidation of hydrazine since the products of hydrazine oxidation are harmless H_2O and N_2 , hydrazine is easy to transport as a liquid at room temperature, and direct hydrazine fuel cells offer large theoretical cell voltage (+1.61 V) and better energy/power density than many other fuel cells.¹⁶⁵

The hydrazine oxidation reaction (HzOR) with assistance of the $\text{CG}\cdots\text{Co}^{2+}$ catalyst was studied step-by-step by geometry optimization of hydrazine, nitrogen, and all intermediate species with and without the catalyst in the aqueous environment (Figure 34 and 35). In the basic environment, the reaction proceeds via four deprotonation steps and four electrochemical steps. In sum, four electrons are released. The HzOR may proceed via two energetically comparable routes (steps 3-5). The $\text{CG}\cdots\text{Co}^{2+}$ catalyst significantly promotes the otherwise energetically demanding deprotonation steps (steps 1, 3, 5, 7) thanks to the ability to decrease the N–H bond polarity. Moreover, the negatively charged intermediate species are stabilized by the charge transfer from N_2H_x ($x = 1-4$) to the $\text{CG}\cdots\text{Co}^{2+}$ catalyst making the reaction steps more feasible. The electron-releasing steps (electrochemical steps 2, 4, 6, and 8) are energetically less demanding without the $\text{CG}\cdots\text{Co}^{2+}$ catalyst.

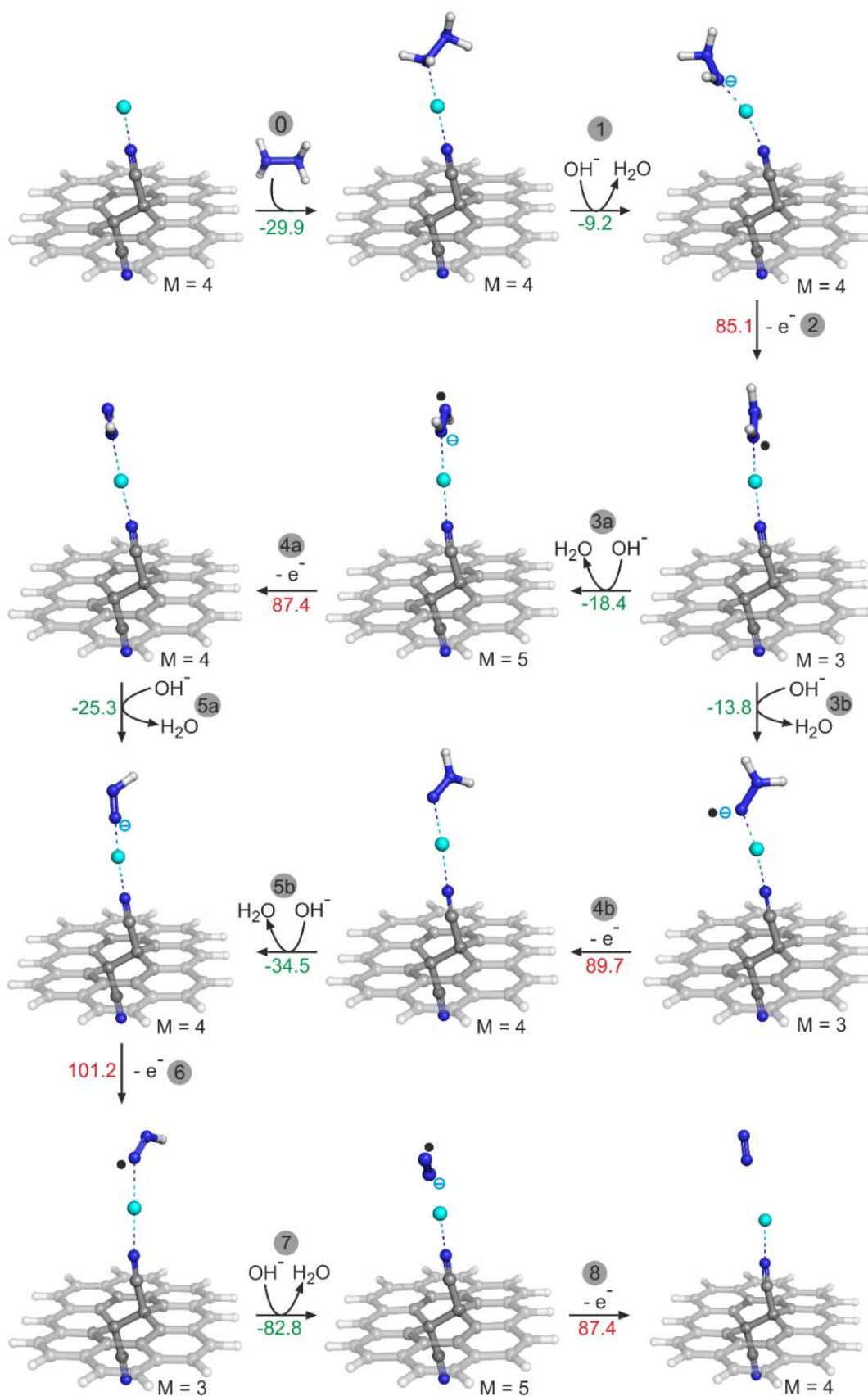


Figure 34: Reaction mechanism of HzOR catalysed by Co²⁺ cations anchored to CG in water. The reaction energies (green) and ionization potentials (red) are in kcal·mol⁻¹. The multiplicities of species (M) are also reported. Carbon atoms are grey, nitrogen blue, hydrogen white, and cobalt cyan.

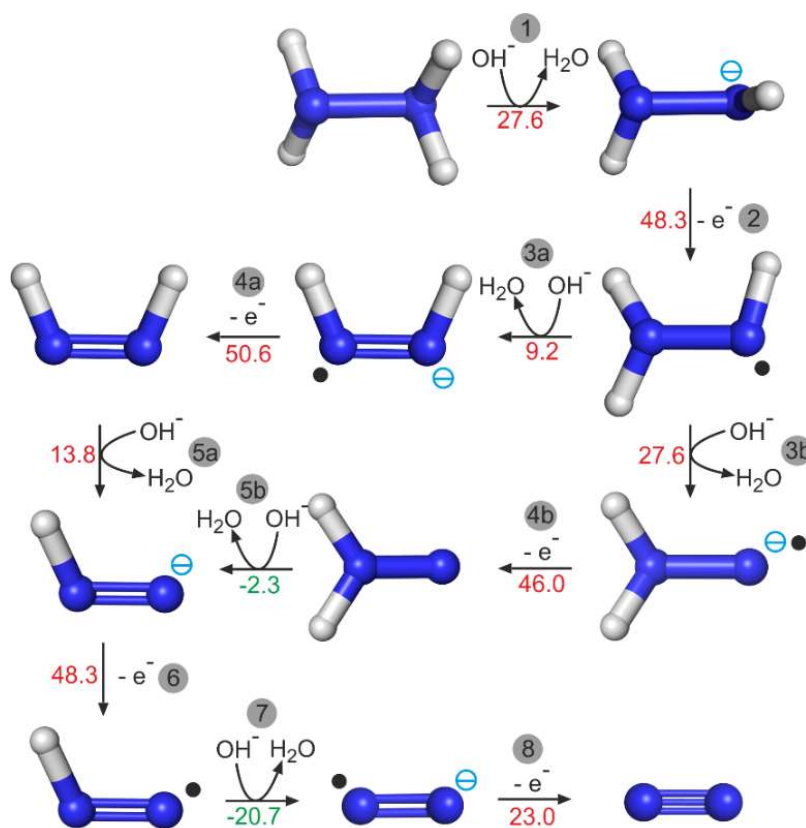


Figure 35: Reaction mechanism of HzOR without the catalyst. The reaction energies and ionization potentials are in $\text{kcal}\cdot\text{mol}^{-1}$. Nitrogen atoms are blue, hydrogen white.

To further improve our model of the catalyst, we have also included explicit water molecules coordinated to the Co^{2+} cation (Figure 36). The water molecules cause a decrease of the positive charge on Co^{2+} and thus lower the interaction energy between the nitrogen of the hydrazine molecule and Co^{2+} from -29.9 to -13.8 $\text{kcal}\cdot\text{mol}^{-1}$ (Figure 34 and 36, step 0). Nevertheless, the reaction energies are not significantly affected by the explicit solvent molecules. For instance, the ΔE_R of step 1 changes from -9.2 to -6.9 $\text{kcal}\cdot\text{mol}^{-1}$ and that of step 2 changes from 85.1 to 69.0 $\text{kcal}\cdot\text{mol}^{-1}$. Noteworthy, the coordinated water molecules may also play an active role in the HzOR (Figure 36, path b).

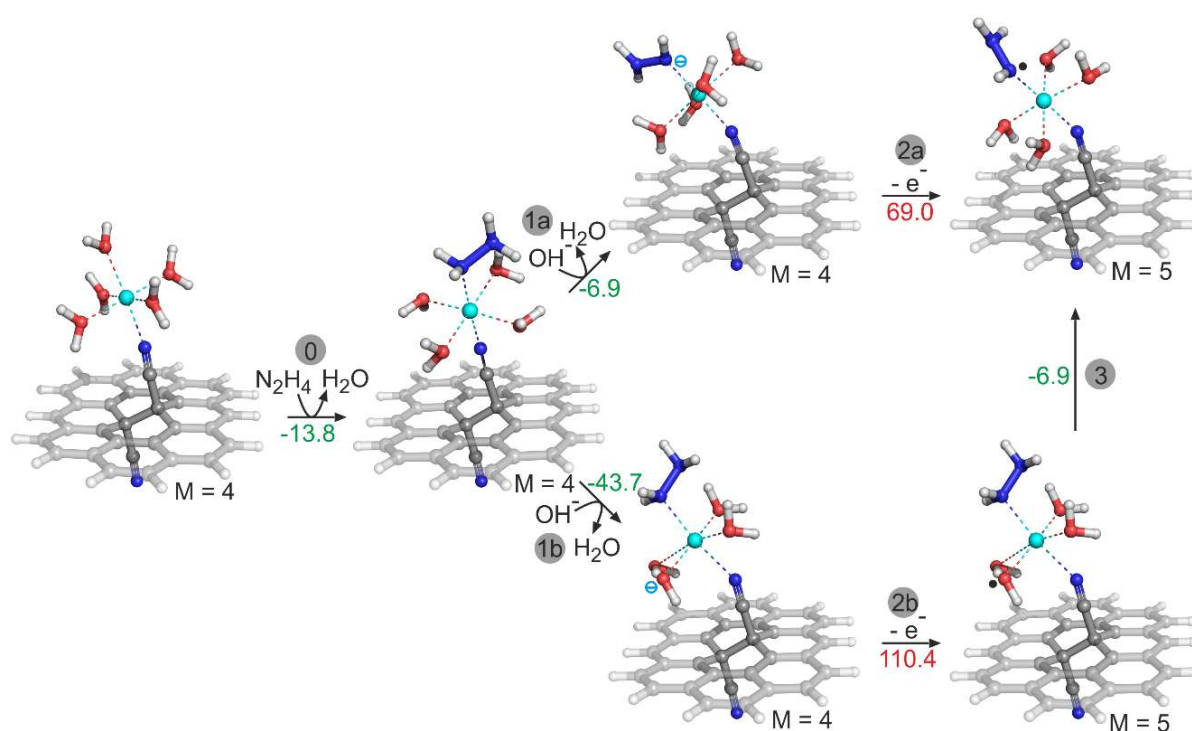


Figure 36: The mechanism of HzOR on the model of CG...Co²⁺ catalyst with explicit water molecules coordinated to Co²⁺. The reaction energies (green) and ionization potentials (red) are in kcal·mol⁻¹. The multiplicities of species (M) are also reported. Carbon atoms are grey, nitrogen blue, oxygen red, hydrogen white, and cobalt cyan.

In conclusion, our results showed a significant variability of binding characteristics in the CG/GA...Me^{0/x+} complexes that are closely related to the electron affinity of the anchored metal atom or cation and to the amount of charge transferred between the metal and the substrate. We believe that the insight into the communication between the anchored metal atoms or cations and the π -conjugated lattice of the graphene-based substrate that leads to the reduction/oxidation of Me^{0/x+} and to complete or partial spin quenching opens a road to new heterogenous SACs and other spintronic and electrochemical applications. The ability of cations anchored to CG to act as catalysts was demonstrated in the mechanism of hydrazine oxidation reaction that was fostered by CG...Co²⁺ complex.

5. Conclusions

The basis of the interesting chemistry of FG lies in the variability of C–F bond nature that is in contradiction with the consensus that C–F bond is one of the strongest bonds in organic chemistry. DFT calculations revealed that the C–F bond strength in (p)FGs varies significantly from 25.6 to 118.2 kcal·mol⁻¹ depending on the local configuration of fluorine ad-atoms and the level of fluorination. Therefore, individual C–F bonds cannot be viewed as equivalent. While defluorination is driven mainly by thermodynamics and leads to the formation of specific structural motifs such as chains or rings of C=C double bonds, fluorination is -to some extent- influenced also by stochasticity. As a result, the properties of partially fluorinated graphene depend on the method of preparation and may evolve in time as the structure relaxes into the most stable configuration. These aspects should be considered when analysing the reactivity of (p)FGs since it can change during chemical reactions in very complex ways. This is a unique property that has no analogue in classical molecular organic chemistry.

Using DFT methods, we have unravelled that direct defluorination of FG initiated by electron transfer to the low-lying σ^* orbital of C–F bond is only possible in the presence of strong reducing agents. However, experimental observations reported that defluorination also occurs in the presence of mild reducing agents. Interestingly, EPR measurements discovered that point defects (radical sites) are naturally present in FG structure and could be a key to explain FG's surprising reactivity because they exhibit much higher electron affinity making them perfect reactive sites for nucleophilic species and mild reducing agents. Our results showed that radical sites may play various roles in the reactivity of FG. First, they can accept an electron in the presence of a sufficiently strong reducing agent and initiate cascade defluorination. Second, they may trigger radical defluorination if sufficiently stable radicals are formed, which was demonstrated by the reaction mechanism of FG defluorination in the DMF solvent which started with the homolytic cleavage of C–H bond of DMF and the formation of DMF•. Third, they can act as electrophilic sites for nucleophilic attack. We have focused on the attack on FG radical sites of four nucleophilic species: NH_2^- , OH^- , CN^- , and S_n^{2-} ($n = 2, 4, 6$) in different solvents. In the case of NH_2^- , OH^- , and CN^- , the first reaction step was thermodynamically favourable. Since the nucleophile brought a negative charge to the system, the reaction proceeded via spontaneous release of a fluoride anion and formation of a new radical site which could be attacked by another nucleophile. In the case of S_n^{2-} , the nucleophilic attack on the radical site is sterically hindered by the surrounding fluorine ad-atoms carrying a partial negative charge. However, the nucleophilic attack of S_n^{2-} was possible on larger defluorinated areas. The radical sites may also be present at the edges of vacancies in FG structure. We have

investigated NH_2^- nucleophilic attack on different types of vacancies (single, double, and triple vacancies) that led to the formation of either graphitic, pyridinic, or pyrrolic nitrogen incorporated into FG lattice. Additionally, it was shown that the FG radical sites may initiate many side-reactions in the reaction system and thus enrich the number of possible by-products of the reaction.

To conclude, it is evident that the radical centres of FG play a vital role in FG chemistry. Different thermodynamics and kinetics of individual reaction steps allow tuning of the obtained material's composition by the choice of the reaction time, solvent, and temperature. This was supported experimentally by the reaction of *N*-octylamine and FG in *o*-dichlorobenzene and DMF that led to different levels of functionalization and defluorination depending on the used solvent and reaction time. In addition, the reaction of FG with NaNH_2 in DMF and ACN that led to different level of N-doping was also significantly influenced by temperature (for experimental results see Appendix C and D). We believe that our results significantly contribute to the understanding of FG's exceptional chemistry and provide a fundamental knowledge that can help in the synthesis of new graphene derivatives with controllable structure and properties.

Graphene derivatives derived from FG such as CG and GA are a promising class of substrate materials for SACs. DFT results of late *3d* and *4d* elements anchored to either CG or GA showed a vast diversity of binding characteristics. The BDEs of CG/GA...Me bonds ranged from 5 to 880 $\text{kcal}\cdot\text{mol}^{-1}$ in the gas phase, while the aqueous environment caused a significant decrease of the range of BDEs (from 1 to 329 $\text{kcal}\cdot\text{mol}^{-1}$). The CG/GA...Me bond strength significantly correlates with the amount of charge transferred between the metal and the substrate as well as the electron affinity of the metal atom or cation. In general, the metals in oxidation states +II and +III are the most strongly bound, indicating the high stability of the complexes in catalytic reactions. In contrast, SACs with zero-valence metals and metal cations in the oxidation state +I can suffer from competitive processes such as aggregation and leaching since the CG/GA...Me bonds are not sufficiently strong. Anchoring of metal atoms and cations to CG and GA is accompanied with metal reduction. The level of reduction can be explained in terms of frontier orbital analysis. In most cases, the HOMO energy of the substrate is laid above the LUMO energy of the metal cation, allowing charge transfer from the substrate to the metal cation, i.e., reduction of the metal cation. The aqueous environment causes a significant decrease of the difference between LUMO energy of $\text{Me}^{0/x+}$ and HOMO energy of the substrate and thus suppressed the charge transfer. The zero-valence metals are either oxidized or negligibly reduced by the substrate, which is related to the fact that their LUMO

energies are above or at a similar level as the HOMO energies of the substrate. Additional calculations of ACN and AcOH as substrates and EDD plots demonstrated that the ability of CG and GA to reduce or oxidize metal atoms and cations is associated with the π -conjugated lattice rather than with the functional groups. In the neutral or basic environment, the lone pairs of oxygen in the carboxylate groups of *dp*-GA and AcO⁻ could also participate in the charge transfer between the metal cation and the substrate. Analysis of the spin populations of anchored metal atoms and cations revealed that some metal atoms and cations are in the same oxidation state regardless of their different initial charge, offering the design of new mixed-valence SACs. Nevertheless, the resultant charges of anchored metal atoms and cations differed enough to be distinguishable by XPS technique. In addition, we have studied the catalytic role of Co²⁺ cations anchored to CG in the reaction mechanism of hydrazine oxidation reaction. DFT calculations showed that the CG \cdots Co²⁺ catalyst fostered the N–H bonds dissociation steps owing to the ability to decrease the N–H bonds polarity.

Our results provide a backbone for designing new materials applicable in various fields. The communication of the anchored metal atoms or cations and the π -conjugated lattice of the graphene-based substrate via the nitrile and carboxylate groups causing reduction/oxidation of Me^{0/x+} and complete or partial spin quenching opens a road not only to new heterogenous SACs but also to other spintronic and electrochemical applications.

6. References

1. Nair, R. R., Ren, W., Jalil, R., Riaz, I., Kravets, V. G., Britnell, L., Blake, P., Schedin, F., Mayorov, A. S., Yuan, S., Katsnelson, M. I., Cheng, H.-M., Strupinski, W., Bulusheva, L. G., Okotrub, A. V., Grigorieva, I. V., Grigorenko, A. N., Novoselov, K. S. and Geim, A. K. Fluorographene: A Two-Dimensional Counterpart of Teflon. *Small* **2010**, 6 (24), 2877-2884, DOI 10.1002/sml.201001555.
2. Zbořil, R., Karlický, F., Bourlinos, A. B., Steriotis, T. A., Stubos, A. K., Georgakilas, V., Šafářová, K., Jančík, D., Trapalis, C. and Otyepka, M. Graphene Fluoride: A Stable Stoichiometric Graphene Derivative and its Chemical Conversion to Graphene. *Small* **2010**, 6 (24), 2885-2891, DOI 10.1002/sml.201001401.
3. Robinson, J. T., Burgess, J. S., Junkermeier, C. E., Badescu, S. C., Reinecke, T. L., Perkins, F. K., Zalalutdniov, M. K., Baldwin, J. W., Culbertson, J. C., Sheehan, P. E. and Snow, E. S. Properties of Fluorinated Graphene Films. *Nano Lett.* **2010**, 10 (8), 3001-3005, DOI 10.1021/nl101437p.
4. Leenaerts, O., Peelaers, H., Hernández-Nieves, A. D., Partoens, B. and Peeters, F. M. First-Principles Investigation of Graphene Fluoride and Graphane. *Phys. Rev. B* **2010**, 82 (19), 195436, DOI 10.1103/PhysRevB.82.195436.
5. Samarakoon, D. K., Chen, Z., Nicolas, C. and Wang, X.-Q. Structural and Electronic Properties of Fluorographene. *Small* **2011**, 7 (7), 965-969, DOI 10.1002/sml.201002058.
6. Walder, B. J. and Alam, T. M. Modes of Disorder in Poly(carbon monofluoride). *J. Am. Chem. Soc.* **2021**, 143 (30), 11714-11733, DOI 10.1021/jacs.1c05234.
7. Mathkar, A., Narayanan, T. N., Alemany, L. B., Cox, P., Nguyen, P., Gao, G., Chang, P., Romero-Aburto, R., Mani, S. A. and Ajayan, P. M. Synthesis of Fluorinated Graphene Oxide and its Amphiphobic Properties. *Part. Part. Syst. Character.* **2013**, 30 (3), 266-272, DOI 10.1002/ppsc.201200091.
8. Lei, F., Yang, M., Jiang, F., Zhang, H., Zhang, Z. and Sun, D. Microwave-assisted Liquid Phase Exfoliation of Graphite Fluoride into Fluorographene. *Chem. Eng. J.* **2019**, 360, 673-679, DOI 10.1016/j.cej.2018.12.044.
9. Jeon, K.-J., Lee, Z., Pollak, E., Moreschini, L., Bostwick, A., Park, C.-M., Mendelsberg, R., Radmilovic, V., Kosteki, R., Richardson, T. J. and Rotenberg, E. Fluorographene: A Wide Bandgap Semiconductor with Ultraviolet Luminescence. *ACS Nano* **2011**, 5 (2), 1042-1046, DOI 10.1021/nn1025274.
10. Wang, X., Dai, Y., Gao, J., Huang, J., Li, B., Fan, C., Yang, J. and Liu, X. High-Yield Production of Highly Fluorinated Graphene by Direct Heating Fluorination of Graphene-oxide. *ACS Appl. Mater. Inter.* **2013**, 5 (17), 8294-8299, DOI 10.1021/am402958p.
11. Poh, H. L., Sofer, Z., Klímová, K. and Pumera, M. Fluorographenes via Thermal Exfoliation of Graphite Oxide in SF₆, SF₄ and MoF₆ Atmospheres. *J. Mater. Chem. C* **2014**, 2 (26), 5198-5207, DOI 10.1039/c4tc00395k.
12. Bruno, G., Bianco, G. V., Giangregorio, M. M., Losurdo, M. and Capezzuto, P. Photothermally Controlled Structural Switching in Fluorinated Polyene-graphene Hybrids. *Phys. Chem. Chem. Phys.* **2014**, 16 (27), 13948-13955, DOI 10.1039/c4cp01643b.

13. Yu, X., Lin, K., Qiu, K., Cai, H., Li, X., Liu, J., Pan, N., Fu, S., Luo, Y. and Wang, X. Increased Chemical Enhancement of Raman Spectra for Molecules Adsorbed on Fluorinated Reduced Graphene Oxide. *Carbon* **2012**, 50 (12), 4512-4517, DOI 10.1016/j.carbon.2012.05.033.
14. Baraket, M., Walton, S. G., Lock, E. H., Robinson, J. T. and Perkins, F. K. The Functionalization of Graphene Using Electron-beam Generated Plasmas. *Appl. Phys. Lett.* **2010**, 96 (23), 231501, DOI 10.1063/1.3436556.
15. Bon, S. B., Valentini, L., Verdejo, R., Garcia Fierro, J. L., Peponi, L., Lopez-Manchado, M. A. and Kenny, J. M. Plasma Fluorination of Chemically Derived Graphene Sheets and Subsequent Modification With Butylamine. *Chem. Mat.* **2009**, 21 (14), 3433-3438, DOI 10.1021/cm901039j.
16. Tahara, K., Iwasaki, T., Matsutani, A. and Hatano, M. Effect of Radical Fluorination on Mono- and Bi-layer Graphene in Ar/F₂ Plasma. *App. Phys. Lett.* **2012**, 101 (16), 163105, DOI 10.1063/1.4760268.
17. Samanta, K., Some, S., Kim, Y., Yoon, Y., Min, M., Lee, S. M., Park, Y. and Lee, H. Highly Hydrophilic and Insulating Fluorinated Reduced Graphene Oxide. *Chem. Commun.* **2013**, 49 (79), 8991-8993, DOI 10.1039/c3cc45376f.
18. Lee, W. H., Suk, J. W., Chou, H., Lee, J., Hao, Y., Wu, Y., Piner, R., Akinwande, D., Kim, K. S. and Ruoff, R. S. Selective-Area Fluorination of Graphene with Fluoropolymer and Laser Irradiation. *Nano Lett.* **2012**, 12 (5), 2374-2378, DOI 10.1021/nl300346j.
19. Gao, X. and Tang, X. Effective Reduction of Graphene Oxide Thin Films by a Fluorinating Agent: Diethylaminosulfur Trifluoride. *Carbon* **2014**, 76, 133-140, DOI 10.1016/j.carbon.2014.04.059.
20. Wang, Z., Wang, J., Li, Z., Gong, P., Liu, X., Zhang, L., Ren, J., Wang, H. and Yang, S. Synthesis of Fluorinated Graphene with Tunable Degree of Fluorination. *Carbon* **2012**, 50 (15), 5403-5410, DOI 10.1016/j.carbon.2012.07.026.
21. Karlický, F. and Otyepka, M. Band Gaps and Optical Spectra of Chlorographene, Fluorographene and Graphane from G₀W₀, GW₀ and GW Calculations on Top of PBE and HSE06 Orbitals. *J. Chem. Theory Comput.* **2013**, 9 (9), 4155-4164, DOI 10.1021/ct400476r.
22. Kumar, N., Sharma, J. D. and Ahluwalia, P. K. First-principle Study of Nanostructures of Functionalized Graphene. *Pramana* **2014**, 82 (6), 1103-1117, DOI 10.1007/s12043-014-0758-x.
23. Liu, H. Y., Hou, Z. F., Hu, C. H., Yang, Y. and Zhu, Z. Z. Electronic and Magnetic Properties of Fluorinated Graphene with Different Coverage of Fluorine. *J. Phys. Chem. C* **2012**, 116 (34), 18193-18201, DOI 10.1021/jp303279r.
24. Makarova, T. L., Shelankov, A. L., Zyrianova, A. A., Veinger, A. I., Tisnek, T. V., Lähderanta, E., Shames, A. I., Okotrub, A. V., Bulusheva, L. G., Chekhova, G. N., Pinakov, D. V., Asanov, I. P. and Šljivančanin, Ž. Edge State Magnetism in Zigzag-interfaced Graphene via Spin Susceptibility Measurements. *Sci. Rep.* **2015**, 5 (1), 13382, DOI 10.1038/srep13382.

25. Tuček, J., Holá, K., Bourlinos, A. B., Błoński, P., Bakandritsos, A., Ugolotti, J., Dubecký, M., Karlický, F., Ranc, V., Čépe, K., Otyepka, M. and Zbořil, R. Room Temperature Organic Magnets Derived from sp^3 Functionalized Graphene. *Nat. Commun.* **2017**, 8 (1), 14525, DOI 10.1038/ncomms14525.
26. Tuček, J., Holá, K., Zoppellaro, G., Błoński, P., Langer, R., Medved', M., Susi, T., Otyepka, M. and Zbořil, R. Zigzag sp^2 Carbon Chains Passing through an sp^3 Framework: A Driving Force toward Room-Temperature Ferromagnetic Graphene. *ACS Nano* **2018**, 12 (12), 12847-12859, DOI 10.1021/acsnano.8b08052.
27. Lvova, N. A. and Ananina, O. Y. Theoretical Study of Graphene Functionalization by F^- and FHF^- Ions from Associates with Water Molecules. *Comp. Mater. Sci.* **2015**, 101, 287-292, DOI 10.1016/j.commatsci.2015.02.007.
28. Tran, N. T. T., Nguyen, D. K., Glukhova, O. E. and Lin, M.-F. Coverage-dependent Essential Properties of Halogenated Graphene: A DFT Study. *Sci. Rep.* **2017**, 7 (1), 17858, DOI 10.1038/s41598-017-18170-8.
29. Karlický, F., Datta, K. K. R., Otyepka, M. and Zbořil, R. Halogenated Graphenes: Rapidly Growing Family of Graphene Derivatives. *ACS Nano* **2013**, 7 (8), 6434-6464, DOI 10.1021/nn4024027.
30. Fan, K., Peng, L., Liu, Y., Li, Y., Chen, Y., Meng, Y., Liu, X., Feng, W. and Wang, X. Giant Enhancement of Fluorescence Emission by Fluorination of Porous Graphene with High Defect Density and Subsequent Application as Fe^{3+} Ion Sensors. *ACS Appl. Mater. Inter.* **2020**, 12 (36), 40662-40672, DOI 10.1021/acsam.0c11141.
31. Yuan, S., Rösner, M., Schulz, A., Wehling, T. O. and Katsnelson, M. I. Electronic Structures and Optical Properties of Partially and Fully Fluorinated Graphene. *Phys. Rev. Lett.* **2015**, 114 (4), 047403, DOI 10.1103/PhysRevLett.114.047403.
32. Wei, W. and Jacob, T. Electronic and Optical Properties of Fluorinated Graphene: A Many-body Perturbation Theory Study. *Phys. Rev. B* **2013**, 87 (11), 115431, DOI 10.1103/PhysRevB.87.115431.
33. Dubecký, M., Karlický, F., Minárik, S. and Mitas, L. Fundamental Gap of Fluorographene by Many-body GW and Fixed-node Diffusion Monte Carlo Methods. *J. Chem. Phys.* **2020**, 153 (18), 184706, DOI 10.1063/5.0030952.
34. Karlický, F. and Otyepka, M. Band Gaps and Optical Spectra from Single- and Double-Layer Fluorographene to Graphite Fluoride: Many-body Effects and Excitonic States. *Ann. Phys.* **2014**, 526 (9-10), 408-414, DOI 10.1002/andp.201400095.
35. Wang, B., Sparks, J. R., Gutierrez, H. R., Okino, F., Hao, Q., Tang, Y., Crespi, V. H., Sofo, J. O. and Zhu, J. Photoluminescence from Nanocrystalline Graphite Monofluoride. *Appl. Phys. Lett.* **2010**, 97 (14), 141915, DOI 10.1063/1.3491265.
36. Wang, X., Dai, Y., Wang, W., Ren, M., Li, B., Fan, C. and Liu, X. Fluorographene with High Fluorine/Carbon Ratio: A Nanofiller for Preparing Low- κ Polyimide Hybrid Films. *ACS Appl. Mater. Inter.* **2014**, 6 (18), 16182-16188, DOI 10.1021/am5042516.
37. Gong, P., Wang, Z., Wang, J., Wang, H., Li, Z., Fan, Z., Xu, Y., Han, X. and Yang, S. One-pot Sonochemical Preparation of Fluorographene and Selective Tuning of its Fluorine Coverage. *J. Mater. Chem.* **2012**, 22 (33), 16950-16956, DOI 10.1039/c2jm32294c.

38. Zhan, L., Yang, S., Wang, Y., Wang, Y., Ling, L. and Feng, X. Fabrication of Fully Fluorinated Graphene Nanosheets Towards High-Performance Lithium Storage. *Adv. Mater. Interfaces* **2014**, 1 (4), 1300149, DOI 10.1002/admi.201300149.
39. Ci, X., Zhao, W., Luo, J., Wu, Y., Ge, T., Xue, Q., Gao, X. and Fang, Z. How the Fluorographene Replaced Graphene as Nanoadditive for Improving Tribological Performances of GTL-8 Based Lubricant Oil. *Friction* **2021**, 9, 488-501, DOI 10.1007/s40544-019-0350-y.
40. Narasaki, M., Wang, H., Nishiyama, T., Ikuta, T. and Takahashi, K. Experimental study on thermal conductivity of free-standing fluorinated single-layer graphene. *Appl. Phys. Lett.* **2017**, 111 (9), 093103, DOI 10.1063/1.5001169.
41. Li, X., Maute, K., Dunn, M. L. and Yang, R. Strain Effects on the Thermal Conductivity of Nanostructures. *Phys. Rev. B* **2010**, 81 (24), 245318, DOI 10.1103/PhysRevB.81.245318.
42. Sun, C., Feng, Y., Li, Y., Qin, C., Zhang, Q. and Feng, W. Solvothermally Exfoliated Fluorographene for High-performance Lithium Primary Batteries. *Nanoscale* **2014**, 6 (5), 2634-2641, DOI 10.1039/c3nr04609e.
43. Fan, R., Yang, B., Li, Z., Ma, D., Yuan, W., Ma, J. and Ren, H. First-principles Study of the Adsorption Behaviors of Li Atoms and LiF on the CF_x (x = 1.0, 0.9, 0.8, 0.5, ~0.0) Surface. *RSC Adv.* **2020**, 10 (53), 31881-31888, DOI 10.1039/d0ra03635h.
44. Bi, X., Li, Y., Qiu, Z., Liu, C., Zhou, T., Zhuo, S. and Zhou, J. Fluorinated Graphene Prepared by Direct Fluorination of N, O-Doped Graphene Aerogel at Different Temperatures for Lithium Primary Batteries. *Materials* **2018**, 11 (7), 1072, DOI 10.3390/ma11071072
45. Feng, W., Long, P., Feng, Y. and Li, Y. Two-Dimensional Fluorinated Graphene: Synthesis, Structures, Properties and Applications. *Adv. Sci.* **2016**, 3 (7), 1500413, DOI 10.1002/advs.201500413.
46. Sorokin, P. B. and Chernozatonskii, L. A. Graphene-based Semiconductor Nanostructures. *Phys. - Usp.* **2013**, 56 (2), 105-122, DOI 10.3367/UFNe.0183.201302a.0113.
47. Wang, X. and Wu, P. Highly Thermally Conductive Fluorinated Graphene Films with Superior Electrical Insulation and Mechanical Flexibility. *ACS Appl. Mater. Inter.* **2019**, 11 (24), 21946-21954, DOI 10.1021/acsami.9b07377.
48. Banerjee, A. N. Graphene and its Derivatives as Biomedical Materials: Future Prospects and Challenges. *Interface Focus* **2018**, 8 (3), 20170056, DOI 10.1098/rsfs.2017.0056.
49. Wang, D., Zhang, Y., Zhai, M., Huang, Y., Li, H., Liu, X., Gong, P., Liu, Z. and You, J. Fluorescence Turn-off Magnetic Fluorinated Graphene Composite with High NIR Absorption for Targeted Drug Delivery. *ChemNanoMat* **2021**, 7 (1), 71-77, DOI 10.1002/cnma.202000539.
50. Mishra, M. and Yagci, Y., Handbook of Vinyl Polymers: Radical Polymerization, Process, and Technology. *CRC Press* **2019**, 784, ISBN 9780367387112
51. Hughes, R. P. Organo-Transition Metal Compounds Containing Perfluorinated Ligands. *Adv. Organomet. Chem.* **1990**, 31, 183-267, DOI 10.1016/S0065-3055(08)60511-0.

52. Nair, R. R., Ren, W., Jalil, R., Riaz, I., Kravets, V., Britnell, L., Blake, P., Schedin, F., Mayorov, A., Yuan, S., Katsnelson, M., Cheng, H.-M., Strupinski, W., Bulusheva, L., Okotrub, A., Grigorieva, I., Grigorenko, A., Novoselov, K. and Geim, A. Fluorographene: A Two-Dimensional Counterpart of Teflon. *Small* **2010**, 6, 2877-2884, DOI 10.1002/sml.201001555.
53. Wang, X., Wang, W., Liu, Y., Ren, M., Xiao, H. and Liu, X. Controllable Defluorination of Fluorinated Graphene and Weakening of C–F Bonding under the Action of Nucleophilic Dipolar Solvent. *Phys. Chem. Chem. Phys.* **2016**, 18 (4), 3285-3293, DOI 10.1039/c5cp06914a.
54. Lee, J. H., Koon, G. K. W., Shin, D. W., Fedorov, V. E., Choi, J.-Y., Yoo, J.-B. and Özyilmaz, B. Property Control of Graphene by Employing “Semi-Ionic” Liquid Fluorination. *Adv. Funct. Mater.* **2013**, 23 (26), 3329-3334, DOI 10.1002/adfm.201202822.
55. Bourlinos, A. B., Safarova, K., Siskova, K. and Zbořil, R. The Production of Chemically Converted Graphenes from Graphite Fluoride. *Carbon* **2012**, 50 (3), 1425-1428, DOI 10.1016/j.carbon.2011.10.012.
56. Costa, S. D., Weis, J. E., Frank, O., Bastl, Z. and Kalbac, M. Thermal Treatment of Fluorinated Graphene: An in Situ Raman Spectroscopy Study. *Carbon* **2015**, 84, 347-354, DOI 10.1016/j.carbon.2014.12.029.
57. Plšek, J., Drogowska, K. A., Valeš, V., Ek Weis, J. and Kalbac, M. Decomposition of Fluorinated Graphene under Heat Treatment. *Chem. - Eur. J.* **2016**, 22 (26), 8990-8997, DOI 10.1002/chem.201600901.
58. Stine, R., Lee, W.-K., Whitener, K. E., Robinson, J. T. and Sheehan, P. E. Chemical Stability of Graphene Fluoride Produced by Exposure to XeF₂. *Nano Lett.* **2013**, 13 (9), 4311-4316, DOI 10.1021/nl4021039.
59. Medved', M., Zoppellaro, G., Ugolotti, J., Matochová, D., Lazar, P., Pospíšil, T., Bakandritsos, A., Tuček, J., Zbořil, R. and Otyepka, M. Reactivity of Fluorographene is Triggered by Point Defects: Beyond the Perfect 2D World. *Nanoscale* **2018**, 10 (10), 4696-4707, DOI 10.1039/c7nr09426d.
60. Dubecky, M., Otyepkova, E., Lazar, P., Karlicky, F., Petr, M., Cepe, K., Banas, P., Zboril, R. and Otyepka, M. Reactivity of Fluorographene: A Facile Way toward Graphene Derivatives. *J. Phys. Chem. Lett.* **2015**, 6 (8), 1430-1434, DOI 10.1021/acs.jpcclett.5b00565.
61. Worsley, K. A., Ramesh, P., Mandal, S. K., Niyogi, S., Itkis, M. E. and Haddon, R. C. Soluble Graphene Derived from Graphite Fluoride. *Chem. Phys. Lett.* **2007**, 445 (1), 51-56, DOI 10.1016/j.cplett.2007.07.059.
62. Li, B., He, T., Wang, Z., Cheng, Z., Liu, Y., Chen, T., Lai, W., Wang, X. and Liu, X. Chemical Reactivity of C–F Bonds Attached to Graphene with Diamines Depending on Their Nature and Location. *Phys. Chem. Chem. Phys.* **2016**, 18 (26), 17495-17505, DOI 10.1039/c6cp01929c.
63. Lai, W., Yuan, Y., Wang, X., Liu, Y., Li, Y. and Liu, X. Radical Mechanism of a Nucleophilic Reaction Depending on a Two-dimensional Structure. *Phys. Chem. Chem. Phys.* **2018**, 20 (1), 489-497, DOI 10.1039/c7cp06708a.
64. Lemal, D. M. Perspective on Fluorocarbon Chemistry. *J. Org. Chem.* **2004**, 69 (1), 1-11, DOI 10.1021/jo0302556.

65. Sandford, G. Perfluoroalkanes. *Tetrahedron* **2003**, 59 (4), 437-454, DOI 10.1016/S0040-4020(02)01568-5.
66. Liu, Y., Noffke, B. W., Gao, X., Lozovyj, Y., Cui, Y., Fu, Y., Raghavachari, K., Siedle, A. R. and Li, L.-s. Reductive Defluorination of Graphite Monofluoride by Weak, Non-nucleophilic Reductants Reveals Low-lying Electron-accepting Sites. *Phys. Chem. Chem. Phys.* **2018**, 20 (21), 14287-14290, DOI 10.1039/c8cp00384j.
67. Siedle, A. R., Losovyj, Y., Karty, J. A., Chen, D., Chatterjee, K., Carta, V., Stein, B. D. and Werner-Zwanziger, U. C–F Bond Activation in the Solid State: Functionalization of Carbon through Reactions of Graphite Fluoride with Amines. *J. Phys. Chem. C* **2021**, 125 (19), 10326-10333, DOI 10.1021/acs.jpcc.1c00734.
68. Matochová, D., Medved', M., Bakandritsos, A., Steklý, T., Zbořil, R. and Otyepka, M. 2D Chemistry: Chemical Control of Graphene Derivatization. *J. Phys. Chem. Lett.* **2018**, 9 (13), 3580-3585, DOI 10.1021/acs.jpcclett.8b01596.
69. Wang, Y., Lee, W. C., Manga, K. K., Ang, P. K., Lu, J., Liu, Y. P., Lim, C. T. and Loh, K. P. Fluorinated Graphene for Promoting Neuro-Induction of Stem Cells. *Adv. Mater.* **2012**, 24 (31), 4285-4290, DOI 10.1002/adma.201200846.
70. Junkermeier, C. E., Badescu, S. C. and Reinecke, T. L. Highly Fluorinated Graphene. *Condens. Matter* **2013**, No. arXiv:1302.6878
71. Vyalikh, A., Bulusheva, L. G., Chekhova, G. N., Pinakov, D. V., Okotrub, A. V. and Scheler, U. Fluorine Patterning in Room-Temperature Fluorinated Graphite Determined by Solid-State NMR and DFT. *J. Phys. Chem. C* **2013**, 117 (15), 7940-7948, DOI 10.1021/jp4028029.
72. Zhou, S., Sherpa, S. D., Hess, D. W. and Bongiorno, A. Chemical Bonding of Partially Fluorinated Graphene. *J. Phys. Chem. C* **2014**, 118 (45), 26402-26408, DOI 10.1021/jp508965q.
73. Sato, Y., Itoh, K., Hagiwara, R., Fukunaga, T. and Ito, Y. On the So-called "Semi-ionic" C–F Bond Character in Fluorine–GIC. *Carbon* **2004**, 42 (15), 3243-3249, DOI 10.1016/j.carbon.2004.08.012.
74. Claves, D. Spectroscopic Study of Fluorinated Carbon Nanostructures. *New J. Chem.* **2011**, 35 (11), 2477-2482, DOI 10.1039/c1nj20239a.
75. Boukhvalov, D. W. Absence of a Stable Atomic Structure in Fluorinated Graphene. *Phys. Chem. Chem. Phys.* **2016**, 18 (19), 13287-13293, DOI 10.1039/c6cp01631f.
76. Han, S. S., Yu, T. H., Merinov, B. V., van Duin, A. C. T., Yazami, R. and Goddard, W. A. Unraveling Structural Models of Graphite Fluorides by Density Functional Theory Calculations. *Chem. Mater.* **2010**, 22 (6), 2142-2154, DOI 10.1021/cm903760t.
77. Sato, Y., Itoh, K., Hagiwara, R., Fukunaga, T. and Ito, Y. Short-range Structures of Poly(dicarbon monofluoride) (C₂F)_n and Poly(carbon monofluoride) (CF)_n. *Carbon* **2004**, 42 (14), 2897-2903, DOI 10.1016/j.carbon.2004.06.042.
78. Parmentier, J., Schlienger, S., Dubois, M., Disa, E., Masin, F. and Centeno, T. A. Structural/textural Properties and Water Reactivity of Fluorinated Activated Carbons. *Carbon* **2012**, 50 (14), 5135-5147, DOI 10.1016/j.carbon.2012.06.054.

79. Kita, Y., Watanabe, N. and Fujii, Y. Chemical Composition and Crystal Structure of Graphite Fluoride. *J. Am. Chem. Soc.* **1979**, 101 (14), 3832-3841, DOI 10.1021/ja00508a020.
80. Lee, S.-S., Jang, S.-W., Park, K., Jang, E. C., Kim, J.-Y., Neuhauser, D. and Lee, S. A Mechanistic Study of Graphene Fluorination. *J. Phys. Chem. C* **2013**, 117 (10), 5407-5415, DOI 10.1021/jp310826d.
81. Asanov, I. P., Bulusheva, L. G., Dubois, M., Yudanov, N. F., Alexeev, A. V., Makarova, T. L. and Okotrub, A. V. Graphene Nanochains and Nanoislands in the Layers of Room-temperature Fluorinated Graphite. *Carbon* **2013**, 59 518-529, DOI 10.1016/j.carbon.2013.03.048.
82. Langer, R., Zaoralová, D., Medved', M., Banáš, P., Błoński, P. and Otyepka, M. Variability of C–F Bonds Governs the Formation of Specific Structural Motifs in Fluorinated Graphenes. *J. Phys. Chem. C* **2019**, 123 (45), 27896-27903, DOI 10.1021/acs.jpcc.9b07552.
83. Stine, R., Ciszek, J. W., Barlow, D. E., Lee, W.-K., Robinson, J. T. and Sheehan, P. E. High-Density Amine-Terminated Monolayers Formed on Fluorinated CVD-Grown Graphene. *Langmuir* **2012**, 28 (21), 7957-7961, DOI 10.1021/la301091f.
84. Bosch-Navarro, C., Walker, M., Wilson, N. R. and Rourke, J. P. Covalent Modification of Exfoliated Fluorographite with Nitrogen Functionalities. *J. Mater. Chem. C* **2015**, 3 (29), 7627-7631, DOI 10.1039/c5tc01633a.
85. Ye, X., Ma, L., Yang, Z., Wang, J., Wang, H. and Yang, S. Covalent Functionalization of Fluorinated Graphene and Subsequent Application as Water-based Lubricant Additive. *ACS Appl. Mater. Inter.* **2016**, 8 (11), 7483-7488, DOI 10.1021/acsami.5b10579.
86. Tuček, J., Holá, K., Bourlinos, A. B., Blonski, P., Bakandritsos, A., Ugolotti, J., Dubecký, M., Karlický, F., Ranc, V., Čépe, K., Otyepka, M. and Zbořil, R. Room Temperature Organic Magnets Derived from sp^3 Functionalized Graphene. *Nat. Commun.* **2017**, 8, 14525, DOI 10.1038/Ncomms14525.
87. Gong, P., Wang, J., Sun, W., Wu, D., Wang, Z., Fan, Z., Wang, H., Han, X. and Yang, S. Tunable Photoluminescence and Spectrum Split from Fluorinated to Hydroxylated Graphene. *Nanoscale* **2014**, 6 (6), 3316-3324, DOI 10.1039/c3nr05725a.
88. Urbanová, V., Holá, K., Bourlinos, A. B., Čépe, K., Ambrosi, A., Loo, A. H., Pumera, M., Karlický, F., Otyepka, M. and Zbořil, R. Thiofluorographene–Hydrophilic Graphene Derivative with Semiconducting and Genosensing Properties. *Adv. Mater.* **2015**, 27 (14), 2305-2310, DOI 10.1002/adma.201500094.
89. Kovaříček, P., Bastl, Z., Valeš, V. and Kalbac, M. Covalent Reactions on Chemical Vapor Deposition Grown Graphene Studied by Surface-Enhanced Raman Spectroscopy. *Chem. - Eur. J.* **2016**, 22 (15), 5404-5408, DOI 10.1002/chem.201504689.
90. Chronopoulos, D. D., Bakandritsos, A., Lazar, P., Pykal, M., Čépe, K., Zbořil, R. and Otyepka, M. High-Yield Alkylation and Arylation of Graphene via Grignard Reaction with Fluorographene. *Chem. Mater.* **2017**, 29 (3), 926-930, DOI 10.1021/acs.chemmater.6b05040.
91. Mazánek, V., Libánská, A., Šturala, J., Bouša, D., Sedmidubský, D., Pumera, M., Janoušek, Z., Plutnar, J. and Sofer, Z. Fluorographene Modified by Grignard Reagents: A Broad Range of Functional Nanomaterials. *Chem. - Eur. J.* **2017**, 23 (8), 1956-1964, DOI 10.1002/chem.201604989.

92. Bakandritsos, A., Pykal, M., Błoński, P., Jakubec, P., Chronopoulos, D. D., Poláková, K., Georgakilas, V., Čépe, K., Tomanec, O., Ranc, V., Bourlinos, A. B., Zbořil, R. and Otyepka, M. Cyanographene and Graphene Acid: Emerging Derivatives Enabling High-Yield and Selective Functionalization of Graphene. *ACS Nano* **2017**, 11 (3), 2982-2991, DOI 10.1021/acsnano.6b08449.
93. Chronopoulos, D., Bakandritsos, A., Pykal, M., Zboril, R. and Otyepka, M. Chemistry, Properties, and Applications of Fluorographene. *Appl. Mater. Today* **2017**, 9, 60-70, DOI 10.1016/j.apmt.2017.05.004.
94. Potsi, G., Bourlinos, A. B., Mouselimis, V., Poláková, K., Chalmpes, N., Gournis, D., Kalytchuk, S., Tomanec, O., Błoński, P., Medved', M., Lazar, P., Otyepka, M. and Zbořil, R. Intrinsic Photoluminescence of Amine-functionalized Graphene Derivatives for Bioimaging Applications. *Appl. Mater. Today* **2019**, 17, 112-122, DOI 10.1016/j.apmt.2019.08.002.
95. Bakandritsos, A., Kadam, R. G., Kumar, P., Zoppellaro, G., Medved', M., Tucek, J., Montini, T., Tomanec, O., Andryskova, P., Drahos, B., Varma, R. S., Otyepka, M., Gawande, M. B., Fornasiero, P. and Zboril, R. Mixed-Valence Single-Atom Catalyst Derived from Functionalized Graphene. *Adv. Mater.* **2019**, 31, 1900323, DOI 10.1002/Adma.201900323.
96. Blanco, M., Mosconi, D., Tubaro, C., Biffis, A., Badocco, D., Pastore, P., Otyepka, M., Bakandritsos, A., Liu, Z., Ren, W., Agnoli, S. and Granozzi, G. Palladium Nanoparticles Supported on Graphene Acid: a Stable and Eco-friendly Bifunctional C–C Homo- and Cross-coupling Catalyst. *Green Chem.* **2019**, 21 (19), 5238-5247, DOI 10.1039/c9gc01436e.
97. Zaoralová, D., Mach, R., Lazar, P., Medved', M. and Otyepka, M. Anchoring of Transition Metals to Graphene Derivatives as an Efficient Approach for Designing Single-Atom Catalysts. *Adv. Mat. Interfaces* **2021**, 8 (8), 2001392, DOI 10.1002/admi.202001392.
98. Kadam, R. G., Zhang, T., Zaoralová, D., Medved', M., Bakandritsos, A., Tomanec, O., Petr, M., Zhu Chen, J., Miller, J. T., Otyepka, M., Zbořil, R., Asefa, T. and Gawande, M. B. Single Co-Atoms as Electrocatalysts for Efficient Hydrazine Oxidation Reaction. *Small* **2021**, 17, 2006477, DOI 10.1002/sml.202006477.
99. Fan, K., Liu, X., Liu, Y., Li, Y., Chen, Y., Meng, Y., Liu, X., Feng, W. and Luo, L. Covalent Functionalization of Fluorinated Graphene Through Activation of Dormant Radicals for Water-based Lubricants. *Carbon* **2020**, 167, 826-834, DOI 10.1016/j.carbon.2020.06.033.
100. Rao, C. N. R., Gopalakrishnan, K. and Govindaraj, A. Synthesis, Properties and Applications of Graphene Doped with Boron, Nitrogen and Other Elements. *Nano Today* **2014**, 9 (3), 324-343, DOI 10.1016/j.nantod.2014.04.010.
101. Maiti, U. N., Lee, W. J., Lee, J. M., Oh, Y., Kim, J. Y., Kim, J. E., Shim, J., Han, T. H. and Kim, S. O. 25th Anniversary Article: Chemically Modified/Doped Carbon Nanotubes & Graphene for Optimized Nanostructures & Nanodevices. *Adv. Mater.* **2014**, 26 (1), 40-67, DOI 10.1002/adma.201303265.
102. Wang, H., Xie, M., Thia, L., Fisher, A. and Wang, X. Strategies on the Design of Nitrogen-Doped Graphene. *J. Phys. Chem. Lett.* **2014**, 5 (1), 119-125, DOI 10.1021/jz402416a.
103. Vineesh, T. V., Nazrulla, M. A., Krishnamoorthy, S., Narayanan, T. N. and Alwarappan, S. Synergistic Effects of Dopants on the Spin Density of Catalytic Active Centres of N-doped Fluorinated Graphene for Oxygen Reduction Reaction. *Appl. Mater. Today* **2015**, 1 (2), 74-79, DOI 10.1016/j.apmt.2015.09.002.

104. Liu, Y., Shen, Y., Sun, L., Li, J., Liu, C., Ren, W., Li, F., Gao, L., Chen, J., Liu, F., Sun, Y., Tang, N., Cheng, H.-M. and Du, Y. Elemental Superdoping of Graphene and Carbon Nanotubes. *Nat. Commun.* **2016**, 7 (1), 10921, DOI 10.1038/ncomms10921.
105. Zoppellaro, G., Bakandritsos, A., Tuček, J., Błoński, P., Susi, T., Lazar, P., Bad'ura, Z., Steklý, T., Opletalová, A., Otyepka, M. and Zbořil, R. Microwave Energy Drives “On–Off–On” Spin-Switch Behavior in Nitrogen-Doped Graphene. *Adv. Mater.* **2019**, 31, 1902587, DOI 10.1002/adma.201902587.
106. Li, Y., Wang, X., Wang, W., Qin, R., Lai, W., Ou, A., Liu, Y. and Liu, X. Nitrogen-Doping Chemical Behavior of Graphene Materials with Assistance of Defluorination. *J. Phys. Chem. C* **2019**, 123 (1), 584-592, DOI 10.1021/acs.jpcc.8b10276.
107. Zaoralová, D., Hrubý, V., Šedajová, V., Mach, R., Kupka, V., Ugolotti, J., Bakandritsos, A., Medved', M. and Otyepka, M. Tunable Synthesis of Nitrogen Doped Graphene from Fluorographene under Mild Conditions. *ACS Sustain. Chem. Eng.* **2020**, 8 (12), 4764-4772, DOI 10.1021/acssuschemeng.9b07161.
108. Mardirossian, N. and Head-Gordon, M. Thirty Years of Density Functional Theory in Computational Chemistry: an Overview and Extensive Assessment of 200 Density Functionals. *Mol. Phys.* **2017**, 115 (19), 2315-2372, DOI 10.1080/00268976.2017.1333644.
109. Cramer, C. J., Essentials of Computational Chemistry: Theories and Models. *John Wiley & Sons* **2004**, 618, ISBN 0470091827
110. Koch, W. and Holthausen, M. C., A Chemist's Guide to Density Functional Theory, *Wiley-VCH Verlag GmbH* **2001**, 313, ISBN 9783527303724
111. Perdew, J. P., Burke, K. and Ernzerhof, M. Generalized Gradient Approximation Made Simple. *Phys. Rev. Lett.* **1996**, 77 (18), 3865-3868, DOI 10.1103/PhysRevLett.77.3865.
112. Grimme, S. Semiempirical GGA-type Density Functional Constructed with a Long-range Dispersion Correction. *J. Comput. Chem.* **2006**, 27 (15), 1787-1799, DOI 10.1002/jcc.20495.
113. Perdew, J. P., Ernzerhof, M. and Burke, K. Rationale for Mixing Exact Exchange with Density Functional Approximations. *J. Chem. Phys.* **1996**, 105 (22), 9982-9985, DOI 10.1063/1.472933.
114. Adamo, C. and Barone, V. Toward Reliable Density Functional Methods without Adjustable Parameters: The PBE0 Model. *J. Chem. Phys.* **1999**, 110 (13), 6158-6170, DOI 10.1063/1.478522.
115. Chai, J.-D. and Head-Gordon, M. Long-range Corrected Hybrid Density Functionals with Damped Atom–atom Dispersion Corrections. *Phys. Chem. Chem. Phys.* **2008**, 10 (44), 6615-6620, DOI 10.1039/b810189b.
116. Chai, J. D. and Head-Gordon, M. Systematic Optimization of Long-range Corrected Hybrid Density Functionals. *J. Chem. Phys.* **2008**, 128 (8), 084106, DOI 10.1063/1.2834918.
117. Ditchfield, R., Hehre, W. J. and Pople, J. A. Self-Consistent Molecular-Orbital Methods. IX. An Extended Gaussian-Type Basis for Molecular-Orbital Studies of Organic Molecules. *J. Chem. Phys.* **1971**, 54 (2), 724-728, DOI 10.1063/1.1674902.

118. Schäfer, A., Horn, H. and Ahlrichs, R. Fully Optimized Contracted Gaussian Basis Sets for Atoms Li to Kr. *J. Chem. Phys.* **1992**, 97 (4), 2571-2577, DOI 10.1063/1.463096.
119. Schäfer, A., Huber, C. and Ahlrichs, R. Fully Optimized Contracted Gaussian Basis Sets of Triple Zeta Valence Quality for Atoms Li to Kr. *J. Chem. Phys.* **1994**, 100 (8), 5829-5835, DOI 10.1063/1.467146.
120. Weigend, F. and Ahlrichs, R. Balanced Basis Sets of Split Valence, Triple Zeta Valence and Quadruple Zeta Valence Quality for H to Rn: Design and Assessment of Accuracy. *Phys. Chem. Chem. Phys.* **2005**, 7 (18), 3297-3305, DOI 10.1039/b508541a.
121. Soubusta, J., Fyzika pevných látek. *Univerzita Palackého v Olomouci* **2012**, 172, ISBN 978-80-244-3096-6
122. Sholl, D. S. and Steckel, J. A., Density Functional Theory: a Practical Introduction. *John Wiley & Sons* **2009**, 256, ISBN 0470373172
123. Marenich, A. V., Cramer, C. J. and Truhlar, D. G. Universal Solvation Model Based on Solute Electron Density and on a Continuum Model of the Solvent Defined by the Bulk Dielectric Constant and Atomic Surface Tensions. *J. Phys. Chem. B* **2009**, 113 (18), 6378-6396, DOI 10.1021/jp810292n.
124. O'Hagan, D. Understanding Organofluorine Chemistry. An Introduction to the C–F Bond. *Chem. Soc. Rev.* **2008**, 37 (2), 308-319, DOI 10.1039/b711844a.
125. Lieb, E. H. 2 Theorems on the Hubbard-Model. *Phys. Rev. Lett.* **1989**, 62 (10), 1201-1204, DOI 10.1103/PhysRevLett.62.1201.
126. Ribas, M. A., Singh, A. K., Sorokin, P. B. and Yakobson, B. I. Patterning Nanoroads and Quantum Dots on Fluorinated Graphene. *Nano Res.* **2011**, 4 (1), 143-152, DOI 10.1007/s12274-010-0084-7.
127. Kashtiban, R. J., Dyson, M. A., Nair, R. R., Zan, R., Wong, S. L., Ramasse, Q., Geim, A. K., Bangert, U. and Sloan, J. Atomically Resolved Imaging of Highly Ordered Alternating Fluorinated Graphene. *Nat. Commun.* **2014**, 5 (1), 4902, DOI 10.1038/ncomms5902.
128. Wang, B., Wang, J. and Zhu, J. Fluorination of Graphene: A Spectroscopic and Microscopic Study. *ACS Nano* **2014**, 8 (2), 1862-1870, DOI 10.1021/nm406333f.
129. Carpenter, J. E. Extension of Lewis Structure Concepts to Open-shell and Excited-state Molecular Species, Ph.D. thesis. *University of Wisconsin, Madison, WI*, **1987**.
130. Carpenter, J. E. and Weinhold, F. Analysis of the Geometry of the Hydroxymethyl Radical by the “Different Hybrids for Different Spins” Natural Bond Orbital Procedure. *J. Mol. Struct. (Theochem)* **1988**, 139, 41-62, DOI 10.1016/0166-1280(88)80248-3.
131. Naaman, R. and Vager, Z., The Structure of Small Molecules and Ions. *Springer US*, **1988**, 351, ISBN 978-1-14684-7424-4.
132. Reed, A. E., Weinstock, R. B. and Weinhold, F. Natural Population Analysis. *J. Chem. Phys.* **1985**, 83 (2), 735-746, DOI 10.1063/1.449486.
133. Reed, A. E. and Weinhold, F. Natural Localized Molecular Orbitals. *J. Chem. Phys.* **1985**, 83 (4), 1736-1740, DOI 10.1063/1.449360.

134. Reed, A. E. and Weinhold, F. Natural Bond Orbital Analysis of Near-Hartree–Fock Water Dimer. *J. Chem. Phys.* **1983**, 78 (6), 4066-4073, DOI 10.1063/1.445134.
135. Liu, J., Bao, Z., Cui, Y., Dufek, E. J., Goodenough, J. B., Khalifah, P., Li, Q., Liaw, B. Y., Liu, P., Manthiram, A., Meng, Y. S., Subramanian, V. R., Toney, M. F., Viswanathan, V. V., Whittingham, M. S., Xiao, J., Xu, W., Yang, J., Yang, X.-Q. and Zhang, J.-G. Pathways for Practical High-energy Long-cycling Lithium Metal Batteries. *Nat. Energy* **2019**, 4 (3), 180-186, DOI 10.1038/s41560-019-0338-x.
136. Evers, S. and Nazar, L. F. New Approaches for High Energy Density Lithium–Sulfur Battery Cathodes. *Acc. Chem. Res.* **2013**, 46 (5), 1135-1143, DOI 10.1021/ar3001348.
137. Peng, H.-J., Huang, J.-Q., Cheng, X.-B. and Zhang, Q. Lithium-Sulfur Batteries: Review on High-Loading and High-Energy Lithium–Sulfur Batteries (Adv. Energy Mater. 24/2017). *Adv. Energy Mat.* **2017**, 7 (24), 1770141, DOI 10.1002/aenm.201770141.
138. Van Hamme, J. D., Singh, A. and Ward, O. P. Recent Advances in Petroleum Microbiology. *Microbiol. Mol. Biol.* **2003**, 67 (4), 503-549, DOI 10.1128/mmbr.67.4.503-549.200.
139. Mikhaylik, Y. V. and Akridge, J. R. Polysulfide Shuttle Study in the Li/S Battery System. *J. Electrochem. Soc.* **2004**, 151 (11), A1969-A1976, DOI 10.1149/1.1806394.
140. Tantis, I., Bakandritsos, A., Zaoralová, D., Medved', M., Jakubec, P., Havláková, J., Zbořil, R. and Otyepka, M. Covalently Interlinked Graphene Sheets with Sulfur-Chains Enable Superior Lithium–Sulfur Battery Cathodes at Full-Mass Level. *Adv. Funct. Mater.* **2021**, 31, 2101326, DOI 10.1002/adfm.202101326.
141. Qian, W., Gao, Q., Li, Z., Tian, W., Zhang, H. and Zhang, Q. Unusual Mesoporous Carbonaceous Matrix Loading with Sulfur as the Cathode of Lithium Sulfur Battery with Exceptionally Stable High Rate Performance. *ACS Appl. Mater. Interfaces* **2017**, 9 (34), 28366-28376, DOI 10.1021/acsami.7b05825 .
142. Liu, Y., Li, G., Fu, J., Chen, Z. and Peng, X. Strings of Porous Carbon Polyhedrons as Self-Standing Cathode Host for High-Energy-Density Lithium-Sulfur Batteries. *Angew. Chem. Int. Ed. Engl.* **2017**, 56 (22), 6176-6180, DOI 10.1002/anie.201700686.
143. Mao, Y., Li, G., Guo, Y., Li, Z., Liang, C., Peng, X. and Lin, Z. Foldable Interpenetrated Metal-organic Frameworks/carbon Nanotubes Thin Film for Lithium–sulfur Batteries. *Nat. Commun.* **2017**, 8 (1), 14628, DOI 10.1038/ncomms14628.
144. Wang, J., He, Y.-S. and Yang, J. Sulfur-Based Composite Cathode Materials for High-Energy Rechargeable Lithium Batteries. *Adv. Mater.* **2015**, 27 (3), 569-575, DOI 10.1002/adma.201402569.
145. Qiao, B. T., Wang, A. Q., Yang, X. F., Allard, L. F., Jiang, Z., Cui, Y. T., Liu, J. Y., Li, J. and Zhang, T. Single-atom Catalysis of CO Oxidation Using Pt-1/FeO_x. *Nat. Chem.* **2011**, 3 (8), 634-641, DOI 10.1038/Nchem.1095.
146. Ji, S., Chen, Y., Wang, X., Zhang, Z., Wang, D. and Li, Y. Chemical Synthesis of Single Atomic Site Catalysts. *Chem. Rev.* **2020**, 120 (21), 11900-11955, DOI 10.1021/acs.chemrev.9b00818.

147. Gawande, M. B., Fornasiero, P. and Zbořil, R. Carbon-Based Single-Atom Catalysts for Advanced Applications. *ACS Catal.* **2020**, 10 (3), 2231-2259, DOI 10.1021/acscatal.9b04217.
148. Grasseschi, D., Silva, W. C., Souza Paiva, R. d., Starke, L. D. and do Nascimento, A. S. Surface Coordination Chemistry of Graphene: Understanding the Coordination of Single Transition Metal Atoms. *Coor. Chem. Rev.* **2020**, 422, 213469, DOI 10.1016/j.ccr.2020.213469.
149. Zhu, Y., Murali, S., Stoller, M. D., Ganesh, K. J., Cai, W., Ferreira, P. J., Pirkle, A., Wallace, R. M., Cychosz, K. A., Thommes, M., Su, D., Stach, E. A. and Ruoff, R. S. Carbon-Based Supercapacitors Produced by Activation of Graphene. *Science* **2011**, 332 (6037), 1537-1541, DOI 10.1126/science.1200770.
150. Zhai, Y., Dou, Y., Zhao, D., Fulvio, P. F., Mayes, R. T. and Dai, S. Carbon Materials for Chemical Capacitive Energy Storage. *Adv. Mater.* **2011**, 23 (42), 4828-4850, DOI 10.1002/adma.201100984.
151. Wang, Y., Shi, Z., Huang, Y., Ma, Y., Wang, C., Chen, M. and Chen, Y. Supercapacitor Devices Based on Graphene Materials. *J. Phys. Chem. C* **2009**, 113 (30), 13103-13107, DOI 10.1021/jp902214f.
152. Choi, C., Back, S., Kim, N.-Y., Lim, J., Kim, Y.-H. and Jung, Y. Suppression of Hydrogen Evolution Reaction in Electrochemical N₂ Reduction Using Single-Atom Catalysts: A Computational Guideline. *ACS Catal.* **2018**, 8 (8), 7517-7525, DOI 10.1021/acscatal.8b00905.
153. Kittel, C. Introduction to Solid State Physics. *Wiley* **2005**, 704, ISBN 978-0471415268
154. He, T., Zhang, C. and Du, A. Single-atom Supported on Graphene Grain Boundary as an Efficient Electrocatalyst for Hydrogen Evolution Reaction. *Chem. Eng. Sci.* **2019**, 194, 58-63, DOI 10.1016/j.ces.2018.03.028.
155. Wang, H., Wang, Q., Cheng, Y., Li, K., Yao, Y., Zhang, Q., Dong, C., Wang, P., Schwingenschlögl, U., Yang, W. and Zhang, X. X. Doping Monolayer Graphene with Single Atom Substitutions. *Nano Lett.* **2012**, 12 (1), 141-144, DOI 10.1021/nl2031629.
156. Zhang, L., Jia, Y., Gao, G., Yan, X., Chen, N., Chen, J., Soo, M. T., Wood, B., Yang, D., Du, A. and Yao, X. Graphene Defects Trap Atomic Ni Species for Hydrogen and Oxygen Evolution Reactions. *Chem* **2018**, 4 (2), 285-297, DOI 10.1016/j.chempr.2017.12.005.
157. Mao, Y., Yuan, J. and Zhong, J. Density Functional Calculation of Transition Metal Adatom Adsorption on Graphene. *J. Phys. - Condens. Mat.* **2008**, 20 (11), 115209, DOI 10.1088/0953-8984/20/11/115209.
158. Cao, C., Wu, M., Jiang, J. and Cheng, H.-P. Transition Metal Adatom and Dimer Adsorbed on Graphene: Induced Magnetization and Electronic Structures. *Phys. Rev. B* **2010**, 81 (20), 205424, DOI 10.1103/PhysRevB.81.205424.
159. Hu, L., Hu, X., Wu, X., Du, C., Dai, Y. and Deng, J. Density functional calculation of transition metal adatom adsorption on graphene. *Physica B Condens. Matter* **2010**, 405 (16), 3337-3341, DOI 10.1016/j.physb.2010.05.001.

160. Valencia, H., Gil, A. and Frapper, G. Trends in the Adsorption of 3d Transition Metal Atoms onto Graphene and Nanotube Surfaces: A DFT Study and Molecular Orbital Analysis. *J. Phys. Chem. C* **2010**, 114 (33), 14141-14153, DOI 10.1021/jp103445v.
161. Nakada, K. and Ishii, A. Migration of Adatom Adsorption on Graphene Using DFT Calculation. *Solid State Commun.* **2011**, 151 (1), 13-16, DOI 10.1016/j.ssc.2010.10.036.
162. Aullón, G. and Alvarez, S. Oxidation States, Atomic Charges and Orbital Populations in Transition Metal Complexes. *Theor. Chem. Acc.* **2009**, 123 (1), 67-73, DOI 10.1007/s00214-009-0537-9.
163. Walsh, A., Sokol, A. A., Buckeridge, J., Scanlon, D. O. and Catlow, C. R. A. Oxidation States and Ionicity. *Nat. Mater.* **2018**, 17 (11), 958-964, DOI 10.1038/s41563-018-0165-7.
164. Kubin, M., Guo, M., Kroll, T., Löchel, H., Källman, E., Baker, M. L., Mitzner, R., Gul, S., Kern, J., Föhlisch, A., Erko, A., Bergmann, U., Yachandra, V., Yano, J., Lundberg, M. and Wernet, P. Probing the Oxidation State of Transition Metal Complexes: a Case Study on How Charge and Spin Densities Determine Mn L-edge X-ray Absorption Energies. *Chem. Sci.* **2018**, 9 (33), 6813-6829, DOI 10.1039/c8sc00550h.
165. Zhang, T. and Asefa, T. Heteroatom-Doped Carbon Materials for Hydrazine Oxidation. *Adv. Mater.* **2019**, 31 (13), 1804394, DOI 10.1002/adma.201804394.
166. Zhang, T., Low, J., Koh, K., Yu, J. and Asefa, T. Mesoporous TiO₂ Comprising Small, Highly Crystalline Nanoparticles for Efficient CO₂ Reduction by H₂O. *ACS Sustain. Chem. Eng.* **2018**, 6 (1), 531-540, DOI 10.1021/acssuschemeng.7b02827.

Appendices

- A. Variability of C–F Bonds Governs the Formation of Specific Structural Motifs in Fluorinated Graphenes
- B. Reactivity of Fluorographene is Triggered by Point Defects: Beyond the Perfect 2D World
- C. 2D Chemistry: Chemical Control of Graphene Derivatization
- D. Tunable Synthesis of Nitrogen Doped Graphene from Fluorographene under Mild Conditions
- E. Covalently Interlinked Graphene Sheets with Sulfur-Chains Enable Superior Lithium-Sulfur Battery Cathodes at Full-Mass Level
- F. Anchoring of Transition Metals to Graphene Derivatives as an Efficient Approach for Designing Single-Atom Catalysts
- G. Single Co-atoms as Electrocatalysts for Efficient Hydrazine Oxidation Reaction

A

Variability of C–F Bonds Governs
the Formation of Specific Structural Motifs
in Fluorinated Graphenes

Variability of C–F Bonds Governs the Formation of Specific Structural Motifs in Fluorinated Graphenes

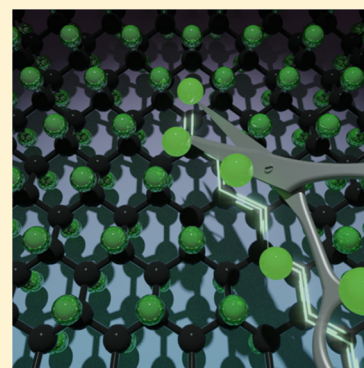
Rostislav Langer,^{†,‡,§} Dagmar Zaoralová,^{†,‡,§} Miroslav Medved',^{*,†} Pavel Banáš,^{†,‡} Piotr Błoński,^{*,†} and Michal Otyepka^{*,†,‡}

[†]Regional Centre of Advanced Technologies and Materials, Faculty of Science, Palacký University in Olomouc, Šlechtitelů 27, 783 71 Olomouc, Czech Republic

[‡]Department of Physical Chemistry, Faculty of Science, Palacký University in Olomouc, 17. Listopadu 12, 771 46 Olomouc, Czech Republic

S Supporting Information

ABSTRACT: Fluorinated graphenes (FGs) are key precursors for the synthesis of many graphene derivatives that significantly expand the application potential of graphene-based materials. The reactivity of FGs is rather surprising because the C–F bond is considered to be one of the strongest single covalent bonds in organic chemistry. However, its strength in FGs varies from 25.6 to 118.2 kcal/mol, depending on the configuration of fluorine ad-atoms. This variability is reflected in the formation of specific structural motifs and topological features during fluorination and defluorination processes; whereas defluorination favors formation of π -conjugated chains, following the path of the weakest C–F bonds, fluorination is driven both by thermodynamics and stochasticity, leading to diverse fluorination patterns. Individual motifs vary in their electronic structures, having either metallic or semiconducting character. We rationalize the complex 2D chemistry of FGs using empirical rules that predict the structural and underlying electronic/magnetic properties of these materials.



INTRODUCTION

The covalent bond formed between carbon and fluorine atoms is commonly included among the strongest single chemical bonds, which imprints extraordinary stability to fluorinated hydrocarbons.¹ Because of its strength, (per)fluorinated hydrocarbons are very stable compounds with many practical applications. Additionally, polytetrafluoroethylene (PTFE), also known by the commercial name Teflon, is a tough, strong, and hydrophobic material that often replaces glass in chemical labs. This gives the impression that all C–F bonds are as strong as those in PTFE and that all compounds with the composition C_xF_y should be rather unreactive. This assumption was called into question by the discovery that the fully fluorinated graphene derivative fluorographene (FG) undergoes chemical transformations involving substitution and reductive defluorination under rather mild reaction conditions.^{2–8} It was later shown that this material's surprising reactivity may originate from the presence of point radical defects.^{9,10} In addition, high-resolution F 1s X-ray photoelectron spectra of FG and partially fluorinated graphenes (pFGs) feature several peaks that can be attributed to different kinds of C–F bonds.^{11,12} Theoretical studies on graphene fluorination suggested that the covalent bonding of a single fluorine ad-atom to a graphene sheet is relatively weak, with estimated bond dissociation energies (BDEs) of 44.9 kcal/mol for infinite dilute limit¹³ and 46.9 kcal/mol corresponding to a low-density FG with a degree of fluorination of ~ 3 at. %, ¹⁴ whereas the BDE of the prototypical C–F bond is 105.4

kcal/mol.¹ On the other hand, the bonding of a single fluorine ad-atom to graphene is stronger than that of other ad-atoms that can adsorb to the top position on a graphene sheet (C–H bond 43.7 kcal/mol, C–Cl bond 29.9 kcal/mol, C–Br bond 23.0 kcal/mol, and C–I bond 18.4 kcal/mol).¹⁵

The available data suggest that the nature of the C–F bond in FGs is complex and that this complexity is closely related to the composition and topology of the graphene derivatives. As the fluorine content increases, the C–F bond shortens (from 1.59 Å for a system with a single F ad-atom bound to a graphene sheet to 1.38 Å in stoichiometric FG), and bond's character changes from semi-ionic to covalent.^{11,12,16} Fluorination of graphene for only a few hours can be reversed by brief annealing at 250 °C, but samples fluorinated for over 20 h are thermally stable up to 450 °C because of the greater C–F bond strength of heavily FGs.¹⁷ Low-fluorinated structures preferentially adopt configurations with C–F bonds in the ortho trans positions, which minimize repulsion between chemisorbed fluorine ad-atoms and maximize C–C π -conjugation.^{12,16,18,19} FGs with higher fluorine contents and specific F/C ratios have been argued to preferentially adopt configurations featuring short chains of ad-atoms separated by polyene-like carbon chains and conjugated graphene-like domains.^{20,21} The highly ordered C_2F , which exhibits selective

Received: August 8, 2019

Revised: October 10, 2019

Published: October 18, 2019

alternating fluorination on one side has also been studied theoretically and experimentally.²² pFGs may act as either hole-doped metallic-like conductors or semiconductors depending on their fluorine content^{11,14,23–26} and geometric structure.^{25–31} Density functional theory (DFT)³² calculations suggest that by varying the content of fluorine ad-atoms in pFGs, one can tune their band gap in the range 0–3.1 eV and control their magnetic properties to produce a nonmagnetic semimetal, a nonmagnetic/magnetic metal, or a magnetic/nonmagnetic semiconductor. The configuration of fluorine ad-atoms on the graphene lattice is another factor affecting the magnetic properties of pFGs.^{33–35}

These results suggest that we must revise our understanding of C–F bonds, and that such a revision could provide new insights into chemical bonding in general, especially in the context of material science. A deeper understanding of the nature of C–F bonds and the dependence of nanopatterning on preparation strategies (fluorination/defluorination) is also needed to enable better control over the properties of FGs, including their electric and magnetic properties. Here, we (i) explain the extraordinary variability of C–F bond characteristics in FGs, (ii) elucidate the rules governing the stability of particular structural configurations, (iii) uncover the key factors governing nanopatterning during fluorination and defluorination processes, and (iv) clarify the dependence of the electronic and magnetic properties of FGs on their composition and topology.

METHODS

The periodic boundary condition calculations were performed by applying the spin-polarized DFT with the Perdew, Burke, and Ernzerhof (PBE) exchange and correlation functional³⁶ and projected augmented wave potentials representing atomic cores, as implemented in the Vienna Ab initio Simulation Package (VASP).^{37–40} The wave functions were expanded in the plane-wave basis set with a minimum cutoff of 400 eV. The Brillouin zone integrations were performed with $6 \times 6 \times 1$ (structure and cell optimization) and $15 \times 15 \times 1$ (static runs) Γ -centered Monkhorst–Pack k -point mesh⁴¹ per conventional 3×3 triclinic cell containing 18 carbon atoms, and also a larger 6×6 triclinic cell containing 72 carbon atoms was used. The C–F bond characteristics discussed in Introduction were obtained by applying the PBE-D2 method⁴² and $5 \times 5 \times 1$ k -point mesh for the 4×4 triclinic cell containing 32 carbon atoms. The different sizes of the unit cell enabled us to study a larger range of the C/F ratios. All the optimized structures were converged to forces of less than 10^{-2} eV/Å, with a criterion 10^{-6} eV for each SCF cycle.

The thermodynamic stability of individual pFG structures with stoichiometry CF_x expressed as the averaged binding energy was calculated as follows

$$E_{\text{bind}} = 1/x(E_{\text{CF}_x} - E_{\text{C}} - xE_{\text{F}}) \quad (1)$$

where E_{CF_x} is the energy of the optimized (p)FG model, E_{C} is the energy of optimized graphene, E_{F} is the energy of a single fluorine ad-atom, and x is the number of fluorine ad-atoms.

The BDE of a particular C–F bond in the structure with stoichiometry CF_x was determined by the equation

$$\text{BDE} = E_{\text{CF}_x} - E_{\text{CF}_{x-1}}^{\text{rx}} - E_{\text{F}} \quad (2)$$

where E_{CF_x} is the energy of the optimized configuration with x fluorine ad-atoms, $E_{\text{CF}_{x-1}}^{\text{rx}}$ is the energy of the optimized (relaxed) configuration with $x - 1$ fluorine ad-atoms, and E_{F} is the energy of a single fluorine ad-atom. Deformation energy (E_{def}) can be defined as

$$E_{\text{def}} = \text{BDE} - E_{\text{int}} \quad (3)$$

where E_{int} is the interaction energy expressed as

$$E_{\text{int}} = E_{\text{CF}_x} - E_{\text{CF}_{x-1}}^{\text{unrlx}} - E_{\text{F}} \quad (4)$$

where E_{CF_x} and E_{F} have the same meaning as in eq 2 and $E_{\text{CF}_{x-1}}^{\text{unrlx}}$ is the energy of the unrelaxed configuration with $x - 1$ fluorine ad-atoms obtained by removing the selected F ad-atom from the CF_x structure.

The polarity of a C–F bond is represented as the difference of partial Bader charges on the carbon and fluorine ad-atom

$$p = \delta_{\text{C}} - \delta_{\text{F}} \quad (5)$$

To consider the random nature of pFGs, we developed a code which systematically generates unique structures of CF_x systems with various stoichiometry and topology. Because the number of possible unique configurations is very large, we have randomly selected 100 structures for each stoichiometry. We examined the stability of various structures with different content and arrangement of fluorine ad-atoms and preferable patterns grown during (de)fluorination. Let us note that although the structures were, in general, selected randomly, we have checked all the stoichiometric sets so that they included the structures with minimal bond tension and the highest possible degree of π -electron delocalization. Consequently, it is reasonable to assume that the lowest-in-energy structures in our sets correspond to the real ground-state (GS) structures for the given stoichiometry.

RESULTS AND DISCUSSION

Although the C–F bond is commonly viewed as “the strongest in organic chemistry”,¹ the properties of C–F bonds in pFGs vary considerably: their BDE and lengths range from 27.1 to 106.7 kcal·mol⁻¹ and 1.38 to 1.59 Å, respectively (Figure 1a). The vast majority of the BDE values reported for these materials are significantly lower than the average BDE of C–F bonds in common organic molecules (105.4 kcal·mol⁻¹),¹ and the calculated range of C–F bond lengths in pFGs is up-shifted by ca 0.1–0.2 Å compared to that for typical C–F bonds in aromatic organic compounds (Figure S1).

One might expect in general that longer C–F bonds would have lower BDEs. However, Figure 1a shows that the correlation between the C–F length and BDE is not at all straightforward. For example, the bonds in the table with the highest and lowest BDE values both have lengths of ca. 1.43 Å. Our findings are consistent with the average length of 1.43 Å reported by Vyalikh et al. for C–F bonds in FGs.⁴³

To examine other factors that may affect the BDE values, additional characteristics of C–F bonds in structures with low F contents were investigated. A statistical analysis revealed (Figure S3) that BDE correlates significantly with four factors: the number of adjacent F ad-atoms in trans positions (coefficient of determination, $R^2 = 0.55$), the number of C–C bonds that enter into π -conjugation upon cleaving a given C–F bond ($R^2 = 0.53$), the C–F bond length ($R^2 = 0.55$), and partly also the C–F bond polarity ($R^2 = 0.33$).

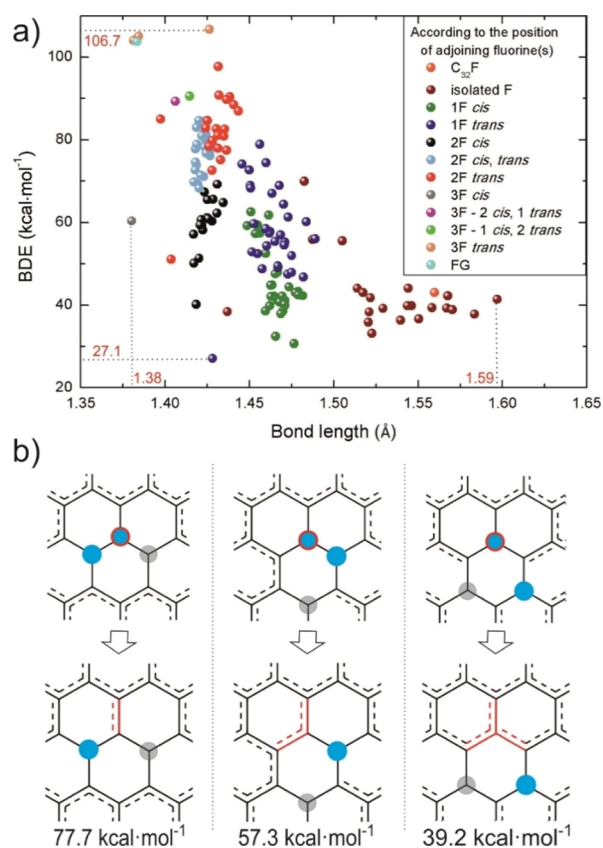


Figure 1. (a) BDEs and C–F lengths for pFGs of various configurations. Configurations are grouped by the number and positioning of fluorine ad-atoms. The notation nF refers to the number of neighboring fluorine atoms (see Figure S2). (b) Illustration of the relationship between the BDE of C–F bonds in FGs and the formation of extended π -conjugation upon removing a fluorine ad-atom. Fluorine ad-atoms projecting above and below the graphene sheet are represented by blue and gray circles, respectively. The ad-atom that is removed in each case is circled in red in the upper images, and the newly formed extended π systems are shown in red in the lower images.

The role of π -conjugation is illustrated in Figure 1b, which depicts three FG configurations having different numbers of C–C bonds that are brought into extended π -conjugation upon dissociation of a C–F bond. The C–F bonds that impose greater disruptions of π -conjugation are clearly weaker, and the stability of configuration is decreased. This finding is in line with the previous study by Marsusi et al.¹³ focused on single-side pFGs. Therefore, the creation of fluorinated islands or ribbons is preferred to a homogenous distribution of fluorine ad-atoms over the lattice. The fact that BDE is significantly influenced by the number of ad-atoms in trans positions suggests that BDE could also be related to the deformation of the graphene plane. In general, more densely packed C–F bonds are more sensitive to the deformation energy (for details, see the Supporting Information). For example, the BDEs for configurations with chains or rings of F ad-atoms correlate strongly with the deformation energy ($R^2 > 0.9$), but the BDEs of C–F bonds with one or no neighboring F ad-atoms are less influenced by structural distortions ($0.4 < R^2 < 0.7$); see Table S1.

There is a rather strong pair correlation between the C–F bond polarity and C–F bond length for the most stable structures ($R^2 = 0.93$, Figure S6b), in keeping with the results

of Zhou et al.¹² The C–F bond polarity also correlates moderately with BDE ($R^2 = 0.33$, Figure S3e), but this correlation is less significant than those for the factors discussed above.

Because some of the studied factors correlate with each other (Table S2), we also performed a multiparametric analysis (Tables S3 and S4). This revealed that BDE is qualitatively predicted (with an error of ± 9.1 kcal/mol at the 95% confidence interval) by the C–F bond length and the number of adjoining ad-atoms in trans positions but also (with an error of ± 10.0 kcal/mol) by two purely topological factors: π -conjugation and the number of adjoining ad-atoms in trans positions. The potential to estimate the C–F BDEs of FGs based on a few purely topological factors may enable large-scale prescreening of many different structures by creating representative sets of configurations to model real pFG samples.

The variable nature of C–F bonds in FGs profoundly affects both the reactivity and the stability of these materials. Weaker bonds are obviously more susceptible to cleavage during defluorination processes. However, thermodynamic stability is determined by the arrangement of all F ad-atoms on the graphene lattice. To identify the most stable configurations, we calculated the Boltzmann distributions of various structural motifs that may exist in thermally equilibrated samples at $T = 293, 400,$ and 600 K (Figure S7). This revealed that (i) the GS arrangements dominate in thermally equilibrated samples for most stoichiometries, with less-favorable structures existing in significant quantities (above 10%) at experimentally relevant temperatures only in the case of specific stoichiometries (e.g., $C_{18}F_6$ and $C_{18}F_{11}$; Figures S7–S20); (ii) in general, the more the F ad-atoms, the greater is the stability of the GS structures; (iii) ground-states structures with even numbers of ad-atoms (evenly located on the two graphene sublattices) are more stable than those with odd numbers, and (iv) structures with homogeneous distributions of fluorine ad-atoms are less stable than those with compact and heterogeneous distributions (Figure S10). Let us note that similar trends were observed for single-side pFGs, that is, the structures with an even number of ad-atoms evenly located on the two graphene sublattices were found to be more stable and the formation of fluorinated islands and ribbons was preferred. The main difference between single- and double-side pFGs is that in the former, the configurations with F ad-atoms in ortho positions are less stable than those with F ad-atoms in para positions because of strong repulsion between negative partial charges on neighboring F ad-atoms.²⁵

Although our thermodynamic analysis suggested a strong preference for GS configurations, NMR and XPS spectra of pFGs prepared using BrF_3 as the fluorinating agent confirmed the presence of various fluorination motifs (e.g., the CF armchair and zigzag chains, cyclohexane rings, and isolated CF pairs) that were randomly distributed across the graphene plane. Upon standing at room temperature for an extended period (several months), these motifs relaxed into an energetically preferable configuration.^{20,43} The experimental evidence thus indicates that the fluorination process is influenced both by thermodynamics and stochasticity; that is to say, the distribution of sites undergoing fluorination exhibits a degree of randomness. The kinetics of graphene fluorination is thus reminiscent of the kinetic partitioning mechanism used to describe (among other things) the folding kinetics of large biomolecules.⁴⁴

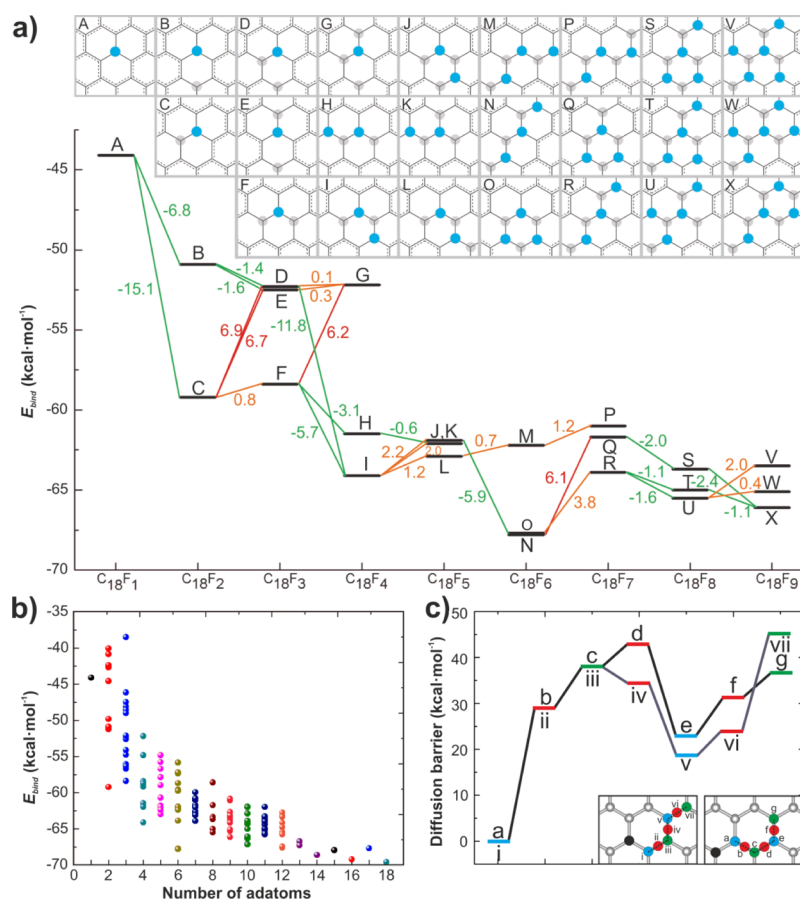


Figure 2. (a) Binding energies of the lowest-in-energy $C_{18}F_x$ ($x = 1-9$) configurations, illustrating possible patterns of fluorine ad-atoms and their evolution during gradual fluorination of graphene. Green, orange, and red lines indicate fluorination pathways that are energetically favorable, mildly disfavored, and strongly disfavored, respectively. The corresponding structures are arranged in columns according to their stoichiometry. (b) Binding energies for low-energy pFG structures of stoichiometry $C_{18}F_x$ ($x = 1-18$). (c) Barriers to the diffusion of fluorine ad-atoms over the graphene lattice of two fluorine ad-atoms on different sides of graphene; the mobility pathways are depicted in the inset. Blue, red, and green bars refer to non-magnetic structures, structures with one fluorine ad-atom in the bridge position, and magnetic structures, respectively.

Various arrangements of fluorine ad-atoms for graphene lattice stoichiometries ranging from low to complete F coverage were considered to model the evolution of motifs as F coverage increases (Figures 2 and S8–S20). Systematically increasing the F/C ratio enabled us to evaluate changes in binding energies and identify the most stable structures as well as energetically convenient fluorination pathways. In general, binding energies decreased as the fluorine content increased, indicating that the initial phase of fluorination is a spontaneous process that forms stable motifs with the composition $C_{18}F_6$ corresponding to the armchair [Figure 2a (O)] and zigzag [Figure 2a (N)] structures. This is consistent with the conclusions of Makarova et al.³³ who identified such motifs in C_3F samples by AFM. Although these structures represent local minima on the binding energy profile, there is a relatively low barrier to further fluorination and progression toward fully FG (Figure 2b). In fluorine-rich structures such as $C_{18}F_9$ and $C_{18}F_{12}$, the formation of zigzag lines and hexagonal rings is also favorable (Figure S21j,m). Importantly, the energy profile of the lowest-in-energy $C_{18}F_x$ systems does not always follow the sequential “lowest energy pathway”, that is, the GS of a system with a given level of F coverage cannot always be formed directly from that of the configuration with one F ad-atom fewer. For instance, the GS of $C_{18}F_9$ [Figure 2a (X)] is grown from the second or third most stable configurations of $C_{18}F_8$

[Figure 2a (S,T)]. However, barriers to the migration of F ad-atoms on the graphene lattice are rather low (Figure 2c), suggesting that the transformation of less-stable structures into more stable ones should be feasible (as also suggested for single-side pFGs),²⁵ in keeping with the effects of aging observed by Makarova et al.³³

It is reasonable to assume that the defluorination of fluorographene follows the weakest bond pathway(s). To better understand processes such as thermal annealing and chemical reduction of fluorographene samples,⁴⁵ we examined the defluorination of fluorographene by reversing the fluorination process (see Section S5 of the Supporting Information and Figures 3 and S23). Removing a single fluorine ad-atom from fully FG (C_1F_1) is very energetically demanding, with a BDE of 118.2 kcal·mol⁻¹ (Figure 3a). However, it should be noted that radical point defects occur naturally in real FG samples.⁹ The removal of the nearest neighboring fluorine ad-atom to the radical point defect results in the formation of a C=C double bond and is much more favorable (BDE 50.9 kcal·mol⁻¹) than removing a more distant fluorine ad-atom (Figure 3b). The nearest neighbor F ad-atom was again easier to remove from $C_{18}F_{16}$ than a more distant ad-atom (Figure 3c). However, its BDE (97.5 kcal·mol⁻¹) was much higher than that of the corresponding F ad-atom in $C_{18}F_{17}$ (50.9 kcal·mol⁻¹). The significantly higher BDE in the

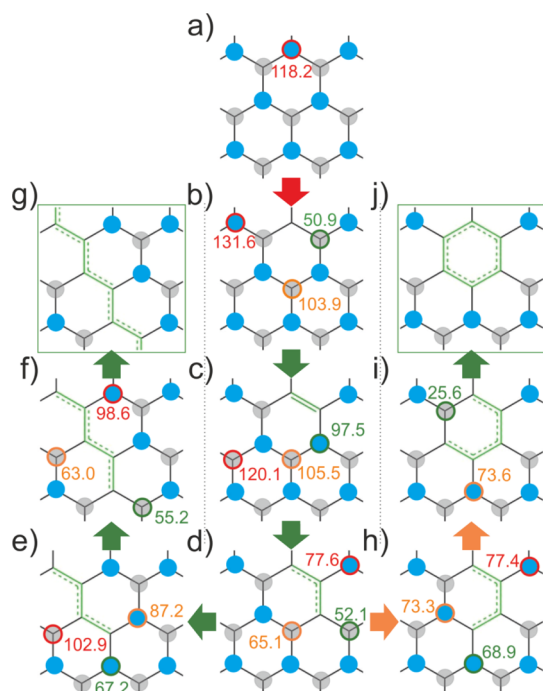


Figure 3. Defluorination of FG. The formation of zigzag lines is more favorable than that of hexagons. The numbers are BDE ($\text{kcal}\cdot\text{mol}^{-1}$) values, and the colors reflect the feasibility of removing the indicated F ad-atoms.

former case is due to formation of a radical (i.e., magnetic) structure, in accordance with Lieb's theorem.⁴⁶

The differences between the BDEs of neighboring and more distant F ad-atoms give rise to distinct defluorination pathways (Figures 3 and S24). The BDE value for F ad-atom removal

from $\text{C}_{18}\text{F}_{15}$ leading to a “zigzag” motif of sp^2 C centers is $52.1 \text{ kcal}\cdot\text{mol}^{-1}$, while that for F removal leading to an “armchair” motif is $65.1 \text{ kcal}\cdot\text{mol}^{-1}$ (Figure 3d). The formation of a star-shaped motif with a biradical character requires even more energy ($77.6 \text{ kcal}\cdot\text{mol}^{-1}$). FG defluorination thus preferentially proceeds along the sp^2 carbon zigzag lines (Figure 3g) rather than involving other sp^2 carbon motifs such as hexagonal rings or armchair lines (Figures 3j and S24). The formation of conjugated sp^2 carbon zigzag chains was also observed in high-resolution transmission electron microscopy experiments conducted by Tuček et al.³⁵ during studies on hydroxofluorographene. Although the branching of existing π -conjugated motifs is less favorable than their extension, it is still significantly energetically less-demanding than detachment of more distant fluorine ad-atoms (Figure 3b), suggesting that defluorination preferentially occurs by expanding existing defluorinated domains rather than by forming homogeneously distributed defluorinated spots.

The distribution of F ad-atoms over the graphene lattice leads to the formation of specific structural motifs (as discussed above) that determine the material's electronic and magnetic properties. While pristine graphene is a nonmagnetic semimetal with a characteristic Dirac point in its band-structure,⁴⁷ pFGs in their GS can have either metallic (for systems with up to 3 F ad-atoms per C_{18} -cell) or semiconducting characters with widely varying band gap widths (that of FG is as high as 3 eV ^{25,26,44}) that generally increase with the number of F ad-atoms (Figure 4). The increase in band gap width is more pronounced for structures with even numbers of ad-atoms (see also Figure S25a).

While pFGs with even numbers of ad-atoms are nonmagnetic in their GS because the two graphene sublattices are equally populated, those with odd numbers of F ad-atoms are magnetic (aside from C_{18}F_1 , which has a spin-symmetric

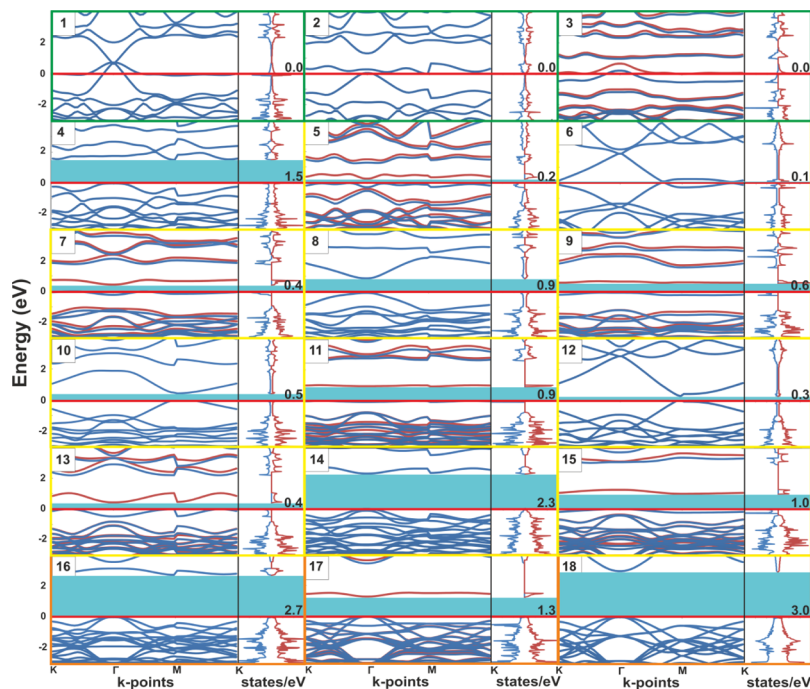


Figure 4. Band structure and density of states of the GS of $\text{C}_{18}\text{F}_{1-18}$ (Figure S21). The numbers in the top left of each image indicate the number of F ad-atoms in the system. Green, yellow, and orange frames indicate metallic, semiconducting, and insulating electronic structures, respectively. Blue bars and numbers (in eV) indicate the band gap width.

density of states plot; see Figure 4). The ground magnetic states of semiconducting structures have a spin number of $S = 0.5$ in accordance with Lieb's theorem.⁴⁶ The only pFG species with a noninteger magnetic moment ($0.86 \mu_B$ per cell, Figure S26) is the metallic species $C_{18}F_3$. The covalent attachment of fluorine adatoms onto graphene rehybridized the carbon atom beneath, destroyed the graphene's $sp^2 \pi$ -delocalized system, and disbalanced graphene's bipartite lattice. According to the theorem by Lieb,⁴⁶ this would induce magnetic moment ($\mu = 1 \mu_B$) in the graphene lattice and lead to the semiconducting electronic structure with spin-polarized localized zero-energy states at the Fermi level. However, the calculation revealed a nonmagnetic solution for $C_{18}F_1$ with the spin-symmetric metallic electronic structure. Following ref 13, additional calculations with on-site U correction and the fixed value of magnetic moment were performed. The nonmagnetic metallic solution remained, however, robust against on-site U correction (Table S5). These findings indicate that prediction of correct magnetic moment is a delicate task, which requires perfect control over the DFT method and calculation setup. Generally, DFT methods including self-interaction error, spin-orbit coupling and setup with sparse k -mesh may fail in providing correct magnetic moments. Magnetic moments of doped graphene by single graphitic nitrogen depending on the high/low k -point mesh represent another typical example.^{48–50} It is worth noting that the relationship between materials' stabilities and their band gap widths was recently investigated in hydroxofluorographene analogs.⁵¹ Larger gaps generally resulted in higher transition temperatures (Figure S25b), which may indicate that magnetic pFGs with higher F contents will be more likely to retain their magnetism at elevated temperatures. Thus, it seems plausible that the partial defluorination of highly fluorinated FG could produce magnetic pFGs with higher transition temperatures than those obtained by brief fluorination of pristine graphene.

CONCLUSIONS

In summary, we have shown that the C–F bonds in FGs have remarkable properties that are inconsistent with the common view of the C–F bond as one of the strongest bonds in organic chemistry. The C–F bonds in a single class of materials can differ markedly in strength (by as much as a factor of 6), so individual C–F bonds cannot be considered equivalent. The strength of individual C–F bonds is highly sensitive to their structural context, so their properties may evolve over time in response to chemically or thermally induced processes. Consequently, the properties of partially fluorinated materials may depend on both their composition and their method of preparation. All these aspects should be taken into account when evaluating and comparing the properties of graphene derivatives as well as when analyzing the reactivity of 2D nanomaterials because their reactivity will change in complex ways during the course of any chemical reaction. This is a material property with no analogue in classical molecular chemistry.

The reactivity of pFGs can lead to the formation of specific structural motifs or patterns that significantly affect material's electronic and magnetic properties. pFGs in their GS may be of either metallic or semiconducting character, with widely varying band gap widths that correlate with their content of F ad-atoms (i.e., the x/y ratio in C_xF_y structures). Lattice imbalances in the bipartite graphene lattice result in the formation of magnetic pFGs with odd numbers of F ad-atoms

or, depending on the topology, to (non)magnetic structures with even numbers of F ad-atoms.

We believe that the results presented here help explain the outcomes of experimental processes including (but not limited to) fluorination, thermal annealing, and chemical reduction of graphene and its fluorinated derivatives and will be valuable in efforts to design new ways of preparing 2D materials with controllable structures and properties suitable for diverse electronic and magnetic applications.

ASSOCIATED CONTENT

Supporting Information

The Supporting Information is available free of charge on the ACS Publications website at DOI: 10.1021/acs.jpcc.9b07552.

Data on the remarkable variability of C–F bonds based on pair correlations and multiple regressions; data on the relative stabilities of pFG structures based on Boltzmann probabilities; lowest-in-energy structures formed by fluorination and defluorination; data on electronic and magnetic properties of pFGs, including the dependence of pFG band gaps on the number of F ad-atoms, relationship between ΔE_{FM-NM} and the band gap; and atom/orbital-resolved density of states and spin density distribution plots (PDF)

AUTHOR INFORMATION

Corresponding Authors

*E-mail: miroslav.medved@upol.cz (M.M.).

*E-mail: piotr.blonski@upol.cz (P.B.).

*E-mail: michal.otyepka@upol.cz (M.O.).

ORCID

Pavel Banáš: 0000-0002-7137-8225

Piotr Błoński: 0000-0002-7072-232X

Michal Otyepka: 0000-0002-1066-5677

Author Contributions

[§]R.L. and D.Z. contributed equally to this work.

Notes

The authors declare no competing financial interest.

ACKNOWLEDGMENTS

The authors gratefully acknowledge the support of the Ministry of Education, the Youth and Sports of the Czech Republic, the Operational Programme for Research, the Development and Education of the European Regional Development Fund (project no. CZ.02.1.01/0.0/0.0/16_019/0000754), ERC (project no. 683024 from the European Union's Horizon 2020), and the Internal Student Grant Agency of the Palacký University in Olomouc, Czech Republic (IGA_PrF_2019_031). We thank Z. Trávníček (RCPTM) for X-ray crystal database survey.

REFERENCES

- (1) Hagan, D. O. Understanding Organofluorine Chemistry. An introduction to the C–F bond. *Chem. Soc. Rev.* **2008**, *37*, 308–319.
- (2) Wang, X.; Wang, W.; Liu, Y.; Ren, M.; Xiao, H.; Liu, X. Controllable Defluorination of Fluorinated Graphene and Weakening of C–F Bonding under the Action of Nucleophilic Dipolar Solvent. *Phys. Chem. Chem. Phys.* **2016**, *18*, 3285–3293.
- (3) Dubecký, M.; Otyepková, E.; Lazar, P.; Karlický, F.; Petr, M.; Čepe, K.; Banáš, P.; Zbořil, R.; Otyepka, M. Reactivity of Fluorographene: A Facile Way toward Graphene Derivatives. *J. Phys. Chem. Lett.* **2015**, *6*, 1430–1434.

- (4) Bourlinos, A. B.; Safarova, K.; Siskova, K.; Zbořil, R. The Production of Chemically Converted Graphenes from Graphite Fluoride. *Carbon* **2012**, *50*, 1425–1428.
- (5) Worsley, K. A.; Ramesh, P.; Mandal, S. K.; Niyogi, S.; Itkis, M. E.; Haddon, R. C. Soluble Graphene Derived from Graphite Fluoride. *Chem. Phys. Lett.* **2007**, *445*, 51–56.
- (6) Lazar, P.; Chua, C. K.; Holá, K.; Zbořil, R.; Otyepka, M.; Pumera, M. Dichlorocarbene-Functionalized Fluorographene: Synthesis and Reaction Mechanism. *Small* **2015**, *11*, 3790–3796.
- (7) Urbanová, V.; Holá, K.; Bourlinos, A. B.; Čépe, K.; Ambrosi, A.; Loo, A. H.; Pumera, M.; Karlický, F.; Otyepka, M.; Zbořil, R. Thiofluorographene-hydrophilic Graphene Derivative with Semiconducting and Genosensing Properties. *Adv. Mater.* **2015**, *27*, 2305–2310.
- (8) Whitener, K. E.; Stine, R.; Robinson, J. T.; Sheehan, P. E. Graphene as Electrophile: Reactions of Graphene Fluoride. *J. Phys. Chem. C* **2015**, *119*, 10507–10512.
- (9) Medved', M.; Zoppellaro, G.; Ugolotti, J.; Matochová, D.; Lazar, P.; Pospíšil, T.; Bakandritsos, A.; Tuček, J.; Zbořil, R.; Otyepka, M. Reactivity of Fluorographene is Triggered by Point Defects: Beyond the Perfect 2D World. *Nanoscale* **2018**, *10*, 4696–4707.
- (10) Matochová, D.; Medved', M.; Bakandritsos, A.; Steklý, T.; Zbořil, R.; Otyepka, M. 2D Chemistry: Chemical Control of Graphene Derivatization. *J. Phys. Chem. Lett.* **2018**, *9*, 3580–3585.
- (11) Kumar, N.; Sharma, J. D.; Ahluwalia, P. K. First-principle Study of Nanostructures of Functionalized Graphene. *Pramana* **2014**, *82*, 1103–1117.
- (12) Zhou, S.; Sherpa, S. D.; Hess, D. W.; Bongiorno, A. Chemical Bonding of Partially Fluorinated Graphene. *J. Phys. Chem. C* **2014**, *118*, 26402–26408.
- (13) Marsusi, F.; Drummond, N. D.; Verstraete, M. J. The Physics of Single-Side Fluorination of Graphene: DFT and DFT + U Studies. *Carbon* **2019**, *144*, 615–627.
- (14) Tran, N. T. T.; Nguyen, D. K.; Glukhova, O. E.; Lin, M.-F. Coverage-dependent Essential Properties of Halogenated Graphene: A DFT Study. *Sci. Rep.* **2017**, *7*, 17858.
- (15) Nakada, K.; Ishii, A. DFT Calculation for Adatom Adsorption on Graphene. In *Graphene Simulation*; Gong, J.R., Ed.; InTech, 2011.
- (16) Parmentier, J.; Schlienger, S.; Dubois, M.; Disa, E.; Masin, F.; Centeno, T. A. Structural/Textural Properties and Water Reactivity of Fluorinated Activated Carbons. *Carbon* **2012**, *50*, 5135–5147.
- (17) Nair, R. R.; Ren, W.; Jalil, R.; Riaz, I.; Kravets, V. G.; Britnell, L.; Blake, P.; Schedin, F.; Mayorov, A. S.; Yuan, S.; Katsnelson, M. I.; Cheng, H.-M.; Strupinski, W.; Bulusheva, L. G.; Okotrub, A. V.; Grigorieva, I. V.; Grigorenko, A. N.; Novoselov, K. S.; Geim, A. K. Fluorographene: A Two-Dimensional Counterpart of Teflon. *Small* **2010**, *6*, 2877–2884.
- (18) Boukhvalov, D. W. Absence of Stable Atomic Structure in Fluorinated Graphene. *Phys. Chem. Chem. Phys.* **2016**, *18*, 13287–13293.
- (19) Lee, S.-S.; Jang, S.-W.; Park, K.; Jang, E. C.; Kim, J.-Y.; Neuhauser, D.; Lee, S. A Mechanistic Study of Graphene Fluorination. *J. Phys. Chem. C* **2013**, *117*, 5407–5415.
- (20) Asanov, I. P.; Bulusheva, L. G.; Dubois, M.; Yudanov, N. F.; Alexeev, A. V.; Makarova, T. L.; Okotrub, A. V. Graphene Nanochains and Nanoislands in the Layers of Room-temperature Fluorinated Graphite. *Carbon* **2013**, *59*, 518–529.
- (21) Okotrub, A. V.; Yudanov, N. F.; Asanov, I. P.; Vyalikh, D. V.; Bulusheva, L. G. Anisotropy of Chemical Bonding in Semifluorinated Graphite C₂F Revealed with Angle-resolved X-ray Absorption Spectroscopy. *ACS Nano* **2013**, *7*, 65–74.
- (22) Kashtiban, R. J.; Dyson, M. A.; Nair, R. R.; Zan, R.; Wong, S. L.; Ramasse, Q.; Geim, A. K.; Bangert, U.; Sloan, J. Atomically resolved imaging of highly ordered alternating fluorinated graphene. *Nat. Commun.* **2014**, *5*, 4902.
- (23) Javaid, S.; Myung, C. W.; Pourasad, S.; Rakshit, B.; Kim, K. S.; Lee, G. Highly Hydrophobic Fluorographene based system as an Interlayer for Electron Transport in Organic-Inorganic Perovskite Solar Cells. *J. Mater. Chem. A* **2018**, *6*, 18635–18640.
- (24) Karlický, F.; Kumara Ramanatha Datta, K.; Otyepka, M.; Zbořil, R. Halogenated Graphenes: Rapidly Growing Family of Graphene Derivatives. *ACS Nano* **2013**, *7*, 6434–6464.
- (25) Santos, H.; Henrard, L. Fluorine Adsorption on Single and Bilayer Graphene: Role of Sublattice and Layer Decoupling. *J. Phys. Chem. C* **2014**, *118*, 27074–27080.
- (26) Robinson, J. T.; Burgess, J. S.; Junkermeier, C. E.; Badescu, S. C.; Reinecke, T. L.; Perkins, F. K.; Zalalutdniov, M. K.; Baldwin, J. W.; Culbertson, J. C.; Sheehan, P. E.; Snow, E. S. Properties of Fluorinated Graphene Films. *Nano Lett.* **2010**, *10*, 3001–3005.
- (27) Karlický, F.; Otyepka, M. Band Gaps and Optical Spectra of Chlorographene, Fluorographene and Graphane from G₀W₀, G₁W₀ and G₂W₀ Calculations on Top of PBE and HSE06 Orbitals. *J. Chem. Theory Comput.* **2013**, *9*, 4155–4164.
- (28) Lvova, N. A.; Ananina, O. Y. Theoretical Study of Graphene Functionalization by F- and FHF- Ions from Associates with Water Molecules. *Comput. Mater. Sci.* **2015**, *101*, 287–292.
- (29) Han, S. S.; Yu, T. H.; Merinov, B. V.; van Duin, A. C. T.; Yazami, R.; Goddard, W. A. Unraveling Structural Models of Graphite Fluorides by Density Functional Theory Calculations. *Chem. Mater.* **2010**, *22*, 2142–2154.
- (30) Charlier, J.-C.; Gonze, X.; Michenaud, J.-P. First-principles Study of Graphite Monofluoride (CF)_n. *Phys. Rev. B: Condens. Matter Mater. Phys.* **1993**, *47*, 16162–16168.
- (31) Shayeganfar, F. Energy Gap Tuning of Graphene Layers with Single Molecular F₂ Adsorption. *J. Phys. Chem. C* **2015**, *119*, 12681–12689.
- (32) Liu, H. Y.; Hou, Z. F.; Hu, C. H.; Yang, Y.; Zhu, Z. Z. Electronic and Magnetic Properties of Fluorinated Graphene with Different Coverage of Fluorine. *J. Phys. Chem. C* **2012**, *116*, 18193–18201.
- (33) Makarova, T. L.; Shelankov, A. L.; Zyrianova, A. A.; Veinger, A. I.; Tisnek, T. V.; Lähderanta, E.; Shames, A. I.; Okotrub, A. V.; Bulusheva, L. G.; Chekhova, G. N.; Pinakov, D. V.; Asanov, I. P.; Šljivčanin, Ž. Edge State Magnetism in Zigzag- interfaced Graphene via Spin Susceptibility Measurements. *Sci. Rep.* **2015**, *5*, 13382.
- (34) Tuček, J.; Holá, K.; Bourlinos, A. B.; Bloński, P.; Bakandritsos, A.; Ugolotti, J.; Dubecký, M.; Karlický, F.; Ranc, V.; Čépe, K.; Otyepka, M.; Zbořil, R. Room Temperature Organic Magnets Derived from sp³ Functionalized Graphene. *Nat. Commun.* **2017**, *8*, 14525.
- (35) Tuček, J.; Holá, K.; Zoppellaro, G.; Bloński, P.; Langer, R.; Medved', M.; Susi, T.; Otyepka, M.; Zbořil, R. Driving Force toward Room Temperature Ferromagnetic Graphene Zig-Zag sp² Carbon Chains Passing through sp³ Framework – A Driving Force toward Room Temperature Ferromagnetic Graphene. *ACS Nano* **2018**, *12*, 12847–12859.
- (36) Perdew, J. P.; Burke, K.; Ernzerhof, M. Generalized Gradient Approximation Made simple. *Phys. Rev. Lett.* **1996**, *77*, 3865–3868.
- (37) Kresse, G.; Furthmüller, J. Efficient Iterative Schemes for Ab initio Total-Energy Calculations Using a Plane-Wave Basis Set. *Phys. Rev. B: Condens. Matter Mater. Phys.* **1996**, *54*, 11169–11186.
- (38) Kresse, G.; Furthmüller, J. Efficiency of Ab-initio Total Energy Calculations for Metals and Semiconductors Using a Plane-Wave Basis Set. *Comput. Mater. Sci.* **1996**, *6*, 15–50.
- (39) Kresse, G.; Joubert, D. From ultrasoft pseudopotentials to the projector augmented-wave method. *Phys. Rev. B: Condens. Matter Mater. Phys.* **1999**, *59*, 1758–1775.
- (40) Blöchl, P. E. Projector Augmented-Wave Method. *Phys. Rev. B: Condens. Matter Mater. Phys.* **1994**, *50*, 17953–17979.
- (41) Monkhorst, H. J.; Pack, J. D. Special Points for Brillouin-zone Integrations. *Phys. Rev. B: Solid State* **1976**, *13*, 5188–5192.
- (42) Grimme, S. Semiempirical GGA-Type Density Functional Constructed with a Long-Range Dispersion Correction. *J. Comput. Chem.* **2006**, *27*, 1787–1799.
- (43) Vyalikh, A.; Bulusheva, L. G.; Chekhova, G. N.; Pinakov, D. V.; Okotrub, A. V.; Scheler, U. Fluorine Patterning in Room-Temperature Fluorinated Graphite Determined by Solid-State NMR and DFT. *J. Phys. Chem. C* **2013**, *117*, 7940–7948.

- (44) Thirumalai, D.; Klimov, D. K.; Woodson, S. A. Kinetic Partitioning Mechanism as a Unifying Theme in the Folding of Biomolecules. *Theor. Chem. Acc.* **1997**, *96*, 14–22.
- (45) Chronopoulos, D. D.; Bakandritsos, A.; Pykal, M.; Zbořil, R.; Otyepka, M. Chemistry, Properties, and Applications of Fluorographene. *Appl. Mat. Today* **2017**, *9*, 60–70.
- (46) Lieb, E. H. Two Theorems on the Hubbard Model. *Phys. Rev. Lett.* **1989**, *62*, 1201–1204.
- (47) Novoselov, K. S.; Geim, A. K.; Morozov, S. V.; Jiang, D.; Katsnelson, M. I.; Grigorieva, I. V.; Dubonos, S. V.; Firsov, A. A. Two-dimensional Gas of Massless Dirac Fermions in Graphene. *Nature* **2005**, *438*, 197–200.
- (48) Błoński, P.; Tuček, J.; Sofer, Z.; Mazánek, V.; Petr, M.; Pumera, M.; Otyepka, M.; Zbořil, R. Doping with Graphitic Nitrogen Triggers Ferromagnetism in Graphene. *J. Am. Chem. Soc.* **2017**, *139*, 3171–3180.
- (49) Babar, R.; Kabir, M. Ferromagnetism in Nitrogen-Doped Graphene. *Phys. Rev. B* **2019**, *99*, 115442.
- (50) Singh, R.; Kroll, P. Magnetism in Graphene due to Single-Atom Defects: Dependence on the Concentration and Packing Geometry of Defects. *J. Phys.: Condens. Matter* **2009**, *21*, 196002.
- (51) Langer, R.; Błoński, P.; Otyepka, M. Tuning the Magnetic Properties of Graphene Derivatives by Functional Group Selection. *Phys. Chem. Chem. Phys.* **2019**, *21*, 12697–12703.






B

Reactivity of Fluorographene
is Triggered by Point Defects: Beyond the
Perfect 2D World



Cite this: *Nanoscale*, 2018, **10**, 4696

Reactivity of fluorographene is triggered by point defects: beyond the perfect 2D world†

Miroslav Medved,^a  *^a Giorgio Zoppellaro,  ^a Juri Ugolotti,^a Dagmar Matochová,^a Petr Lazar,^a Tomáš Pospíšil,^b Aristides Bakandritsos,^a Jiří Tuček,  ^a Radek Zbořil  ^a and Michal Otyepka  *^a

Preparation of graphene derivatives using fluorographene (FG) as a precursor has become a key strategy for the large-scale synthesis of new 2-D materials (e.g. graphene acid, cyanographene, allyl-graphene) with tailored physicochemical properties. However, to gain full control over the derivatization process, it is essential to understand the reaction mechanisms and accompanying processes that affect the composition and structure of the final products. Despite the strength of C–F bonds and high chemical stability of perfluorinated hydrocarbons, FG is surprisingly susceptible to reactions under ambient conditions. There is clear evidence that nucleophilic substitution on FG is accompanied by spontaneous defluorination, and solvent-induced defluorination can occur even in the absence of any nucleophilic agent. Here, we show that distributed radical centers (fluorine vacancies) on the FG surface need to be taken into account in order to rationalize the defluorination mechanism. Depending on the environment, these radical centers can react as electron acceptors, electrophilic sites and/or cause homolytic bond cleavages. We also propose a new radical mechanism of FG defluorination in the presence of *N,N*-dimethylformamide (DMF) solvent. Spin-trap experiments as well as ¹⁹F NMR measurements unambiguously confirmed formation of *N,N*'-dimethylformyl radicals and also showed that *N,N*'-dimethylcarbamoyl fluoride plays a key role in the proposed mechanism. These findings imply that point defects in 2D materials should be considered as key factor determining their chemical properties and reactivity.

Received 18th December 2017,
Accepted 6th February 2018

DOI: 10.1039/c7nr09426d

rsc.li/nanoscale

1. Introduction

The discovery of graphene¹ in 2004 opened a route to a new class of carbon-based 2D materials with unique chemical, electronic and magnetic properties. Whereas graphene itself is chemically a low reactive semimetal with high electron conductivity, even dilute concentrations of chemisorbed impurities can dramatically change its band structure and induce local magnetic moments.² Increasing the adsorbate concentration can further disrupt the π -conjugated network, transforming the conducting material to an insulator through a variety of intermediate states.^{3,4} Possibilities for tuning the band gap characteristics and associated electronic and mag-

netic properties by graphene derivatization provide an auspicious base for future technological advancements, including development of batteries,^{5–7} biosensing,⁸ gas sensing on surfaces⁹ and solar cell technologies.¹⁰ Nevertheless, selective and controllable covalent graphene functionalization remains a challenging task due to the limited reactivity of graphene.^{11,12} Many proposed direct derivatization strategies suffer from a low degree of functionalization^{13–16} or require harsh reaction conditions that strongly affect the final stoichiometry and chemical structure of the resulting graphene derivative.^{17,18}

Fluorographene (FG)^{19–21} offers a promising alternative for graphene derivatization because (i) chemisorption of monovalent fluorine atoms prevents formation of complex (non-stoichiometric) structures; (ii) the material is thermally stable up to 400 K; (iii) the pristine 3D material, graphite fluoride, is available in large-scale as an industrial lubricant; and (iv) FG reacts readily as an electrophile under mild conditions.^{22–26} Owing to these features, FG has recently been used as a precursor for the synthesis of several graphene derivatives, including amino-graphenes,^{26–30} cyanographene,³¹ carboxygraphene (graphene acid),³¹ sulfur-linked derivatives^{25,32} and alkylated graphenes.³³ During the chemical transformation of FG, substitution of fluorine atoms proceeds simultaneously with

^aRegional Centre of Advanced Technologies and Materials, Department of Physical Chemistry, Faculty of Science, Palacky University in Olomouc, 17. listopadu 1192/12, 771 46 Olomouc, Czech Republic. E-mail: Miroslav.Medved@upol.cz, Michal.Otyepka@upol.cz

^bCentre of the Region Haná for Biotechnological and Agricultural Research, Department of Chemical Biology and Genetics, Faculty of Science, Palacky University in Olomouc, 17. listopadu 1192/12, 771 46 Olomouc, Czech Republic

† Electronic supplementary information (ESI) available. See DOI: 10.1039/c7nr09426d



reductive defluorination. It has been suggested that bimolecular nucleophilic substitution S_N2 is the preferred mechanism of substitution of the fluorine atoms.²³ Also important is the role of the solvent, which can significantly affect the whole process, not only by the common (de)stabilization solvation effects but also by triggering and/or enhancing the defluorination process. Wang *et al.*³⁴ has shown that FG spontaneously defluorinates in the presence of highly nucleophilic (dipolar) solvents, such as *N,N'*-dimethylformamide (DMF), dimethylacetamide (DMAc) and *N*-methyl-2-pyrrolidone (NMP). The authors rationalized the defluorination effect of these solvents in terms of strong dipolar–dipolar interactions of the solvent molecules with the electron-deficient carbon atom of the C–F bond. All these findings indicate that unusual chemistry drives the reactivity of FG, and its intricacies need to be deciphered in order to rationalize the process of graphene derivatization using FG.

In our work, we present a description of the mechanism of the reactivity of FG obtained by combining electron paramagnetic resonance (EPR) and ^{19}F NMR experiments with theoretical calculations. We focus on FG in DMF, which is a widely used solvent for FG exfoliation and chemical treatment. EPR experiments confirmed the presence of radical centers (fluorine vacancies) in FG and allowed their distribution and time-evolution to be studied. We observed defluorination in DMF, despite the fact that it is not a sufficiently strong reducing agent for FG. Based on theoretical calculations, we suggest a new mechanism involving *N,N'*-dimethylformyl radicals (DMF $^{\cdot}$), formation of which was evidenced by a series of spin-trap experiments. In addition, ^{19}F NMR measurements unambiguously confirmed formation of *N,N'*-dimethylcarbamoyl fluoride, which plays a key role in the proposed mechanism. These findings show that defects present in FG determine the chemical behavior of this 2D material and make it susceptible to defluorination and subsequent substitution and addition reactions. Such defects may be important in determining the reactivity of other 2D materials because they may initiate reactions which then propagate on the surface of 2D materials.

2. Experimental setup & computational details

2.1 Chemicals

All chemicals and reagents were used as obtained from the suppliers without further purification. Graphite fluoride (GrF, $\text{C}_1\text{F}_{1.1}$), anhydrous DMF (99.8%, CAS number: 68-12-2), α -4-pyridyl-1-oxide-*N*-*tert*-butylnitrone (POBN, 99%, CAS number: 66893-81-0) and dry benzene (99.8%, CAS number: 71-43-2) were provided by Sigma-Aldrich. Fluorographene used for the experiments described in section 3.6 was obtained by exfoliation of GrF in DMF.³⁵ *N,N'*-Dimethylcarbamoyl fluoride (F-DMF) was obtained by fluorination of the corresponding *N,N'*-dimethylcarbamoyl chloride (Sigma-Aldrich) with KF/CaF_2 (Sigma-Aldrich) in acetonitrile (Penta), following a procedure reported in the literature.³⁶

2.2 Characterization

EPR spectra were recorded on a JEOL JES-X320 electron spin resonance spectrometer operating at the X-band frequency (~ 9.16 – 9.17 GHz) and equipped with variable temperature control ES 13060DVT5 apparatus. The cavity Q quality factor was kept above 6000 in all measurements and signal saturation was avoided by working at low-applied microwave powers. Concentrated suspensions of GrF (15 mg GrF per mL solvent, DMF or benzene) thoroughly degassed under N_2 were mechanically stirred at 40 °C without sonication and kept in airtight and oxygen-free vials, and EPR spectra of the resulting dense suspensions were recorded during a 10 day time-frame. Use of very concentrated suspensions of GrF was necessary for successful spin-trapping experiments with POBN (see ESI for details, section 1.2†). Generally, 0.1 mL of GrF suspension was loaded into the EPR tubes by using airtight syringes. In the case of GrF powder, 10 mg were used. For the spin-trap experiments, the reaction mixtures (GrF/solvent/POBN reacted together at RT for 40 min) were centrifuged prior to loading 0.1 mL of the supernatants into the EPR tubes. Discussion on the use of GrF instead of FG for the EPR studies and radical formation on the carbon lattice is available in the ESI.† Highly-pure quartz tubes were employed (Suprasil, Wilmad, ≤ 0.5 OD). Simulation of the EPR resonances were carried out using the WinEPR SimFonia software (V.1.25, Dr Ralph T. Weber, EPR Division, Bruker Instruments, Inc. Billerica, MA USA) with second-order perturbation theory. The frequency unit can be converted into magnetic fields units through the following relation: 0.1 mT equals to 2.8025 MHz. Nuclear magnetic resonance (^{19}F) spectra were obtained with a JEOL ECA-500 NMR spectrometer (^{19}F frequency 470 MHz, $\text{CFCl}_3 = 0$ ppm). Further experimental details can be found in the ESI.†

2.3 Computational details

The ground state (GS) structures of all the investigated species were optimized by the $\omega\text{B97X-D}$ method³⁷ using 6-31+G(d) and 6-31++G(d,p) basis sets.³⁸ Solvent effects were included by using the universal continuum solvation model based on solute electron density (SMD).³⁹ Whereas the structures of small and medium size systems (F, F^- , HF, DMF, F-DMF, *etc.*) were fully relaxed in geometry optimizations, to mimic the semilocal flexibility of FG sheets, FG-like structures were obtained by constrained geometry optimizations, keeping the edge carbon atoms frozen. All calculations were performed with the Gaussian09 program.⁴⁰

3. Results and discussion

3.1 EPR spectra of GrF in benzene and DMF

The stability of GrF dispersed in two model solvents (benzene and DMF) was probed using electron paramagnetic resonance (EPR) spectroscopy by monitoring the variation of the respective EPR envelopes over time. Fig. 1a shows the frozen matrix ($T = 123$ K) X-band EPR envelope recorded for the freshly prepared GrF/benzene suspension. Although the overall reso-



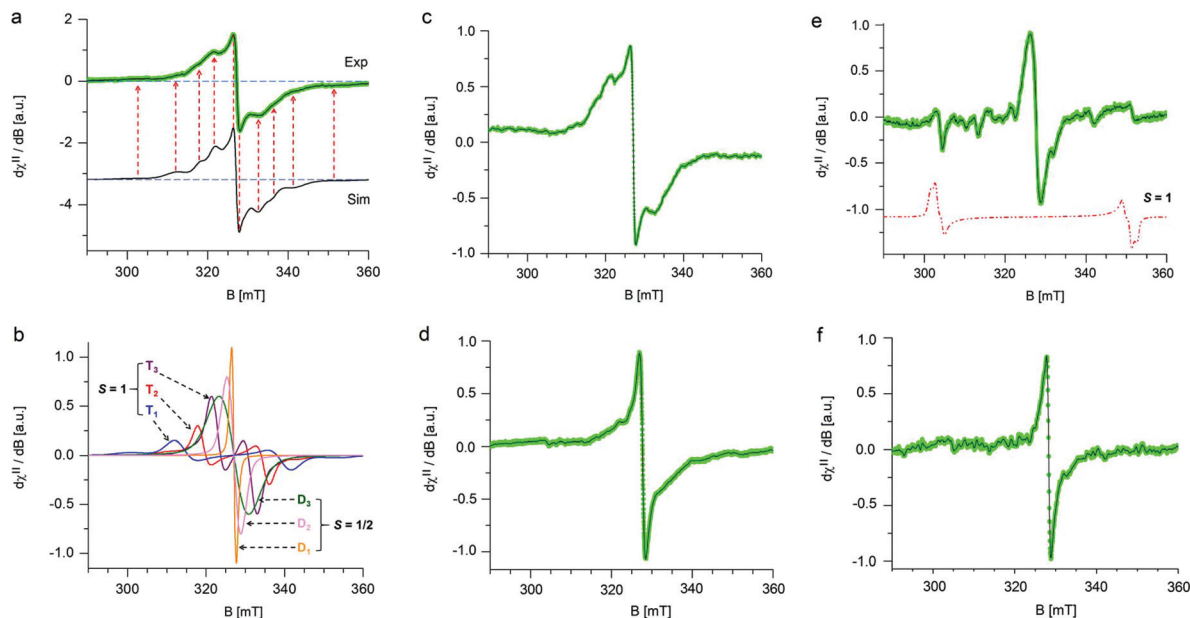


Fig. 1 Low temperature ($T = 123$ K) frozen matrix X-band EPR spectra of GrF dispersed in benzene or DMF recorded at various times. (a) GrF freshly dispersed in benzene (green line, Exp) and its EPR simulation (black line, Sim). (b) Overview of the diverse spin components encoded in the EPR envelope shown in (a, Sim); the labels T_1 , T_2 and T_3 indicate triplet ($S = 1$) species, whereas D_1 , D_2 and D_3 indicate doublet ($S = 1/2$) species. The relative weights were as follows: T_1 (4.3%), T_2 (8.4%), T_3 (16.9%), D_1 (31.0%), D_2 (22.5%), D_3 (16.9%). (c) GrF freshly dispersed in DMF. (d) GrF/DMF solution after 7 days. (e) GrF/DMF solution after 10 days. Experimental parameters: 9.14–9.16 GHz frequency, 100 kHz modulation frequency, 30 ms time constant, 0.5–0.8 mT modulation width, 0.4–0.6 mW applied microwave power. In (a) and (c–f), the solid black line corresponds to the resolution enhanced EPR resonance line (Savitzky–Golay, denoise algorithm).

nance line of the system in benzene was rather broad (~ 30 mT field-spread), it exhibited several small resonances that developed symmetrically with respect to an intense narrow central line, a signature of overlapped contributions of triplet and doublet spin-states. The observed g -averaged (g_{avg}) value was estimated to be 2.000 and validated by recording the spectrum together with the Mn(II)/MgO standard (JEOL internal reference standard, Mn(II), $g_{\text{eff}} = 2.00101 \pm 0.00005$, ESI, Fig. S5 and S6[†]). A comparable EPR spectrum was observed for the neat GrF powder (ESI, Fig. S1a and S3[†]). Similar EPR spectra have been previously reported around the $g = 2$ region (~ 280 – 380 mT) by Panich and co-authors⁴¹ on polycrystalline graphite fluoride (CF)_n obtained by fluorination of petroleum coke as well as by Giraudet and co-authors in a later report (~ 310 – 380 mT region).⁴² However, we noticed that by recording the EPR signal of the GrF powder in a broader magnetic-sweep range (50–550 mT), a broad tail emerged in the high field region (360–550 mT) together with a broad resonance signal in the low field region (around $g = 4$) (ESI, Fig. S3[†]). These features became strongly weakened in the diluted systems (GrF/benzene and GrF/DMF). The ESI provides additional EPR spectra for GrF, including the EPR power-saturation behavior (Fig. S1a, S2–S4[†]). Panich and co-authors suggested that the fine structure observed around $g = 2.00$ in GrF was due to resolved hyperfine components (A_F) with ~ 5 mT of splitting value, originating from the interaction of an unpaired spin ($S = 1/2$) with six neighboring fluorine nuclei. The authors also

found that these hyperfine lines were rather broad ($\Delta H = 30$ G by simulation), a factor that pointed towards the joint effect of dipole–dipole and exchange interactions between paramagnetic centers. In the later work, Giraudet and co-authors took the similar approach in the simulation of the observed EPR envelope for GrF, but with the addition of two broad resonance lines. The simulation of the signal was obtained by adding the hyperfine contribution of six fluorine nuclei ($A = 45 \pm 2$ G, line width of 36 ± 2 G, and g factor of 2.003 ± 0.001). As stated by the authors, and similar to the Panich’s work, “the large line width is interpreted by the joint effect of dipole–dipole and exchange interactions between paramagnetic centers”. In the case of the GrF/benzene frozen matrix sample, we therefore tried to disentangle these effects previously anticipated by ref. 41 and 42 and carried out an EPR simulation of the resonance signal in the $g = 2.0$ region under the assumption of an overlapped contribution of different spin components (Fig. 1a, black line, Sim, and Fig. 1b showing the individual spin components with their relative weights). The observed EPR signal of GrF/benzene shown in Fig. 1a (Exp) can be interpreted as a superposition of three effective triplet states ($S = 1$) and three sets of spin-doublets ($S = 1/2$), *i.e.*, in GrF exists a distribution of spin-carrying defects, some close enough (through-space distance) to show signatures of high-spin systems and others behaving as isolated $S = 1/2$ defects. This hypothesis is supported by the observation that the low field signal around $g = 4.0$ observed in neat GrF can still be observed in the dilute



GrF/benzene suspension through signal accumulation (ESI, Fig. 1b,† GrF/benzene system, 133 K, 4 mW, 40 scan accumulated and averaged) and may represent the half-field transition ($\Delta m_s = 2$) of these high spin ($S = 1$) components. The triplet signatures (Fig. 1b, marked T_1 , T_2 , and T_3 , with g -tensor (x,y,z) of 2.000, 2.000, 2.000) gave from simulation the following axial values (D): one large with $|D|$ of 701 MHz (marked as T_1) and negligible ^{19}F hyperfine contribution, one intermediate (marked as T_2) with $|D|$ of 462 MHz and with line broadening by hyperfine terms (four ^{19}F nuclei, $A_{x,y,z}$ of 56.0, 14.0, 14.0 MHz), and one much smaller (marked as T_3) with $|D|$ of 202 MHz, with similarly broadened resonances (two ^{19}F nuclei, $A_{x,y,z}$ of 38.0, 12.0, 12.0 MHz). From the point-dipole-approach, these triplet configurations (and D values) indicate a spread of through-space distances among the spin-carrying centers that are effectively magnetically coupled together, with $S_{1/2}$ - $S_{1/2}$ through-space distances that lie within 4.8–7.3 Å. These distances are an estimate, assuming dominant $1/r^3$ dependence on the D value and a dominant spin-spin (SS) contribution.⁴³ The biquadratic zero-field-splitting (ZFS) D -tensor comprised two contributions: (i) a first order term arising from direct magnetic dipoles SS interaction, and (ii) a second-order contribution arising from spin-orbit coupling (SOC). In organic based magnets, the first term usually dominates. It is known that the point-dipole approach gives rather poor estimation of inter-center radical distances (compared to X-ray radical distances) if the radical units interact *via* π -bond pathways. In contrast, when the interacting radicals are connected through an array of σ -bonds, which tends to hamper spin delocalization, the point dipole approach gives fairly accurate distances, comparable to those obtained by X-ray.^{44–46} The other types of spin active species are shown by the three sets of $S = 1/2$ signals in Fig. 1b, marked as D_1 , D_2 and D_3 . One doublet (D_1 , line-width tensor L_{xyz} of 28.0, 28.0, 56.0 MHz) corresponded to the relatively sharp and slightly asymmetric central signal at $g_{\text{eff}} = 2.000$. This fingerprint indicates that the $S = 1/2$ spins experienced the strong exchange regime, *i.e.*, the exchange energy (H_{ex}) of the spin packet was much larger than H_{dip} (the dipolar interaction component), which in turn was greater than H_{hf} (the hyperfine component). Considering the upper limit of the strongest triplet obtained by simulation (701 MHz), this indicates that the exchange term (J) associated to these spins was stronger than 0.02 cm^{-1} . Since the applied microwave power was kept low and under non-saturating conditions ($\ll 1 \text{ mW}$), this sharp central line could not have arisen from a double-quantum transition and very unlikely originated from a quartet spin state ($S = 3/2$). The second broad doublet (D_3 , Fig. 1b) belonged to an ensemble of $S = 1/2$ spins that experienced weak dipolar interaction ($< 100 \text{ MHz}$) but still larger than ^{19}F hyperfine ($H_{\text{dip}} > H_{\text{hf}}$). This effect resulted in a very broad line-width (L_{xyz}) of 250.0, 196.0, 196.0 MHz encoded in the electronic transition. The third doublet (D_2 , Fig. 1b) corresponded to $S = 1/2$ spins that experienced an intermediate regime with $H_{\text{dip}} \sim H_{\text{hf}}$ and a relatively narrow line-width tensor in the frozen matrix (L_{xyz}) of 98.0, 98.0, 98.0 MHz. Overall, our observations support the earlier description of Grigorieva and

co-authors on the dominant spin-half paramagnetism for GrF-based materials.⁴⁷ Following GrF aging in benzene solution, we did not observe severe changes in the overall EPR resonance line, which remained after 6 days and 10 days similar to that shown at the beginning of the process (ESI, Fig. S8†). Thus, benzene can be considered a “nearly inert” solvent for GrF which does not induce substantial degradation of the paramagnetic centers. Chemical stability of GrF in benzene was also confirmed by measurement of the XPS spectrum for a 10-days aged GrF sample in benzene (Fig. S25 in ESI†). After dispersion of GrF in DMF, the freshly prepared suspension showed the same EPR fingerprints in a frozen matrix (Fig. 1c) as witnessed for GrF/benzene (Fig. 1a). Additional EPR spectra for GrF/DMF are given in the ESI† (power saturation behavior of the entire resonance line, from 50 to 550 mT, Fig. S9a–c†). The concentration of spin centers on the GrF surface at this stage was estimated to be 23.2×10^{18} spin per g, which corresponds to *ca.* 1 center per area of $5 \text{ nm} \times 5 \text{ nm}$ (see ESI, section 1.2†). This value closely resembles the estimated spin concentration found to near stoichiometric C/F ratios in GrF (C/F_{0.9–1.0}) by Grigorieva and co-authors, which were obtained from in-depth analysis of bulk magnetic susceptibility experiments ($\sim 22\text{--}17 \times 10^{18}$ spin per g).⁴⁷ However, already after 6 h stirring at 40 °C, the GrF/DMF suspension darkened considerably. The X-band EPR spectrum ($T = 123 \text{ K}$) observed after 6 h revealed some changes in the overall resonance line (Fig. 1d) compared to the initial spectrum. The doublet component ($S = 1/2$, D_1 in the simulation shown in Fig. 1b) appeared to increase strongly in intensity (relative increase) at the expense of the T_1 , T_2 and T_3 triplet components (see $S = 1$ components, Fig. 1b and ESI, Fig. S10†) and the doublet component D_2 . After 7 days of stirring, the EPR spectrum of FG/DMF showed more significant changes (Fig. 1e). Besides still being centered at $g_{\text{eff}} = 2.000$, the doublet components D_1 and D_2 became dominant, several resonances appeared throughout the spectrum and a novel but very minor triplet emerged. The spin-Hamiltonian simulation of this species was very tentative (shown by the dotted red-line in Fig. 1e). This system should exhibit a large axial value ($|D|$ of 1345 MHz, $|E/D|$ of 0.04). In this case, the inter-spin (through-space) distance of the triplet configuration ($S = 1$, arising from two interacting $S = 1/2$) was estimated from the point-dipole approach to fall short, at about 3.87 Å. This value corresponded well with the minimum through-space spin-spin distance of the spin carrying defects estimated by theory (*vide infra*, Fig. 4b). It is important to note that at such later stage of the GrF aging process, an alternative explanation for the appearance of the large triplet signal reported above can be put forward. Namely, it may arise from voids in the GrF sheets, especially in the areas corresponding to sp^2 islands that are formed upon extended defluorination. As discussed by Palacios and co-authors,⁴⁸ the presence of voids, such as type A3B, can lead to non-vanishing local magnetic moments. Consequently, $S = 1$ signatures can arise in the EPR spectrum from the presence of these sublattice imbalances ($N_I = N_A - N_B$). When the Hubbard repulsion is active, Lieb’s theorem grants the $S = 1$ spin state to such defect struc-



tures.^{48,49} Further aging, and after 10 days of stirring, the dense GrF DMF solution became very dark brownish and the EPR spectrum revealed signatures of only $S = 1/2$ species (Fig. 1f and ESI, Fig. S11†), with no clear indications of remaining higher spin-states. The spin concentration decreased to 5.4×10^{18} spin per g, *i.e.* to 23% of the initial value. These results clearly indicate that, unlike benzene, DMF cannot be considered an inert solvent for GrF but rather a reactant for GrF, capable of inducing degradation of the spin carrying defects present in GrF.

3.2 Origin of radical centers

The experimental evidence of radical centers in FG raises questions concerning their origin. Let us first assume a perfect perfluorinated graphene structure corresponding to an unperturbed domain on the FG surface and consider creation of radical centers on such an ideal structure. In spite of the outstanding stability of perfluorocarbons (PFCs) related to the high strength of C–F bonds,²³ it was observed that defluorination of PFCs can be achieved by using strong reducing agents, such as metals (metal surfaces, amalgams or transition metal complexes as catalysts), electron rich organic donors (*e.g.*, organic radical anions, thiolates, sulfonates)^{50–52} or photochemically.⁵³ The partial sensitivity of PFCs to reduction is often explained in terms of enhanced reactivity of the most electron-deficient tertiary C–F bonds, which are therefore sometimes termed the “Achilles heel” of PFCs.^{54,55} Referring to works by Borden,⁵⁶ which discuss that various phenomena of fluorocarbon chemistry can be explained by the ability of C–F σ^* orbitals to act as electron acceptors, Sandford⁵⁷ suggested that the defluorination of PFCs (*e.g.*, perfluorodecalin) is initiated by transfer of an electron to the σ^* orbital of a tertiary C–F bond to give a radical anion. To obtain a more detailed picture about the role of the C–F σ^* orbitals and ability to accept an electron by larger PFC structures, we computed gas phase vertical (VEA) and adiabatic (AEA) electron affinities and the HOMO–LUMO gap at the ω B97X-D/6-31++G(d,p) level of theory for a series of medium-sized model fluorinated polycyclic hydrocarbons and their radical counterparts (see Table S1 in ESI†). We found that for the parent closed-shell systems, the VEA values were negative and even AEA, taking into account geometry relaxation of the corresponding radical anions, were very small. Although the VEA values increased with increasing size of the fluorinated PHC systems, due to a possibility of larger delocalization of the negative charge, it can be expected that even for larger (perfect) FG structures, the electron affinity (EA) will be small, in line with the relatively large theoretically predicted band gap of FG varying from 3.1 to 7.5 eV (depending on the approach).^{58,59} Variation of the VEA values with the system size was in line with the qualitative picture provided by the HOMO/LUMO analysis. The positive LUMO energies and rather large HOMO–LUMO gap in closed-shell systems were consistent with their low electron acceptor strength. As anticipated by Sandford and others,⁵⁷ the LUMO was predicted to have σ^* character and was mainly located on the central tertiary carbon atom (Fig. S27 in ESI†). In line with our results on

EA, the extent of its delocalization increased with the system size. To sum up, although the energetically low-lying C–F σ^* orbital doubtlessly plays an important role in fluorine chemistry (*e.g.*, through orbital mixing, as explained by Borden applying the second-order perturbation theory⁵⁶), it is improbable that mild reducing agents could initiate a radical cascade process of defluorination by direct electron transfer to the C–F σ^* orbital.

Although formation of radical centers on an ideal C_1F_1 layer was expected to be hampered by the low EA, the experimental evidence of observable spin concentrations in C_1F_1 structures clearly proves the presence of isolated sp^3 carbon sites. The origin of such centers depends largely on the preparation process. Recent experimental surface imaging techniques have shown that fluorination of CVD graphene with XeF_2 leads to formation of highly ordered sizable (150 nm) CF , C_2F chair and unfluorinated domains,⁶⁰ whereas fluorination with CF_4 plasma gives rise to inhomogeneous and disordered microscopic configurations.⁶¹ From a radical center formation point of view, in the former case, the carbon atoms at the boundary between these domains can remain unfluorinated as the attachment of fluorine on such sites would lead to a *cis* configurations, which would be energetically unfavorable.⁶² On the other hand, the inhomogeneous spatial distribution of fluorine on CVD graphene treated with CF_4 plasma is accompanied by formation of multilayer islands and structural features such as folds, wrinkles, and ripples that are less fluorinated, which consequently increases the probability of spin center emergence.

3.3 Electron affinities of radical centers

The presence of radical centers (even in very low concentrations) can obviously dramatically change the behavior of FG in the presence of reducing agents or nucleophilic species. As shown in Table S1 (see ESI†), the electron affinities of radical species derived from parent perfluorinated model systems are very high. For instance, AEA of a fluorinated coronene radical is $80.6 \text{ kcal mol}^{-1}$, *i.e.*, it is even larger than that of a fluorine atom ($78.4 \text{ kcal mol}^{-1}$). These extremely large values of EA of perfluorinated radicals are mainly due to the electron-withdrawing effect of highly electronegative fluorine atoms bound to the nearest carbon atoms but also increased delocalization of the negative charge with increasing size of the system. This delocalization is closely related to the presence of the already discussed C–F σ^* orbitals on neighboring carbons, which can stabilize the SOMO orbital in a pyramidal configuration of the radical center by mutual orbital mixing.^{56,63} The extraordinary oxidizing power of highly fluorinated organic radicals can initiate the defluorination process in the presence of even mild reducing agents. Therefore, we probed a possible scenario of initial phases of the cascade reduction of FG in which defluorination spreads outwards from a radical center (Fig. 2).

Although the total reaction enthalpies of the reduction steps depend on the strength of reducing agent as well as solvation enthalpies of the involved species, it can be seen that, in general, they are energetically favorable and polar solvents



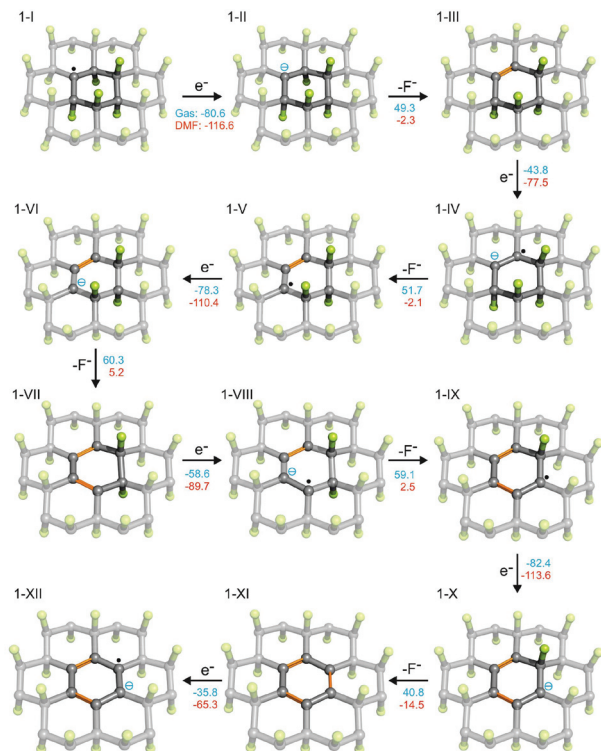


Fig. 2 Possible scenario for the initial phases of reduction of FG (the F atoms in green, the C atoms in grey/black, newly formed C=C bonds in orange). The reaction energies are given in kcal mol⁻¹ (blue in gas phase and red in DMF).

stabilize the charged intermediates. As expected, the oxidizing power of the radical species is much higher (by about a factor of 2) than that of closed-shell systems occurring in the reduction process. However, even for the latter, the EA is rather high as a consequence of the effect of highly polar C-F bonds on the neighboring carbon atoms. Note that EA of the final structure **1-IX**, which is fully π -conjugated, is significantly lower than that of the other structures. It is therefore possible that depending on the power of the reducing agent, the cascade defluorination process may cease after formation of larger π -conjugated domains. Finally, let us consider possible formation of fluorine radicals by charge transfer from fluoride anions to the radical center. Although the gas phase value of the EA of **1-I** is slightly larger than that of an F atom, the stability of a small fluoride anion is significantly increased in polar solvents (much more than **1-II**), and therefore formation of F radicals by this mechanism would be unfavorable. Let us also underline that our results for model systems well reproduce those obtained for larger systems and are also in good correspondence with periodic calculations (see section 2.5 in ESI†).

3.4 Radical defluorination mechanism in DMF

We have shown that radical centers on FG act as efficient electron acceptors. Although such electron transfer can be a trigger for cascade defluorination, in the case of a sufficiently strong reducing agent, it does not explain the defluorination

of FG observed in solvents with ionization potential in the liquid phase significantly higher than the EA of FG point defects. An example of such a solvent is DMF (discussed in section 3.1), which has an ionization potential in the liquid phase of 149 kcal mol⁻¹, compared to the EA of a radical center **1-I** of 117 kcal mol⁻¹ in the same solvent. Let us recall that electron affinities of the subsequent species are even smaller. Clearly, DMF can hardly be considered a direct reductant of FG in the sense of direct electron transfer to such radical centers.

To rationalize the observed spontaneous defluorination of FG in DMF, we suggest a mechanism initiated by hydrogen atom transfer from DMF to the FG radical center (Fig. 3). In

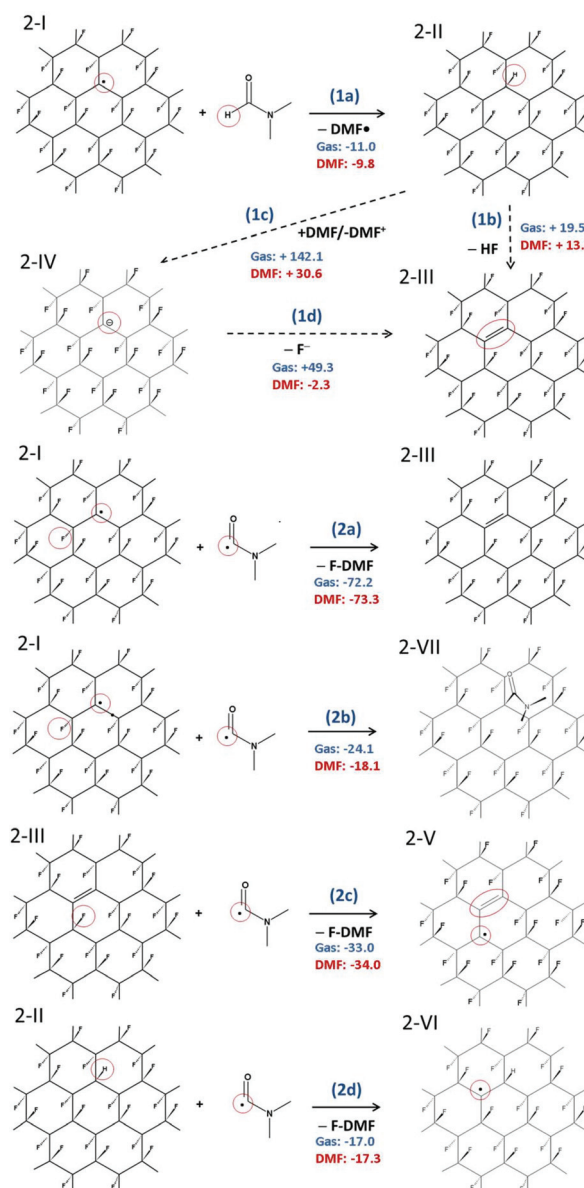


Fig. 3 Radical mechanism of defluorination of FG in DMF. (1a–c) Initial phases of defluorination. (2a–d) Re-creation of FG radical center. The reaction energies are given in kcal mol⁻¹.



this mechanism, the energetically favorable initiation step (1a) involves hydrogenation of a radical center and formation of a DMF[•] radical. In principle, a *cis* isomer of 2-II can also be formed, but the *trans* isomer is much more stable (by *ca.* 36 kcal mol⁻¹). In the next step, a HF molecule can possibly be released forming a double bond in 2-III by reaction (1b), although this step is energetically less favorable and may require some activation energy.

Nevertheless, the defluorinated structure 2-III can be formed *via* reaction (2a) of a DMF[•] radical with another FG radical, leading to formation of *N,N'*-dimethylcarbamoyl fluoride (F-DMF), which appears to be a significantly more favorable process than recombination of FG[•] and DMF[•] radicals by reaction (2b). Reactions (2c) and (2d) show possible ways of recreating radical centers, the former leading to a cascade (radical) defluorination process. Note that subtraction of fluorine atoms from the FG surface by organic radicals (namely 2,2,6,6-tetramethylpiperidine-1-oxyl) triggering the defluorination process, which is in line with the proposed steps, has very recently been observed by Lai *et al.*⁶⁴ Since it can be expected that the hydrogen atom in 2-II is moderately acidic due to the electron-withdrawing effect of fluorine atoms bound to the nearest carbons, we also considered the possibility of proton transfer to a DMF molecule (1c). Although the charged products are significantly stabilized in a polar environment compared to the gas phase, the reaction energy appears to be too large to accept this channel as a direct source of FG anions. However, taking into account the energetically advantageous release of the fluoride anion from 2-IV (*cf.* step 2 in Fig. 2), concerted transformation of 2-II to 2-III cannot be excluded under harsher conditions. Let us also underline that our model systems with fluorine atoms in the *trans* configuration represent the most stable (*i.e.* the least reactive) radical structures⁶⁵ and less stable structures (*e.g.* radical centers on deformed domains or edges) can enhance the defluorination process by providing even more favorable thermodynamic and kinetic conditions.

As the EPR spectra of FG in DMF confirmed the presence of biradical centers (besides monoradical sites) on the FG surface, we also studied a radical mechanism of defluorination starting from structure 3-I (Fig. 4), for which the theoretical distance between the spin centers (3.91 Å) was in reasonable

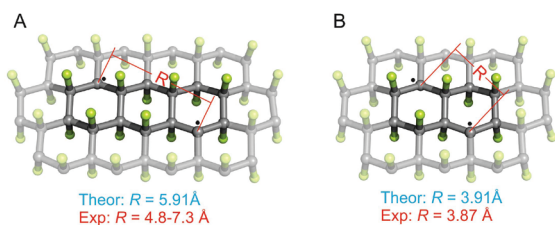


Fig. 4 Structure of biradical sites on FG surface: typical biradical present on the FG surface (A); biradical 3-I observed in the later phases of the defluorination process (B). The experimental distances were estimated from the analysis of EPR spectra (see section 3.1).

agreement with the experimentally derived value (3.87 Å). The energetics of the key reaction steps were very similar to those predicted for the monoradical case (see ESI, Fig. S29[†]). An important feature of this mechanism, which is in line with the experimental observations discussed in section 3.1, is the successive annihilation of the biradical centers. A critical step in this context appears to be reaction of 3-III with a DMF[•] radical, which could potentially lead to regeneration of biradicals (Fig. S29b[†]). Although such regeneration is energetically allowed, it is much less favorable than the formation of π -conjugated motifs (Fig. 5).

3.5 Evidence of DMF[•] radical entrapment

To validate the presence and chemical nature of the radical species (besides those residing on GrF) developing during the aging process of GrF in DMF, we employed the EPR technique in conjunction with spin-trapping experiments using α -4-pyridyl-1-oxide-*N-tert*-butylnitrone (POBN) as a chemical trapping agent (Fig. 6a). After addition of solid POBN to the GrF/DMF suspension, followed by incubation of these components at RT for 40 min, a large number of radical species were detected by EPR in the supernatant collected after centrifugation. The recorded solution EPR spectrum is shown in Fig. 6c and its frozen matrix in Fig. 6d. Additional EPR spectra are provided in the ESI (Fig. S14, S16 and S19[†]). The observed three-lines pattern (with $\sim 1 : 1 : 1$ intensity) shown in Fig. 6c is characteristic for nitroxide-radicals.^{66,67} The observed resonance envelope is here found very similar to that shown by TEMPO free radical (2,2,6,6-tetramethyl-piperidine 1-oxyl radical, ESI, Fig. S17[†]), and strongly suggests that the formed POBN radical adduct originated from entrapment of a tertiary-carbon radical, possibly the carbamoyl DMF[•] radical, with structure shown in Fig. 6b. Simulation of the EPR envelopes (Fig. 6c and d, red-line simulated spectra) with the WinEPR SimFonia software gave the following spin-Hamiltonian parameters: $g_{\text{iso}} = 2.0049$, $1A_{\text{N}} = 1.340$ mT (37.55 MHz), $1A_{\text{H}} = 0.172$ mT (4.82 MHz), $L_{\text{w}} = 0.210$ mT (5.88 MHz), Lorentzian/Gaussian ratio = 0.20 (Fig. 6c, red-line) and $g_{xx} = 2.0066$, $g_{yy} = 2.0059$, $g_{zz} = 2.0022$, $A(\text{N})_{xx} = 0.40$ mT (11.21 MHz), $A(\text{N})_{yy} = 0.50$ mT (14.01 MHz), $A(\text{N})_{zz} = 3.15$ mT (88.28 MHz), $L_{\text{w}(x,y,z)} = 0.70, 1.10, 0.80$ mT (19.6, 30.83, 22.42 MHz), Lorentzian/Gaussian ratio = 0.63 (spherical integration using theta, phi of 200 200, Fig. 6d, red-line).

The same trapped radical species by POBN was obtained when the GrF/DMF solution was aged for a longer time (1 day, 7 days), whereas negative results were consistently found for a

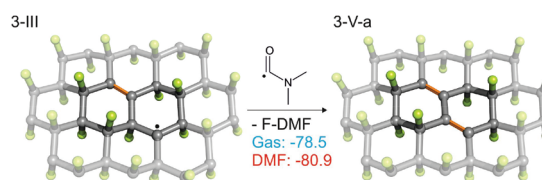


Fig. 5 Reaction of 3-III with a DMF[•] radical. For alternative (less favorable) reactions see Fig. S13b in ESI.[†]



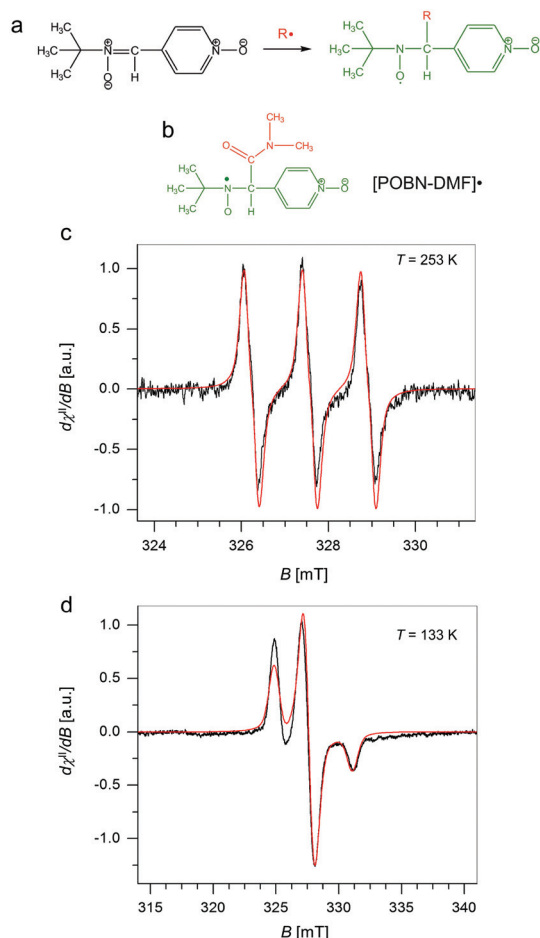


Fig. 6 (a) Scheme for the reaction of α -4-pyridyl-1-oxide-*N*-*tert*-butylnitrone (POBN) with free radicals to generate the corresponding spin-trapped nitroxide radical. (b) Chemical structure of a DMF radical trapped by POBN. (c) X-band EPR spectra obtained from spin-trap (POBN) experiments carried out on the supernatant from a GrF/DMF/POBN mixture ($T = 253$ K) together with its EPR simulation (red-trace), and (d) corresponding spectrum obtained in a frozen matrix ($T = 133$ K) compared with simulation (red-trace). Experimental parameters: 9.16–9.17 GHz frequency, 100 kHz modulation frequency, 30 ms time constant, 0.2 mT (c) or 0.8 mT (d) modulation width, 0.3 mW (d) or 4.0 mW (c) applied microwave power. Simulation parameters are given in the text.

GrF/benzene solution aged in the presence of POBN (see ESI, section 1.3, Fig. S13 \dagger). These findings suggest that DMF reacts with GrF *via* a radical mechanism. It is important to note that there is no clear report in literature of direct trapping of carbamoyl radical derived from DMF. However, in the recent study of cross-benzoin and Stetter-type reactions mediated by $KOtBu$ -DMF by Massi *et al.*, the authors observed generation of a weak EPR signal of difficult interpretation in the solution of $KOtBu$ -DMF in presence of spin-trap agent PBN, signal that became well resolved into a doublet of triplet upon addition of diaryl α -diketone.⁶⁸ The EPR signal encoded hyperfine splitting coupling constants similar to those observed here for the GrF/DMF/POBN trapped radical species, with $A_N = 1.33$ mT

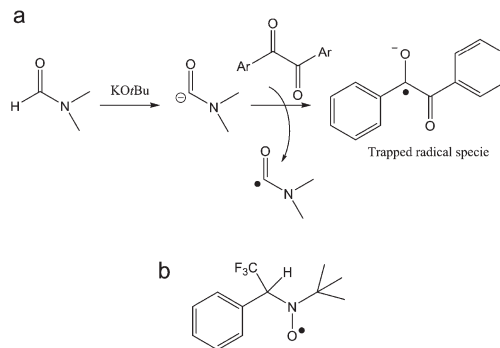


Fig. 7 (a) Possible pathway of the trapped benzyl anion radical by PBN during the cross-benzoin like reaction as adapted from ref. 68. (b) The trifluoromethyl-PBN radical adduct from ref. 69.

and $A_H = 0.177$ mT, which the authors attributed to the successful entrapment of benzyl anion radical by PBN (Fig. 7a, trapped radical species). Furthermore, Aggarwal *et al.*⁶⁹ recently reported the successful entrapment of a trifluoromethyl radical by PBN in DMF at 298 K (Fig. 7b), which exhibited $g = 2.0044$, $A_N = 1.411$ mT, $A_H = 0.1664$ mT, $A_F = 0.1781$ mT, hence, similar g_{iso} , A_N and A_H as found for the GrF/DMF/POBN trapped radical system. Thus, because our system contains only GrF, and the POBN radical adducts can be trapped in DMF but not in benzene, the generation of the carbamoyl-radical trapped by POBN (POBN-DMF radical) as shown in Fig. 6b, is plausible.

The use of other experimental setups, *e.g.*, GrF sonication, as often employed for its fast dispersion in organic solvents, leads to generation of an admixture of radical species due to the fast temperature gradients induced in the solution. Due to the number of other experimental variables to dissect (*e.g.* sonication time, power applied) such study will be devoted for future work. As an example of other EPR signatures detected following the sequence of a specific sonication-time/applied power conditions (30 min, 40 kHz applied power) for the GrF/DMF/POBN mixture is given in the ESI (Fig. S20–S24 \dagger). However, the present findings wish to stress the notion that radical defluorination reactions of GrF occurs even under mild conditions in DMF.

3.6 Evidence of *N,N'*-dimethylcarbamoyl fluoride

As can be seen in Fig. 3, *N,N'*-dimethylcarbamoyl fluoride (F-DMF) plays a key role in the proposed mechanism since its formation leads directly to defluorination and also generation of new radical centers. To confirm formation of F-DMF, we performed a series of ^{19}F NMR measurements on FG/DMF samples treated in different ways (see details in ESI \dagger). The first sample was sonicated for 2 hours at room temperature and stirred overnight. The day after, the suspension was still pale-grey, the color of the starting suspension. ^{19}F NMR analysis of the supernatant solution did not show the presence of any F-containing compounds. A second sample of FG/DMF was treated at 120 $^\circ\text{C}$ for 5 hours and then left stirring overnight at



room temperature. This time, the suspension appeared black, indicating that defluorination of FG had taken place. Using ^{19}F NMR, the supernatant liquid showed the presence of one peak at -26 ppm, which was attributed to F-DMF (Fig. 8a). Two more peaks, at -138 and -152 ppm, were also visible, which could be attributed to some soluble FG fragments (*cf.*, -135.85 , -162.45 ppm for 1,2,3-trifluorobenzene, and -139.93 , -157.07 ppm for 1,2,3,4-tetrafluorobenzene⁷⁰) or to a product of reaction of fluoride ions with borosilicate glass (*cf.*, -152.2 ppm for BF_4^- (ref. 71)). The peak at -26 ppm was confirmed to be due to the F-DMF compound by separately preparing F-DMF,^{36,72} whose ^{19}F NMR spectrum in DMF also consisted of a peak at -26 ppm (Fig. 8b). The stability of F-DMF under the experimental conditions was also assessed by adding an aliquot of the compound to a FG/DMF suspension heated at 120 °C for 5 hours and then stirred overnight. In this case, the supernatant liquid showed again the presence of the compound peak at -26 ppm (see ESI, Fig. S26†). Although it cannot be fully excluded that F-DMF can be produced by recombining DMF^\bullet and F^\bullet radicals (possibly formed during sonication process), the presence of the F-DMF peak in ^{19}F NMR spectrum supports our hypothesis that defluorination of FG in DMF results from the direct reaction between DMF^\bullet and FG. The requirement of higher temperature indicates that steps (2a, 2c, 2d) in the proposed mechanism require some activation energy.

Finally, we will briefly comment on recent experimental work by Wang *et al.*,³⁴ in which defluorination of FG in the presence of selected solvents was studied by various instrumental techniques, including XRD, FTIR, TEM, TGA and UV-

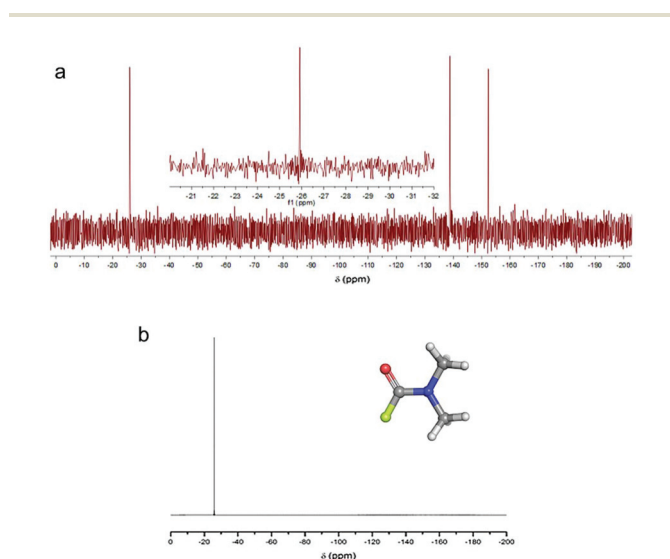


Fig. 8 (a) ^{19}F NMR spectrum (in DMF, 470 MHz) of the supernatant liquid obtained from a FG/DMF suspension heated at 120 °C for 5 hours and stirred at room temperature overnight (in the inset, a close-up of the peak at -26 ppm is shown). (b) ^{19}F NMR spectrum (in DMF, 470 MHz) of the separately prepared compound F-DMF (structure shown in inset). (b) ^{19}F NMR spectrum (in DMF, 470 MHz) of the separately prepared compound F-DMF (structure shown in inset).

vis reflectance spectroscopy. They found that highly polar (dipolar) solvents, including DMF, were able to facilitate the FG defluorination. They rationalized this capability in terms of high nucleophilicity, arguing that dipolar solvents can interact *via* dipole-dipole interactions with the electron-deficient carbon atom of a C-F bond, providing sufficient energy to rupture the C-F bond. To verify this hypothesis, we calculated the interaction energy of a DMF molecule with an ideal FG surface by using the implicit SMD model to account for the polar DMF environment (see ESI, Fig. S31†). Although the interaction energy was indeed found to be relatively high (4 kcal mol $^{-1}$) compared to ordinary weakly interacting systems, it was still far below the dissociation energy of a C-F bond (~ 100 kcal mol $^{-1}$ for fluorinated coronene). Therefore, although we agree that the nucleophilicity of the solvent plays an important role in the later phases of defluorination, we believe that the proposed radical mechanism supported by the experimental evidence of the DMF^\bullet radical is a more plausible explanation of the initial steps of the FG defluorination process occurring in DMF.

3.7 Consequences for the reactivity of FG

We have shown that, depending on the chemical composition of the sample, the presence of radical centers on FG can initiate two important processes. On the one hand, direct reduction of FG (*i.e.*, formation of anionic centers) can occur in the presence of mild reducing agents. On the other hand, a radical mechanism initiated by hydrogen atom transfer can take place provided that species sensitive to homolytic R-H bond dissociation are present in the environment. In both cases, a cascade defluorination process can commence, leading preferentially to compact motifs stabilized by π -conjugation of C=C double bonds. It can be expected that the defluorinated chains of carbons carrying partial positive charge due to surrounding C-F bonds will be highly sensitive to nucleophilic substitutions. In fact, the idea of competitive substitution and reductive defluorination has already been applied to account for experimental observations during the covalent functionalization of graphene based on reactions of FG with various nucleophilic agents, including OH^- ,²³ CN^- ,³¹ Grignard reagents³³ and others. In such reactions, the main indication of concurrent substitution and defluorination was

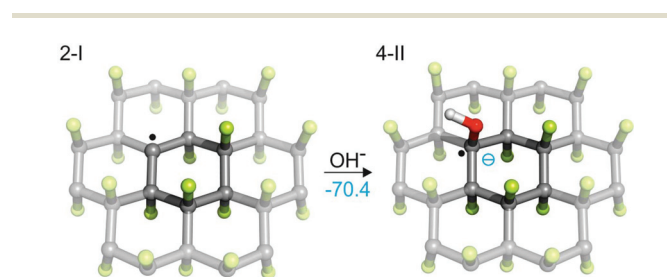


Fig. 9 Direct attack of a nucleophilic species (here OH^-) on a radical site is energetically very favorable (energy in kcal mol $^{-1}$ in the gas phase).



the composition of the resulting material, which showed only partial functionalization of graphene (e.g., ca. 15% in the case of G-CN) with negligible fluorine content. Nevertheless, the presence of radical centers in FG opens possibilities for direct attack of nucleophilic species on the radical site (Fig. 9). Such attacks could play an important role in the initiation of S_N reactions in solvents that are not able to trigger defluorination on their own (e.g., methanol, ethanol, chloroform). Our calculations showed that formation of a radical anion (**4-II**) is energetically highly favorable ($\Delta E = -70.4 \text{ kcal mol}^{-1}$ for the gas phase), which strongly supports the idea that early-phase defluorination can be caused by direct interaction of a nucleophile with a radical center.

Conclusions

Defluorination of FG is a complex process involving direct reduction, nucleophilic substitution or radical substitution reactions depending on the reductive and nucleophilic strengths of the solvent environment and/or presence of dissolved reactive agents. By combining DFT calculations with spectroscopic (EPR and NMR) studies, we have shown that it is the imperfectness of the FG sheets that induces its observed reactivity, distinguishing this 2D material from unreactive perfluorinated hydrocarbons, such as Teflon. The low-lying C-F σ^* orbitals in an ideal FG sheet could, in principle, render the structure susceptible to defluorination in the presence of strong reductants. However, it is improbable that mild reducing agents could initiate a cascade process of defluorination by direct electron transfer to the σ^* orbital. On the other hand, FG radical centers recorded by EPR measurements exhibit much higher electron affinities, making them ideal reactive sites for mild reducing agents and/or nucleophilic species. Nevertheless, even the relatively large electron acceptor strength of FG spin centers does not explain defluorination of FG in weakly reductive environments, such as DMF. In such cases, point defects can trigger a radical mechanism, provided that species sensitive to homolytic R-H bond dissociation are present in the environment. The proposed mechanism was supported by spin-trap experiments as well as ^{19}F NMR measurements, which suggested formation of DMF $^{\cdot}$ radicals under mild reaction conditions (room temperature, simple stirring) and formation of F-DMF (under harsher conditions such as prolonged heating at 120 °C). To sum up, it is clear that point defects play a key role in the reactivity of FG. Understanding relationships between the reductive/nucleophilic strengths of the environment, possible formation of free radicals and point defect redox characteristics seems to be crucial for achieving full control over the functionalization of FG.

Conflicts of interest

There are no conflicts to declare.

Acknowledgements

We acknowledge financial support from the Ministry of Education, Youth and Sports of the Czech Republic (grants LO1305, CZ.1.05/2.1.00/19.0377 and the Research Infrastructure NanoEnviCz: project no. LM2015073), the ERC (Consolidator grant 683024 from the European Union's Horizon 2020 research and innovation programme), and the Neuron fund. We also thank Martin Petr for measuring the XPS spectra and Martin Pykal for preparing the TOC.

References

- 1 K. S. Novoselov, A. K. Geim, S. V. Morozov, D. Jiang, Y. Zhang, S. V. Dubonos, I. V. Grigorieva and A. A. Firsov, *Science*, 2004, **306**, 666–669.
- 2 E. J. Duplock, M. Scheffler and P. J. D. Lindan, *Phys. Rev. Lett.*, 2004, **92**, 225502.
- 3 S. H. Cheng, K. Zou, F. Okino, H. R. Gutierrez, A. Gupta, N. Shen, P. C. Eklund, J. O. Sofo and J. Zhu, *Phys. Rev. B: Condens. Matter Mater. Phys.*, 2010, **81**, 205435.
- 4 D. C. Elias, R. R. Nair, T. M. G. Mohiuddin, S. V. Morozov, P. Blake, M. P. Halsall, A. C. Ferrari, D. W. Boukhvalov, M. I. Katsnelson, A. K. Geim and K. S. Novoselov, *Science*, 2009, **323**, 610–613.
- 5 L. G. Bulusheva, V. A. Tur, E. O. Fedorovskaya, I. P. Asanov, D. Pontiroli, M. Riccò and A. V. Okotrub, *Carbon*, 2014, **78**, 137–146.
- 6 A. Vizintin, M. Lozinsek, R. K. Chellappan, D. Foix, A. Krainc, G. Mali, G. Drazic, B. Genorio, R. Dedryvere and R. Dominko, *Chem. Mater.*, 2015, **27**, 7070–7081.
- 7 J. J. Xie, C. L. Li, Z. H. Cui and X. X. Guo, *Adv. Funct. Mater.*, 2015, **25**, 6519–6526.
- 8 V. Urbanova, F. Karlicky, A. Matej, F. Sembera, Z. Janousek, J. A. Perman, V. Ranc, K. Cepe, J. Michl, M. Otyepka and R. Zboril, *Nanoscale*, 2016, **8**, 12134–12142.
- 9 S.-Z. Liang, G. Chen, A. R. Harutyunyan, M. W. Cole and J. O. Sofo, *Appl. Phys. Lett.*, 2013, **103**, 233108.
- 10 S. Das, P. Sudhagar, V. Verma, D. Song, E. Ito, S. Y. Lee, Y. S. Kang and W. Choi, *Adv. Funct. Mater.*, 2011, **21**, 3729–3736.
- 11 L. Liao, H. L. Peng and Z. F. Liu, *J. Am. Chem. Soc.*, 2014, **136**, 12194–12200.
- 12 J. Park and M. D. Yan, *Acc. Chem. Res.*, 2013, **46**, 181–189.
- 13 S. P. Economopoulos, G. Rotas, Y. Miyata, H. Shinohara and N. Tagmatarchis, *ACS Nano*, 2010, **4**, 7499–7507.
- 14 J. M. Englert, C. Dotzer, G. A. Yang, M. Schmid, C. Papp, J. M. Gottfried, H. P. Steinruck, E. Spiecker, F. Hauke and A. Hirsch, *Nat. Chem.*, 2011, **3**, 279–286.
- 15 S. D. Bian, A. M. Scott, Y. Cao, Y. Liang, S. Osuna, K. N. Houk and A. B. Braunschweig, *J. Am. Chem. Soc.*, 2013, **135**, 9240–9243.
- 16 G. Dubey, R. Urcuyo, S. Abb, G. Rinke, M. Burghard, S. Rauschenbach and K. Kern, *J. Am. Chem. Soc.*, 2014, **136**, 13482–13485.



- 17 A. Y. S. Eng, C. K. Chua and M. Pumera, *Nanoscale*, 2015, **7**, 20256–20266.
- 18 S. Gilje, S. Han, M. Wang, K. L. Wang and R. B. Kaner, *Nano Lett.*, 2007, **7**, 3394–3398.
- 19 R. R. Nair, W. C. Ren, R. Jalil, I. Riaz, V. G. Kravets, L. Britnell, P. Blake, F. Schedin, A. S. Mayorov, S. J. Yuan, M. I. Katsnelson, H. M. Cheng, W. Strupinski, L. G. Bulusheva, A. V. Okotrub, I. V. Grigorieva, A. N. Grigorenko, K. S. Novoselov and A. K. Geim, *Small*, 2010, **6**, 2877–2884.
- 20 J. T. Robinson, J. S. Burgess, C. E. Junkermeier, S. C. Badescu, T. L. Reinecke, F. K. Perkins, M. K. Zalalutdniov, J. W. Baldwin, J. C. Culbertson, P. E. Sheehan and E. S. Snow, *Nano Lett.*, 2010, **10**, 3001–3005.
- 21 R. Zboril, F. Karlicky, A. B. Bourlinos, T. A. Steriotis, A. K. Stubos, V. Georgakilas, K. Safarova, D. Jancik, C. Trapalis and M. Otyepka, *Small*, 2010, **6**, 2885–2891.
- 22 K. A. Worsley, P. Ramesh, S. K. Mandal, S. Niyogi, M. E. Itkis and R. C. Haddon, *Chem. Phys. Lett.*, 2007, **445**, 51–56.
- 23 M. Dubecky, E. Otyepkova, P. Lazar, F. Karlicky, M. Petr, K. Cepe, P. Banas, R. Zboril and M. Otyepka, *J. Phys. Chem. Lett.*, 2015, **6**, 1430–1434.
- 24 P. Lazar, C. K. Chua, K. Hola, R. Zboril, M. Otyepka and M. Pumera, *Small*, 2015, **11**, 3790–3796.
- 25 V. Urbanova, K. Hola, A. B. Bourlinos, K. Cepe, A. Ambrosi, A. H. Loo, M. Pumera, F. Karlicky, M. Otyepka and R. Zboril, *Adv. Mater.*, 2015, **27**, 2305–2310.
- 26 K. E. Whitener, R. Stine, J. T. Robinson and P. E. Sheehan, *J. Phys. Chem. C*, 2015, **119**, 10507–10512.
- 27 R. Stine, J. W. Ciszek, D. E. Barlow, W. K. Lee, J. T. Robinson and P. E. Sheehan, *Langmuir*, 2012, **28**, 7957–7961.
- 28 C. Bosch-Navarro, M. Walker, N. R. Wilson and J. P. Rourke, *J. Mater. Chem. C*, 2015, **3**, 7627–7631.
- 29 B. Y. Li, T. J. He, Z. M. Wang, Z. Cheng, Y. Liu, T. Chen, W. C. Lai, X. Wang and X. Y. Liu, *Phys. Chem. Chem. Phys.*, 2016, **18**, 17495–17505.
- 30 X. Y. Ye, L. M. Ma, Z. G. Yang, J. Q. Wang, H. G. Wang and S. R. Yang, *ACS Appl. Mater. Interfaces*, 2016, **8**, 7483–7488.
- 31 A. Bakandritsos, M. Pykal, P. Blonski, P. Jakubec, D. D. Chronopoulos, K. Polakova, V. Georgakilas, K. Cepe, O. Tomanec, V. Ranc, A. B. Bourlinos, R. Zboril and M. Otyepka, *ACS Nano*, 2017, **11**, 2982–2991.
- 32 P. Kovaricek, Z. Bastl, V. Vales and M. Kalbac, *Chem. – Eur. J.*, 2016, **22**, 5404–5408.
- 33 D. D. Chronopoulos, A. Bakandritsos, P. Lazar, M. Pykal, K. Cepe, R. Zboril and M. Otyepka, *Chem. Mater.*, 2017, **29**, 926–930.
- 34 X. Wang, W. M. Wang, Y. Liu, M. M. Ren, H. N. Xiao and X. Y. Liu, *Phys. Chem. Chem. Phys.*, 2016, **18**, 3285–3293.
- 35 J. Tuček, K. Holá, A. B. Bourlinos, P. Błoński, A. Bakandritsos, J. Ugolotti, M. Dubecký, F. Karlický, V. Ranc, K. Čepe, M. Otyepka and R. Zbořil, *Nat. Commun.*, 2017, **8**, 14525.
- 36 J. Ichihara, T. Matsuo, T. Hanafusa and T. Ando, *J. Chem. Soc., Chem. Commun.*, 1986, 793–794.
- 37 J.-D. Chai and M. Head-Gordon, *Phys. Chem. Chem. Phys.*, 2008, **10**, 6615–6620.
- 38 R. Ditchfield, W. J. Hehre and J. A. Pople, *J. Chem. Phys.*, 1971, **54**, 724–728.
- 39 A. V. Marenich, C. J. Cramer and D. G. Truhlar, *J. Phys. Chem. B*, 2009, **113**, 6378–6396.
- 40 M. J. Frisch, G. W. Trucks, H. B. Schlegel, G. E. Scuseria, M. A. Robb, J. R. Cheeseman, G. Scalmani, V. Barone, B. Mennucci, G. A. Petersson, H. Nakatsuji, M. Caricato, X. Li, H. P. Hratchian, A. F. Izmaylov, J. Bloino, G. Zheng, J. L. Sonnenberg, M. Hada, M. Ehara, K. Toyota, R. Fukuda, J. Hasegawa, M. Ishida, T. Nakajima, Y. Honda, O. Kitao, H. Nakai, T. Vreven, J. A. Montgomery, J. E. Peralta, F. Ogliaro, M. Bearpark, J. J. Heyd, E. Brothers, K. N. Kudin, V. N. Staroverov, R. Kobayashi, J. Normand, K. Raghavachari, A. Rendell, J. C. Burant, S. S. Iyengar, J. Tomasi, M. Cossi, N. Rega, J. M. Millam, M. Klene, J. E. Knox, J. B. Cross, V. Bakken, C. Adamo, J. Jaramillo, R. Gomperts, R. E. Stratmann, O. Yazyev, A. J. Austin, R. Cammi, C. Pomelli, J. W. Ochterski, R. L. Martin, K. Morokuma, V. G. Zakrzewski, G. A. Voth, P. Salvador, J. J. Dannenberg, S. Dapprich, A. D. Daniels, O. Farkas, J. B. Foresman, J. V. Ortiz, J. Cioslowski and D. J. Fox, *Gaussian 09, Revision D.01*, Wallingford CT, 2009.
- 41 A. M. Panich, A. I. Shames and T. Nakajima, *J. Phys. Chem. Solids*, 2001, **62**, 959–964.
- 42 J. Giraudet, M. Dubois, A. Hamwi, W. E. E. Stone, P. Pirotte and F. Masin, *J. Phys. Chem. B*, 2005, **109**, 175–181.
- 43 R. Jain, M. B. Sponsler, F. D. Coms and D. A. Dougherty, *J. Am. Chem. Soc.*, 1988, **110**, 1356–1366.
- 44 C. Riplinger, J. P. Y. Kao, G. M. Rosen, V. Kathirvelu, G. R. Eaton, S. S. Eaton, A. Kutateladze and F. Neese, *J. Am. Chem. Soc.*, 2009, **131**, 10092–10106.
- 45 G. Zoppellaro, V. Enkelmann, A. Geies and M. Baumgarten, *Org. Lett.*, 2004, **6**, 4929–4932.
- 46 G. Zoppellaro, A. Geies, K. K. Andersson, V. Enkelmann and M. Baumgarten, *Eur. J. Org. Chem.*, 2008, 1431–1440.
- 47 R. R. Nair, M. Sepioni, I. L. Tsai, O. Lehtinen, J. Keinonen, A. V. Krasheninnikov, T. Thomson, A. K. Geim and I. V. Grigorieva, *Nat. Phys.*, 2012, **8**, 199–202.
- 48 J. J. Palacios, J. Fernández-Rossier and L. Brey, *Phys. Rev. B: Condens. Matter Mater. Phys.*, 2008, **77**, 195428.
- 49 E. H. Lieb, *Phys. Rev. Lett.*, 1989, **62**, 1201–1204.
- 50 J. Burdeniuc and R. H. Crabtree, *Science*, 1996, **271**, 340–341.
- 51 J. L. Kiplinger and T. G. Richmond, *Chem. Commun.*, 1996, 1115–1116.
- 52 J. L. Kiplinger and T. G. Richmond, *J. Am. Chem. Soc.*, 1996, **118**, 1805–1806.
- 53 J. Burdeniuc, P. E. M. Siegbahn and R. H. Crabtree, *New J. Chem.*, 1998, **22**, 503–510.
- 54 R. P. Hughes, T. LeHusebo, S. M. Maddock, A. L. Rheingold and I. A. Guzei, *J. Am. Chem. Soc.*, 1997, **119**, 10231–10232.
- 55 T. G. Richmond, *Angew. Chem., Int. Ed.*, 2000, **39**, 3241–3244.



- 56 W. T. Borden, *Chem. Commun.*, 1998, 1919–1925.
- 57 G. Sandford, *Tetrahedron*, 2003, **59**, 437–454.
- 58 F. Karlický and M. Otyepka, *J. Chem. Theory Comput.*, 2013, **9**, 4155–4164.
- 59 M. A. Ribas, A. K. Singh, P. B. Sorokin and B. I. Yakobson, *Nano Res.*, 2011, **4**, 143–152.
- 60 R. J. Kashtiban, M. A. Dyson, R. R. Nair, R. Zan, S. L. Wong, Q. Ramasse, A. K. Geim, U. Bangert and J. Sloan, *Nat. Commun.*, 2014, **5**, 4902.
- 61 B. Wang, J. J. Wang and J. Zhu, *ACS Nano*, 2014, **8**, 1862–1870.
- 62 A. M. Suarez, *Theory and Simulation of Atomic Hydrogen, Fluorine, and Oxygen on Graphene*, The Pennsylvania State University, 2012.
- 63 D. M. Lemal, *J. Org. Chem.*, 2004, **69**, 1–11.
- 64 W. Lai, D. Xu, X. Wang, Z. Wang, Y. Liu, X. Zhang, Y. Li and X. Liu, *Phys. Chem. Chem. Phys.*, 2017, **19**, 24076–24081.
- 65 D. K. Samarakoon, Z. Chen, C. Nicolas and X.-Q. Wang, *Small*, 2011, **7**, 965–969.
- 66 G. R. Buettner, *Free Radicals Biol. Med.*, 1987, **3**, 259–303.
- 67 G. M. K. Humphries and H. M. McConnell, Nitroxide Spin Labels, in *Methods in Experimental Physics*, ed. C. Marton, Academic Press, New York, 1982, vol. 20, pp. 53–122.
- 68 R. Ragno, A. Zaghi, G. Di Carmine, P. P. Giovannini, O. Bortolini, M. Fogagnolo, A. Molinari, A. Venturini and A. Massi, *Org. Biomol. Chem.*, 2016, **14**, 9823–9835.
- 69 Y. Wang, A. Noble, C. Sandford and V. K. Aggarwal, *Angew. Chem., Int. Ed.*, 2017, **56**, 1810–1814.
- 70 N. Y. Adonin, S. A. Prikhod'ko, V. V. Bardin and V. N. Parmon, *Mendeleev Commun.*, 2009, **19**, 260–262.
- 71 H. Fenton, I. S. Tidmarsh and M. D. Ward, *Dalton Trans.*, 2009, 4199–4207.
- 72 R. P. Singh and J. n. M. Shreeve, *Chem. Commun.*, 2001, 1196–1197.



C

2D Chemistry: Chemical Control
of Graphene Derivatization

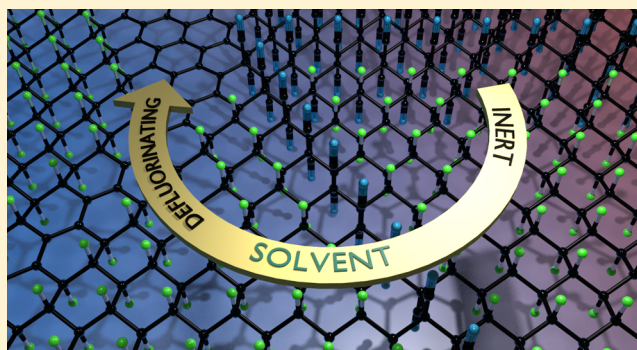
2D Chemistry: Chemical Control of Graphene Derivatization

Dagmar Matochová, Miroslav Medved',* Aristides Bakandritsos, Tomáš Steklý, Radek Zbořil, and Michal Otyepka*[✉]

Regional Centre of Advanced Technologies and Materials, Department of Physical Chemistry, Faculty of Science, Palacký University in Olomouc, 17. listopadu 1192/12, 771 46 Olomouc, Czech Republic

S Supporting Information

ABSTRACT: Controllable synthesis of graphene derivatives with defined composition and properties represents the holy grail of graphene chemistry, especially in view of the low reactivity of graphene. Recent progress in fluorographene (FG) chemistry has opened up new routes for synthesizing a plethora of graphene derivatives with widely applicable properties, but they are often difficult to control. We explored nucleophilic substitution on FG combining density functional theory calculations with experiments to achieve accurate control over the functionalization process. In-depth analysis revealed the complexity of the reaction and identified basic rules for controlling the 2D chemistry. Their application, that is, choice of solvent and reaction time, enabled facile control over the reaction of FG with *N*-octylamine to form graphene derivatives with tailored content of the alkylamine functional group (2.5–7.5% N atomic content) and F atoms (31.5–3.5% F atomic content). This work substantially extends prospects for the controlled covalent functionalization of graphene.



derivatives with tailored content of the alkylamine functional group (2.5–7.5% N atomic content) and F atoms (31.5–3.5% F atomic content). This work substantially extends prospects for the controlled covalent functionalization of graphene.

The controllable functionalization of graphene is undoubtedly one of the most ambitious goals in current 2D material chemistry.^{1–9} Unfortunately, graphene is rather unreactive;^{10–13} therefore, direct functionalization usually leads to a low degree of functionalization^{14–16} and requires harsh reaction conditions, negatively affecting the structure and composition of the resulting derivatives.^{17–20} On the contrary, fluorographene (FG)^{21–24} is an attractive precursor for synthesizing numerous graphene derivatives with well-defined structure and stoichiometry, for example, graphane,²⁵ aminographanes,^{26–30} cyanographene,³¹ graphene acid,³¹ sulphydryl derivatives,³² hydroxyl derivatives,³³ and alkylated graphenes.^{34,35} Graphane (i.e., hydrogenated graphene) was found to be a promising 2D material, extending the functionalization strategies by taking advantage of the presence of weaker (compared to FG) and almost nonpolar C–H bonds.^{36–38} However, to achieve full control over graphene derivatives prepared from FG, it is necessary to understand the reaction mechanisms at the microscopic level. The main factor that needs to be taken into account is the high bond dissociation energy (BDE) of the C–F bonds,³⁹ which disfavors reactions involving their direct cleavage.⁴⁰ The first attempt to rationalize the observed reaction of FG with nucleophile (Nu) species proposed a bimolecular nucleophilic substitution (S_N2) mechanism, in which the penalty for cleavage of the C–F bond is repaid by simultaneous formation of a new C–Nu bond.⁴⁰ It was also suggested that low-lying C–F σ^* orbitals and radical defects of FG may be involved in the process.^{39,41–43} Recent work⁴⁴ elucidated possible pathways of

FG defluorination, which occurs simultaneously with substitution, and addressed the role of solvent. However, despite progress in this field, no conclusive mechanism of FG reactivity has been achieved.

In the present work, we analyzed the full path of the S_N2 reaction of FG with Nu species, focusing on the solvent effects and possible activation of the C–F bond by electron transfer from a Nu. We also considered possible nucleophilic attack on FG radical defects, which have strong electrophilic character.⁴⁴ We showed that the different thermodynamic and kinetic parameters of individual reactions steps, their dependence on solvent characteristics, and also the active role of solvent can be used to control possible pathways. We applied the ω B97X-D method⁴⁵ with the 6-31++G(d,p) basis set. The solvent effects were included by using the universal continuum solvation model based on solute electron density (SMD).⁴⁶ Further computational details can be found in the [Supporting Information](#). We experimentally tested the suggested principles on the reaction of FG with *N*-octylamine (OA) and proved (by IR, XPS, TEM, and Raman spectroscopy) that the final composition of FG derivatives can be controlled by changing the solvent and reaction time.

We probed the S_N2 mechanism considering three Nu species (OH^- , NH_2^- , and CN^-) differing in their nucleophilicity, the ability to form hydrogen bonds with fluorine atoms on FG, and

Received: May 22, 2018

Accepted: June 11, 2018

Published: June 11, 2018



the strength of the C–Nu bond formed by the reaction. It should be noted that OH^- and CN^- have previously been shown to successfully react with FG.^{31,40} Besides gas-phase reaction, we also considered four solvents commonly used in syntheses of graphene derivatives from FG,^{31,32,34,40} that is, tetrahydrofuran (THF), acetone, methanol and *N,N*-dimethylformamide (DMF). Among them, THF is the least polar and inert with respect to FG. Acetone can promote the reduction of FG⁴⁷ and has been used as a solvent in the reaction of FG with NaOH.⁴⁰ Polar protic solvents like methanol can form hydrogen bonds with FG and do not promote the rupture of C–F bonds.^{48,49} Finally, DMF causes defluorination, which can be initiated via hydrogen transfer to radical sites on FG.⁴⁴

Energy profiles of the $\text{S}_{\text{N}}2$ reaction of FG with Nu^- in the gas phase were found to significantly differ from those in solvents (Figure 1). Stabilization of the reactants, that is, small

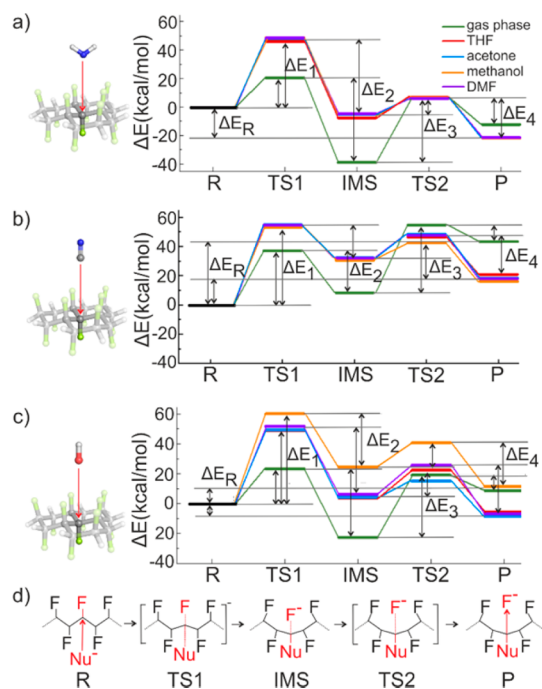


Figure 1. Reaction profiles of the $\text{S}_{\text{N}}2$ reaction of fluorographene (a) NH_2^- , (b) CN^- , and (c) OH^- in different solvents obtained at the $\omega\text{B97X-D/6-31++G(d,p)/SMD}$ level of theory. (d) Reaction scheme. Carbon atoms, gray; fluorine, green; nitrogen, blue; oxygen, red; hydrogen, white.

anions, in polar environments caused an increase in the energy barrier to ~ 50 kcal·mol⁻¹, whereas in the gas phase, it was significantly lower (~ 20 kcal·mol⁻¹ for OH^- and NH_2^- and 37 kcal·mol⁻¹ for CN^-). After the first transition state (TS1), the reaction proceeded through an intermediate state (IMS), where the departing F^- remains trapped between carbon atoms and neighboring fluorine atoms carrying partial negative charge. To release these F^- , the system must overcome another energy barrier (TS2) ranging from 10 to 20 kcal·mol⁻¹ in solvent to reach the final state (P). The product of CN^- attack was less stable than those of OH^- and NH_2^- due to their different nucleophilicity (the natural bond orbital (NBO) partial charge on the carbon atom of CN^- is -0.2 e, whereas the charges on oxygen/nitrogen atoms of $\text{OH}^-/\text{NH}_2^-$ are -1.4 e and -1.6 e, respectively) and the ability of OH^- and NH_2^- to form hydrogen bonds with neighboring fluorine atoms. In

the reaction of FG with OH^- in methanol, the protic solvent caused an overall increase in the energy profile. This can be rationalized by the formation of strong hydrogen bonds between the hydroxide anion and methanol, leading to a higher solvation energy of OH^- (92.8 kcal·mol⁻¹) compared with NH_2^- (78.0 kcal·mol⁻¹) and CN^- (63.1 kcal·mol⁻¹).

The presented calculations indicate that the $\text{S}_{\text{N}}2$ reaction mechanism cannot fully explain the reaction of FG with nucleophiles. Even for strong nucleophiles, such as OH^- or NH_2^- , the calculated barriers of Walden inversion are too high, in contradiction with the experimentally determined activation barrier of the FG reaction with NaOH in acetone (14 ± 5 kcal·mol⁻¹).⁴⁰ Lai et al.⁵⁰ suggested that the defluorination of FG may start by single electron transfer (SET) from a nucleophile to FG, followed by rupture of the C–F bond and creation of a radical site on the carbon atom. Although it has been suggested that C–F σ^* orbitals in perfluorinated polycyclic hydrocarbons can act as electron acceptors,^{39,41–43} the electron affinity of FG is too low (~ 4 kcal·mol⁻¹) to explain the sensitivity of FG to reduction in the presence of mild reducing agents.⁴⁴ Considering that the ionization potential of OH^- is 38.7 kcal·mol⁻¹, the suggested SET mechanism does not seem to be plausible (see Table S7 in the SI).

Recent studies showed that radical defects exist in FG with enough concentration (of 1 defect per 1000 carbon atoms) to trigger the FG reactivity.⁴⁴ The graph of reaction energies in Figure 2a shows that nucleophilic attack on radical sites existing on pristine FG⁴⁴ was energetically favorable in all environments. A polar solvent environment generally caused a decrease in the released energy due to stabilization of the negatively charged Nu species. The amide anion had the largest affinity to FG ($\Delta E = -60$ kcal·mol⁻¹ in solvent) owing to its high nucleophilicity and also the formation of a hydrogen bond between the $-\text{NH}_2$ group and released F^- (structure Ia in Figure S4). On the contrary, ΔE for CN^- was only about -10 kcal·mol⁻¹. As for $\text{S}_{\text{N}}2$ reaction on pristine FG, the stabilization of OH^- in methanol led to a smaller ΔE compared with other solvents. In comparison to the $\text{S}_{\text{N}}2$ mechanism, the reaction barriers of Nu attack on an FG radical center were much smaller (in DMF, 21 kcal·mol⁻¹ for NH_2^- , almost 8 kcal·mol⁻¹ for CN^- , and ca. 15 kcal·mol⁻¹ for OH^- ; see Figure 3). In the case of OH^- , the estimated barrier was in good agreement with the experimental value (14 ± 5 kcal·mol⁻¹).⁴⁰

Because the Nu species contributes a negative charge to FG, the neighboring C–F bonds become susceptible to heterolytic cleavage, releasing fluoride anions to the environment (Figure 2b). In all cases, cleavage of a C–F bond on carbon in the ortho position was preferred. Although release of F^- in the gas phase is inconvenient, stabilization of F^- in a polar environment makes the process favorable (with low activation energies; Figure 3 and Figure S5), especially in the case of OH^- and CN^- . Even for NH_2^- , the required energy was low in the polar solvent, suggesting that the release of F^- can occur at room temperature. The newly created radical center after F^- detachment can be attacked by another nucleophile. Figure 2c shows that this reaction is also energetically favorable in all environments and follows similar trends as the first attack.

Our results show that the radical centers on FG may play multiple roles in the reactivity of the material, as (i) electron acceptors (in the presence of a sufficiently strong reducing agent),^{44,50} (ii) triggering points for radical defluorination (if sufficiently stable radicals can be formed),⁴⁴ or (iii) electro-

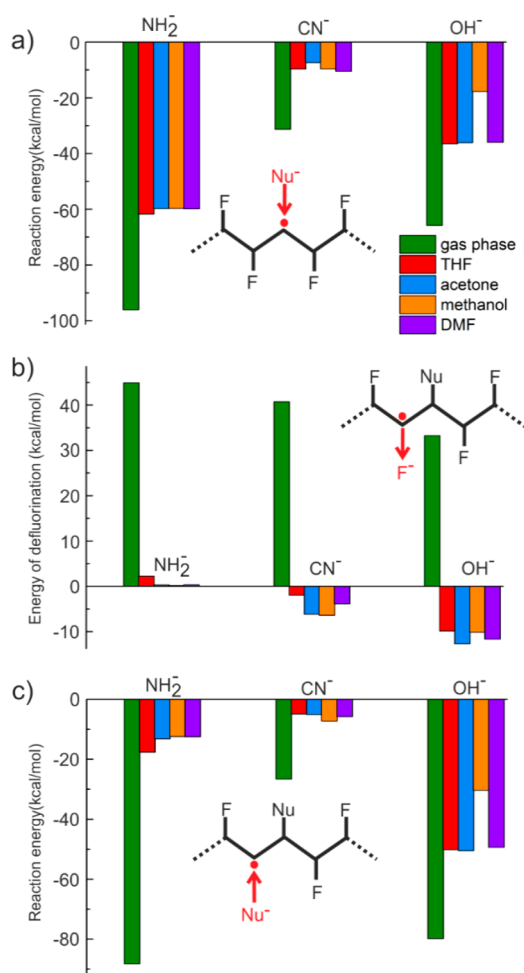


Figure 2. (a) Reaction energies for nucleophilic attack on a radical site of FG. (b) Energies of heterolytic dissociation of the C–F bond neighboring the C–Nu bond. (c) Reaction energies of the second nucleophilic attack on the radical center.

philic centers for nucleophilic attack (Scheme 1). Scheme 1 shows that whereas paths A and B lead to partial or complete defluorination, path C results in substitution. All three pathways can occur concurrently. However, the different kinetic and thermodynamic parameters of individual steps and their dependence on solvent characteristics enable control over the processes of defluorination and substitution. For instance, reaction of FG with a nucleophilic agent (e.g., NaCN) in an inert solvent (e.g., methanol) under mild conditions should preferentially proceed via path C, resulting in a high content of sp^3 carbon atoms in the lattice, whereas the degree of substitution (CN/F ratio) could be controlled by the reaction time. Use of the same nucleophile in a defluorinating solvent (e.g., DMF) leads to Gr-CN with very low content of fluorine, as reported in ref 31. Another option could be to control the topology of functionalization. Namely, instead of using a nucleophile in reducing solvent, as in the previous case, one could start with the reducing phase (without Nu), during which sp^2 carbon domains would be preferentially formed in the lattice, and then a Nu would be added afterward.

To demonstrate the potential for controlling FG reactivity, we used an amine-group-bearing compound (*N*-octylamine) as a nucleophile and carried out the reaction in two types of solvents (*o*-dichlorobenzene (*o*-DCB) and DMF) using

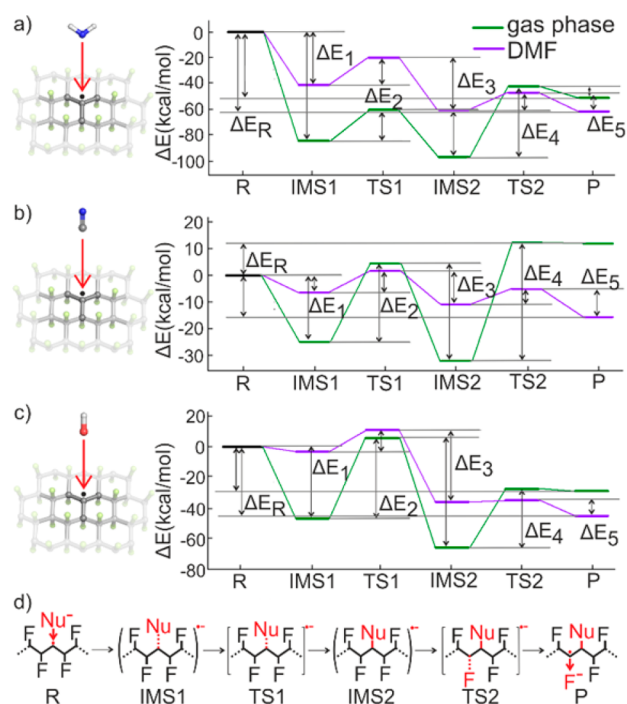
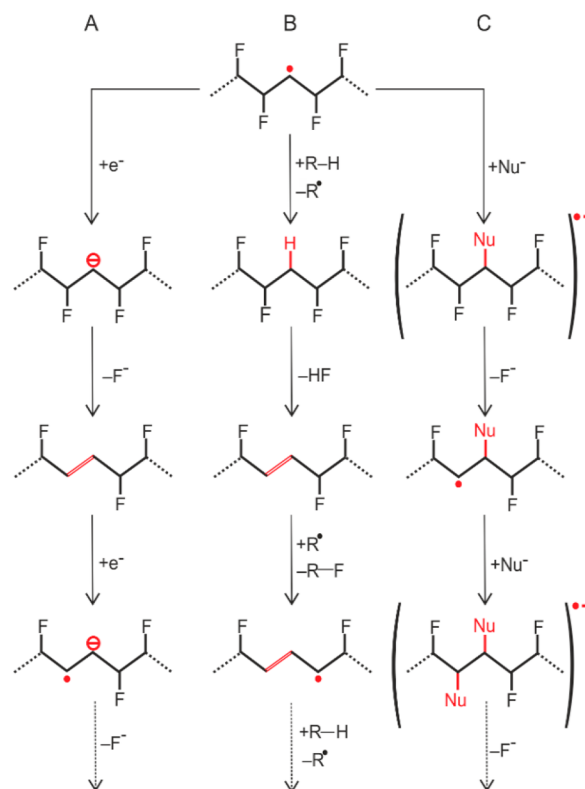


Figure 3. Reaction profiles for nucleophilic attack of (a) NH₂⁻, (b) CN⁻, and (c) OH⁻ on a FG radical site, followed by release of F⁻ from the neighboring carbon atom. (d) Reaction scheme. Carbon atoms, gray; fluorine, green; nitrogen, blue; oxygen, red; and hydrogen, white.

Scheme 1. Possible Reaction Pathways of Defluorination and Nucleophilic Substitution Starting on FG Radical Centers: (A) Electron Transfer, (B) Hydrogen Transfer, and (C) Nucleophilic Attack



variable reaction time. *o*-DCB was chosen as an inert, that is, nondefluorinating solvent (see the SI), unlike DMF. The progress of reaction of FG with OA significantly differed in the two solvents. In the case of DMF, the reaction proceeded quickly. Within 20 min, the purified FG derivative displayed intense C–H stretching vibrations originating from the attachment of OA aliphatic chains (Figure 4a). After 6 h, the

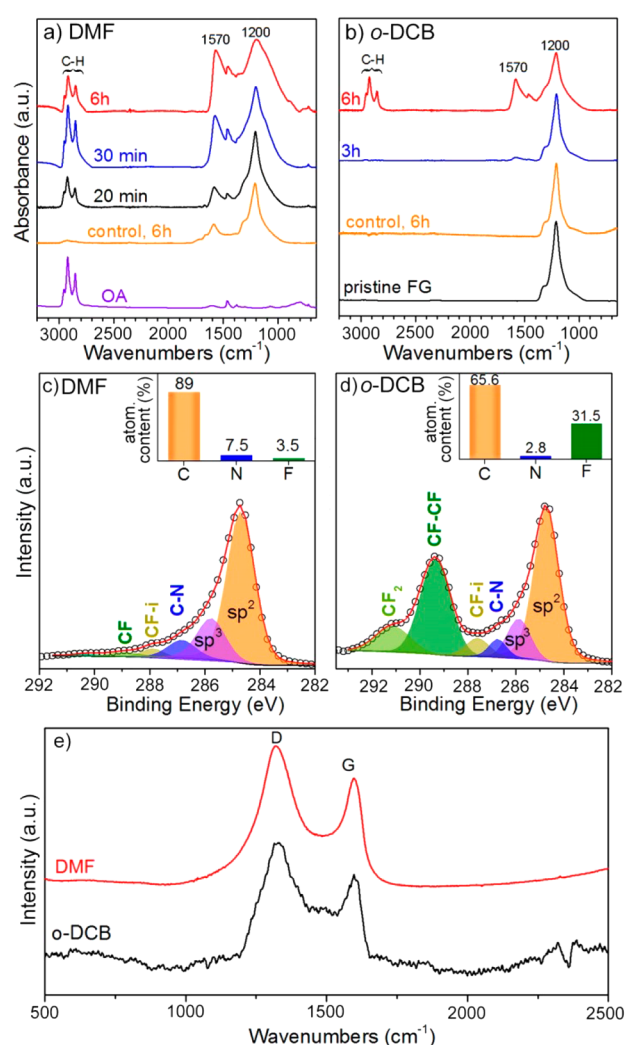


Figure 4. FT-IR spectra of graphene–octylamine derivatives after reaction in (a) DMF and (b) *o*-DCB, along with spectra of pristine octylamine, graphene, and products from control reactions. C 1s HR-XPS spectra and atomic analysis results (insets) of the graphene–octylamine derivatives after reaction in (c) DMF and (d) *o*-DCB. (e) Raman spectra of the *N*-octylamine-functionalized FG derivatives after 6 h of reaction in the two solvents.

sp^2 band in XPS visibly increased, and almost complete defluorination (3.5 at % of F, Figure 4c) occurred. In the case of *o*-DCB, after 6 h of reaction, a C–H stretching vibration band appeared, but the C–F band was still prominent (Figure 4b) and the F content remained high at 31.5 at % (Figure 4d). The nitrogen content also differed considerably (7.5 and 3.8 at % for DMF and *o*-DCB, respectively), corroborating the previous results. Slower kinetics of the reaction in *o*-DCB is in line with the higher activation barrier predicted by the DFT calculations (Figure S6). According to the N content (after subtraction of the N content measured in control reactions,

Table S9), the functionalization degree was calculated as 11.4 and 6.5% for the derivatives prepared in DMF and *o*-DCB, respectively. Apart from the very low F content in the 6 h derivative in DMF, after 20 and 30 min, the F/N atomic content could be further controlled at 21.5:3.7% and 14:5.4%, respectively. The Raman spectra of the 6 h products displayed high I_D/I_G ratios (ca. 1.3 and 1.4 for DMF and *o*-DCB samples, respectively), which, along with the band broadening, indicated high functionalization degree⁵¹ (Figure 4e). Finally, chemical mapping with energy-dispersive X-ray spectroscopy in STEM showed the homogeneous incorporation of N (thus OA) in the flakes, suggesting the production of similarly homogeneous OA-functionalized graphene derivatives (Figure S7). These results clearly demonstrate that the composition of functionalized graphenes prepared by FG chemistry can be controlled by varying the solvent and reaction time, opening new doors for fine-tuning the properties of graphene derivatives.

■ ASSOCIATED CONTENT

📄 Supporting Information

The Supporting Information is available free of charge on the ACS Publications website at DOI: 10.1021/acs.jpcllett.8b01596.

Further computational details, assessments of model size, basis set, and method, and theoretical and experimental data on the reaction of butylamine with FG (PDF)

■ AUTHOR INFORMATION

Corresponding Authors

*M.M.: E-mail: Miroslav.Medved@upol.cz.

*M.O.: E-mail: Michal.Otyepka@upol.cz.

ORCID

Michal Otyepka: 0000-0002-1066-5677

Notes

The authors declare no competing financial interest.

■ ACKNOWLEDGMENTS

We gratefully acknowledge financial support from the Ministry of Education, Youth and Sports of the Czech Republic (LO1305 and CZ.1.05/2.1.00/19.0377 and the Research Infrastructure NanoEnvicZ: project no. LM2015073), the European Research Council (ERC Consolidator grant 683024 from the European Union's Horizon 2020 Research and Innovation Programme), and the Operational Programme Research, Development and Education – European Regional Development Fund, project no. CZ.02.1.01/0.0/0.0/16_019/0000754. D.M. acknowledges support from the Palacký University in Olomouc (IGA PrF_2018_015). We thank J. Stráská for TEM measurements.

■ REFERENCES

- (1) Thakur, V. J.; Thakur, M. K. *Chemical Functionalization of Carbon Nanomaterials: Chemistry and Applications*; CRC Press: Boca Raton, FL, 2018.
- (2) Pumera, M.; Sofer, Z. Towards stoichiometric analogues of graphene: graphane, fluorographene, graphol, graphene acid and others. *Chem. Soc. Rev.* **2017**, *46*, 4450–4463.
- (3) Bueno, R. A.; Martinez, J. I.; Luccas, R. F.; del Arbol, N. R.; Munuera, C.; Palacio, I.; Palomares, F. J.; Lauwaet, K.; Thakur, S.; Baranowski, J. M.; Strupinski, W.; Lopez, M. F.; Mompean, F.; Garcia-

Hernandez, M.; Martin-Gago, J. A. Highly selective covalent organic functionalization of epitaxial graphene. *Nat. Commun.* **2017**, *8*, 15306.

(4) Georgakilas, V. *Functionalization of Graphene*; Wiley-VCH: Weinheim, Germany, 2014.

(5) Criado, A.; Melchionna, M.; Marchesan, S.; Prato, M. The Covalent Functionalization of Graphene on Substrates. *Angew. Chem., Int. Ed.* **2015**, *54*, 10734–10750.

(6) Eigler, S.; Hirsch, A. Chemistry with Graphene and Graphene Oxide—Challenges for Synthetic Chemists. *Angew. Chem., Int. Ed.* **2014**, *53*, 7720–7738.

(7) Chaban, V. V.; Prezhdo, O. V. Synergistic Amination of Graphene: Molecular Dynamics and Thermodynamics. *J. Phys. Chem. Lett.* **2015**, *6*, 4397–4403.

(8) Sturala, J.; Luxa, J.; Pumera, M.; Sofer, Z. Chemistry of Graphene Derivatives: Synthesis, Applications, and Perspectives. *Chem. - Eur. J.* **2018**, *24*, 5992–6006.

(9) Englert, J. M.; Dotzer, C.; Yang, G. A.; Schmid, M.; Papp, C.; Gottfried, J. M.; Steinruck, H. P.; Spiecker, E.; Hauke, F.; Hirsch, A. Covalent bulk functionalization of graphene. *Nat. Chem.* **2011**, *3*, 279–286.

(10) Liao, L.; Peng, H. L.; Liu, Z. F. Chemistry Makes Graphene beyond Graphene. *J. Am. Chem. Soc.* **2014**, *136*, 12194–12200.

(11) Park, J.; Yan, M. D. Covalent Functionalization of Graphene with Reactive Intermediates. *Acc. Chem. Res.* **2013**, *46*, 181–189.

(12) Holzwarth, J.; Amsharov, K. Y.; Sharapa, D. I.; Reger, D.; Roshchyna, K.; Lungerich, D.; Jux, N.; Hauke, F.; Clark, T.; Hirsch, A. Highly Regioselective Alkylation of Hexabenzocoronenes: Fundamental Insights into the Covalent Chemistry of Graphene. *Angew. Chem., Int. Ed.* **2017**, *56*, 12184–12190.

(13) Sun, Z. Z.; James, D. K.; Tour, J. M. Graphene Chemistry: Synthesis and Manipulation. *J. Phys. Chem. Lett.* **2011**, *2*, 2425–2432.

(14) Economopoulos, S. P.; Rotas, G.; Miyata, Y.; Shinohara, H.; Tagmatarchis, N. Exfoliation and Chemical Modification Using Microwave Irradiation Affording Highly Functionalized Graphene. *ACS Nano* **2010**, *4*, 7499–7507.

(15) Bian, S.; Scott, A. M.; Cao, Y.; Liang, Y.; Osuna, S.; Houk, K. N.; Braunschweig, A. B. Covalently Patterned Graphene Surfaces by a Force-Accelerated Diels–Alder Reaction. *J. Am. Chem. Soc.* **2013**, *135*, 9240–9243.

(16) Dubey, G.; Urcuyo, R.; Abb, S.; Rinke, G.; Burghard, M.; Rauschenbach, S.; Kern, K. Chemical Modification of Graphene via Hyperthermal Molecular Reaction. *J. Am. Chem. Soc.* **2014**, *136*, 13482–13485.

(17) Eng, A. Y. S.; Chua, C. K.; Pumera, M. Refinements to the structure of graphite oxide: absolute quantification of functional groups via selective labelling. *Nanoscale* **2015**, *7*, 20256–20266.

(18) Gilje, S.; Han, S.; Wang, M.; Wang, K. L.; Kaner, R. B. A Chemical Route to Graphene for Device Applications. *Nano Lett.* **2007**, *7*, 3394–3398.

(19) Mazanek, V.; Jankovsky, O.; Luxa, J.; Sedmidubsky, D.; Janousek, Z.; Sembera, F.; Mikulics, M.; Sofer, Z. Tuning of fluorine content in graphene: towards large-scale production of stoichiometric fluorographene. *Nanoscale* **2015**, *7*, 13646–13655.

(20) Collins, W. R.; Lewandowski, W.; Schmois, E.; Walsh, J.; Swager, T. M. Claisen Rearrangement of Graphite Oxide: A Route to Covalently Functionalized Graphenes. *Angew. Chem., Int. Ed.* **2011**, *50*, 8848–8852.

(21) Nair, R. R.; Ren, W. C.; Jalil, R.; Riaz, I.; Kravets, V. G.; Britnell, L.; Blake, P.; Schedin, F.; Mayorov, A. S.; Yuan, S. J.; Katsnelson, M. I.; Cheng, H. M.; Strupinski, W.; Bulusheva, L. G.; Okotrub, A. V.; Grigorieva, I. V.; Grigorenko, A. N.; Novoselov, K. S.; Geim, A. K. Fluorographene: A Two-Dimensional Counterpart of Teflon. *Small* **2010**, *6*, 2877–2884.

(22) Robinson, J. T.; Burgess, J. S.; Junkermeier, C. E.; Badescu, S. C.; Reinecke, T. L.; Perkins, F. K.; Zalalutdniov, M. K.; Baldwin, J. W.; Culbertson, J. C.; Sheehan, P. E.; Snow, E. S. Properties of Fluorinated Graphene Films. *Nano Lett.* **2010**, *10*, 3001–3005.

(23) Zbořil, R.; Karlický, F.; Bourlinos, A. B.; Steriotis, T. A.; Stubos, A. K.; Georgakilas, V.; Šafářová, K.; Jančík, D.; Trapalis, C.; Otyepka,

M. Graphene Fluoride: A Stable Stoichiometric Graphene Derivative and its Chemical Conversion to Graphene. *Small* **2010**, *6*, 2885–2891.

(24) Chronopoulos, D. D.; Bakandritsos, A.; Pykal, M.; Zbořil, R.; Otyepka, M. Chemistry, properties, and applications of fluorographene. *Appl. Mater. Today* **2017**, *9*, 60–70.

(25) Eng, A. Y. S.; Sofer, Z.; Bouša, D.; Sedmidubský, D.; Huber, Š.; Pumera, M. Near-Stoichiometric Bulk Graphene from Halogenated Graphenes (X = Cl/Br/I) by the Birch Reduction for High Density Energy Storage. *Adv. Funct. Mater.* **2017**, *27*, 1605797–1605805.

(26) Whitener, K. E.; Stine, R.; Robinson, J. T.; Sheehan, P. E. Graphene as Electrophile: Reactions of Graphene Fluoride. *J. Phys. Chem. C* **2015**, *119*, 10507–10512.

(27) Stine, R.; Ciszek, J. W.; Barlow, D. E.; Lee, W.-K.; Robinson, J. T.; Sheehan, P. E. High-Density Amine-Terminated Monolayers Formed on Fluorinated CVD-Grown Graphene. *Langmuir* **2012**, *28*, 7957–7961.

(28) Bosch-Navarro, C.; Walker, M.; Wilson, N. R.; Rourke, J. P. Covalent modification of exfoliated fluorographite with nitrogen functionalities. *J. Mater. Chem. C* **2015**, *3*, 7627–7631.

(29) Li, B.; He, T.; Wang, Z.; Cheng, Z.; Liu, Y.; Chen, T.; Lai, W.; Wang, X.; Liu, X. Chemical reactivity of C-F bonds attached to graphene with diamines depending on their nature and location. *Phys. Chem. Chem. Phys.* **2016**, *18*, 17495–17505.

(30) Ye, X.; Ma, L.; Yang, Z.; Wang, J.; Wang, H.; Yang, S. Covalent Functionalization of Fluorinated Graphene and Subsequent Application as Water-based Lubricant Additive. *ACS Appl. Mater. Interfaces* **2016**, *8*, 7483–7488.

(31) Bakandritsos, A.; Pykal, M.; Blonski, P.; Jakubec, P.; Chronopoulos, D. D.; Polakova, K.; Georgakilas, V.; Cepe, K.; Tomanec, O.; Ranc, V.; Bourlinos, A. B.; Zboril, R.; Otyepka, M. Cyanographene and Graphene Acid: Emerging Derivatives Enabling High-Yield and Selective Functionalization of Graphene. *ACS Nano* **2017**, *11*, 2982–2991.

(32) Urbanova, V.; Hola, K.; Bourlinos, A. B.; Cepe, K.; Ambrosi, A.; Loo, A. H.; Pumera, M.; Karlický, F.; Otyepka, M.; Zboril, R. Thiofluorographene-Hydrophilic Graphene Derivative with Semiconducting and Genosensing Properties. *Adv. Mater.* **2015**, *27*, 2305–2310.

(33) Tucek, J.; Hola, K.; Bourlinos, A. B.; Blonski, P.; Bakandritsos, A.; Ugolotti, J.; Dubecky, M.; Karlický, F.; Ranc, V.; Cepe, K.; Otyepka, M.; Zboril, R. Room temperature organic magnets derived from sp³ functionalized graphene. *Nat. Commun.* **2017**, *8*, 14525–14533.

(34) Chronopoulos, D. D.; Bakandritsos, A.; Lazar, P.; Pykal, M.; Čepe, K.; Zbořil, R.; Otyepka, M. High-Yield Alkylation and Arylation of Graphene via Grignard Reaction with Fluorographene. *Chem. Mater.* **2017**, *29*, 926–930.

(35) Mazanek, V.; Libanska, A.; Sturala, J.; Bousa, D.; Sedmidubsky, D.; Pumera, M.; Janousek, Z.; Plutnar, J.; Sofer, Z. Fluorographene Modified by Grignard Reagents: A Broad Range of Functional Nanomaterials. *Chem. - Eur. J.* **2017**, *23*, 1956–1964.

(36) Sun, Z.; Pint, C. L.; Marcano, D. C.; Zhang, C.; Yao, J.; Ruan, G.; Yan, Z.; Zhu, Y.; Hauge, R. H.; Tour, J. M. Towards hybrid superlattices in graphene. *Nat. Commun.* **2011**, *2*, 559–564.

(37) Pumera, M.; Wong, C. H. A. Graphene and hydrogenated graphene. *Chem. Soc. Rev.* **2013**, *42*, 5987–5995.

(38) Sofer, Z.; Simek, P.; Mazanek, V.; Sembera, F.; Janousek, Z.; Pumera, M. Fluorographene (C₁H_xF_{1-x}[small delta]): synthesis and properties. *Chem. Commun.* **2015**, *51*, 5633–5636.

(39) Sandford, G. Perfluoroalkanes. *Tetrahedron* **2003**, *59*, 437–454.

(40) Dubecky, M.; Otyepkova, E.; Lazar, P.; Karlický, F.; Petr, M.; Cepe, K.; Banas, P.; Zboril, R.; Otyepka, M. Reactivity of Fluorographene: A Facile Way toward Graphene Derivatives. *J. Phys. Chem. Lett.* **2015**, *6*, 1430–1434.

(41) Hughes, R. P.; LeHusebo, T.; Maddock, S. M.; Rheingold, A. L.; Guzei, I. A. Thallium(I) selectively abstracts fluoride from a tertiary carbon-fluorine bond under conditions where silver(I)

selectively abstracts iodide from rhodium. *J. Am. Chem. Soc.* **1997**, *119*, 10231–10232.

(42) Richmond, T. G. Organometallic transformations demonstrate that fluorocarbons are reactive molecules. *Angew. Chem., Int. Ed.* **2000**, *39*, 3241–3244.

(43) Borden, W. T. Effects of electron donation into C-F sigma* orbitals: explanations, predictions and experimental tests. *Chem. Commun.* **1998**, *0*, 1919–1925.

(44) Medved, M.; Zoppellaro, G.; Ugolotti, J.; Matochova, D.; Lazar, P.; Pospisil, T.; Bakandritsos, A.; Tucek, J.; Zboril, R.; Otyepka, M. Reactivity of fluorographene is triggered by point defects: beyond the perfect 2D world. *Nanoscale* **2018**, *10*, 4696–4707.

(45) Chai, J. D.; Head-Gordon, M. Long-range corrected hybrid density functionals with damped atom-atom dispersion corrections. *Phys. Chem. Chem. Phys.* **2008**, *10*, 6615–6620.

(46) Marenich, A. V.; Cramer, C. J.; Truhlar, D. G. Universal Solvation Model Based on Solute Electron Density and on a Continuum Model of the Solvent Defined by the Bulk Dielectric Constant and Atomic Surface Tensions. *J. Phys. Chem. B* **2009**, *113*, 6378–6396.

(47) Lee, J. H.; Koon, G. K. W.; Shin, D. W.; Fedorov, V. E.; Choi, J. Y.; Yoo, J. B.; Ozyilmaz, B. Property Control of Graphene by Employing "Semi-Ionic" Liquid Fluorination. *Adv. Funct. Mater.* **2013**, *23*, 3329–3334.

(48) Wang, X.; Wang, W. M.; Liu, Y.; Ren, M. M.; Xiao, H. N.; Liu, X. Y. Controllable defluorination of fluorinated graphene and weakening of C-F bonding under the action of nucleophilic dipolar solvent. *Phys. Chem. Chem. Phys.* **2016**, *18*, 3285–3293.

(49) Fedorov, V. E.; Grayfer, E. D.; Makotchenko, V. G.; Nazarov, A. S.; Shin, H. J.; Choi, J. Y. Highly Exfoliated Graphite Fluoride as a Precursor for Graphene Fluoride Dispersions and Films. *Croat. Chem. Acta* **2012**, *85*, 107–112.

(50) Lai, W. C.; Yuan, Y. H.; Wang, X.; Liu, Y.; Li, Y. L.; Liu, X. Y. Radical mechanism of a nucleophilic reaction depending on a two-dimensional structure. *Phys. Chem. Chem. Phys.* **2018**, *20*, 489–497.

(51) Englert, J. M.; Vecera, P.; Knirsch, K. C.; Schäfer, R. A.; Hauke, F.; Hirsch, A. Scanning-Raman-Microscopy for the Statistical Analysis of Covalently Functionalized Graphene. *ACS Nano* **2013**, *7*, 5472–5482.

D

Tunable Synthesis of Nitrogen Doped
Graphene from Fluorographene
under Mild Conditions

Tunable Synthesis of Nitrogen Doped Graphene from Fluorographene under Mild Conditions

Dagmar Zaoralová,[§] Vítězslav Hrubý,[§] Veronika Šedajová, Radim Mach, Vojtěch Kupka, Juri Ugolotti, Aristides Bakandritsos,* Miroslav Medved',* and Michal Otyepka*



Cite This: *ACS Sustainable Chem. Eng.* 2020, 8, 4764–4772



Read Online

ACCESS |



Metrics & More



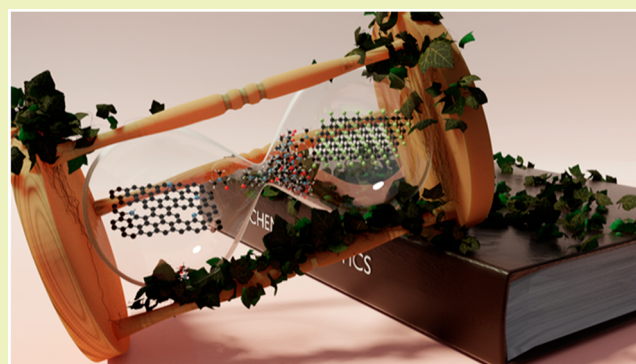
Article Recommendations



Supporting Information

ABSTRACT: The nitrogen doping of graphene via mild and low energy processes to afford homogeneous product composition and topology with high nitrogen content (>10 at. %) remains a challenge of contemporary 2D materials chemistry. Here, we report a previously unexplored route to synthesize N-doped graphene (NG) with exceptionally high N content (up to 18.2 at. %) by reaction of fluorographene (FG) with NaNH_2 in *N,N*-dimethylformamide (at 130 °C) or acetonitrile (at 70 °C). The N content can be tuned by changing the reaction time, temperature, and/or solvent, ranging from 6.6 to 18.2 at. %, mainly in the form of pyridinic and pyrrolic configurations. With thermal annealing, the N content remained constant up to 400 °C but then decreased by ~50% upon being further annealed to 1000 °C. Density functional theory (DFT) calculations showed that nitrogen incorporation into the carbon lattice mostly occurred at vacancies present in the starting material. We also conducted a thorough rationalization of side-reaction pathways leading to byproducts, which were confirmed by GC-MS analysis. This is the highest yet recorded N content for a wet chemical doping procedure and at such a low temperature of 70 °C. The reported synthetic approach thus offers a sustainable and cost-effective way to prepare NG with a broad tunability window of N content for potential applications related to energy storage and catalysis.

KEYWORDS: Nitrogen-doped graphene, Fluorographene, Wet chemistry, Eco-friendly organic synthesis, Density functional theory, Reaction mechanism



INTRODUCTION

Doping graphene with heteroatoms can significantly alter its electronic structure, giving rise to novel 2D materials with tunable electronic, magnetic, and chemical properties that can be exploited in diverse applications.^{1,2} In particular, nitrogen doping can imprint active centers on graphene suitable for (electro)catalytic,^{3–7} electrochemical (energy storage and sensors),³ and spintronic applications.^{8–12} Currently, methods for preparing nitrogen-doped graphene (NG) mostly rely on chemical vapor deposition of nitrogen-containing molecules,^{13,14} high temperature NH_3 treatment of GO¹⁵ and graphene,⁵ or solvothermal reaction of GO with N-containing molecules (e.g., melamine, acetonitrile, pyridine, urea, hydrazine) with subsequent annealing at high temperatures.^{16,17} Comprehensive reviews of synthetic pathways for NG can be found in pertinent articles.^{1,3,6,18} Although high N-content NGs (ca. 7 at. %) can be obtained through solvothermal pathways and annealing,^{16,17} or high temperature treatment of oxidized graphenes,^{5,15,19} such pathways are energy-demanding due to the high temperatures required (usually ≥ 800 °C). In addition, solid state reactions often lead

to an inhomogeneous distribution of nitrogen in the lattice.^{20,21}

Interestingly, fluorographene (FG) has been reported to undergo N-doping after Hummers oxidation to form fluorographene oxide, which after heating at 800 °C with melamine affords NG with N levels of 2 at. %.⁴ However, although a structurally well-defined graphene derivative²² was used as a substrate, allowing homogeneous doping, the pathway relied on established high temperature routes and yielded only low N content. It was also demonstrated that FG can undergo direct N-doping by ammonia gas which occurs simultaneously with defluorination at temperatures between 200 and 400 °C.^{23,24} Density functional theory (DFT) calculations have revealed that the first reaction step involves nucleophilic substitution of fluorine atoms by amino groups,

Received: November 30, 2019

Revised: February 2, 2020

Published: February 25, 2020

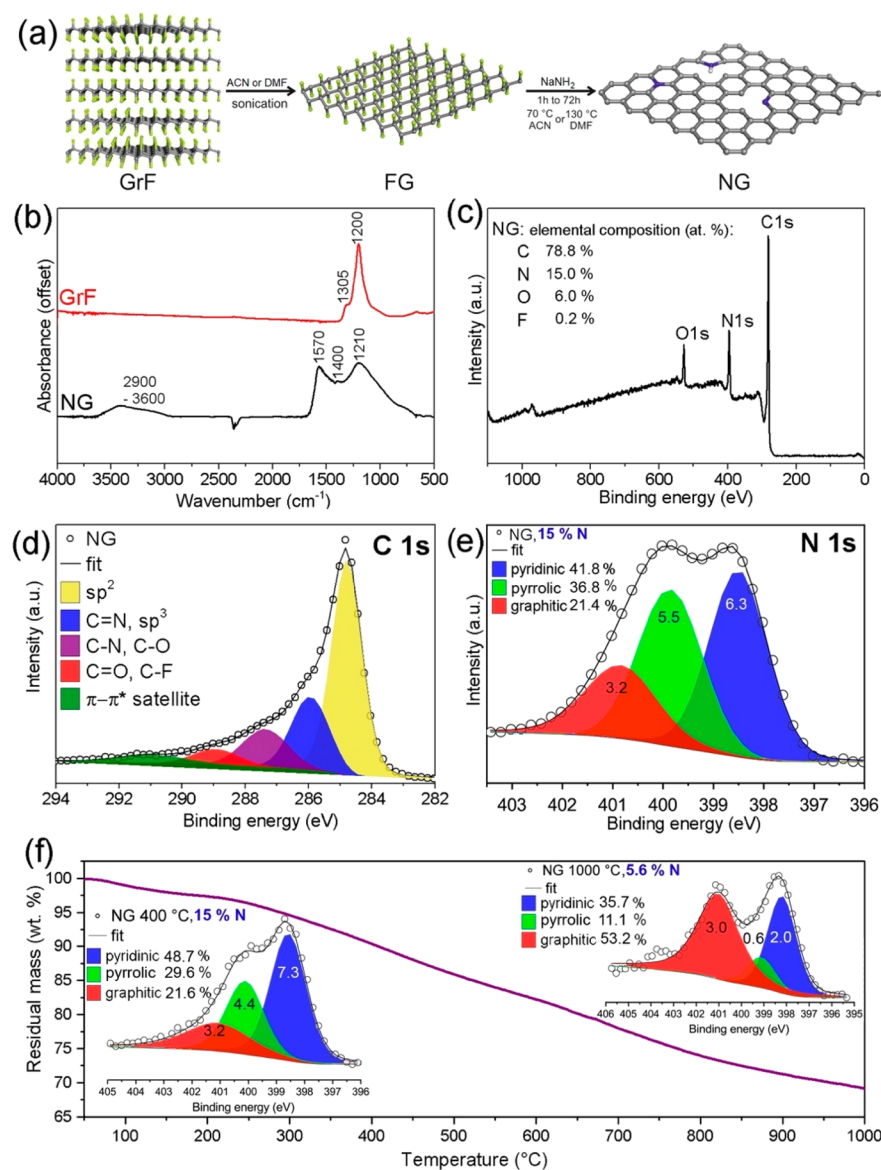


Figure 1. (a) General synthetic route toward NG. (b) FT-IR spectra of starting material (GrF) and product (NG). (c) XPS survey spectrum of NG synthesized at 130 $^\circ\text{C}$ in DMF. (d) Deconvoluted C 1s, and (e) N 1s XPS envelopes (the numbers in the legends represent the atomic contents of different N configurations with respect to nitrogen atoms only; the numbers inside the curves represent the atomic contents of different N configurations with respect to all atoms in the material). (f) TGA of NG in N_2 (insets show deconvoluted N 1s envelopes of NG samples withdrawn at 400 and 1000 $^\circ\text{C}$).

which can then undergo deprotonation and cyclization into aziridinic configurations. These could potentially be transformed into either pyridinic or graphitic N in the honeycomb carbon lattice. Owing to formation of NH_4F during the solid state synthesis (with characteristic double IR band of $[\text{NH}_4]^+$ at *ca.* 3250 cm^{-1} present at 300–400 $^\circ\text{C}$, along with some XRD peaks), the nitrogen content might not solely be attributed to doping. Despite these interesting results, the methods still rely on rather high temperatures (300–500 $^\circ\text{C}$) and usage of toxic, flammable, and environmentally dangerous ammonia gas. Recently, we reported the synthesis of NG²⁵ with 8.6 at. % N content (or 9.8 N/C at. ratio) homogeneously distributed in the graphene lattice by exploiting the expanding wet chemistry of FG.²⁶ In particular, FG reacted with $\text{NH}_2\text{OH}\cdot\text{HCl}$ in DMF at 130 $^\circ\text{C}$ for 30 h. The N-doping was explained to have begun with decomposition of NH_2OH into ammonia, which then reacted with vacancies present in the FG lattice,

incorporating mostly pyridinic N atoms. Nevertheless, $\text{NH}_2\text{OH}\cdot\text{HCl}$ is acutely toxic²⁷ and the achieved N-content remained at similar levels as previously reported. Therefore, the development of a simple, cost-effective, and eco-friendly synthetic pathway that gives access to homogeneous N-doping with elevated N content continues to be an experimental challenge. Moreover, the achievement of high levels of N doping would be beneficial for a wide range of NG materials applications, such as in (electro)catalysis for energy production and materials for energy storage.

In the present work, we showed that wet chemistry of FG, even at mild temperatures as low as 70 $^\circ\text{C}$, afforded up to 18.2 at. % N-doping when the more reactive and less health-hazardous²⁸ NaNH_2 was used (Figure 1a). Interestingly, the N-doping was tunable by the tweaking of the reaction conditions, such as time, temperature, and solvent environment. In particular, the reaction proceeded in DMF (r.t.–130

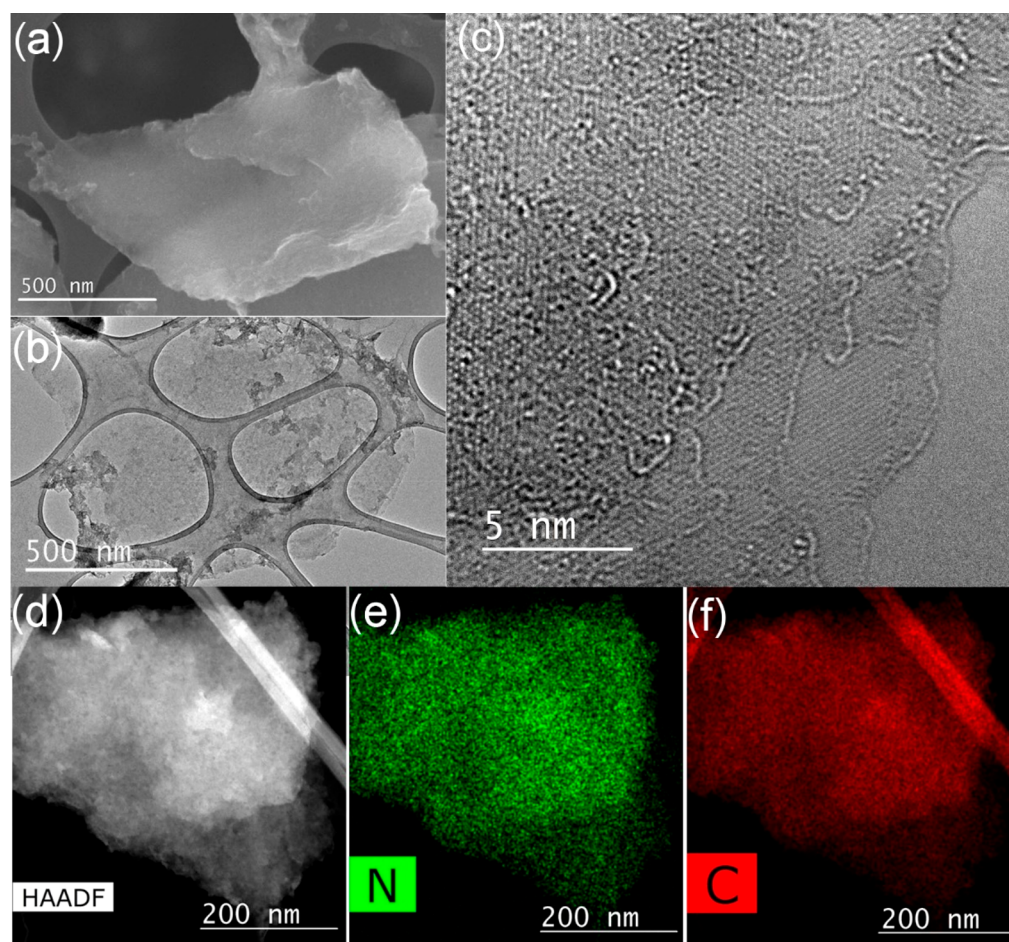


Figure 2. (a) SEM and (b) HR-TEM images of a few-layered NG flake. (c) Magnification of the same flake showing its edge structure and the atomic lattice of the graphene skeleton. (d) High angle annular dark-field (HAADF) TEM image of the flake used for energy-dispersive X-ray spectroscopy chemical mapping (EDS) for (e) nitrogen and (f) carbon.

°C), acetonitrile (ACN, 70 °C), and propylene carbonate (PC, 130 °C) as solvents. The solvent DMF is relatively environmentally friendly as it is rapidly biodegradable when released to water and soil (with a half-life of 18–36 h) and photo-oxidizable in air over a period of days.²⁹ With acetonitrile, we obtained not only a more environmentally friendly process but also one that was safer to human health than that with DMF,^{30–32} combined with homogeneous and record N-doping levels (18.2 at. %). To elucidate the high-yield incorporation of N atoms into the graphene lattice, we employed DFT calculations. Vacancies in FG were shown to act as reactive centers for $[\text{NH}_2]^-$ nucleophilic attack, followed by healing or expansion of the vacancies, whereas direct N incorporation into the unperturbed FG lattice was found to be energetically demanding.

RESULTS AND DISCUSSION

Synthesis and Characterization of Nitrogen-Doped Graphene. NG was synthesized using graphite fluoride (GrF) as a starting material, which was first exfoliated by sonication in solvent into several-layered sheets of FG and then reacted with sodium amide (NaNH_2) at 130 °C (DMF) or 70 °C (ACN) for a maximum of 3 days (Figure 1a). The FT-IR spectrum of the starting GrF (Figure 1b) showed only bands from the CF and CF_2 bonds (1200 and 1305 cm^{-1} , respectively), whereas the spectrum of the NG derivative in DMF was dominated by

bands at 1570 and 1210 cm^{-1} due to the developed sp^2 carbon network. Both the latter vibrations are typical for carbon and heterocyclic aromatic rings.³³ Additional vibrational modes of the aromatic rings appearing at 1400 cm^{-1} were ascribed to heteroatom substitution (such as in pyridinic configurations).^{33,34} Theoretical IR calculations were also in agreement with the present interpretation.^{35,36} The 1210 cm^{-1} band in NG overlapped with that of CF vibrations, but XPS confirmed (Figure 1c) that almost all F atoms (0.2 at. % residue) were eliminated. A weak and broad feature in the region between 3600 and 2900 cm^{-1} may indicate the minor presence of N–H, C–H, and O–H groups. The Raman spectrum of NG consisted of two features at 1300 and 1590 cm^{-1} , corresponding to D and G bands, respectively (Figure S2). The broad character of the D-band and high I_D/I_G ratio value of 1.3 suggested the presence of a large number of point defects and/or highly functionalized graphene materials, whereas the G-band was assigned to vibrations of sp^2 carbon domains formed by the reductive defluorination of FG.⁸ As discussed later, the NG products obtained from reaction at shorter times (1 to 24 h) or in ACN exhibited very similar features.

According to XPS analysis, the product was doped with exceptionally high N content of 15 at. % in DMF (Figure 1c) and 18.2 at. % in ACN (Figure 3c), and was practically fluorine-free (F: 0.2–0.9 at. %). In comparison to the material

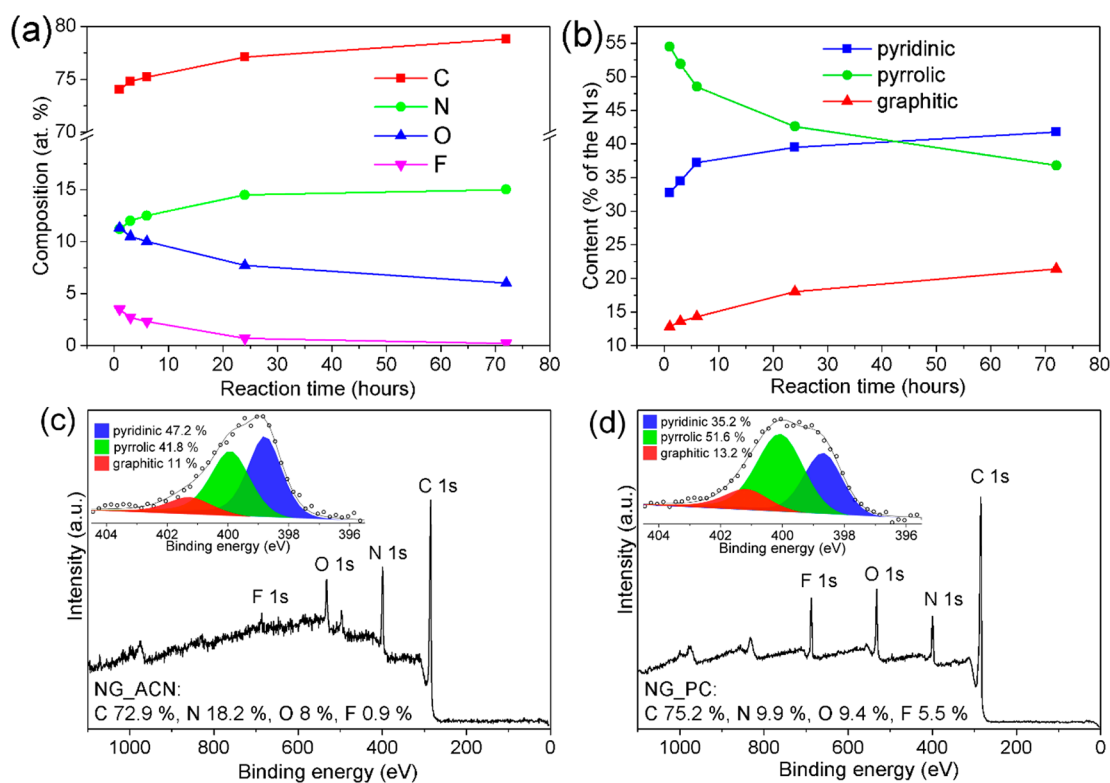


Figure 3. (a) Time evolution of the elemental composition of NG materials synthesized at 130 °C. (b) Time evolution of nitrogen group components acquired by deconvolution of N 1s XPS regions of NG materials synthesized at 130 °C. (c) Survey XPS spectrum of NG_ACN material prepared at 70 °C with its deconvoluted N 1s region (inset). (d) Survey XPS spectrum of NG_PC with its deconvoluted N 1s region (inset).

reported by Zoppellaro et al.²⁵ (F: 7.7 at. % and N: 8.2 at. %), the reaction with NaNH_2 achieved a much higher degree of defluorination and significantly higher (almost twice) nitrogen doping level. Indeed, deconvolution of the high-resolution C 1s XPS (HR-XPS) profile (Figure 1d) showed that the NGs consisted mostly of sp^2 -hybridized carbons and other components at higher binding energies (BEs), corresponding to carbons bonded to nitrogen and oxygen atoms with significantly overlapping binding energy values.^{3,8,25,37,38} The HR-XPS N 1s profile suggested the presence of three components (Figure 1e) with BEs of ~ 398.5 , ~ 400 , and ~ 401.2 eV, typically assigned to pyridinic, pyrrolic, and graphitic configurations, respectively.^{3,8,25,36,38} After the thermal treatment of NG at 400 °C in an inert atmosphere (Figure 1f), the N content remained practically unchanged (15 at. %, Figure S3). However, the deconvoluted N 1s envelopes (insets in Figure 1f) revealed that pyrrolic nitrogens were partly transformed to thermodynamically more stable pyridinic nitrogens. At 1000 °C, the pyrrolic nitrogens were further reduced with a concomitant reduction of pyridinic nitrogen, while the content of graphitic nitrogen remained virtually the same, as expected for this configuration. It should be noted that in the BE range for pyrrolic nitrogens, other groups may also appear, such as amino and aziridinic groups. Nevertheless, presence of these groups is less probable in view of the high stability of this component up to 400 °C, which would not be expected for such out-of-plane functionalities. Ninhydrin tests (Figure S4) also did not support the presence of amino groups.³⁹ The component ascribed to pyrrolic nitrogens probably contained a significant amount of protonated pyridinic nitrogens, as suggested by significant changes of the

spectral areas at ~ 398.5 and ~ 400 eV in the N 1s XPS profiles of the NG material after acidic and basic washings³⁶ (Figure S5). The dominant presence of pyridinic nitrogens was also supported by the 5.4 point of zero charge of the NG (Figure S6), which coincided with the pK_a of pyridine (5.2).³⁶ However, for the sake of clarity, the component at 400 eV is denoted throughout the text as pyrrolic.

SEM imaging revealed few-layered flakes or agglomerates with a lateral size of up to 1 μm (Figure 2a), in agreement with HR-TEM images showing almost transparent flakes of *ca.* 1 μm (Figure 2b). Magnification of the edges confirmed a layered structure of stacked sheets with a distinguishable lattice in each layer (Figure 2c). Importantly, EDS chemical mapping revealed the homogeneous distribution of nitrogen atoms over the carbon lattice (Figure 2d–f). The specific surface areas of the products as obtained by N_2 and CO_2 adsorption isotherms were 110 and 287 m^2/g , respectively (Figure S7a). The higher value from the CO_2 measurement was attributed to its higher diffusion rate ensuring better accessibility in narrow pores; it thus probed constricted spaces more accurately than N_2 at 77 K. Adsorption of CO_2 revealed micropore volume filling of around 0.025 cm^3/g (Figure S7b); on the contrary, N_2 did not show filling of the micropores. According to pore size distribution characteristics, the size of the micropores was around 0.4 nm, i.e., in the range of ultramicropores (<0.7 nm).

To gain a deeper insight into the N-doping process of FG, samples were synthesized using different reaction times, temperatures, and solvents. The XPS spectra of the samples withdrawn at different times of the reaction performed at 130 °C suggested that the initial phase of the reaction was very fast. Within 1 h, the fluorine content decreased from 52.3 at. %

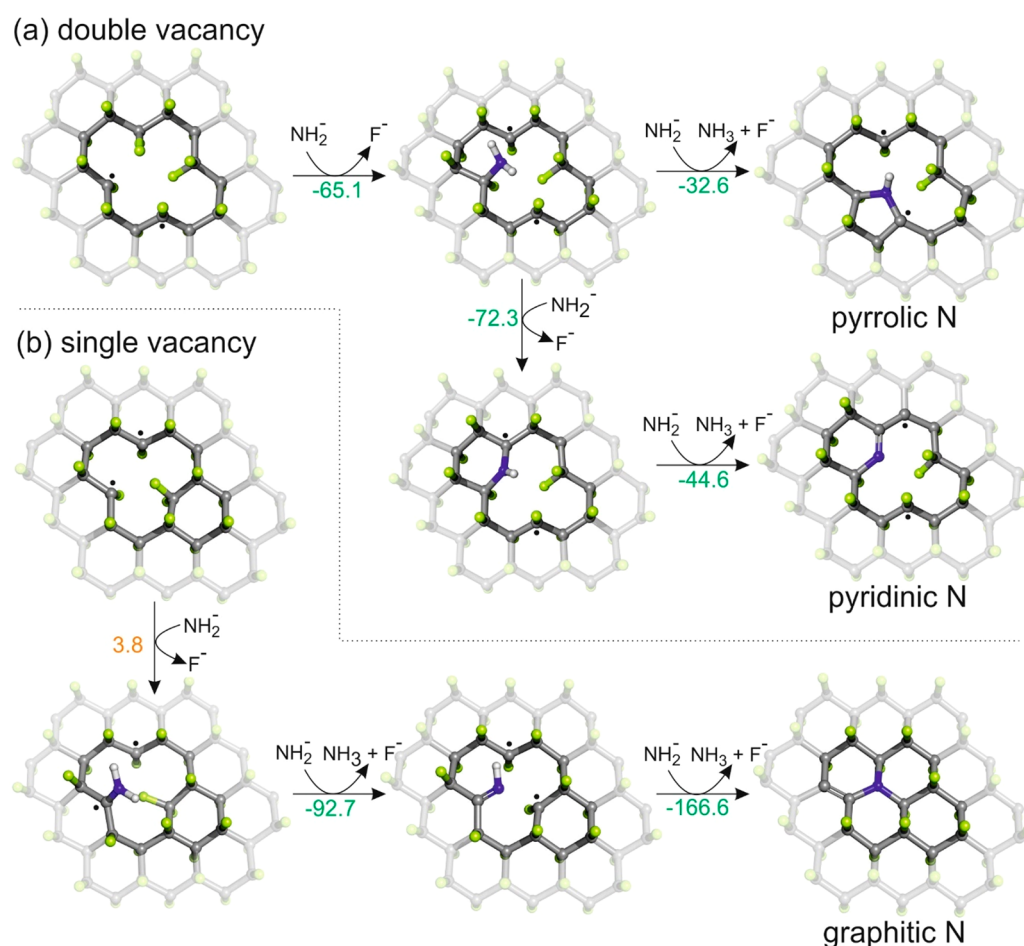


Figure 4. Nucleophilic attack of NH_2^- on a biradical center of (a) DV(14) leading to the formation pyrrolic or pyridinic nitrogen and (b) SV leading to the formation graphitic nitrogen. Carbon atoms are gray, fluorine green, nitrogen blue, and hydrogen white. Reaction energies are in kcal·mol⁻¹.

%) with a lower proportion of pyridinic groups and more nitrogen atoms with BEs of around 400 eV. The possible reason for the higher N content in the case of ACN and DMF might be related to the fact that NaNH_2 is notably less soluble in PC than in the other two solvents. Another possible reason could be the higher reactivity of carbonate esters (like PC) with strong nucleophiles (here, the NH_2^- anion),⁴² which can lead to more efficient competitive reactions compared to those in DMF and ACN.

Insights into the Reaction Mechanism. Various scenarios of nitrogen incorporation into the FG lattice were studied by DFT at the $\omega\text{B97X-D}/6\text{-31++G(d,p)}$ level of theory^{43,44} using the Gaussian09 program.⁴⁵ Solvent effects were taken into account by using the universal continuum solvation model based on electron density (SMD).⁴⁶ First, a reaction pathway involving a point defect in FG was investigated (Figure S20). Radical point defects (one fluorine atom missing) present in real FG samples have previously been identified as strong electrophiles responsible for the reactivity of FG.^{47,48} Thus, we anticipated that the reaction might proceed via nucleophilic attack of NH_2^- on a point defect, followed by dissociation of an adjoining C–F bond (reaction energy $\Delta E_{\text{R}} = -62.1$ kcal·mol⁻¹). The amino groups can either react with radical species leading to byproducts observed experimentally (see Scheme 1) or be transformed to aziridinic arrangements ($\Delta E_{\text{R}} = -42.7$ kcal·mol⁻¹, Figure S20-III.a), as

also proposed for the attack of NH_3 on FG.⁴⁹ C–F bond dissociation and release of F^- and HF (transformed to F^- by reaction with NH_2^-) were supported by the experimental observation of NaF based on XRD measurements (Figure S15a). As the aziridinic group is highly reactive, it would be chemically transformed in a reaction mixture containing strong nucleophiles and radicals (see Scheme 1). Therefore, neither amino nor aziridinic functionalities should be expected in NG, in line with the N 1s XPS data.

Taking into account the high reactivity of the aziridinic group, we considered a reaction mechanism that could potentially lead to the formation of an in-plane nitrogen configuration (Figure S20). However, the reaction step involving the cleavage of lattice C–C bonds was found to be prohibited due to a high energy barrier ($E_{\text{a}} > 100$ kcal·mol⁻¹, Figures S21 and S22). Therefore, the direct insertion of nitrogen into an unperturbed FG lattice seems to be highly improbable, and the presence of vacancies in the lattice needs to be considered to explain the feasibility of the N-doping process under mild conditions.

To investigate the types of vacancies that may occur in the starting material, we performed periodic boundary condition (PBC) calculations using spin-polarized DFT in combination with the Perdew, Burke, and Ernzerhof functional with Grimme correction (PBE-D2)⁵⁰ and projected augmented wave potentials (PAW) representing atomic cores, as

implemented in the Vienna ab initio simulation package (VASP).^{51–54} For further computational details, see the SI. Several types of vacancies are known to occur in a graphene lattice⁵⁵ and may also exist in FG: point defects (e.g., Stone–Wales vacancy SW(55–77)), single vacancies (SV), double vacancies (DV), triple vacancies (TV), etc. Since a distribution of spin-carrying sites was found in FG samples,⁴⁸ we also included vacancies with radical centers as well as biradical sites. The distances between radical centers on the edges of vacancies (2.9–7.5 Å) corresponded to values estimated experimentally using electron paramagnetic resonance (EPR) (4.8–7.3 Å in freshly prepared sample, 3.9 Å after treatment with DMF).⁴⁸

On the basis of a comparison of cohesion energies (eq S1 in SI), SW(55–77) and DV(555–777) vacancies were identified as the most stable (Figure S23). However, a combination of these vacancies with a point defect is not probable due to the high C–F bond dissociation energy, which is comparable with that of unperturbed FG (~100 kcal·mol⁻¹). Therefore, we studied the nucleophilic attack of NH₂⁻ on radical centers of the third and fourth most stable vacancies, namely SV and DV(14) (Figure 4a,b and Figures S24 and S25). The first reaction step, i.e., NH₂⁻ nucleophilic attack accompanied by release of a fluorine anion, was more favorable for DV(14) ($\Delta E_R = -65.1$ kcal·mol⁻¹, Figure 4a) than for SV ($\Delta E_R = 3.8$ kcal·mol⁻¹, Figure 4b). The reaction then proceeded via dehydrogenation and further defluorination. N incorporation into SV led to formation of graphitic nitrogen and was energetically the most favorable ($\Delta E_R = -255.5$ kcal·mol⁻¹). In the case of DV(14), we considered the formation of both pyridinic and pyrrolic N. While the creation of a six-membered ring with pyridinic N was found to be feasible ($\Delta E = -72.3$ kcal·mol⁻¹, Figure 4a), the formation of a five-membered ring with pyrrolic N was less favorable ($\Delta E = -32.6$ kcal·mol⁻¹). These findings suggest that the N-doping process predominantly involves the formation of graphitic and pyridinic structures. It should also be noted that nucleophilic attack can lead to the expansion of a vacancy (Figure S34). This process can increase the number of active sites on the lattice and thus significantly affect the amount of incorporated nitrogen atoms.

We also employed GC-MS to verify the suggested reaction mechanism in DMF. GC-MS analysis of supernatants acquired by centrifugation of the reaction mixture revealed that various species were formed during the N-doping process (Tables S1, S2, Figures S16–S19). The main byproducts included dimethylamine (DMA), dimethylaminoacetonitrile (DMAACN), tetramethylurea (TMU), dimethylurea (DMU), and formyltrimethylurea (FTMU). Hence, the reaction system of FG mixed with NaNH₂ in DMF evidently involved many side-reactions. By conducting a thorough theoretical exploration of possible reactions of FG with NH₂⁻ and those encompassing DMF, we rationalized the occurrence of all the main byproducts observed experimentally (shown in green frames in Scheme 1). Species in orange frames are important for other reactions in the system; some of them are created without the presence of FG and/or NaNH₂ (see more comprehensive Schemes S1–S3 in the SI). It is worth noting that the radical centers of FG enable radical reactions and significantly enrich the number of possible byproducts in comparison with DMF and DMF + NaNH₂ systems. The GC-MS analysis of a supernatant acquired from the reaction mixture in ACN was also performed (see Table S3). The formation of the main byproducts was rationalized by

theoretical calculations (Scheme S4). In comparison to those in the reaction in DMF, the byproducts were less diverse, and their formation was energetically less favorable, confirming that ACN is the least reactive environment among the used solvents.

CONCLUSIONS

The synthesis of highly N-doped graphene by the reaction of FG with NaNH₂ under mild and sustainable conditions was reported. The highest yet recorded nitrogen content of 18.2 at. % in graphene at mild conditions was attained in acetonitrile as solvent at 70 °C. The nitrogen atoms were assigned as pyrrolic, pyridinic, and graphitic configurations. The product retained the same nitrogen composition and content up to 400 °C, a finding which might have significant applicability in catalysis at elevated temperatures.

DFT calculations revealed that the nucleophilic attack of NH₂⁻ on point defects and vacancies naturally present in the starting material was energetically favorable and could explain the formation of pyrrolic, pyridinic, and graphitic configurations observed experimentally. In addition, the suggested mechanism and rationalization of side-reaction pathways corroborated the experimentally determined byproducts of the reaction. It was concluded that the radical centers of FG may trigger a chain of radical side-reactions and enrich the number of byproducts in the reaction system.

The developed synthesis of highly N-doped graphene under mild conditions in solution by exploiting the susceptibility of FG toward nucleophilic agents appears to be a tunable, cost-effective, and environmentally friendly pathway for preparing N-doped graphene materials that could have wide applicability in (electro)catalysis, energy production, and storage.

ASSOCIATED CONTENT

Supporting Information

The Supporting Information is available free of charge at <https://pubs.acs.org/doi/10.1021/acssuschemeng.9b07161>.


Materials; synthesis of the nitrogen doped graphene (NG); experimental techniques; characterization of materials (XPS, Raman and FTIR spectra, TGA, ζ potential, gas adsorption/desorption isotherms, GC-MS, NMR); computational details; energy profiles for selected reactions; classification of vacancies; schemes describing side reactions (PDF)

AUTHOR INFORMATION

Corresponding Authors

Aristides Bakandritsos – Regional Centre of Advanced Technologies and Materials, Faculty of Science, Palacký University in Olomouc, 783 71 Olomouc, Czech Republic; Email: aristeidis.bakandritsos@upol.cz

Miroslav Medved' – Regional Centre of Advanced Technologies and Materials, Faculty of Science, Palacký University in Olomouc, 783 71 Olomouc, Czech Republic; Email: miroslav.medved@upol.cz

Michal Otyepka – Regional Centre of Advanced Technologies and Materials, Faculty of Science and Department of Physical Chemistry, Faculty of Science, Palacký University in Olomouc, 783 71 Olomouc, Czech Republic;  orcid.org/0000-0002-1066-5677; Email: michal.otyepka@upol.cz

Authors

Dagmar Zaoralová – Regional Centre of Advanced Technologies and Materials, Faculty of Science and Department of Physical Chemistry, Faculty of Science, Palacký University in Olomouc, 783 71 Olomouc, Czech Republic

Vítězslav Hrubý – Regional Centre of Advanced Technologies and Materials, Faculty of Science and Department of Physical Chemistry, Faculty of Science, Palacký University in Olomouc, 783 71 Olomouc, Czech Republic

Veronika Šedajová – Regional Centre of Advanced Technologies and Materials, Faculty of Science and Department of Physical Chemistry, Faculty of Science, Palacký University in Olomouc, 783 71 Olomouc, Czech Republic

Radim Mach – Regional Centre of Advanced Technologies and Materials, Faculty of Science and Department of Physical Chemistry, Faculty of Science, Palacký University in Olomouc, 783 71 Olomouc, Czech Republic

Vojtěch Kupka – Regional Centre of Advanced Technologies and Materials, Faculty of Science and Department of Physical Chemistry, Faculty of Science, Palacký University in Olomouc, 783 71 Olomouc, Czech Republic

Juri Ugolotti – Regional Centre of Advanced Technologies and Materials, Faculty of Science, Palacký University in Olomouc, 783 71 Olomouc, Czech Republic

Complete contact information is available at:

<https://pubs.acs.org/10.1021/acssuschemeng.9b07161>

Author Contributions

[§]These authors contributed equally to this work.

Notes

The authors declare no competing financial interest.

ACKNOWLEDGMENTS

We acknowledge financial support from MEYS (CZ.02.1.01/0.0/0.0/16_019/0000754, CZ.1.05/2.1.00/19.0377), the ERC (683024 from the H2020) and the Internal Student Grant Agency of the Palacký University in Olomouc, Czech Republic (IGA_PrF_2019_031). Ondřej Tomanec (HR-TEM), Cecilia Maria Reyes Pérez (SEM), Martin Petr (XPS), Jana Havláková (TGA), Kateřina Štymplová and Dr. Zuzana Chaloupková (Raman), Dr. Claudia Aparicio (XRD), and Dr. Eva Otyepková (GC-MS) are acknowledged for the measurements.

REFERENCES

- (1) Rao, C. N. R.; Gopalakrishnan, K.; Govindaraj, A. Synthesis, properties and applications of graphene doped with boron, nitrogen and other elements. *Nano Today* **2014**, *9* (3), 324–343.
- (2) Maiti, U. N.; Lee, W. J.; Lee, J. M.; Oh, Y.; Kim, J. Y.; Kim, J. E.; Shim, J.; Han, T. H.; Kim, S. O. 25th Anniversary Article: Chemically Modified/Doped Carbon Nanotubes & Graphene for Optimized Nanostructures & Nanodevices. *Adv. Mater.* **2014**, *26* (1), 40–67.
- (3) Wang, H.; Maiyalagan, T.; Wang, X. Review on Recent Progress in Nitrogen-Doped Graphene: Synthesis, Characterization, and Its Potential Applications. *ACS Catal.* **2012**, *2* (5), 781–794.
- (4) Vineesh, T. V.; Nazrulla, M. A.; Krishnamoorthy, S.; Narayanan, T. N.; Alwarappan, S. Synergistic effects of dopants on the spin density of catalytic active centres of N-doped fluorinated graphene for oxygen reduction reaction. *Appl. Mater. Today* **2015**, *1* (2), 74–79.
- (5) Guo, D.; Shibuya, R.; Akiba, C.; Saji, S.; Kondo, T.; Nakamura, J. Active sites of nitrogen-doped carbon materials for oxygen reduction reaction clarified using model catalysts. *Science* **2016**, *351* (6271), 361–365.

- (6) Wei, Q.; Tong, X.; Zhang, G.; Qiao, J.; Gong, Q.; Sun, S. Nitrogen-Doped Carbon Nanotube and Graphene Materials for Oxygen Reduction Reactions. *Catalysts* **2015**, *5* (3), 1574–1602.

- (7) Liang, P.; Zhang, C.; Duan, X.; Sun, H.; Liu, S.; Tade, M. O.; Wang, S. N-Doped Graphene from Metal–Organic Frameworks for Catalytic Oxidation of p-Hydroxybenzoic Acid: N-Functionality and Mechanism. *ACS Sustainable Chem. Eng.* **2017**, *5* (3), 2693–2701.

- (8) Błoński, P.; Tuček, J.; Sofer, Z.; Mazánek, V.; Petr, M.; Pumera, M.; Otyepka, M.; Zbořil, R. Doping with Graphitic Nitrogen Triggers Ferromagnetism in Graphene. *J. Am. Chem. Soc.* **2017**, *139* (8), 3171–3180.

- (9) Miao, Q.; Wang, L.; Liu, Z.; Wei, B.; Xu, F.; Fei, W. Magnetic properties of N-doped graphene with high Curie temperature. *Sci. Rep.* **2016**, *6*, 21832–21842.

- (10) Ito, Y.; Christodoulou, C.; Nardi, M. V.; Koch, N.; Kläui, M.; Sachdev, H.; Müllen, K. Tuning the Magnetic Properties of Carbon by Nitrogen Doping of Its Graphene Domains. *J. Am. Chem. Soc.* **2015**, *137* (24), 7678–7685.

- (11) Alegaonkar, A. P.; Kumar, A.; Patil, S. H.; Patil, K. R.; Pardeshi, S. K.; Alegaonkar, P. S. Spin Transport and Magnetic Correlation Parameters for Graphene-like Nanocarbon Sheets Doped with Nitrogen. *J. Phys. Chem. C* **2013**, *117* (51), 27105–27113.

- (12) Friedman, A. L.; Cress, C. D.; Schmucker, S. W.; Robinson, J. T.; van 't Erve, O. M. J. Electronic transport and localization in nitrogen-doped graphene devices using hyperthermal ion implantation. *Phys. Rev. B: Condens. Matter Mater. Phys.* **2016**, *93* (16), 161409–161418.

- (13) Ito, Y.; Christodoulou, C.; Nardi, M. V.; Koch, N.; Sachdev, H.; Müllen, K. Chemical Vapor Deposition of N-Doped Graphene and Carbon Films: The Role of Precursors and Gas Phase. *ACS Nano* **2014**, *8* (4), 3337–3346.

- (14) Scardamaglia, M.; Aleman, B.; Amati, M.; Ewels, C.; Pochet, P.; Reckinger, N.; Colomer, J. F.; Skaltsas, T.; Tagmatarchis, N.; Snyder, R.; Gregoratti, L.; Bittencourt, C. Nitrogen implantation of suspended graphene flakes: Annealing effects and selectivity of sp² nitrogen species. *Carbon* **2014**, *73*, 371–381.

- (15) Wang, L.; Sofer, Z.; Luxa, J.; Pumera, M. Nitrogen doped graphene: influence of precursors and conditions of the synthesis. *J. Mater. Chem. C* **2014**, *2* (16), 2887–2893.

- (16) Sui, Z.-Y.; Wang, C.; Yang, Q.-S.; Shu, K.; Liu, Y.-W.; Han, B.-H.; Wallace, G. G. A highly nitrogen-doped porous graphene – an anode material for lithium ion batteries. *J. Mater. Chem. A* **2015**, *3* (35), 18229–18237.

- (17) Chang, D. W.; Lee, E. K.; Park, E. Y.; Yu, H.; Choi, H.-J.; Jeon, I.-Y.; Sohn, G.-J.; Shin, D.; Park, N.; Oh, J. H.; Dai, L.; Baek, J.-B. Nitrogen-Doped Graphene Nanoplatelets from Simple Solution Edge-Functionalization for n-Type Field-Effect Transistors. *J. Am. Chem. Soc.* **2013**, *135* (24), 8981–8988.

- (18) Wang, H.; Xie, M.; Thia, L.; Fisher, A.; Wang, X. Strategies on the Design of Nitrogen-Doped Graphene. *J. Phys. Chem. Lett.* **2014**, *5* (1), 119–125.

- (19) Song, J.; Yu, Z.; Gordin, M. L.; Wang, D. Advanced Sulfur Cathode Enabled by Highly Crumpled Nitrogen-Doped Graphene Sheets for High-Energy-Density Lithium–Sulfur Batteries. *Nano Lett.* **2016**, *16* (2), 864–870.

- (20) Liu, D.; Lei, W.; Portehault, D.; Qin, S.; Chen, Y. High N-content holey few-layered graphene electrocatalysts: scalable solventless production. *J. Mater. Chem. A* **2015**, *3* (4), 1682–1687.

- (21) Jeon, I. Y.; Choi, H. J.; Ju, M. J.; Choi, I. T.; Lim, K.; Ko, J.; Kim, H. K.; Kim, J. C.; Lee, J.-J.; Shin, D.; Jung, S.-M.; Seo, J.-M.; Kim, M.-J.; Park, N.; Dai, L.; Baek, J.-B. Direct nitrogen fixation at the edges of graphene nanoplatelets as efficient electrocatalysts for energy conversion. *Sci. Rep.* **2013**, *3*, 2260–2267.

- (22) Karlický, F.; Kumara Ramanatha Datta, K.; Otyepka, M.; Zbořil, R. Halogenated Graphenes: Rapidly Growing Family of Graphene Derivatives. *ACS Nano* **2013**, *7* (8), 6434–6464.

- (23) Li, Y.; Wang, X.; Wang, W.; Qin, R.; Lai, W.; Ou, A.; Liu, Y.; Liu, X. Nitrogen-Doping Chemical Behavior of Graphene Materials

with Assistance of Defluorination. *J. Phys. Chem. C* **2019**, *123* (1), 584–592.

(24) Liu, Y.; Shen, Y.; Sun, L.; Li, J.; Liu, C.; Ren, W.; Li, F.; Gao, L.; Chen, J.; Liu, F.; Sun, Y.; Tang, N.; Cheng, H.-M.; Du, Y. Elemental superdoping of graphene and carbon nanotubes. *Nat. Commun.* **2016**, *7* (1), 10921–10930.

(25) Zoppellaro, G.; Bakandritsos, A.; Tuček, J.; Błoński, P.; Susi, T.; Lazar, P.; Bađ'ura, Z.; Steklý, T.; Opletalová, A.; Otyepka, M.; Zbořil, R. Microwave Energy Drives "On–Off–On" Spin-Switch Behavior in Nitrogen-Doped Graphene. *Adv. Mater.* **2019**, *31* (37), 1902587–1902597.

(26) Chronopoulos, D. D.; Bakandritsos, A.; Pykal, M.; Zbořil, R.; Otyepka, M. Chemistry, properties, and applications of fluorographene. *Appl. Mater. Today* **2017**, *9*, 60–70.

(27) National Center for Biotechnology Information. PubChem Database. Hydroxylamine hydrochloride, CID = 443297, <https://pubchem.ncbi.nlm.nih.gov/compound/Hydroxylamine-hydrochloride> (accessed on Nov. 6, 2019).

(28) National Center for Biotechnology Information. PubChem Database. Sodium Amide, CID = 24533, <https://pubchem.ncbi.nlm.nih.gov/compound/Sodium-amide> (accessed on Nov. 6, 2019).

(29) Long, G.; Meek, M. E. N, N-dimethylformamide: Hazard characterization and exposure-response analysis. *J. Environ. Sci. Heal. C* **2001**, *19* (1), 161–187.

(30) National Center for Biotechnology Information. PubChem Database. N,N-Dimethylformamide, CID = 6228, https://pubchem.ncbi.nlm.nih.gov/compound/N_N-Dimethylformamide (accessed on Nov. 6, 2019).

(31) National Center for Biotechnology Information. PubChem Database. Propylene carbonate, CID = 7924, <https://pubchem.ncbi.nlm.nih.gov/compound/Propylene-carbonate> (accessed on Nov. 6, 2019).

(32) National Center for Biotechnology Information. PubChem Database. Acetonitrile, CID = 6342, <https://pubchem.ncbi.nlm.nih.gov/compound/Acetonitrile> (accessed on Nov. 6, 2019).

(33) Mayo, D. W. *Course Notes on the Interpretation of Infrared and Raman Spectra* (Eds. Mayo, D. W.; Miller, F. A.; Hannah, R. W.), John Wiley & Sons, Inc.: 2004; pp 101–140.

(34) Senthilnathan, J.; Weng, C.-C.; Liao, J.-D.; Yoshimura, M. Submerged Liquid Plasma for the Synthesis of Unconventional Nitrogen Polymers. *Sci. Rep.* **2013**, *3* (1), 2414–2421.

(35) Bakandritsos, A.; Kadam, R. G.; Kumar, P.; Zoppellaro, G.; Medved', M.; Tuček, J.; Montini, T.; Tomanec, O.; Andryskova, P.; Drahos, B.; Varma, R. S.; Otyepka, M.; Gawande, M. B.; Fornasiero, P.; Zboril, R. Mixed-Valence Single-Atom Catalyst Derived from Functionalized Graphene. *Adv. Mater.* **2019**, *31* (17), 1900323–1900332.

(36) Lazar, P.; Mach, R.; Otyepka, M. Spectroscopic Fingerprints of Graphitic, Pyrrolic, Pyridinic, and Chemisorbed Nitrogen in N-Doped Graphene. *J. Phys. Chem. C* **2019**, *123* (16), 10695–10702.

(37) Bakandritsos, A.; Pykal, M.; Błoński, P.; Jakubec, P.; Chronopoulos, D. D.; Poláková, K.; Georgakilas, V.; Čepe, K.; Tomanec, O.; Ranc, V.; Bourlinos, A. B.; Zbořil, R.; Otyepka, M. Cyanographene and Graphene Acid: Emerging Derivatives Enabling High-Yield and Selective Functionalization of Graphene. *ACS Nano* **2017**, *11* (3), 2982–2991.

(38) Kumar, A.; Ganguly, A.; Papakonstantinou, P. Thermal stability study of nitrogen functionalities in a graphene network. *J. Phys.: Condens. Matter* **2012**, *24* (23), 235503–235510.

(39) Potsi, G.; Bourlinos, A. B.; Mouselimis, V.; Poláková, K.; Chalmpes, N.; Gournis, D.; Kalytchuk, S.; Tomanec, O.; Błoński, P.; Medved', M.; Lazar, P.; Otyepka, M.; Zbořil, R. Intrinsic photoluminescence of amine-functionalized graphene derivatives for bioimaging applications. *Appl. Mater. Today* **2019**, *17*, 112–122.

(40) Luo, G.; Liu, L.; Zhang, J.; Li, G.; Wang, B.; Zhao, J. Hole Defects and Nitrogen Doping in Graphene: Implication for Supercapacitor Applications. *ACS Appl. Mater. Interfaces* **2013**, *5* (21), 11184–11193.

(41) Wang, X.; Sun, G.; Routh, P.; Kim, D.-H.; Huang, W.; Chen, P. Heteroatom-doped graphene materials: syntheses, properties and applications. *Chem. Soc. Rev.* **2014**, *43* (20), 7067–7098.

(42) Tundo, P.; Musolino, M.; Aricò, F. The reactions of dimethyl carbonate and its derivatives. *Green Chem.* **2018**, *20* (1), 28–85.

(43) Chai, J.-D.; Head-Gordon, M. Long-range corrected hybrid density functionals with damped atom–atom dispersion corrections. *Phys. Chem. Chem. Phys.* **2008**, *10* (44), 6615–6620.

(44) Ditchfield, R.; Hehre, W. J.; Pople, J. A. Self-Consistent Molecular-Orbital Methods. IX. An Extended Gaussian-Type Basis for Molecular-Orbital Studies of Organic Molecules. *J. Chem. Phys.* **1971**, *54* (2), 724–728.

(45) Frisch, M. J. et al. *Gaussian 09*. 2016, Gaussian, Inc., Wallingford CT.

(46) Marenich, A. V.; Cramer, C. J.; Truhlar, D. G. Universal Solvation Model Based on Solute Electron Density and on a Continuum Model of the Solvent Defined by the Bulk Dielectric Constant and Atomic Surface Tensions. *J. Phys. Chem. B* **2009**, *113* (18), 6378–6396.

(47) Matochová, D.; Medved', M.; Bakandritsos, A.; Steklý, T.; Zbořil, R.; Otyepka, M. 2D Chemistry: Chemical Control of Graphene Derivatization. *J. Phys. Chem. Lett.* **2018**, *9* (13), 3580–3585.

(48) Medved', M.; Zoppellaro, G.; Uğolotti, J.; Matochová, D.; Lazar, P.; Pospíšil, T.; Bakandritsos, A.; Tuček, J.; Zbořil, R.; Otyepka, M. Reactivity of fluorographene is triggered by point defects: beyond the perfect 2D world. *Nanoscale* **2018**, *10* (10), 4696–4707.

(49) Li, X.-F.; Lian, K.-Y.; Liu, L.; Wu, Y.; Qiu, Q.; Jiang, J.; Deng, M.; Luo, Y. Unraveling the formation mechanism of graphitic nitrogen-doping in thermally treated graphene with ammonia. *Sci. Rep.* **2016**, *6*, 23495–23504.

(50) Grimme, S. Semiempirical GGA-type density functional constructed with a long-range dispersion correction. *J. Comput. Chem.* **2006**, *27* (15), 1787–1799.

(51) Kresse, G.; Furthmüller, J. Efficient iterative schemes for ab initio total-energy calculations using a plane-wave basis set. *Phys. Rev. B: Condens. Matter Mater. Phys.* **1996**, *54* (16), 11169–11186.

(52) Kresse, G.; Furthmüller, J. Efficiency of ab-initio total energy calculations for metals and semiconductors using a plane-wave basis set. *Comput. Mater. Sci.* **1996**, *6* (1), 15–50.

(53) Kresse, G.; Joubert, D. From ultrasoft pseudopotentials to the projector augmented-wave method. *Phys. Rev. B: Condens. Matter Mater. Phys.* **1999**, *59* (3), 1758–1775.

(54) Blöchl, P. E. Projector augmented-wave method. *Phys. Rev. B: Condens. Matter Mater. Phys.* **1994**, *50* (24), 17953–17979.

(55) Banhart, F.; Kotakoski, J.; Krasheninnikov, A. V. Structural Defects in Graphene. *ACS Nano* **2011**, *5* (1), 26–41.

E

Covalently Interlinked Graphene Sheets with
Sulfur-Chains Enable Superior Lithium-Sulfur
Battery Cathodes at Full-Mass Level

Covalently Interlinked Graphene Sheets with Sulfur-Chains Enable Superior Lithium–Sulfur Battery Cathodes at Full-Mass Level

Iosif Tantis, Aristides Bakandritsos,* Dagmar Zaoralová, Miroslav Medved, Petr Jakubec, Jana Havláková, Radek Zbořil,* and Michal Otyepka*

Sulfur represents a low-cost, sustainable, and high theoretical capacity cathode material for lithium–sulfur batteries, which can meet the growing demand in portable power sources, such as in electric vehicles and mobile information technologies. However, the shuttling effect of the formed lithium polysulfides, as well as their low conductivity, compromise the electrochemical performance of lithium–sulfur cells. To tackle this challenge, a so far unexplored cathode, composed of sulfur covalently bonded directly on graphene is developed. This is achieved by leveraging the nucleophilicity of polysulfide chains, which react readily with the electrophilic centers in fluorographene, as experimental and theoretical data unveil. The reaction leads to the formation of carbon–sulfur covalent bonds and a particularly high sulfur content of 80 mass%. Owing to these features, the developed cathode exhibits excellent performance with only 5 mass% of conductive carbon additive, delivering very high full-cathode-mass capacities and rate capability, combined with superior cycling stability. In combination with a fluorinated ether as electrolyte additive, the capacity persists at $\approx 700 \text{ mAh g}^{-1}$ after 100 cycles at 0.1 C, and at $\approx 644 \text{ mAh g}^{-1}$ after 250 cycles at 0.2 C, keeping $\approx 470 \text{ mAh g}^{-1}$ even after 500 cycles.

corporation.^[1,2] With the rapid development and broad application of mobile devices, electric and unmanned vehicles, as well as with the rise of smart grids and networks for “the internet of things,” the demand for batteries with higher performance and lower cost is rapidly growing.^[3,4] Lithium–sulfur batteries (LSBs) could offer a promising alternative for energy storage because of the high theoretical capacity (1672 mAh g^{-1}) and specific energy (2600 Wh kg^{-1}).^[5–8] Moreover, sulfur is environmentally friendly and a key byproduct of the petroleum industry, with attractive features for commercialization, such as abundance and low cost.^[9–12] However, several bottlenecks hamper the practical development of the LSBs,^[13,14] including the sulfur’s poor conductivity, its large volume change, and the “shuttling-effect” of lithium polysulfides (PSs), formed during the charge/discharge process.^[15] The dissolution of these lithium PSs (Li_2S_n , $n \geq 4$) into the liquid electrolyte leads to low

Coulombic efficiency, poor sulfur utilization, fast capacity fading, and other parasitic reactions with the Li anode.^[16,17]

To address these challenges, different strategies emerged in the past few years for the development of advanced composite cathodes designed for high sulfur utilization and stability. In particular, pinning of sulfur in engineered materials acting as

1. Introduction

Lithium–ion batteries are electrochemical rechargeable energy storage systems leading the battery market of portable electronics for telecommunications and information processing since the 1990’s, after the first commercial cell was introduced by Sony

Dr. I. Tantis, Dr. A. Bakandritsos, D. Zaoralová, Dr. M. Medved, Dr. P. Jakubec, J. Havláková, Prof. R. Zbořil, Prof. M. Otyepka
Regional Centre of Advanced Technologies and Materials
Czech Advanced Technology and Research Institute
Palacký University
Křížkovského 511/8, Olomouc 77900, Czech Republic
E-mail: a.bakandritsos@upol.cz; radek.zboril@upol.cz
michal.otyepka@upol.cz

Dr. A. Bakandritsos, Prof. R. Zbořil
Nanotechnology Centre
Centre of Energy and Environmental Technologies
VŠB-Technical University of Ostrava
17. listopadu 2172/15, Ostrava-Poruba 70800, Czech Republic

 The ORCID identification number(s) for the author(s) of this article can be found under <https://doi.org/10.1002/adfm.202101326>.

D. Zaoralová
Department of Physical Chemistry
Faculty of Science
Palacký University Olomouc
17. listopadu 1192/12, Olomouc 77900, Czech Republic
J. Havláková
Department of Experimental Physics
Faculty of Science
Palacký University Olomouc
17. listopadu 1192/12, Olomouc 77900, Czech Republic

DOI: 10.1002/adfm.202101326

high-affinity hosts for sulfur and development of functional separators which hinder the shuttling of lithium PSs have been pursued.^[18–22] In this frame, nanostructured carbon-based materials are intensively explored as sulfur hosts because of their lightweight nature, good electrical conductivity, large surface area, and excellent mechanical properties.^[23–25] In a pioneering work, an ordered mesoporous carbon was exploited to encapsulate sulfur in order to improve its utilization and restrain the shuttling-effect of the lithium-PS species.^[12] However, such pure carbon hosts, although being porous, suffer from sluggish cycling stability due to the weak interactions between the PSs and the carbon surface. Therefore, the design and development of new nanocarbons with sulfur-binding surface groups is essential.^[26,27] Such functional groups can offer strong anchoring sites for the robust immobilization of the sulfur and PS species, effectively limiting the shuttling-effect during charging/discharging for long and stable lifecycle.^[28,29] In addition, nanocarbons, especially carbon nanotubes and graphene, may not only act as sulfur hosts, but can also mitigate its low electrical conductivity and improve the mechanical properties.^[30–34] However, most of the reported strongly immobilized or covalently-bonded sulfur cathodes have achieved low cycle-life, low sulfur loading contents, or were obtained on nonconductive matrices (e.g., polymers or amorphous carbons), necessitating the addition of high amounts of conductive, but electrochemically inactive additives, and thus, eventually, limiting the true (i.e., total mass-based) cathode capacities (Table S1, Supporting Information). Therefore, the strong covalent bonding of sulfur on conductive materials, affording cathodes with appropriately high sulfur loading, is challenging but essential for leveraging the full potential of LSBs and high utilization of sulfur.

In this work, we report the successful development of a graphene-sulfur cathode with very high sulfur loading, whereby the sulfur chains are immobilized by covalent bonding to graphene. The loading in covalent-sulfur reached an unprecedented 80 mass%, increasing the full-cell specific capacity and, importantly, limiting the shuttling-effect even at very low specific currents, thus ascribing outstanding cycling stability. Moreover, achieving such a high covalent-sulfur loading on graphene instead of graphene oxide or porous/amorphous carbons did not compromise the cathode's electrical conductivity and thus allowed operation with a very low content of conductive, but electrochemically inactive additives. Accessing such highly and covalently sulfur-derivatized graphene was only possible via the rich chemistry of fluorographene (FG),^[35,36] exploiting the high electrophilicity and chain-propagating reactivity of its carbon-centered radicals.^[36,37] Remarkably, the use of sodium polysulfide (NaPS) and FG (instead of elemental sulfur, metal sulfides, or graphene) was discovered as a unique pathway, offering adequately nucleophilic centers at the PS chain ends, reacting effectively and extensively with the respective electrophilic carbon sites developed through defluorination of FG, affording a densely sulfurized graphene cathode.

2. Results and Discussion

Recently, it was shown that the use of strong nucleophiles in aprotic solvents is a very effective way of FG functionalization

through nucleophilic attack, initiated on the electrophilic radical centers at the defect sites of FG.^[37,38] Because the nucleophile delivers a negative charge, the neighboring C–F bonds become susceptible to heterolytic cleavage, promoting the next step of defluorination and substitution.^[37,38] Here, we explored the strong nucleophilicity of PS ions (demonstrated by their ability to attack the electrophilic carbons of alkylhalides^[39,40] according to the $[X-R-X + Na_2S_x \text{ accord}_n + 2NaX]$ pathway), but applied for the first time in the reaction with FG in *N*-methyl-2-pyrrolidone (NMP) at 80 °C (Figure 1a, and Experimental Section). FT-IR analysis of the purified reaction product (graphene-polysulfide, GPS), unveiled the development of covalent C–S bonds, and the extensive defluorination of FG (Figure 1b). In particular, the C–F band of FG at $\approx 1200 \text{ cm}^{-1}$ decreased and a new band at $\approx 1580 \text{ cm}^{-1}$ emerged in GPS due to the aromatic ring stretching, indicating the successful defluorination and the formation of conjugated C=C bonds, respectively.^[41] Importantly, the band at $\approx 1150 \text{ cm}^{-1}$ demonstrated the development of covalent C–S bonds (stretching vibration).^[42] In contrast, the spectrum of a control sample obtained after a reaction of FG with elemental sulfur (GS, Figure 1b) showed a very intense C–F band and no C–S vibrations, while the strong S–S bands originated from deposited elemental sulfur. The high sulfur content in the GS control sample, as IR suggests, is only due to weak sulfur interactions with FG. Indeed, a treatment of GS with carbon disulfide—a very good solvent for sulfur—clearly demonstrated the sulfur-leaching in GS, unlike covalent GPS (Figure S1a, Supporting Information). A dramatic difference on the stability was also clearly demonstrated in the electrochemical testing of the two materials, as discussed later. The spectra of the starting NaPS and sulfur are also shown in Figure 1b, confirming the absence of the C–S vibration band at 1150 cm^{-1} which was only observed in the case of the GPS product.

The sulfur content for each sample was determined via thermogravimetric analysis (TGA, Figure 1c), based on the mass loss between 200 and 350 °C.^[43] Accordingly, ≈ 80 and ≈ 85 mass% of sulfur was found for GPS and GS, respectively. Lower sulfur loading could be achieved by reaction of FG with a lower amount of NaPS with respect to the FG and/or by a shorter reaction time. On the other hand, the lower content in PSs would also lead to higher content in fluorine atoms, since both processes, that is, defluorination and substitution, occur simultaneously (as discussed below). The higher content in fluorine atoms is, however, undesirable because C–F bonds increase the band gap of graphene and hinder the material's electrical conductivity.^[44] Another control reaction (identical to the reaction for obtaining GPS but using electrochemically exfoliated graphene instead of FG) showed only 5 at.% sulfur content (product EEGS, Figure S1b, Supporting Information), corroborating the important role of FG for developing covalent bonding of NaPS chains to graphene. Evolved gas analysis (EGA) with mass spectroscopy for the GS and GPS materials during TGA under air (Figure 1d) showed that the SO and SO₂ evolution profiles were wider for GPS than for GS, indicating stronger interaction with graphene in the former case, due to the covalent bonding of PSs on the graphene skeleton, in line with the IR analysis. Furthermore, the TGA thermogram from GPS showed a smooth transition point to the mass-stable

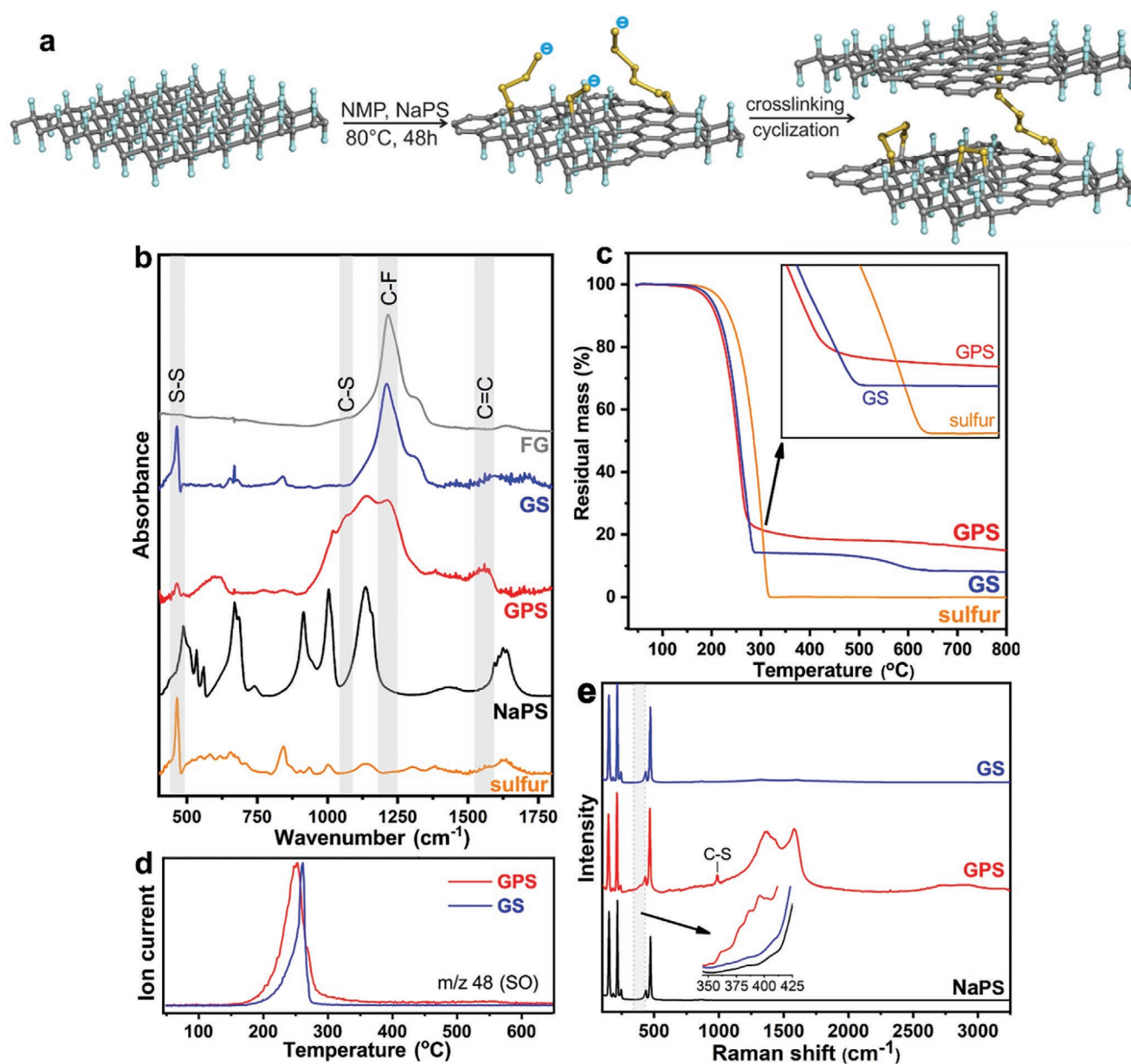


Figure 1. a) Reaction scheme for covalent binding of sodium polysulfide (NaPS) to fluorographene (FG) leading to graphene-polysulfide (GPS), b) FTIR spectra for elemental sulfur, NaPS, GPS, the sulfur-reacted FG derivative (GS), and the starting FG, c) thermograms of sulfur, GS, and GPS. d) Evolved gas analysis with mass spectrometry for SO and SO₂ fragments during TGA of GS and GPS (normalized ion currents at maximum) and e) Raman spectra of GS, GPS, and NaPS.

region after total sulfur loss, in contrast to a sharp transition point observed for GS and elemental sulfur samples (Figure 1c, and inset). The smooth transition point is an indirect evidence of sulfur trapping or covalent immobilization on surfaces,^[32,45] corroborating the direct evidence of the C–S bonds obtained from the IR spectra.

The successful covalent sulfur-functionalization of FG via its reaction with NaPS was also confirmed by Raman spectroscopy (Figure 1e). The GS, GPS, and NaPS spectra showed the characteristic S–S bonds from the NaPS chains at 149, 212, and 470 cm⁻¹ (ref. [46]), while in EGS the S–S bonds were present only at noise level (Figure S1c, Supporting Information). It is noted that FG

does not have any Raman peaks due to the absence of aromatic rings and high fluorescence.^[36] Importantly, GPS showed two peaks at 395 and 987 cm⁻¹ (Figure 1e, and inset), corresponding to covalent C–S bending and stretching vibrations, respectively.^[47,48] In contrast, they were absent in NaPS and GS, verifying further the presence of covalent C–S bonds between the PS chain ends on the graphenic skeleton of GPS. Furthermore, GPS exhibited the characteristic D and G bands at around 1330 and 1580 cm⁻¹, respectively, due to the restoration of the aromatic network^[49] after the defluorination. The ratio of *I*_D and *I*_G band intensities for GPS was 0.96, which along with the broadening of the bands, demonstrated a high degree of graphene functionalization.^[50]

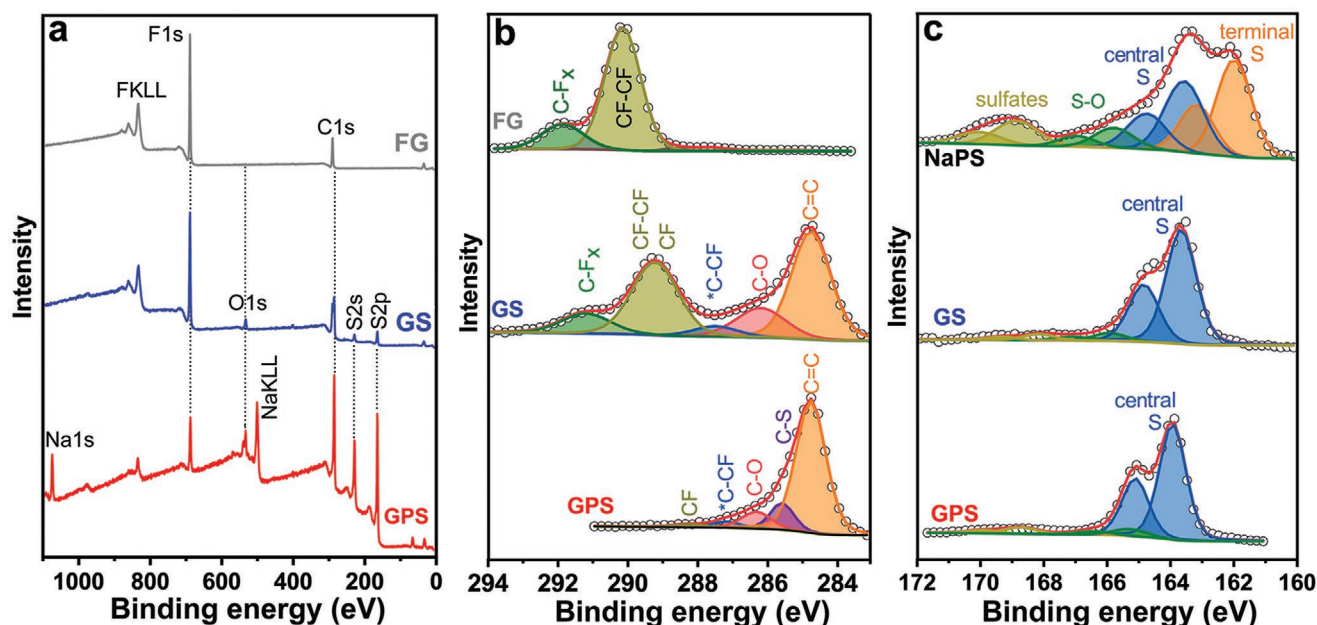


Figure 2. a) XPS survey spectra of GPs, GS, and pristine FG, b) C 1s HR-XPS spectra of pristine FG, GPs, and GS, respectively and c) S 2p HR-XPS spectra of pristine NaPS, GPs, and GS, respectively.

X-ray photoelectron spectroscopy (XPS) spectra confirmed the high sulfur content in GPs and the drastically reduced F 1s peak, indicated the efficacy of the reaction through the substitution–defluorination propagation pathway (Figure 2a,b). The Na 1s peak was also observed due to a few unreacted PS chain ends, as discussed below. More specifically, the deconvoluted C 1s spectra of pristine FG (Figure 2b) displayed two components at 290.1 eV due to CF–CF and at ≈ 291.8 eV due to C–F.^[44,51] On the other hand, the C 1s region of GPs showed a dominant component at 284.8 eV corresponding to graphitic sp² carbons, while the C–F components practically disappeared, explaining the low F content (Table S2, Supporting Information). Another component emerged at 285.6 eV corresponding to carbons covalently bonded to sulfur.^[32] In antithesis, the various covalent CF components were preserved at a significantly high extent in GS (Figure 2b), indicating that sulfur did not effectively react with FG in this case, but mostly deposited on the surface through weak interactions.^[52] The S 2p spectrum of GPs, indicated strong modification of the electronic density distribution of the PS chains after the functionalization reaction, in comparison to the starting NaPS (Figure 2c). In particular, NaPS displayed four doublets at 162.0 eV (terminal S atoms), 163.5 eV (central S atoms), and 165.8 and 168.9 eV due to small amount of oxidized sulfur and sulfates, respectively.^[53] On the other hand, the terminal S component was drastically reduced in GPs, indicating that a cyclization and crosslinking reaction took place, retaining only a few unmodified PS ends in the product. Control samples confirmed the extremely low sulfur content in EGS (1.6 at.%, Table S2 and Figure S1d, Supporting Information), further indicating the necessity of the synergy between the strong nucleophilic centers in NaPS and reactive electrophilic sites in FG, for the reaction to proceed.^[54]

The morphology of GPs corresponded to few-layered graphene sheets densely covered by sulfur, as observed with

scanning electron microscopy (SEM, Figure 3a). Further inspection with high-resolution transmission electron microscopy (HR-TEM, Figure 3b) showed few-layered graphene sheets with high content of sulfur, as energy-dispersive X-ray spectroscopy (EDS, Figure 3b, inset) and chemical mapping (Figure 3c,d) indicated. It is also worth noting that the sulfur/carbon rich and poor regions perfectly coincided (e.g., arrows in Figure 3e,f), providing further evidence that sulfur was intimately bonded to graphene, without forming independent sulfur-rich areas. Even after 250 charge/discharge cycles and thorough washing, the SEM of the cathode showed that the distribution of sulfur on the sheets was fully preserved (Figure 3g,h).

To provide mechanistic insight into the formation of covalent C–S bonds during the reaction of NaPS with FG, the nucleophilic attack of short PS chains (S_x^{2-} , $x = 2, 4,$ and 6) on various FG structures (Figure 4a–c; Figures S2–S4, Supporting Information) was explored by density functional theory (DFT) calculations. Interestingly, unlike in the case of smaller nucleophiles,^[37,38] a direct attack of PS on single atomic radical centers in highly fluorinated graphenes was not found energetically favorable, due to sterical hindrance from the neighboring fluorine atoms carrying partial negative charge. However, the low ionization energy of PS chains and relatively high electron affinity of the FG radical centers (Table S3, Supporting Information) suggest that a defluorination reaction can be initiated by electron transfer from the PS chains to the radical centers of FG.^[37] NMP solvent can also trigger defluorination of FG,^[55] as also shown here in the FT-IR and Raman spectra of the pristine FG and the FG after 24 h treatment in NMP at 80 °C (Figure S5a,b, Supporting Information). Indeed, the nucleophilic attack of PS chains became more favorable on the larger defluorinated graphene domains (Figure 4a–c; Figures S2–S4, Supporting Information), which exhibit electrophilic character in the vicinity of C–F bonds showing increasing susceptibility of FG to the

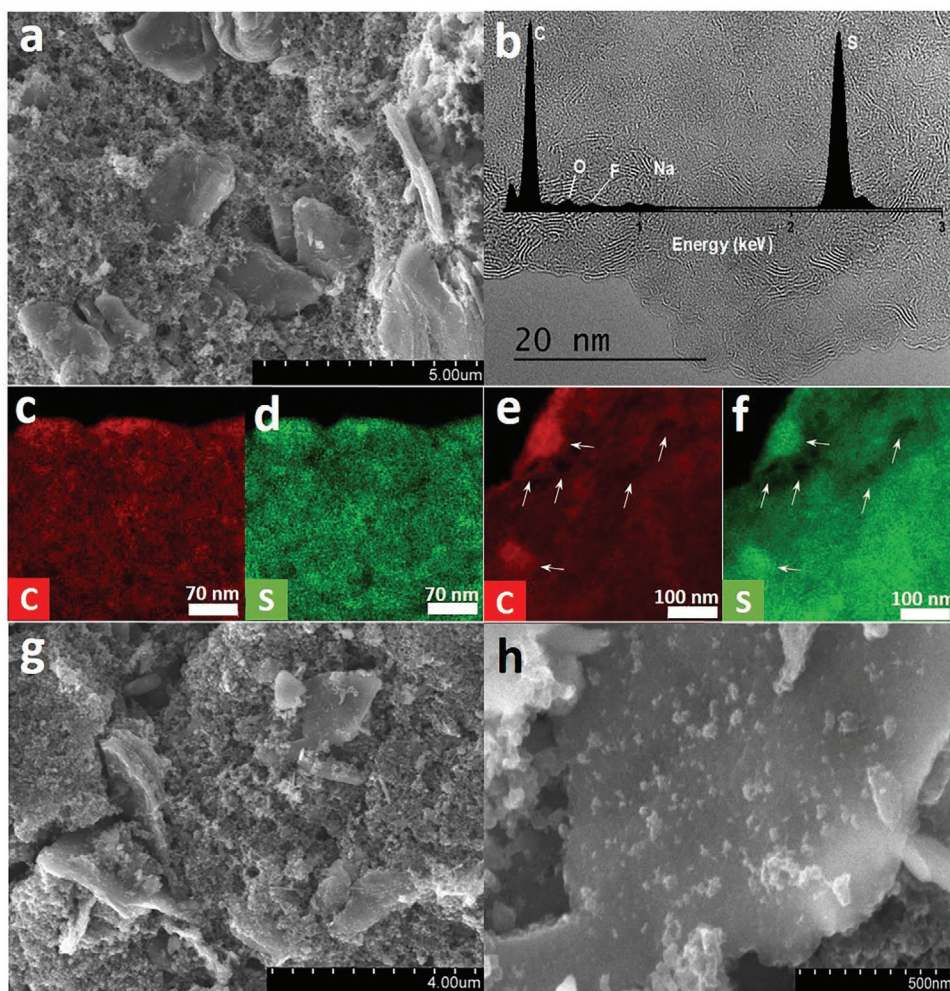


Figure 3. a) SEM image of a GPS electrode before testing and b) HR-TEM image of the GPS material (with EDS spectra in inset). c–f) Carbon and sulfur EDS maps of GPS at two different areas. Arrows on panels e,f) highlight the perfect overlap of sulfur and carbon rich or poor regions. g,h) SEM images of the GPS material after testing 250 charge per discharge cycles.

PS nucleophilic attack with decreasing fluorine content. The formation of a C–S bond and the charge transfer from PS to FG caused spontaneous detachment of a fluoride ion from the substrate. Importantly, the free end of the PS chain could act as a nucleophile in subsequent reaction steps leading either to crosslinking of graphene sheets (in the case of longer chains) or to cyclization (in the case of short chains, Figure 4d).

In order to evaluate the electrochemical performance of GPS, cathode electrodes were prepared by doctor blading of a paste containing 90% GPS as active material. Since GPS contains few-layered graphene (rather than graphene oxide or other non-conductive carbon matrices), the need of conductive additive was limited to only 5 mass%, which is of key importance toward high full-cathode-mass capacities. The final cathode was evaluated against lithium metal in an 1 M lithium bis(trifluoromethanesulfonyl)imide (LiTFSI) electrolyte dissolved in dioxolane (DOL) mixture with a fluorinated ether (TTE, 1,1,2,2-tetrafluoroethyl 2,2,3,3-tetrafluoropropyl ether, known to limit the solubility of lithium PSs^[56]). Cyclic voltammetry of GPS (Figure 5a) at 0.1, 0.2, and 0.5 mV s⁻¹ showed a broad anodic peak during charging, and a two-step sulfur

reduction, similar to DOL/DME (dimethoxy ethane, Figure S6, Supporting Information). The oxidation of the cathode was completed in two stages, with the broad peak at ≈ 2.45 V representing the conversion of $\text{Li}_2\text{S}_{1-2}$ to Li_2S_n ($n > 2$) and the formation of elemental sulfur. The reduction was also completed in two clearly separated steps: the peak at 2.25 V is ascribed at the reduction of elemental sulfur to Li_2S_n ($4 \leq n \leq 8$) while the peak at 1.7 V corresponds to the subsequent reduction of Li_2S_n to $\text{Li}_2\text{S}_{1-2}$.^[57] A typical charge/discharge curve of a LSB consists of two plateaus during discharge. The first one corresponds to a solid (S_8) \rightarrow liquid (Li_2S_n) transition with a theoretical capacity of 418 mAh g⁻¹ while the second discharge plateau corresponds to further reduction of lithium PSs to $\text{Li}_2\text{S}_2/\text{Li}_2\text{S}$ with a theoretical capacity of 1254 mAh g⁻¹.^[58] On the other hand, short sulfur chain cycling is performed through a solid-solid phase transition from S to Li_2S having only one discharge plateau at ≈ 1.8 V.^[59] In the present case the discharge curve of GPS combines the typical long-sulfur-chain LSB characteristics with the short sulfur chain discharge plateau (Figure 5b). Interestingly, as it was shown by the theoretical calculations, both short and longer chains of PSs can react covalently with the

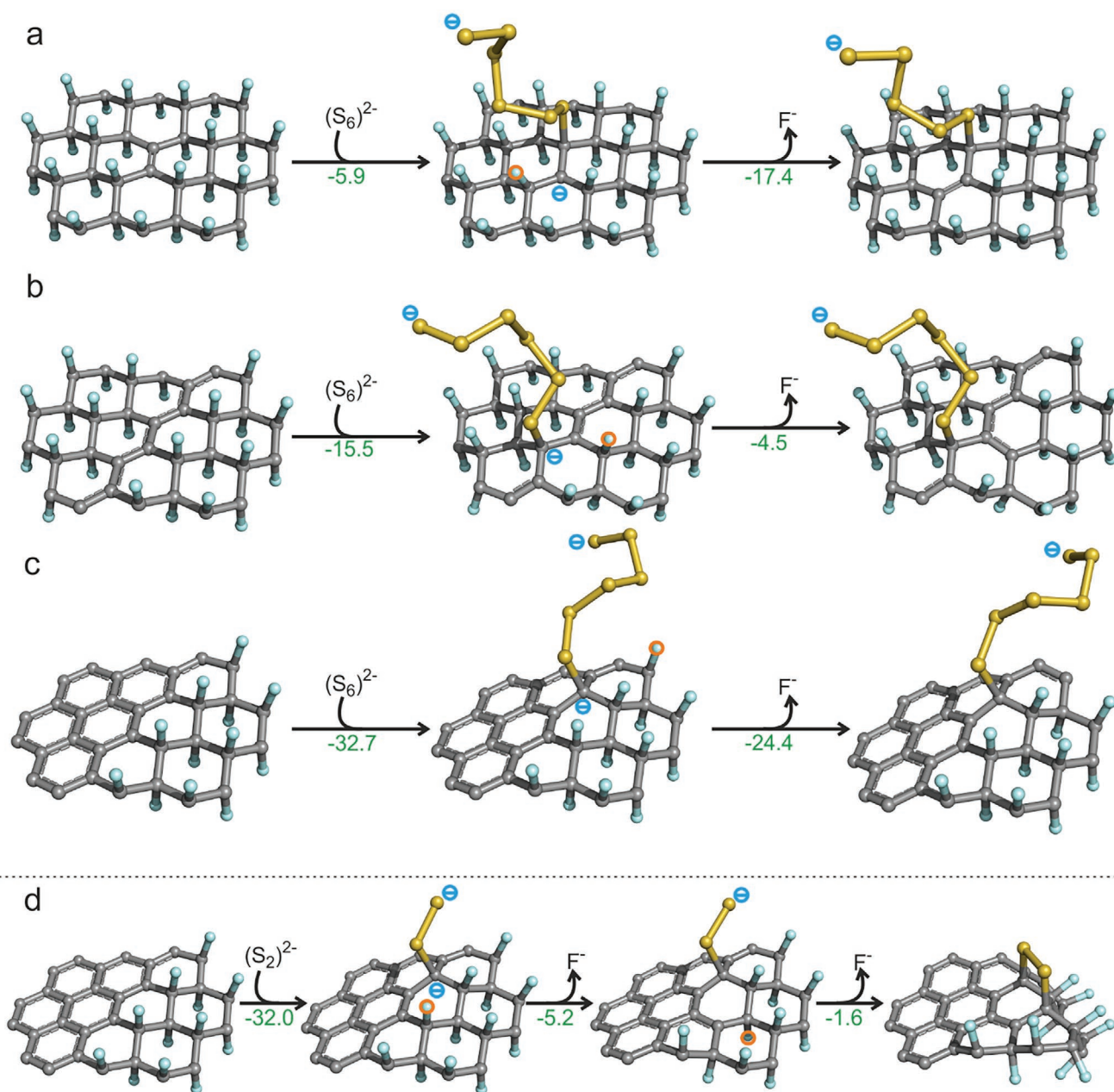


Figure 4. a–c) Nucleophilic attack of $(S_6)^{2-}$ on FG with different level of defluorination. d) Nucleophilic attack of $(S_2)^{2-}$ on the edge of fluorinated and defluorinated areas of FG resulting in a cyclized structure of the PS chain. Fluorine atoms detached in the next reaction step are marked by an orange circle. Reaction energies are in kcal·mol⁻¹. Carbon atoms are grey, fluorine blue, and sulfur yellow. Hydrogen atoms on edges of model molecules are hidden for clarity.

graphene backbone (Figure 4). Therefore, the discharge plateaus at 2.3 and ≈ 2 V are related with the longer sulfur chains while the discharge plateau at ≈ 1.8 V corresponds to the short sulfur chain phase transition ($S_{2-4} \rightarrow S^2$). The reduction peak potential values are down-shifted compared to DOL/DME solvent due to the low lithium PS solubility in TTE, leading to controlled Li_2S precipitation.^[60] The electrochemical profiles recorded during the galvanostatic charging/discharging of the GPS cathode were well maintained for more than 50 cycles at a specific current of 0.1 C (167 mA g⁻¹, Figure 5b), owing to

the high electrochemical reversibility. Upon cycling, the plateau contribution from the short sulfur chains increased at the expense of the long sulfur chains, indicating a disproportionation of the long chains to shorter ones, along with some Li_2S_n losses in the electrolyte. This can also account for the small capacity fade in the subsequent cycles. The stability of GPS was outstanding for both high and low specific currents; the initial capacities of 636 mAh g⁻¹ (1 C), 930 mAh g⁻¹ (0.2 C), and 920 mAh g⁻¹ (0.1 C) were maintained at 470 mAh g⁻¹ after 500 cycles, 644 mAh g⁻¹ after 250 cycles, and >700 mAh g⁻¹ after

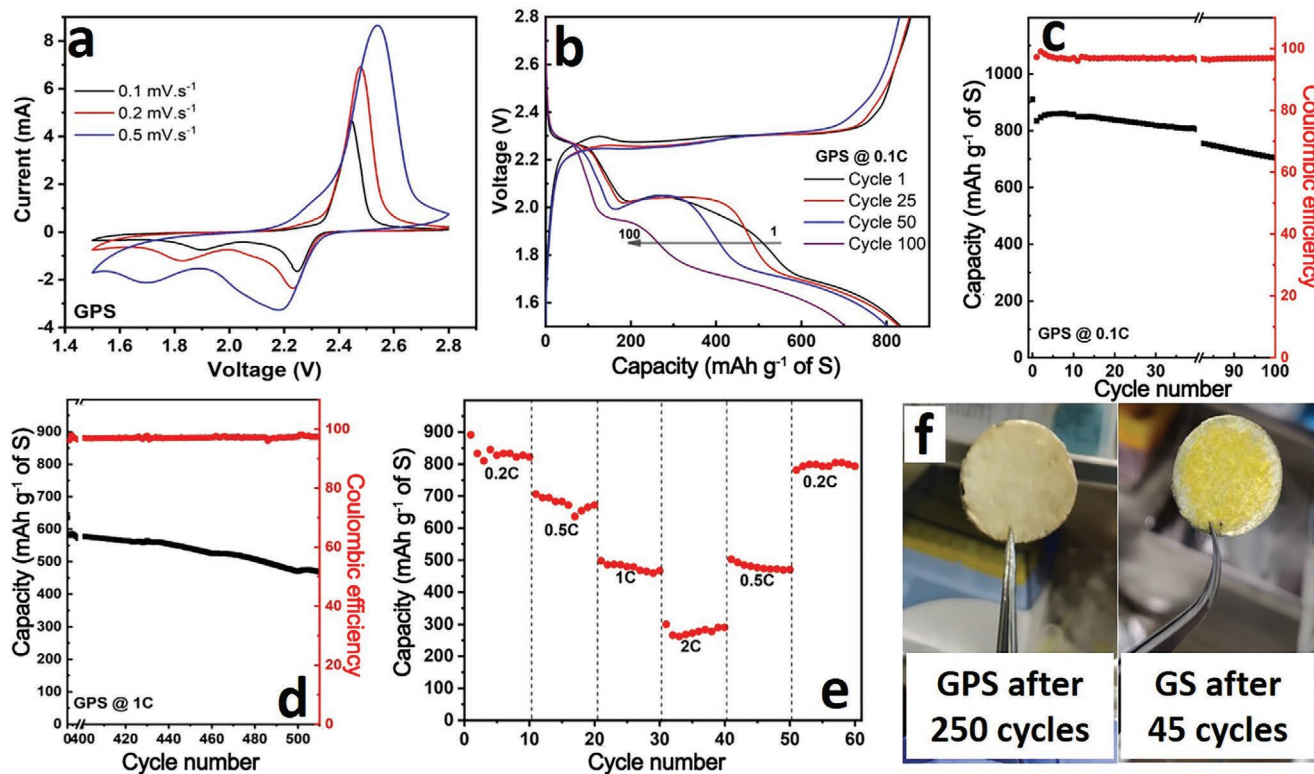


Figure 5. Electrochemical performance of the GPS cathode against lithium metal in 1 M LiTFSI in 1:1 DOL:TTE electrolyte. a) CV curves at 0.1, 0.2, and 0.5 mV g⁻¹, b) charge/discharge profiles at 0.1 C, c,d) cycling performance at different C-rates, e) rate capability at rates varied from 0.2 to 2 C, and f) photos of the glass fiber separator after cycling for the GPS and GS cathodes (1 C = 1672 mA g⁻¹). The specific capacities in the figure refer to the sulfur-based mass.

100 cycles, respectively (Figure 5c,d; Figure S7, Supporting Information). The 700 mAh g⁻¹ value corresponds to 630 mAh g⁻¹ with respect to the active material (90% GPS content), and 507 mAh g⁻¹ with respect to the whole cathode material mass (Table S1, Supporting Information). The cathode was also endowed with excellent rate capability (Figure 5e), with capacities of 485 mAh g⁻¹ at 1 C (1.67 A g⁻¹) and 290 mAh g⁻¹ even at 2 C (3.3 A g⁻¹). Importantly, after the rate capability test, the cathode regained its initial capacity of ≈800 mAh g⁻¹, when the C-rate returned back at 0.2 C (Figure 5e).

The above results were attainable only in the case of GPS, since the non-covalent GS derivative obtained with elemental sulfur showed very low initial capacity of 380 and ≈260 mAh g⁻¹ after only 15 cycles at 1 C (Figure S8, Supporting Information), tested under the same conditions as the GPS cathode. Moreover, the initial Coulombic efficiency was 108%, indicating a very strong shuttling-effect during the first charge.^[61] The dissolution of the yellow elemental sulfur was also clearly visible in the glass fiber separator after 45 cycles of the GS cathode (Figure 5f), in contrast to the case of GPS.

To interpret the results in perspective with the current state of the art, a comparison between the GPS cathode and other sulfur-based materials studied in LSBs was necessary (Table S1, Supporting Information). The capacity values were calculated with respect to the total mass of the cathode material containing all additives and non-active components, at the last recorded cycle, which is beneficial for evaluating better their

practical application potential. Most of the so far developed cathodes required high amounts of conductive additives (e.g., 20 mass%, ref. [62–65] 10 mass%, ref. [66–69]), or/and could sustain only low sulfur loadings,^[25,63,64,66–70] thus compromising the full-cathode-mass capacity. For example, Zhou et al.^[67] achieved 600 mAh g⁻¹ at 0.5 C, which translated into 220 mAh g⁻¹ with respect to full cathode mass, since the sulfur content was limited at 46 mass%. Similarly, Zheng et al.^[71] reported an outstanding capacity of 775 mAh g⁻¹ after 150 cycles, but this value reduced to 400 mAh g⁻¹ with respect to full cathode mass. In another instance, carbonized metal organic framework crystals to trap sulfur in the pores, interwoven with carbon nanotubes to increase conductivity, delivered 650 mAh g⁻¹ at 0.2 C, but only 260 mAh g⁻¹ with respect to full cathode mass.^[25] In addition, the use of nonconductive metal oxides (MgO,^[62] or BaTiO₃^[64]) to capture the lithium PSs resulted to 60–66% sulfur loading, but a 20% conductive binder was necessary. Furthermore, quite often, multistep and high temperature procedures were required, increasing the cost and environmental impact of the products.^[24,29,70,72–75] For example, Zhang et al.^[29] reported carbon nanocages as a sulfur host achieving 77 mass% sulfur loading and good electrochemical performance. However, the synthetic procedure required the preparation of graphene oxide, reduction with hydrazine, immobilization of a polymer, growth of iron oxide nanoparticles, high temperature hydrothermal treatment for 15 h, calcination at 800 °C, and acidic dissolution of the inorganic particles, before the loading of sulfur

through additional steps. Therefore, the herein GPS cathode presented very high full-cathode-mass capacities and rate capability combined with outstanding cycling stability (464 mAh g⁻¹ after 250 cycles at 0.2 C), attained through a particularly simple, one-step procedure, via the chemical reaction of FG with NaPS in NMP at 80 °C. Importantly, these features were attained at a controlled low-temperature of 25 °C, unlike other top-rated materials whose performance is not yet connected with specific temperature conditions.^[32,74–76] This is of particular importance since the usually fluorinated electrolytes or additives used in LSBs are of high viscosity, thus small temperature differences induce dramatic changes on the capacities recorded.^[77,78] It should be emphasized that for the reaction there was no size-selection procedure after the sonication of bulk graphite fluoride, leading to full material economy, which is of significant importance for the cost and applicability of the cathode. This is further strengthened considering that graphite fluoride, first synthesized in 1934^[79,80] and heavily explored since the 70's as a primary lithium battery electrode^[81,82] (Matsushita Electric Co. 1975^[83]), is easily accessible on the market and produced in large quantities as an industrial lubricant.^[84–86]

3. Conclusion

An efficient and straightforward approach to prepare a highly and covalently sulfurized graphene cathode for LSBs is reported, exploiting the nucleophilicity of PS anions and the electrophilic centers in FG. The chemical reaction affords an electrochemically active cathode material with a remarkably high covalent sulfur content of 80 mass%. The covalent bonding was clearly observed and verified with infrared and Raman spectroscopies, as well as with theoretical calculations unveiling the mechanism of the nucleophilic attack of the PS chains primarily on carbons adjacent to fluorinated areas. Electrochemical cycling of the sulfurized-graphene material against metallic lithium exhibited top-rated performance with only 5 mass% of conductive additives and at a low temperature of 25 °C. The cathode showed high sulfur utilization and specific capacities at both low and high current rates, excellent cycling stability, and high rate capabilities. The described methodology offers an effective pathway for the development and study of previously unexplored cathode materials for LSBs, exploiting the alkylhalide-like and elegant chemistry of fluorinated carbon matrices. The simple, eco-friendly, and cost-effective cathode combined with the very high sulfur loading could represent a strong candidate for practically efficient LSBs.

4. Experimental Section

Sodium Polysulfide Preparation: 1 M of sodium sulfide nonahydrate (Na₂S·9H₂O) was dissolved in a water-ethanol mixed solvent (1:1 volume ratio) and 1 M of sulfur (S) was added subsequently. The solution turned from yellow to dark orange indicating the gradually increasing chain-length of the PSs while reacting at 30 °C for 3 h (Figure S9, Supporting Information).^[34] The solvent was vacuum dried and the residue was milled in a mortar to create a fine powder.

GPS Preparation and Control Samples: To prepare the covalently modified graphene with sulfur (GPS), FG (250 mg) was stirred in NMP (15 mL) for

48 h at room temperature, followed by further exfoliation via sonication for 4 h. After the exfoliation, NaPS (2 g) was added and the mixture reacted at 80 °C under reflux for 48 h, in N₂ atmosphere. The final product (GPS) was centrifuged, washed with NMP, distilled water, ethanol, and acetone and finally it was freeze dried to form a fine powder.

The same procedure was repeated using electrochemically exfoliated graphene^[87] (instead of FG) and NaPS, affording the control sample EEGS, which contained very low sulfur amount. The reaction between elemental sulfur (instead of NaPS) and FG afforded the control sample GS, with high amount of sulfur, in which C–S covalent bonds were not detected. In both control samples the same mass ratios of C:S were used during the synthesis, as in the main GPS product.

Structural and Chemical Characterization: FT-IR spectra were recorded on an iS5 FTIR spectrometer (Thermo Nicolet) using the KBr pellet accessory. Spectra were recorded by summing 50 scans, using pure KBr for the background acquisition. Baseline corrections were applied to the collected spectra. TGA with EGA was performed with a Netzsch STA 449 C Jupiter thermo-microbalance instrument at a heating rate of 10 °C min⁻¹ under an N₂ flow in the furnace. The masses of released gases over the range 18–64 *m/z* were determined with a QMS 403 Aëolos instrument (Netzsch) under a synthetic air flow. To avoid overloading the spectrometer with adsorbed water, a heating to 100 °C and consequent cooling to room temperature was performed prior to the EGA measurements. Raman spectra were collected using a DXR Raman spectroscope (Thermo Scientific) equipped with a laser operating at a wavelength of 633 nm. XPS was carried out with a PHI VersaProbe II (Physical Electronics) spectrometer using an Al Kα source (15 kV, 50 W). The obtained data were evaluated and deconvoluted with the MultiPak (Ulvac-PHI, Inc.) software package. The spectral analysis included Shirley background subtraction and peak deconvolution employing mixed Gaussian-Lorentzian functions. Electron microscopy images were obtained using a JEOL 2010 TEM equipped with a LaB₆ type emission gun operating at 160 kV. EDS was recorded on an Oxford x-MAX 80T (SSD) at 200 kV accelerating voltage. Scanning transmission electron microscopy high-angle annular dark-field imaging analyses for EDS mapping of elemental distributions on the products were performed with an FEI Titan HRTEM microscope operating at 80 kV.

Theoretical Calculations: To explore possible reaction mechanism of sulfur covalent binding to graphene, DFT calculations were performed to model the nucleophilic attack of short PS chains (S_x²⁻, *x* = 2, 4, and 6) on various FG structures. Ground state structures of all investigated species were optimized at the ωB97X-D/6-31++G(d,p) level of theory^[88,89] using Gaussian16 software.^[90] Solvent effects were taken into account by the universal continuum solvation model based on electron density (SMD).^[91] Ovalene molecule with three different levels of fluorination was used as a model of partially defluorinated FG (Figures S2–S4, Supporting Information).

Electrochemical Characterization: The slurries were prepared by mixing the active material (GPS), Ketjen black and polyvinylidene fluoride (polymer binder) with a weight ratio of 90:5:5 (total mass 40 mg), using NMP as solvent (around 0.4 mL). The homogenization of the slurries was performed in a ultrasonication bath for 2 h to break any agglomerates and then using a planetary mixer (Thinky ARV-310LED) for 10 min at 2000 rpm under vacuum. This procedure was repeated three times.

After homogenization, the slurries were casted, on a carbon coated Al foil, which was used as a substrate and current collector, using a 180 μm stainless steel doctor blade. After casting, the electrodes were dried at 80 °C under vacuum overnight. The mass loading of total material on an 18 mm diameter coin was ≈4 mg (≈1.6 or 1.15 mg cm⁻² of sulfur). The electrodes were tested in sealed electrochemical cells (El-cell) using lithium foil as the counter electrode, and a glass fiber separator (0.26 mm, El-cell). The electrolyte contained 1 M LiTFSI (Aldrich) in a mixed solvent of 1,3-dioxolane (DOL, Aldrich) and dimethoxy ethane (DME, Aldrich) or TTE (TCI) (DOL:DME or DOL/TTE, 1:1 by volume) and 100 μL of the electrolyte was introduced in each cell.

The cells were assembled in Ar-filled glovebox (both H₂O and O₂ contents were below 1.0 ppm). Galvanostatic discharge/charge test was

carried out on a battery test system (BCS-810, Biologic) in the range of 1.5–2.8 V at 25 °C. Cyclic voltammetry was performed at different scan rates from 0.1 to 0.5 mV s⁻¹. All the current densities, C-rates, and specific capacities were based on the weight of sulfur (unless otherwise stated).

Supporting Information

Supporting Information is available from the Wiley Online Library or from the author.

Acknowledgements

The work was supported by the ERDF/ESF project “Nano4Future” (No. CZ.02.1.01/0.0/0.0/16_019/0000754). I.T. acknowledges the support by the Operational Programme Research, Development and Education—Project No. CZ.02.1.01/0.0/0.0/15_003/0000416 of the Ministry of Education, Youth and Sports of the Czech Republic. R.Z. and A.B. acknowledge the funding from the Czech Science Foundation, project GA CR—EXPRO, 19-27454X. M.O. acknowledges the ERC grand 2D-CHEM, No 683024 from H2020. Operation of XPS and TEM facilities were partly funded from by the Research Infrastructure NanoEnviCz, supported by the Ministry of Education, Youth and Sports of the Czech Republic under Project No. LM2018124. D.Z. thanks the Student project by Palacký University Olomouc (IGA_PrF_2021_031). J.H. thanks the Student project by Palacký University Olomouc (IGA_PrF_2020_011). The authors thank V. Šedajová for XPS, J. Stráská and O. Tomanec for TEM/HR-TEM, E. Ioannou and C. M. Reyes Pérez for SEM, and K. Štymplová for Raman measurements.

Conflict of Interest

A European patent application is currently under consideration.

Data Availability Statement

Data available from the authors upon request

Keywords

covalent functionalization, crosslinking, fluorographene, graphene, lithium–sulfur batteries, sodium polysulfide

Received: February 7, 2021

Revised: March 31, 2021

Published online:

- [1] M. Armand, J.-M. Tarascon, *Nature* **2008**, 451, 652.
 [2] N.-S. Choi, Z. Chen, S. A. Freunberger, X. Ji, Y.-K. Sun, K. Amine, G. Yushin, L. F. Nazar, J. Cho, P. G. Bruce, *Angew. Chem., Int. Ed.* **2012**, 51, 9994.
 [3] J. Liu, Z. Bao, Y. Cui, E. J. Dufek, J. B. Goodenough, P. Khalifah, Q. Li, B. Y. Liaw, P. Liu, A. Manthiram, Y. S. Meng, V. R. Subramanian, M. F. Toney, V. V. Viswanathan, M. S. Whittingham, J. Xiao, W. Xu, J. Yang, X.-Q. Yang, J.-G. Zhang, *Nat. Energy* **2019**, 4, 180.
 [4] N. Nitta, F. Wu, J. T. Lee, G. Yushin, *Mater. Today* **2015**, 18, 252.
 [5] S. Evers, L. F. Nazar, *Acc. Chem. Res.* **2013**, 46, 1135.
 [6] Y.-X. Yin, S. Xin, Y.-G. Guo, L.-J. Wan, *Angew. Chem., Int. Ed.* **2013**, 52, 13186.

- [7] H.-J. Peng, J.-Q. Huang, X.-B. Cheng, Q. Zhang, *Adv. Energy Mater.* **2017**, 7, 1700260.
 [8] Y.-S. Su, Y. Fu, T. Cochell, A. Manthiram, *Nat. Commun.* **2013**, 4, 2985.
 [9] J. D. V. Hamme, A. Singh, O. P. Ward, *Microbiol. Mol. Biol. Rev.* **2003**, 67, 503.
 [10] D. Peramunage, S. Licht, *Science* **1993**, 261, 1029.
 [11] P. G. Bruce, S. A. Freunberger, L. J. Hardwick, J.-M. Tarascon, *Nat. Mater.* **2012**, 11, 19.
 [12] X. Ji, K. T. Lee, L. F. Nazar, *Nat. Mater.* **2009**, 8, 500.
 [13] A. Bhargava, J. He, A. Gupta, A. Manthiram, *Joule* **2020**, 4, 285.
 [14] A. Manthiram, Y. Fu, Y.-S. Su, *Acc. Chem. Res.* **2013**, 46, 1125.
 [15] Y. V. Mikhaylik, J. R. Akridge, *J. Electrochem. Soc.* **2004**, 151, A1969.
 [16] Z. W. Seh, W. Li, J. J. Cha, G. Zheng, Y. Yang, M. T. McDowell, P.-C. Hsu, Y. Cui, *Nat. Commun.* **2013**, 4, 1331.
 [17] X. Ji, S. Evers, R. Black, L. F. Nazar, *Nat. Commun.* **2011**, 2, 325.
 [18] W. G. Chong, J.-Q. Huang, Z.-L. Xu, X. Qin, X. Wang, J.-K. Kim, *Adv. Funct. Mater.* **2017**, 27, 1604815.
 [19] G. Zhou, L. Li, D.-W. Wang, X. Shan, S. Pei, F. Li, H.-M. Cheng, *Adv. Mater.* **2015**, 27, 641.
 [20] Y. He, Y. Qiao, H. Zhou, *Dalton Trans.* **2018**, 47, 6881.
 [21] B. Liu, R. Bo, M. Taheri, I. Di Bernardo, N. Motta, H. Chen, T. Tsuzuki, G. Yu, A. Tricoli, *Nano Lett.* **2019**, 19, 4391.
 [22] L. Xiao, Y. Cao, J. Xiao, B. Schwenzer, M. H. Engelhard, L. V. Saraf, Z. Nie, G. J. Exarhos, J. Liu, *Adv. Mater.* **2012**, 24, 1176.
 [23] W. Qian, Q. Gao, Z. Li, W. Tian, H. Zhang, Q. Zhang, *ACS Appl. Mater. Interfaces* **2017**, 9, 28366.
 [24] Y. Liu, G. Li, J. Fu, Z. Chen, X. Peng, *Angew. Chem., Int. Ed.* **2017**, 56, 6176.
 [25] Y. Mao, G. Li, Y. Guo, Z. Li, C. Liang, X. Peng, Z. Lin, *Nat. Commun.* **2017**, 8, 14628.
 [26] J. Wang, Y.-S. He, J. Yang, *Adv. Mater.* **2015**, 27, 569.
 [27] B. Wang, T. Ruan, Y. Chen, F. Jin, L. Peng, Y. Zhou, D. Wang, S. Dou, *Energy Storage Mater.* **2020**, 24, 22.
 [28] R. Fang, K. Chen, L. Yin, Z. Sun, F. Li, H.-M. Cheng, *Adv. Mater.* **2019**, 31, 1800863.
 [29] J. Zhang, C.-P. Yang, Y.-X. Yin, L.-J. Wan, Y.-G. Guo, *Adv. Mater.* **2016**, 28, 9539.
 [30] J. Li, J. Zhou, T. Wang, X. Chen, Y. Zhang, Q. Wan, J. Zhu, *Nanoscale* **2020**, 12, 8991.
 [31] L. Fan, R. Ma, Y. Yang, S. Chen, B. Lu, *Nano Energy* **2016**, 28, 304.
 [32] G. Li, J. Sun, W. Hou, S. Jiang, Y. Huang, J. Geng, *Nat. Commun.* **2016**, 7, 10601.
 [33] F. Liu, J. Liang, C. Zhang, L. Yu, J. Zhao, C. Liu, Q. Lan, S. Chen, Y.-C. Cao, G. Zheng, *Results Phys.* **2017**, 7, 250.
 [34] Y. Zhang, Y. Peng, Y. Wang, J. Li, H. Li, J. Zeng, J. Wang, B. J. Hwang, J. Zhao, *Sci. Rep.* **2017**, 7, 11386.
 [35] A. Bakandritsos, M. Pykal, P. Błoński, P. Jakubec, D. D. Chronopoulos, K. Poláková, V. Georgakilas, K. Čépe, O. Tomanec, V. Ranc, A. B. Bourlinos, R. Zbořil, M. Otyepka, *ACS Nano* **2017**, 11, 2982.
 [36] D. D. Chronopoulos, A. Bakandritsos, M. Pykal, R. Zbořil, M. Otyepka, *Appl. Mater. Today* **2017**, 9, 60.
 [37] M. Medved, G. Zoppellaro, J. Ugolotti, D. Matochová, P. Lazar, T. Pospíšil, A. Bakandritsos, J. Tuček, R. Zbořil, M. Otyepka, *Nanoscale* **2018**, 10, 4696.
 [38] D. Matochová, M. Medved, A. Bakandritsos, T. Steklý, R. Zbořil, M. Otyepka, *J. Phys. Chem. Lett.* **2018**, 9, 3580.
 [39] R. Steudel, in *Encyclopedia of Inorganic Chemistry*, Wiley, Hoboken, NJ **2007**.
 [40] H. Becker, W. Berger, G. Domschke, *Organicum: Practical Handbook of Organic Chemistry*, Elsevier, Amsterdam **2013**.
 [41] D. D. Chronopoulos, M. Medved, G. Potsi, O. Tomanec, M. Scheibe, M. Otyepka, *Chem. Commun.* **2020**, 56, 1936.
 [42] S. S. Zhang, *Front. Energy Res.* **2013**, 1, 10.

- [43] S. W. Shin, J. H. Han, J. Y. Lee, Y. C. Park, G. L. Agawane, A. V. Moholkar, M.-G. Gang, C. H. Jeong, J. H. Kim, J. H. Yun, *Appl. Surf. Sci.* **2013**, 270, 572.
- [44] E. C. Vermisoglou, P. Jakubec, A. Bakandritsos, M. Pykal, S. Talande, R. Zboril, *Chem. Mater.* **2019**, 31, 4698.
- [45] Y. Z. Zhang, S. Liu, G. C. Li, G. R. Li, X. P. Gao, *J. Mater. Chem. A* **2014**, 2, 4652.
- [46] A. T. Ward, *J. Phys. Chem.* **1968**, 72, 4133.
- [47] M. Hagen, P. Schiffels, M. Hammer, S. Dörfler, J. Tübke, M. J. Hoffmann, H. Althues, S. Kaskel, *J. Electrochem. Soc.* **2013**, 160, A1205.
- [48] X. Yu, J. Xie, J. Yang, H. Huang, K. Wang, Z. Wen, *J. Electroanal. Chem.* **2004**, 573, 121.
- [49] A. C. Ferrari, D. M. Basko, *Nat. Nanotechnol.* **2013**, 8, 235.
- [50] J. M. Englert, P. Vecera, K. C. Knirsch, R. A. Schäfer, F. Hauke, A. Hirsch, *ACS Nano* **2013**, 7, 5472.
- [51] A. Kouloumpis, D. D. Chronopoulos, G. Potsi, M. Pykal, J. Vlček, M. Scheibe, M. Otyepka, *Chem. - Eur. J.* **2020**, 26, 6518.
- [52] F. Karlický, E. Otyepková, R. Lo, M. Pitoňák, P. Jurečka, M. Pykal, P. Hobza, M. Otyepka, *J. Chem. Theory Comput.* **2017**, 13, 1328.
- [53] M. Fantauzzi, *RSC Adv.* **2015**, 5, 75953.
- [54] V. Urbanová, K. Holá, A. B. Bourlinos, K. Čépe, A. Ambrosi, A. H. Loo, M. Pumera, F. Karlický, M. Otyepka, R. Zbořil, *Adv. Mater.* **2015**, 27, 2305.
- [55] X. Wang, W. Wang, Y. Liu, M. Ren, H. Xiao, X. Liu, *Phys. Chem. Chem. Phys.* **2016**, 18, 3285.
- [56] W. Weng, V. G. Pol, K. Amine, *Adv. Mater.* **2013**, 25, 1608.
- [57] M.-Q. Zhao, Q. Zhang, J.-Q. Huang, G.-L. Tian, J.-Q. Nie, H.-J. Peng, F. Wei, *Nat. Commun.* **2014**, 5, 3410.
- [58] R. Fang, S. Zhao, Z. Sun, D.-W. Wang, H.-M. Cheng, F. Li, *Adv. Mater.* **2017**, 29, 1606823.
- [59] S. Xin, L. Gu, N.-H. Zhao, Y.-X. Yin, L.-J. Zhou, Y.-G. Guo, L.-J. Wan, *J. Am. Chem. Soc.* **2012**, 134, 18510.
- [60] M. Cuisinier, P.-E. Cabelguen, B. D. Adams, A. Garsuch, M. Balasubramanian, L. F. Nazar, *Energy Environ. Sci.* **2014**, 7, 2697.
- [61] R. Elazari, G. Salitra, A. Garsuch, A. Panchenko, D. Aurbach, *Adv. Mater.* **2011**, 23, 5641.
- [62] X. Tao, J. Wang, C. Liu, H. Wang, H. Yao, G. Zheng, Z. W. Seh, Q. Cai, W. Li, G. Zhou, C. Zu, Y. Cui, *Nat. Commun.* **2016**, 7, 11203.
- [63] S.-K. Park, J. Lee, T. Hwang, Y. Piao, *J. Mater. Chem. A* **2017**, 5, 975.
- [64] K. Xie, Y. You, K. Yuan, W. Lu, K. Zhang, F. Xu, M. Ye, S. Ke, C. Shen, X. Zeng, X. Fan, B. Wei, *Adv. Mater.* **2017**, 29, 1604724.
- [65] D. Cai, M. Lu, L. Li, J. Cao, D. Chen, H. Tu, J. Li, W. Han, *Small* **2019**, 15, 1902605.
- [66] Z. Xu, J. Wang, J. Yang, X. Miao, R. Chen, J. Qian, R. Miao, *Angew. Chem., Int. Ed.* **2016**, 55, 10372.
- [67] Y. Zhou, C. Zhou, Q. Li, C. Yan, B. Han, K. Xia, Q. Gao, J. Wu, *Adv. Mater.* **2015**, 27, 3774.
- [68] Q. Sun, B. He, X.-Q. Zhang, A.-H. Lu, *ACS Nano* **2015**, 9, 8504.
- [69] M. Yu, J. Ma, M. Xie, H. Song, F. Tian, S. Xu, Y. Zhou, B. Li, D. Wu, H. Qiu, R. Wang, *Adv. Energy Mater.* **2017**, 7, 1602347.
- [70] X. Yang, L. Zhang, F. Zhang, Y. Huang, Y. Chen, *ACS Nano* **2014**, 8, 5208.
- [71] J. Zheng, G. Ji, X. Fan, J. Chen, Q. Li, H. Wang, Y. Yang, K. C. DeMella, S. R. Raghavan, C. Wang, *Adv. Energy Mater.* **2019**, 9, 1803774.
- [72] R. Fang, S. Zhao, S. Pei, X. Qian, P.-X. Hou, H.-M. Cheng, C. Liu, F. Li, *ACS Nano* **2016**, 10, 8676.
- [73] X. Liang, Y. Rangom, C. Y. Kwok, Q. Pang, L. F. Nazar, *Adv. Mater.* **2017**, 29, 1603040.
- [74] G. Hu, C. Xu, Z. Sun, S. Wang, H.-M. Cheng, F. Li, W. Ren, *Adv. Mater.* **2016**, 28, 1603.
- [75] H. Zhang, W. Zhao, M. Zou, Y. Wang, Y. Chen, L. Xu, H. Wu, A. Cao, *Adv. Energy Mater.* **2018**, 8, 1800013.
- [76] H.-J. Peng, J.-Q. Huang, M.-Q. Zhao, Q. Zhang, X.-B. Cheng, X.-Y. Liu, W.-Z. Qian, F. Wei, *Adv. Funct. Mater.* **2014**, 24, 2772.
- [77] C.-W. Lee, Q. Pang, S. Ha, L. Cheng, S.-D. Han, K. R. Zavadil, K. G. Gallagher, L. F. Nazar, M. Balasubramanian, *ACS Cent. Sci.* **2017**, 3, 605.
- [78] C. V. Amanchukwu, Z. Yu, X. Kong, J. Qin, Y. Cui, Z. Bao, *J. Am. Chem. Soc.* **2020**, 142, 7393.
- [79] O. Ruff, O. Bretschneider, *Z. Anorg. Allg. Chem.* **1934**, 217, 1.
- [80] Y. Liu, L. Jiang, H. Wang, H. Wang, W. Jiao, G. Chen, P. Zhang, D. Hui, X. Jian, *Nanotechnol. Rev.* **2019**, 8, 573.
- [81] J. Liu, Y. Wan, W. Liu, Z. Ma, S. Ji, J. Wang, Y. Zhou, P. Hodgson, Y. Li, *J. Mater. Chem. A* **2013**, 1, 1969.
- [82] N. F. Watanabe, US3700502A **1972**.
- [83] M. Fukuda, T. Iijima, in *Power Sources 5*, (Ed: D. H. Collins) Academic Press, New York **1975**, 5, p. 713.
- [84] X. Ye, L. Ma, Z. Yang, J. Wang, H. Wang, S. Yang, *ACS Appl. Mater. Interfaces* **2016**, 8, 7483.
- [85] R. L. Fusaro, H. E. Sliney, A. S. L. E. *Trans.* **1970**, 13, 56.
- [86] N. Watanabe, T. H. Nakajima Touhara, in *Graphite Fluorides: Studies in Inorganic Chemistry*, Vol. 8, Elsevier, Amsterdam **1988**.
- [87] H. Barès, A. Bakandritsos, M. Medved, J. Ugolotti, P. Jakubec, O. Tomanec, S. Kalytchuk, R. Zbořil, M. Otyepka, *Carbon* **2019**, 145, 251.
- [88] J.-D. Chai, M. Head-Gordon, *Phys. Chem. Chem. Phys.* **2008**, 10, 6615.
- [89] R. Ditchfield, W. J. Hehre, J. A. Pople, *J. Chem. Phys.* **1971**, 54, 724.
- [90] M. J. Frisch, G. W. Trucks, H. B. Schlegel, G. E. Scuseria, M. A. Robb, J. R. Cheeseman, G. Scalmani, V. Barone, G. A. Petersson, H. Nakatsuji, X. Li, M. Caricato, A. Marenich, J. Bloino, B. G. Janesko, R. Gomperts, B. Mennucci, H. P. Hratchian, J. V. Ortiz, A. F. Izmaylov, J. L. Sonnenberg, D. Williams-Young, F. Ding, F. Lipparini, F. Egidi, J. Goings, B. Peng, A. Petrone, T. Henderson, D. Ranasinghe, et al, *Gaussian 09, Revision A.02*, Gaussian, Inc., Wallingford CT **2016**.
- [91] A. V. Marenich, C. J. Cramer, D. G. Truhlar, *J. Phys. Chem. B* **2009**, 113, 6378.

F

Anchoring of Transition Metals to Graphene
Derivatives as an Efficient Approach for
Designing Single-Atom Catalysts

Anchoring of Transition Metals to Graphene Derivatives as an Efficient Approach for Designing Single-Atom Catalysts

Dagmar Zaoralová, Radim Mach, Petr Lazar, Miroslav Medved',* and Michal Otyepka*

Graphene derivatives with anchored metal atoms represent a promising class of single-atom catalysts (SACs). To elucidate factors determining the bond strength between metal atoms and graphene derivatives, a series of late 3d and 4d elements, including the iron triad, light platinum group elements, and coinage metals (Fe, Co, Ni, Ru, Rh, Pd, Cu, Ag, and Au), in different oxidation states (from 0 to +III) bonded to either cyanographene (CG) or graphene acid (GA) is explored. The vast diversity of N...Me and O...Me bond dissociation energies is related to charge transfer between the metal and substrate. The ability of CG and GA to reduce metal cations and oxidize metal atoms is attributed to the π -conjugated lattice of the graphene derivatives. The binding energies of core electrons of the anchored metals are predicted to enable experimental identification via X-ray photoelectron spectroscopy. The anchoring of metals is accompanied by either complete or partial spin quenching, leading in most cases to the same oxidation state of the metal regardless of its initial charge. The identified features can be utilized in designing new materials with a high potential in heterogenous SACs as well as electrochemical and spintronic applications.

the hydrophilic/hydrophobic, porosity, and surface properties of graphene-based materials.^[7] For a long time, the low reactivity of graphene hindered its controllable sp^3 -functionalization, but various successful strategies have now been proposed, opening up routes toward a vast spectrum of possible graphene derivatives.^[8] In particular, advances in fluorographene (FG)^[9] chemistry have significantly enlarged the family of graphene derivatives with a number of new members.^[10] Hydroxyl, thio, cyano, alkyl/aryl, and doubly functionalized derivatives with controllable composition have been successfully prepared by the partial nucleophilic substitution/reduction of FG.^[10a,11] Cyanographene (CG), i.e., graphene densely functionalized by -CN groups, and its oxidized successor graphene acid (GA), i.e., graphene functionalized by -COOH groups,^[11b] facilitate further functionalization because they

can serve as a covalent trap for metal species, e.g., single metal atoms, ions or metal nanoclusters.^[12]

Single metal atoms immobilized on a supporting material have been used in heterogenous catalysis as so-called single-atom catalysts (SACs).^[13] Owing to reduced size of metal particles, the SACs exhibit extraordinary catalytic activity and selectivity. Thus far, SACs have been employed in CO oxidation,^[13a,14] the oxygen reduction reaction,^[15] hydrogen evolution reaction,^[16] selective hydrogenation,^[17] dehydrogenation,^[18] and photocatalytic reactions.^[19] Many different materials such as potassium vanadate/carbon nanoribbon networks,^[20] graphitic carbon nitride,^[21] nitrogen-doped graphene,^[22] defective nanodiamond-graphene hybrid,^[17c,17d,18] MXene,^[23] alumina,^[14c] and metal organic framework^[16c,24] have been employed as a support of SACs which are synthesized mostly via thermal exfoliation, atomic-layer deposition, wet impregnation, and hydrothermal methods. However, these methods usually require high temperatures and/or reducing atmosphere, and thus resulting materials can act as a support only to a narrow group of metal elements. On the other hand, owing to the facile synthesis and the presence of homogeneously distributed -CN and -COOH groups, CG and GA can serve as low-cost and stable platforms for a wide portfolio of metal atoms and cations implying their high potential for SACs applications.


Recently, CG has been employed for the robust coordination of Cu(II)/Cu(I) ions, resulting in a mixed-valence catalyst

1. Introduction

Graphene derivatives belong to the most studied 2D materials owing to their extraordinary chemical, electronic, and magnetic properties, which have been utilized in an ever-growing range of applications, including electronics, spintronics, catalysis, and energy storage.^[1] The potential applications of graphene have been significantly extended by both doping and functionalization.^[2] Substitutional doping of the lattice carbons by heteroatoms, such as nitrogen,^[3] boron,^[4] and sulfur,^[5] has been established as an efficient way to modulate the electronic, magnetic, and spintronic properties of graphene.^[6] Noncovalent functionalization enables control over

D. Zaoralová, R. Mach, Dr. P. Lazar, Dr. M. Medved', Prof. M. Otyepka
Regional Centre of Advanced Technologies and Materials
Faculty of Science
Palacký University Olomouc
Šlechtitelů 27, Olomouc 783 71, Czech Republic
E-mail: miroslav.medved@upol.cz; michal.otyepka@upol.cz

D. Zaoralová, R. Mach
Department of Physical Chemistry
Faculty of Science
Palacký University Olomouc
17. listopadu 12, Olomouc 786 41, Czech Republic

 The ORCID identification number(s) for the author(s) of this article can be found under <https://doi.org/10.1002/admi.202001392>.

DOI: 10.1002/admi.202001392

that can flawlessly perform the oxidative coupling of amines and oxidation of benzylic C–H bonds.^[12a] Mild impregnation of GA with Pd(OAc)₂ has yielded GA–Pd nanohybrids that can serve as highly active catalysts in the Suzuki–Miyaura cross-coupling reaction.^[12c] Applications of the novel hybrids have not been restricted to catalysis. Single Pt adatoms have been successfully anchored to CG, overcoming their relatively low interaction with a pristine graphene layer.^[25] CG with covalently bound silver has been shown to have unprecedented antibacterial activity, even higher than that of free ionic silver (D. Panáček, work in preparation). The charge transfer between an atom/ion and CG/GA support may also be utilized in graphene-based supercapacitors.^[26] However, anchoring of single metal atoms on graphene-based substrates remains challenging due to competitive processes, such as aggregation into larger clusters or adsorption onto the graphene plane or into defects in the graphene lattice.^[27] Chemical moieties such as nitrile and carboxyl groups homogeneously distributed on a graphene lattice can improve the binding of single atoms and prevent undesirable processes.

In the work described in this paper, we aimed to gain a general overview of the nature of chemical binding and oxidation states of single metal atoms and ions grafted on CG and GA substrates through density functional theory calculations. An extensive series of model structures containing atoms and ions of late 3d and 4d elements, including the iron triad, light platinum group elements, and coinage metals (Fe, Co, Ni, Ru, Rh, Pd, Cu, Ag, and Au), in different oxidation states (ranging from 0 to +III) bonded to CG or GA was analyzed in terms of bond dissociation energy and charge exchange at the PBE0/Def2TZVP level of theory^[28] using the Gaussian09 program.^[29] Solvent effects were taken into account by using the universal continuum solvation model based on electron density.^[30] X-ray photoelectron spectroscopy (XPS) binding energies of the investigated metal atoms and ions were calculated by the FHI-aims code^[31] using the PBE0 functional with the *tight* basis set (for further computational details, see the Supporting Information) to facilitate experimental identification of the hybrid materials. We anticipate that all the considered nanomaterials are stable enough to be considered suitable SACs, although those containing metals in low oxidation states may suffer from competitive processes, such as on-surface adsorption and/or agglomeration, especially in polar environments.

2. Results and Discussion

First, we compared the bond dissociation energies (BDEs) of the metal atoms and ions in the gas phase. BDEs largely depend on the oxidation state (charge) of the metal ion rather than the chemical nature of the element (Figure 1). In the gas phase, the range of BDEs was rather wide—from ≈5 to 50 kcal mol⁻¹ in the case of zero-valent metal atoms (Figure 1b,c, red bars), 50 to 80 kcal mol⁻¹ for Me⁺ (Figure 1b,c, green bars), 240 to 370 kcal mol⁻¹ for Me²⁺ (Figure 1b,c, blue bars), and 600 to 880 kcal mol⁻¹ for Me³⁺ (Figure 1b,c, orange bars). It is also worth noting that in the gas phase, the BDE values of a particular metal atom/cation on CG and protonated GA were comparable

(maximum difference of ≈15 kcal mol⁻¹, Table S1, Supporting Information).

The aqueous environment significantly narrowed the range of BDEs (Figure 1d,i)—from 1 kcal mol⁻¹ (Au⁰ on CG) to 329 kcal mol⁻¹ (Au³⁺ on dp-GA), and also differences between the oxidation states were less regular, indicating a strong impact of the polar solvent on the stability of CG/GA⋯Me complexes in solution. Since we considered the deprotonated form of GA (i.e., dp-GA) in the aqueous environment, BDEs of metal cations on dp-GA were larger than those on CG (by 2–7 kcal mol⁻¹ in the case of Me⁺, 19–24 kcal mol⁻¹ for Me²⁺, and 31–41 kcal mol⁻¹ for Me³⁺, see Table S2, Supporting Information) due to stronger electrostatic interactions between the metal and dp-GA.

Importantly, metal atoms and cations in oxidation states +I may also adsorb on the graphene plane and/or into vacancies in the graphene structure since the adsorption energies in the gas phase ranged from ≈1 to 60 kcal mol⁻¹ on these sites,^[27] comparable to the BDEs from nitrile and carboxyl groups. Moreover, aggregation of Me⁰ and Me⁺ into larger clusters may also occur, which could suppress the catalytic activity of the material (the cohesive energy of the metals ranged from ≈60 to ≈160 kcal mol⁻¹).^[32] However, the BDEs of metals in oxidation states +II and +III were much higher, and therefore Me²⁺ and Me³⁺ ions anchored to -CN and -COOH groups are likely to have higher stability.

Both CG and GA are known to act as electron donating substrates, reducing the charge on an adsorbed metal atom/cation.^[12a,c] The degree of reduction again strongly depends on the initial charge of the binding particle. In the gas phase, the most significant charge transfer (i.e., most dramatic decrease of the initial charge) was found in the case of Me³⁺ and the lowest in the case on Me⁰ (Figure 1c,h). The reduction strengths of CG and GA were comparable, which indicated that the electron donating potential of these two substrates was predominantly associated with the π -conjugated carbon lattice rather than with the functional groups. Although the same trend was observed in the aqueous environment, the charge transfer was significantly suppressed (Figure 1e,j). In addition, although the negatively charged carboxylate group was involved in charge transfer between dp-GA and the metal (vide infra), the reduction capacity of dp-GA was only very slightly larger than that of CG (the differences in the transferred charge were in the range of 0.0–0.3 e, see Table S2, Supporting Information).

Similar trends in BDEs and the resultant charges confirmed the expected connection between these two parameters. In the gas phase, there was a strong correlation between the BDE and charge transferred between the metal and CG (Δq) (Figure 2a, coefficient of determination $R^2 = 0.93$). However, the correlation was practically lost in water (Figure 2b, $R^2 = 0.17$). This was apparently related to solvation effects. Cations possessing higher initial charge were more stabilized in the aqueous environment. Thus, their BDE values were more reduced. Indeed, after subtraction of the solvation energy (E_{solv}) from the BDE, pair correlation showed a notably higher coefficient of determination ($R^2 = 0.62$, Figure S2a, Supporting Information), although not as high as in the gas phase. Analogous results were obtained for GA/dp-GA (Figures S2b and S3, Supporting Information).

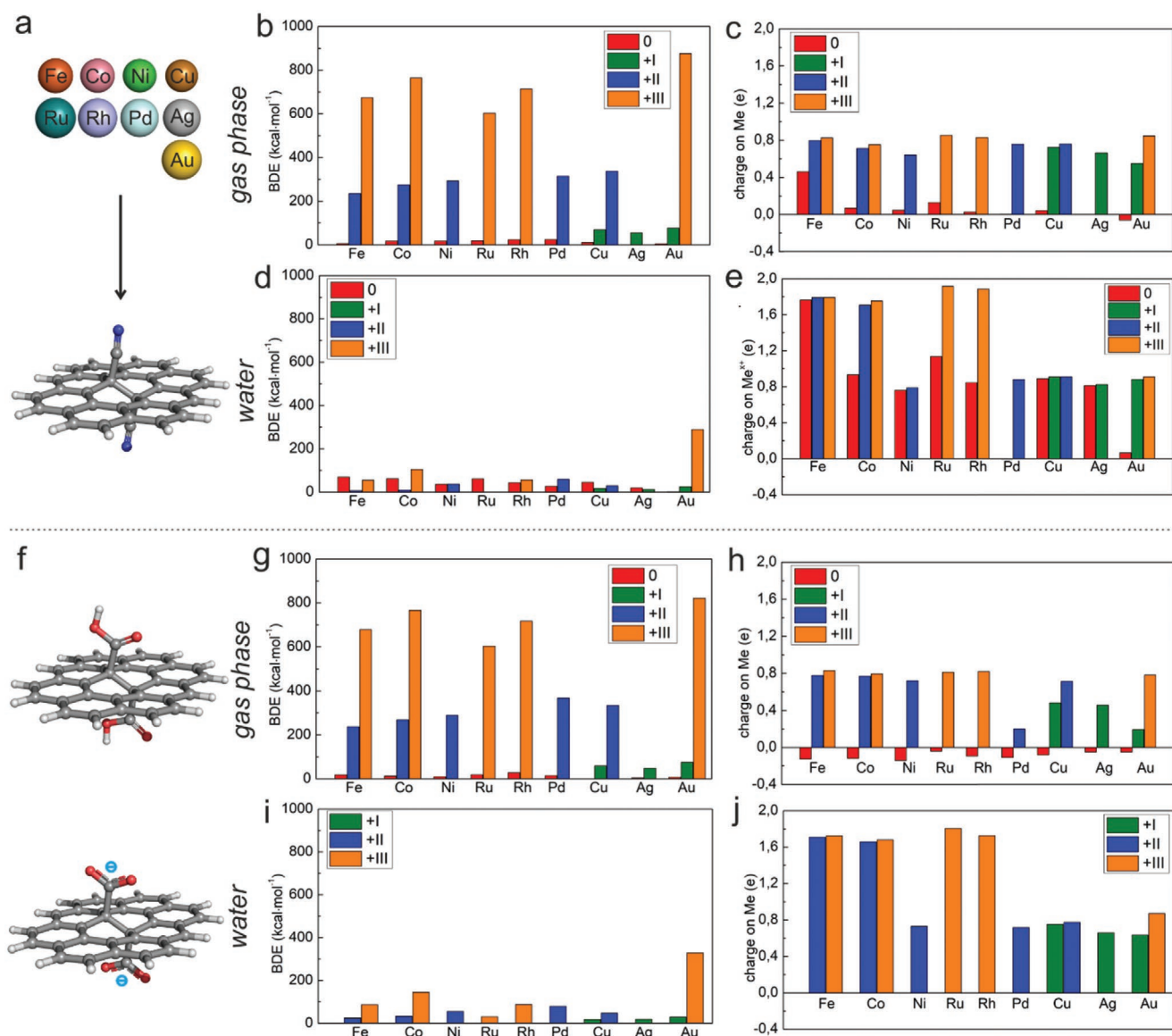


Figure 1. a,f) Scheme of considered metal elements and model molecules representing CG (top), GA neutral (middle), and deprotonated GA (dp-GA, bottom). BDEs of metals on b,d) CG and g,i) GA in the gas phase and dp-GA in aqueous solution, respectively. Mulliken charges on metal atoms/cations after binding on c,e) CG and h,j) GA/dp-GA in the gas phase and water, respectively. The colors of the bars indicate the initial charge on the metal atom/cation. Carbon atoms are gray, nitrogen blue, oxygen red, and hydrogen white.

To elucidate the rules that govern the charge transfer between the metals and substrate, we also plotted results for the pair correlation of Δq and electron affinity (EA)^[33] of metal atoms/cations (Figure 2c,d for CG and Figure S3c,d, Supporting Information, for GA/dp-GA). The plots showed a strong dependence ($R^2 = 0.98$ for CG and 0.95 for GA) in the gas phase and notably lower correlation ($R^2 = 0.77$ and 0.65 for CG and dp-GA, respectively) in water. Thus, the reduction of metals is largely ruled by their electron affinity in the gas phase, whereas in the aqueous environment other factors, such as the polarity of the CG/dp-GA \cdots Me^{x+} bond, hydration enthalpy of partially reduced Me^{x+} and MO energy shifts (vide infra), can also play an important role. In general, the metal cations were reduced less in water than in the gas phase.

2.1. Iron Triad (Fe, Co, Ni)

Whereas the metal cations acted as electron acceptors, most of zero-valent metals (Fe, Co, Ni, Ru, Rh together with Cu and Ag) were oxidized, and their oxidation was enhanced in water compared to the gas phase (Figure 1c,e for CG). The ability of the substrates to reduce or oxidize a particular atom/ion can be rationalized in terms of frontier orbitals of a free metal atom/cation and CG/GA (see also Figures S14 and S15, Supporting Information). For example, the more pronounced oxidation of Fe⁰ by CG in water ($\Delta q = -0.5$ e and -1.8 e in the gas phase and water, respectively) was apparently related to the slightly higher highest occupied molecular orbital (HOMO) energies of Fe⁰ (3d(beta): -2.2 eV, 4s(alpha): -3.2 eV, Figure 3b) compared

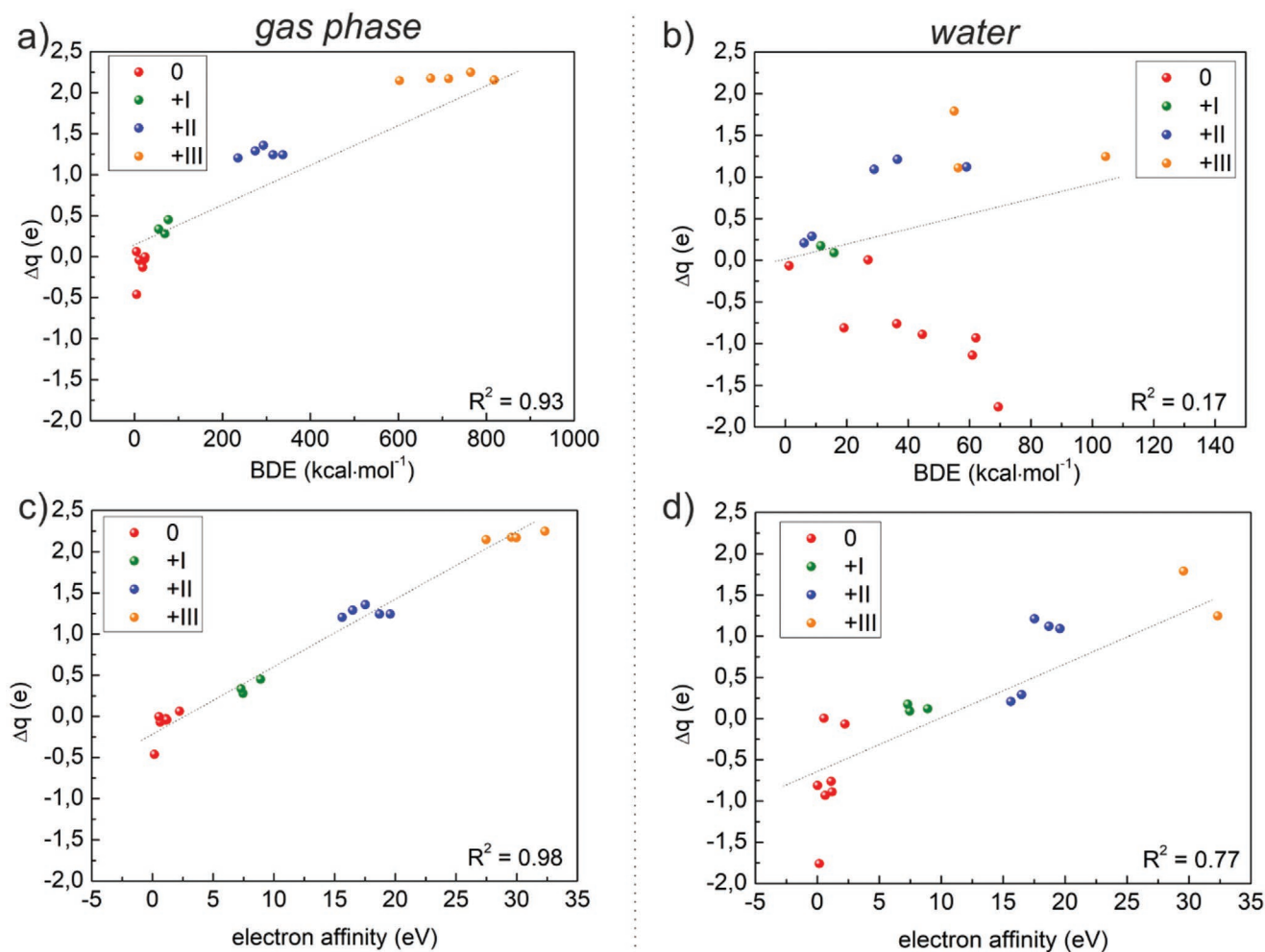


Figure 2. Pair correlations of BDE and Δq (calculated based on Mulliken charges) between CG and a metal in a) the gas phase and b) water, and pair correlations of the electron affinity of a free metal atom/cation and Δq in c) the gas phase and d) water. The groups were divided according to the initial charge on the metal atom/cation.

to the lowest unoccupied molecular orbital (LUMO) energy of CG (-3.3 eV) in water. In contrast, in the gas phase, the HOMO energies of Fe^0 ($3d(\text{beta})$: -4.2 eV, $4s(\text{alpha})$: -5.1 eV) lay between the HOMO and LUMO of CG (-5.2 and -3.4 eV, respectively, see Figure 3a). Consequently, efficient electron transfer (mainly from $4s$, $3d_{z^2}$, and $3d_{x^2-y^2}$ orbitals of Fe^0 according to natural bond orbital (NBO) analysis,^[34] Table S4, Supporting Information) can occur in water, whereas in the gas phase, changes in the electron density distribution are mainly associated with delocalization of electrons from the occupied valence orbitals of Fe^0 to the LUMO of CG (Table S3, Supporting Information). Although Co^0 and Ni^0 exhibited similar trends (Figures S6 and S7, Supporting Information), Δq decreased along the row from Fe to Ni due to the decreasing HOMO energy of the respective metal atom, i.e., with increasing ionization potential of the metals. In the case of GA, the HOMO and LUMO energies (-4.7 and -2.9 eV in the gas phase, respectively) were slightly upshifted with respect to those of CG, and thus Fe^0 , Co^0 , and Ni^0 were not oxidized but negligibly reduced ($\Delta q = 0.1$ e in all cases). It is worth noting that the small differences between the HOMO/LUMO energies of CG and GA lead systematically

to slightly larger charge transfer (by 0.1 – 0.6 e) from the latter substrate to all studied zero-valent atoms (see Table S1, Supporting Information). In water, Fe^0 was oxidized by dp-GA, similarly to $\text{CG}\cdots\text{Fe}^0$, which is rather surprising considering the negative charge of dp-GA (Table S2 and Figure S4, Supporting Information).

As mentioned above, in the case of metal cations, both CG and GA acted as reducing agents, with less pronounced charge transfer in water compared to the gas phase. The frontier orbital analysis showed that solvent effects had a dramatic impact on the HOMO and LUMO energies of metallic cations (Figure 3c–f and Figures S6–S13, Supporting Information). For example, the LUMO energy of Fe^{2+} increased from -20.5 eV (gas phase) to -1.6 eV (water), and the LUMO energy of Fe^{3+} increased from -36.6 eV (gas phase) to -7.4 eV (water). As the HOMO of CG was practically unaffected by solvent effects (-5.2 and -5.1 eV in the gas phase and water, respectively), Fe^{2+} was reduced more in the gas phase ($\Delta q = 1.2$ e) than in water ($\Delta q = 0.2$ e). In addition, the removal of an electron from the HOMO of CG (forming a CG cation) decreased its energy to -9.6 eV in the gas phase, meaning that Fe^{3+} could accept two electrons ($\Delta q = 2.2$ e).

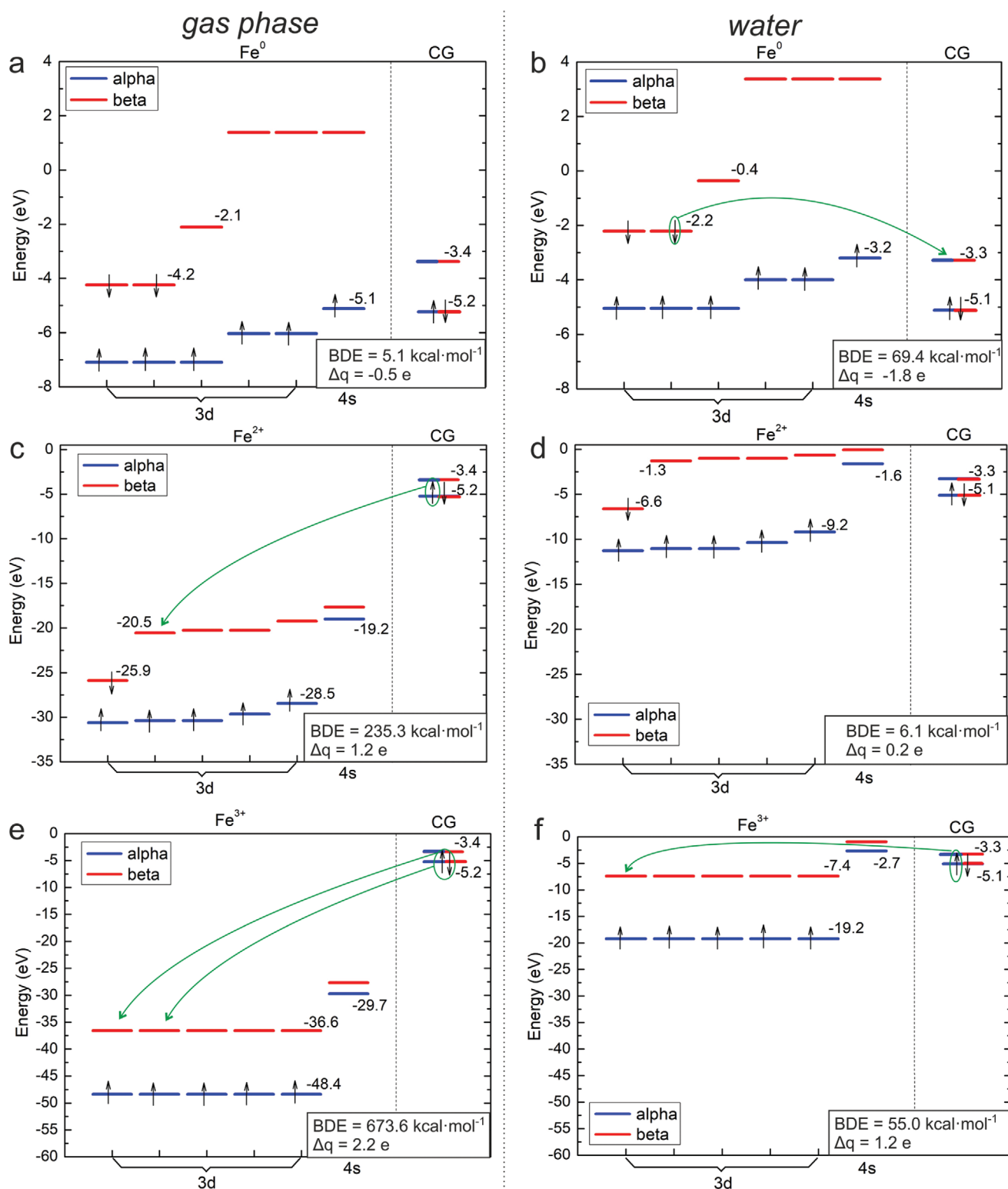


Figure 3. Comparison of HOMO and LUMO energies of CG and free metal atoms/cations: a) Fe^0 in the gas phase, b) Fe^0 in water, c) Fe^{2+} in the gas phase, d) Fe^{2+} in water, e) Fe^{3+} in the gas phase, and f) Fe^{3+} in water. Green arrows mark charge transfer between the metal and CG according to NBO analysis (Tables S3 and S4, Supporting Information).

On the other hand, the HOMO energy of the CG cation was -5.9 eV in water (Figure S16, Supporting Information), and

thus approximately only one electron was transferred from CG to Fe^{3+} ($\Delta q = 1.2 e$).

Table 1. Results for metal atoms/cations bound to CG in the gas phase and water: initial charge on Me^{x+} in e (q_i), most favorable multiplicity of the free metal atom/cation (M_i), resultant charge on Me^{x+} after geometry optimization in e (q_f), most favorable multiplicity of the CG-Me complex (M_f), spin density on Me in the CG-Me complex (ρ_σ), oxidation state of metal atom/cation in complex with CG (ox.), and XPS binding energies in eV (XPS).

Me	gas phase						Water						
	q_i	M_i	q_f	M_f	ρ_σ	XPS ^{a)}	q_i	M_i	q_f	M_f	ρ_σ	ox.	
Fe	0	5	0.5	3	2.9	717.6	705.7	0	5	1.8	5	4.0	II
	2	5	0.8	5	3.1	727.5	715.6	2	5	1.8	5	4.0	II
	3	6	0.8	4	3.0	730.1	718.2	3	6	1.8	6	4.0	II
Co	0	4	0.1	4	2.8	790.0	775.4	0	2	0.9	4	2.1	0
	2	4	0.7	2/4	2.0 ^{b)}	796.8	781.9	2	4	1.7	2/4	3.0 ^{b)}	II
	3	5	0.8	3/5	2.0 ^{b)}	799.1	784.5	3	5	1.8	3/5	3.0 ^{b)}	II
Ni	0	3	0.0	3	1.7	866.0	847.8	0	3	0.8	3	1.0	I
	2	3	0.6	3	1.0	873.7	856.5	2	3	0.8	3	1.0	I
Ru	0	5	0.1	3	2.2	471.8	449.0	0	5	1.1	5	3.2	I
	3	6	0.9	6	3.1	484.6	461.6	3	6	1.9 ^{d)}	6	2.0	II
Rh	0	4	0.0	2	1.0	309.3	304.5	0	4	0.9	2	3.0	II
	3	5	0.8	3	2.0	322.0	317.2	3	5	1.9	5	3.0	II
Pd	0	1	0.0	1	0.0	337.8	332.3	0	1	0.0	1	0.0	0
	2	3	0.8	3	0.9	348.8	343.3	2	3	0.9	3	1.0	I
Cu	0	2	0.0	2	0.7	947.3	926.5	0	2	0.9	2	0.0	I
	1	1	0.7	1	0.0	952.4	931.7	1	1	0.9	1	0.0	I
	2	2	0.8	2	0.0	955.1	934.3	2	2	0.9	2	0.0	I
Ag	0	2	- ^{b)}	-	-	-	-	0	2	0.8	2	0.0	I
	1	1	0.7	1	0.0	376.7	370.6	1	1	0.8	1	0.0	I
Au	0	2	-0.1	2	0.9	88.7	84.8	0	2	0.1	2	1.0	0
	1	1	0.6	1	0.0	94.2	90.4	1	1	0.9	1	0.0	I
	3	3	0.9	1	0.0	100.1	93.3	3	1	0.9	1	0.0	I

^{a)}The spin densities on Me for different multiplicities M_f are the same; ^{b)}No binding minimum was found; ^{c)}Energies of $2p_{1/2}$ and $2p_{3/2}$ orbitals of Fe, Co, Ni, Cu, $3d_{3/2}$ and $3d_{5/2}$ orbitals of Ag, Pd, Rh, $4f_{5/2}$ and $4f_{7/2}$ orbitals of Au; ^{d)}Results of loosely converged geometry optimization.

Analogous results were observed for Co^{2+} and Co^{3+} (Figure S6, Supporting Information). However, because the LUMO energy of the metal cation decreased from Fe to Ni, the LUMO of Ni^{2+} in water (-5.5 eV) was lower than the HOMO of CG (-5.1 eV), resulting in much higher charge transfer (1.2 e, Figure S7d, Supporting Information) than for Fe^{2+} and Co^{2+} (0.2 e and 0.3 e, respectively). Interestingly, two spin states of $\text{CG}\cdots\text{Co}^{2+}$ in the gas phase ($M = 2$ and 4) and $\text{CG}\cdots\text{Co}^{3+}$ ($M = 3$ and 5) in both environments were equally favorable. This was because the spin densities on the metal cation were practically the same (Table 1), resulting from partial spin quenching by the substrate (Figure S5, Supporting Information). GA exhibited similar reduction strengths in both the gas phase and water because the HOMO and LUMO energies of GA (-4.7 and -2.9 eV) and dp-GA (-4.4 and -2.7 eV) were comparable to those of CG. Therefore, mainly results of CG will be discussed further (for results of GA/dp-GA, see Tables S1 and S2, Supporting Information).

2.2. Light Platinum Group Metals (Ru, Rh, Pd)

In the gas phase, the zero-valent atoms of groups 8–10 4d elements were more strongly bound to CG/GA substrates than their 3d element counterparts (see BDE values in Table S1, Supporting Information). However, the oxidation of Ru^0 , Rh^0 , and Pd^0 in the aqueous environment was less pronounced than that of respective 3d elements resulting in weaker electrostatic interactions and thus slightly lower BDE (Table S2, Supporting Information). It is worth noting that Pd^0 is the only element from groups 8–10 that was not oxidized in the aqueous environment.

The binding characteristics of Ru^{3+} can be compared with those of Fe^{3+} . In the gas phase, the LUMO energy of Ru^{3+} was higher than that of Fe^{3+} by ≈ 3 eV (Figure S8c, Supporting Information), which enabled the transfer of two electrons from the CG substrate, resulting in a very similar degree of reduction ($\Delta q(\text{Fe}^{3+}) = 2.2$ e and $\Delta q(\text{Ru}^{3+}) = 2.1$ e). Despite similar resultant charges on the metals and also bond distances ($d(\text{N}\cdots\text{Fe}^{3+}) = 1.93$ Å and $d(\text{N}\cdots\text{Ru}^{3+}) = 1.99$ Å), the BDE of Ru^{3+} was about 70 kcal mol⁻¹ smaller because the two-electron transfer occurred to a less stable LUMO orbital.

In group 9, we observed a similar degree of charge transfer ($\Delta q(\text{Co}^{3+}) = 2.3$ e, $\Delta q(\text{Rh}^{3+}) = 2.2$ e in the gas phase and $\Delta q(\text{Co}^{3+}) = 1.3$ e, $\Delta q(\text{Rh}^{3+}) = 1.1$ e in water) stemming from a low-lying LUMO in both cations (Figures S6 and S9, Supporting Information). Binding of Rh^{3+} was slightly weaker (by ≈ 50 kcal mol⁻¹ in both environments) than that of Co^{3+} , mainly due to the lower stability of the LUMO in Rh^{3+} , although other factors, such as electrostatic attraction between the Me^{x+} and neighboring nitrogen or differences in bond distances ($d(\text{N}\cdots\text{Co}^{3+}) = 1.90$ Å, $d(\text{N}\cdots\text{Rh}^{3+}) = 2.02$ Å in the gas phase and $d(\text{N}\cdots\text{Co}^{3+}) = 2.09$ Å, $d(\text{N}\cdots\text{Rh}^{3+}) = 2.17$ Å in water), may also have played some role.

In group 10, the higher lying LUMO of doubly valent Pd^{2+} cations only allowed approximately one-electron transfer, similarly to the case of Ni^{2+} ($\Delta q(\text{Pd}^{2+}) = 1.2$ e, $\Delta q(\text{Ni}^{2+}) = 1.4$ e in the gas phase, $\Delta q(\text{Pd}^{2+}) = 1.1$ e, $\Delta q(\text{Ni}^{2+}) = 1.2$ e in water). Despite a larger bond distance for Pd^{2+} ($d(\text{N}\cdots\text{Pd}^{2+}) = 2.00$ Å vs $d(\text{N}\cdots\text{Ni}^{2+}) = 1.87$ Å in the gas phase, $d(\text{N}\cdots\text{Pd}^{2+}) = 1.99$ Å vs $d(\text{N}\cdots\text{Ni}^{2+}) = 1.85$ Å, in water), the BDE value of Pd^{2+} was ≈ 20 kcal mol⁻¹ larger than that of Ni^{2+} in both environments, consistent with the slightly lower energy of the LUMO in Pd^{2+} (Figures S7 and S10, Supporting Information).

2.3. Coinage Metals (Cu, Ag, Au)

Zero-valent Cu and Ag exhibited pronounced oxidation in the aqueous environment ($\Delta q(\text{Cu}^0) = -0.9$ e and $\Delta q(\text{Ag}^0) = -0.8$ e in water), since their HOMO orbitals lay between the HOMO and LUMO orbitals of CG (Figures S11 and S12, Supporting Information). Apart from lower electrostatic interaction, the lower BDE of Ag^0 (by ≈ 25 kcal mol⁻¹) can be explained in terms of its larger atomic radius than that of Cu^0 , resulting in a longer $\text{CG}\cdots\text{Me}^0$ bond ($d(\text{N}\cdots\text{Cu}^0) = 1.86$ Å vs $d(\text{N}\cdots\text{Ag}^0) = 2.14$ Å). However, due to the lower lying HOMO orbital of Au^0 (Figure S13, Supporting Information), the charge on Au was unaffected ($\Delta q = 0.1$ both in the gas phase and water). This in combination

with the longest bond ($d(\text{N}\cdots\text{Au}^0) = 2.21$ and 2.24 Å in the gas phase and water, respectively) resulted in the lowest BDE (4.6 and 1.3 kcal mol⁻¹ in the gas phase and water, respectively) of all the considered metals.

Monovalent copper and silver cations were comparably reduced in the gas phase by CG ($\Delta q(\text{Cu}^+) = 0.3$ e, $\Delta q(\text{Ag}^+) = 0.3$ e) due to their similar LUMO energies (Figures S11 and S12, Supporting Information). A higher binding energy of Cu⁺ (by ≈ 15 kcal mol⁻¹) can be explained in terms of its smaller ionic radius, and thus shorter bond length ($d(\text{N}\cdots\text{Cu}^+) = 1.85$ Å, $d(\text{N}\cdots\text{Ag}^+) = 2.10$ Å), resulting in stronger electrostatic interaction. However, the significantly lower LUMO energy of Au⁺ (Figure S13, Supporting Information) enhanced charge transfer ($\Delta q(\text{Au}^+) = 0.5$ e). This, in combination with the bond distance of 2.01 Å, resulted in a higher BDE for Au⁺ by ≈ 6 kcal mol⁻¹ than that of Cu⁺. In contrast, the LUMO energies of Cu⁺ and Ag⁺ in the aqueous environment differed more substantially (Figures S11 and S12, Supporting Information), leading to slightly stronger charge transfer to the latter ($\Delta q(\text{Cu}^+) = 0.1$ e, $\Delta q(\text{Ag}^+) = 0.2$ e). However, the bond length of Cu⁺ was again shorter ($d(\text{N}\cdots\text{Cu}^+) = 1.86$ Å, $d(\text{N}\cdots\text{Ag}^+) = 2.15$ Å), resulting in a lower BDE for Ag⁺ (by ≈ 5 kcal mol⁻¹). Although Au⁺ exhibited similar charge transfer ($\Delta q(\text{Au}^+) = 0.1$ e), the bond length of 1.97 Å in combination with the low lying LUMO orbital (Figure S13, Supporting Information) caused the BDE to be higher by ≈ 8 and ≈ 12 kcal mol⁻¹ than that of Cu⁺ and Ag⁺, respectively.

Double-valent cation Cu²⁺ can be compared to its neighbor Ni²⁺ in the same row of the periodic table. Although Ni²⁺ was reduced more by CG ($\Delta q(\text{Ni}^{2+}) = 1.4$ and 1.2 e in the gas phase and water, respectively, Figure S7, Supporting Information) than Cu²⁺ ($\Delta q(\text{Cu}^{2+}) = 1.2$ and 1.1 e in the gas phase and water, respectively, Figure S11, Supporting Information) and the bond lengths were comparable ($d(\text{N}\cdots\text{Ni}^{2+}) = 1.87$ and 1.85 Å in the gas phase and water, respectively, and $d(\text{N}\cdots\text{Cu}^{2+}) = 1.87$ Å both in the gas phase and water), the BDE of Cu²⁺ was higher in the gas phase (by ≈ 45 kcal mol⁻¹) due to electron transfer to a lower lying LUMO orbital (-25.3 and -23.4 eV for Cu²⁺ and Ni²⁺, respectively). However, the aqueous environment destabilized the LUMO orbital of Cu²⁺ (-5.1 eV) more greatly than that of Ni²⁺ (-5.5 eV), resulting in a stronger bond for Ni²⁺ in water (by ≈ 7 kcal mol⁻¹).

The BDE of Au³⁺ was the highest of all the studied metals in both environments. Since the LUMO energy of Au³⁺ (-37.1 eV in the gas phase and -17.5 eV in water, Figure S13, Supporting Information) was less affected by the aqueous environment than the other Me³⁺ cations, transfer of two electrons from the substrate to Au³⁺ took place in both environments ($\Delta q(\text{Au}^{3+}) = 2.2$ e and 2.1 e in the gas phase and water, respectively).

2.4. The Role of π -Conjugated Electron-Donating Substrates

To investigate the roles of π -conjugation in a substrate and different anchoring functional groups, we considered acetonitrile (ACN) and acetic acid (AcOH/AcO⁻) as molecular substrates analogous to CG and GA/dp-GA, respectively. The ability of substrates to reduce a metal atom/cation was clearly related to their HOMO and LUMO energies. Figure 4 shows an example of a palladium atom/cation bonded to different substrates. As

already mentioned, the HOMO/LUMO energies of GA/dp-GA were only slightly upshifted compared to those of CG, resulting in similar values of Δq . However, it is worth noting that the small difference of HOMO/LUMO energies of CG/GA leads to a dissimilarity in the case of Me⁰ which are oxidized by CG (except for Au⁰) but negligibly reduced by GA in the gas phase (see Figure 1 and Table S1, Supporting Information). On the other hand, the lower HOMO energies of ACN (-9.5 eV both in the gas phase and water) and AcOH/AcO⁻ (-8.1 eV in the gas phase and -6.8 eV in water) made the charge transfer from the substrate to metal atom/cation less favorable. Similarly, the higher LUMO energies of ACN (0.9 eV in the gas phase and 1.0 eV in water) and AcOH/AcO⁻ (0.3 eV in the gas phase and 1.6 eV in water) made charge transfer in the reverse direction less efficient.

Electron density difference (EDD) plots of Pd²⁺ bound to different substrates in an aqueous environment (Figure 4e–h) demonstrated that the charge was transferred from the π -conjugated network of CG rather than from a nonconjugated functional group, as in the case of ACN. The capability of nitrile groups in CG to facilitate electron transfer between the conductive π -conjugated carbon lattice and anchored metal cations makes the material of great potential for electrocatalysis and electrochemistry in general. On the other hand, the negatively charged dp-GA and AcO⁻ can both provide electrons from lone-pair orbitals of oxygen. Different amounts of charge transfer were evident in EDD plots of CG–Me complexes of different initial charge of Me (Figure S17, Supporting Information).

To describe the properties of SACs in an acidic environment, we considered a protonated form of GA in water. Protonation of the carboxylate groups caused only a slight upshift of the HOMO/LUMO energies (-4.4 – -2.7 eV for dp-GA and -4.8 – -3.1 eV for GA). Therefore, the charge transfer was comparable in both environments. However, BDEs were notably smaller in the case of protonated GA because of weaker electrostatic interactions, as shown for Co²⁺ and Co³⁺ complexes (Figure S18, Supporting Information).

2.5. Oxidation States and XPS Binding Energies of Anchored Metal Atoms/Ions

Oxidation states could not be directly derived from the resultant charge on metal atoms/cations due to their known poor correlation.^[35] However, the formal oxidation state could be estimated from the spin population on the metal atom/cation.^[36] In general, the anchoring of metal cations on CG/(dp-)GA was accompanied by the reduction of Me^{x+} and led to either complete (Cu²⁺) or partial spin quenching (e.g., the multiplicity of free Fe³⁺ cations of 6 was decreased to 4 and 5 in the gas phase and water, respectively), opening up possibilities for monitoring the entrapment of metal species by electron paramagnetic resonance (EPR). The capability for preserving unpaired electrons on the metal center in Fe³⁺ makes these materials attractive for spintronic applications. Interestingly, the resultant spin population on the metal, and thus their oxidation states, were often the same regardless of the initial charge on the metal cation. For the cation pairs Fe²⁺/Fe³⁺, Co²⁺/Co³⁺, and Cu⁺/Cu²⁺, this feature in combination with their high BDE values can be

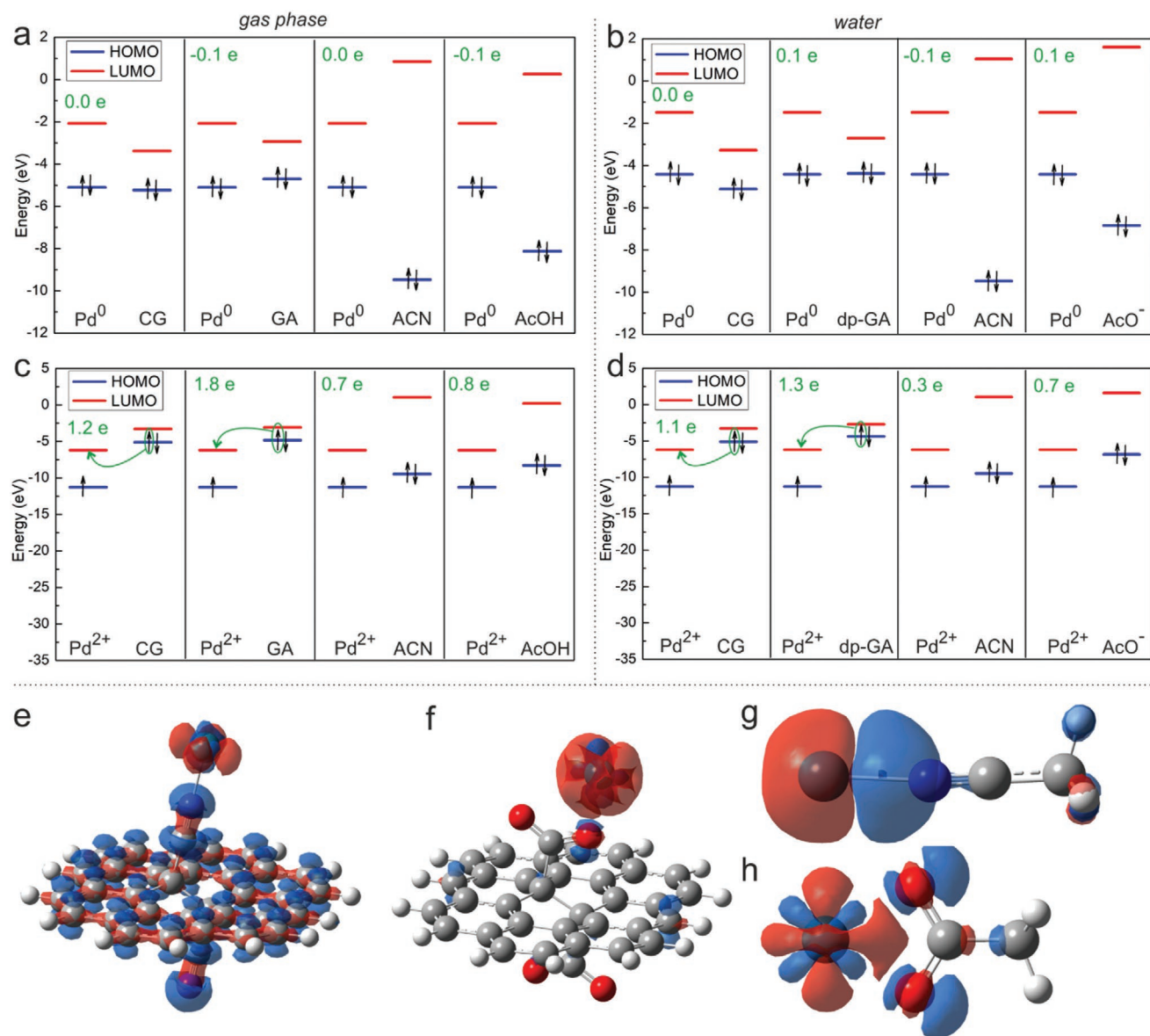


Figure 4. Comparison of HOMO (blue) and LUMO (red) energies of different substrates (CG, GA, ACN, and AcOH) and a free atom/cation of a) Pd⁰ in the gas phase, b) Pd⁰ in water, c) Pd²⁺ in the gas phase, and d) Pd²⁺ in water. Electron density difference (EDD) plots of Pd²⁺ bound to e) CG, f) dp-GA, g) ACN, and h) AcO⁻. The isosurface value was set to e,g) 0.015 a. u. and f,h) 0.003 a. u.; a blue/red isosurface indicates decreased/increased electron density. Green arrows show charge transfer between a metal and substrate, green numbers are differences in Mulliken charges on the metal before and after bonding to substrate. Carbon atoms are gray, nitrogen blue, oxygen red, hydrogen white, and palladium cyan.

utilized for designing new efficient mixed-valence SACs, as already reported for the CG ··· Cu⁺/Cu²⁺ material.^[12a]

The XPS binding energies were sufficiently distinct to allow different oxidation states of the anchored metal species to be distinguished in an experimental spectrum (Table 1). For instance, the oxidation states of iron Fe⁰, Fe²⁺, and Fe³⁺ have 2p_{3/2} binding energies of 705.7, 715.6, and 718.2 eV, respectively. Likewise, zero-valent copper and its cations (Cu⁰/Cu⁺/Cu²⁺) have 2p_{3/2} binding energies of 926.5, 931.7, and 934.3 eV, respectively. Notably, Cu⁺/Cu²⁺ ions were successfully anchored to CG and the Cu 2p_{3/2} envelope measured by high-resolution XPS showed peaks at 932.6 and at 934.9 eV.^[12a]

in excellent agreement with the calculated values. The mutual agreement of experimental peak positions and our calculated values for Cu⁺ and Cu²⁺ ions corroborates the reliability of our theoretical approach and usefulness of the binding energies for the identification of synthesized CG/GA ··· Me^{x+} nanomaterials.

3. Conclusions

Late 3d and 4d elements, including the iron triad, light platinum group elements, and coinage metals, of different initial

oxidation states and multiplicities anchored on CG and GA exhibited a vast diversity of binding characteristics. The BDEs calculated in the gas phase were in the range 5–880 kcal mol⁻¹ and were significantly decreased in an aqueous environment (1–329 kcal mol⁻¹). The CG/GA···Me bond strength was closely related to the amount of charge transferred between the metal atom/cation and substrate and to the electron affinity of a particular metal atom/cation. In water, the most strongly bound atoms/cations to CG were Au³⁺ and Co³⁺, with respective BDEs of 289 and 104 kcal mol⁻¹, whereas the lowest BDEs (below 10 kcal mol⁻¹) were found for Fe²⁺, Co²⁺, and Au⁰. Due to the negative charge of dp-GA, and thus strong electrostatic interactions, the BDE values of the most strongly bound cations (Au³⁺ and Co³⁺) were upshifted by ≈40 kcal mol⁻¹, in contrast to the most weakly bound cations (Ag⁺ and Cu⁺) with BDEs of 10–20 kcal mol⁻¹ on both substrates. BDEs of metals in oxidation states +II and +III were much higher, which may indicate a higher stability for an SAC based on Me²⁺ and Me³⁺ ions anchored on CG/GA.

In general, the anchoring of metal cations on CG/GA substrates was associated with metal reduction. In the case of zero-valent metals, either negligible charge transfer or oxidation can occur. The level of oxidation/reduction of a metal atom/cation can be explained in terms of the HOMO and LUMO energies of the respective metal atom/cation and the substrate. As the HOMOs of the substrates lay higher than the LUMOs of metal cations, electrons could be transferred from the substrate to the metal (metal reduction). In an aqueous environment, the difference between the LUMO (Me^{x+}) and HOMO (substrate) was significantly decreased, suppressing the charge transfer. On the other hand, the HOMO energies of zero-valent metals were in the range of the HOMO and LUMO (or even higher than LUMO) of the substrates, allowing charge transfer from the metal to the substrate (metal oxidation) to take place.

The ability of CG and GA to oxidize/reduce metal atoms/cations took place due to the presence of the π -conjugated network in the graphene lattice rather than different functional groups. Examples of metal atoms/cations bonded to acetonitrile (ACN) and acetic acid (AcOH) demonstrated lower charge transfer due to the higher HOMO and lower LUMO energies of ACN/AcOH compared to the graphene-based substrates. In a neutral/basic environment, the lone electron pairs of oxygens in carboxylic groups of dp-GA and AcO⁻ may also be involved in electron transfer from the substrate to metal.

Spin populations of the metal atoms/cations indicated that the same oxidation state could be assigned to some metal atoms/cations of different initial charge, opening a route toward mixed-valence SACs. Despite the same oxidation states, in many cases, notable differences between the final partial charges were predicted, and consequently, the oxidation states can be distinguished by their corresponding XPS binding energies. The large spread of binding energies and significant variations of the partial charges and spin population on the metallic centers arising from their communication with the conductive π -conjugated carbon lattice via the nitrile or carboxylate groups indicate the huge potential of these materials for heterogenous SACs and other electrochemical and spintronic applications.

Supporting Information

Supporting Information is available from the Wiley Online Library or from the author.

Acknowledgements

The authors gratefully acknowledge the support from the Ministry of Education, Youth and Sports of the Czech Republic, Operational Programme for Research, Development and Education of the European Regional Development Fund (project no. CZ.02.1.01/0.0/0.0/16_019/0000754), ERC (project no. 683024 from the European Union's Horizon 2020), and Internal Student Grant Agency of the Palacký University in Olomouc, Czech Republic (IGA_PrF_2020_022).

Conflict of Interest

The authors declare no conflict of interest.

Keywords

cyanographene, density functional theory, graphene acid, single-atom catalysts, transition metals

Received: August 7, 2020

Revised: October 20, 2020

Published online:

- [1] a) M. Pumera, Z. Sofer, *Chem. Soc. Rev.* **2017**, *46*, 4450; b) B. Wang, T. Ruan, Y. Chen, F. Jin, L. Peng, Y. Zhou, D. Wang, S. Dou, *Energy Storage Mater.* **2020**, *24*, 22; c) C. Wang, K. Xia, H. Wang, X. Liang, Z. Yin, Y. Zhang, *Adv. Mater.* **2019**, *31*, 1801072; d) Z. W. Chen, L. X. Chen, C. C. Yang, Q. Jiang, *J. Mater. Chem. A* **2019**, *7*, 3492.
- [2] a) C. N. R. Rao, K. Gopalakrishnan, A. Govindaraj, *Nano Today* **2014**, *9*, 324; b) U. N. Maiti, W. J. Lee, J. M. Lee, Y. Oh, J. Y. Kim, J. E. Kim, J. Shim, T. H. Han, S. O. Kim, *Adv. Mater.* **2014**, *26*, 40; c) C. Hu, L. Dai, *Adv. Mater.* **2019**, *31*, 1804672.
- [3] a) L. Qu, Y. Liu, J.-B. Baek, L. Dai, *ACS Nano* **2010**, *4*, 1321; b) H. Wang, T. Maiyalagan, X. Wang, *ACS Catal.* **2012**, *2*, 781.
- [4] a) Z.-S. Wu, W. Ren, L. Xu, F. Li, H.-M. Cheng, *ACS Nano* **2011**, *5*, 5463; b) X. Yu, P. Han, Z. Wei, L. Huang, Z. Gu, S. Peng, J. Ma, G. Zheng, *Joule* **2018**, *2*, 1610.
- [5] a) Z. Yang, Z. Yao, G. Li, G. Fang, H. Nie, Z. Liu, X. Zhou, X. a. Chen, S. Huang, *ACS Nano* **2012**, *6*, 205; b) J. Tuček, P. Błoriski, Z. Sofer, P. Šimek, M. Petr, M. Pumera, M. Otyepka, R. Zbořil, *Adv. Mater.* **2016**, *28*, 5045.
- [6] a) H. Liu, Y. Liu, D. Zhu, *J. Mater. Chem.* **2011**, *21*, 3335; b) R. Lv, Q. Li, A. R. Botello-Méndez, T. Hayashi, B. Wang, A. Berkdemir, Q. Hao, A. L. Elías, R. Cruz-Silva, H. R. Gutiérrez, Y. A. Kim, H. Muramatsu, J. Zhu, M. Endo, H. Terrones, J.-C. Charlier, M. Pan, M. Terrones, *Sci. Rep.* **2012**, *2*, 586; c) P. Rani, V. K. Jindal, *RSC Adv.* **2013**, *3*, 802.
- [7] a) K. Yang, L. Feng, X. Shi, Z. Liu, *Chem. Soc. Rev.* **2013**, *42*, 530; b) V. Georgakilas, J. N. Tiwari, K. C. Kemp, J. A. Perman, A. B. Bourlinos, K. S. Kim, R. Zbořil, *Chem. Rev.* **2016**, *116*, 5464.
- [8] a) B. Bosch-Navarro, M. Walker, N. R. Wilson, J. P. Rourke, *J. Mater. Chem. C* **2015**, *3*, 7627; b) A. Y. S. Eng, Z. Sofer, D. Bousa, D. Sedmidubský, S. Huber, M. Pumera, *Adv. Funct. Mater.* **2017**, *27*, 1605797; c) R. Paupitz, P. A. S. Autreto, S. B. Legoas, S. Goverapat

- Srinivasan, A. C. T. van Duin, D. S. Galavao, *Nanotechnology* **2013**, *24*, 035706.
- [9] R. R. Nair, W. Ren, R. Jalil, I. Riaz, V. Kravets, L. Britnell, P. Blake, F. Schedin, A. Mayorov, S. Yuan, M. Katsnelson, H.-M. Cheng, W. Strupinski, L. Bulusheva, A. Okotrub, I. Grigorieva, A. Grigorenko, K. Novoselov, A. Geim, *Small* **2010**, *6*, 2877.
- [10] a) K. E. Whitener, R. Stine, J. T. Robinson, P. E. Sheehan, *J. Phys. Chem. C* **2015**, *119*, 10507; b) M. Dubecký, E. Otyepková, P. Lazar, F. Karlický, M. Petr, K. Čépe, P. Banáš, R. Zbořil, M. Otyepka, *J. Phys. Chem. Lett.* **2015**, *6*, 1430; c) M. Medved', G. Zoppellaro, J. Ugolotti, D. Matochová, P. Lazar, T. Pospíšil, A. Bakandritsos, J. Tuček, R. Zbořil, M. Otyepka, *Nanoscale* **2018**, *10*, 4696; d) D. Chronopoulos, A. Bakandritsos, M. Pykal, R. Zboril, M. Otyepka, *Appl. Mater. Today* **2017**, *9*, 60.
- [11] a) V. Urbanová, K. Holá, A. B. Bourlinos, K. Čépe, A. Ambrosi, A. H. Loo, M. Pumera, F. Karlický, M. Otyepka, R. Zbořil, *Adv. Mater.* **2015**, *27*, 2305; b) A. Bakandritsos, M. Pykal, P. Błoński, P. Jakubec, D. D. Chronopoulos, K. Poláková, V. Georgakilas, K. Čépe, O. Tomanec, V. Ranc, A. B. Bourlinos, R. Zbořil, M. Otyepka, *ACS Nano* **2017**, *11*, 2982; c) D. D. Chronopoulos, M. Medved', G. Potsi, O. Tomanec, M. Scheibe, M. Otyepka, *Chem. Commun.* **2020**, *56*, 1936; d) J. Sturala, S. Hermanová, L. Artigues, Z. Sofer, M. Pumera, *Nanoscale* **2019**, *11*, 10695; e) W. Lai, J. Liu, L. Luo, X. Wang, T. He, K. Fan, X. Liu, *Chem. Commun.* **2018**, *54*, 10168; f) V. Mazánek, A. Libánská, J. Šturala, D. Bouša, D. Sedmidubský, M. Pumera, Z. Janoušek, J. Plutnar, Z. Sofer, *Chem. – Eur. J.* **2017**, *23*, 1956; g) K. A. Worsley, P. Ramesh, S. K. Mandal, S. Niyogi, M. E. Itkis, R. C. Haddon, *Chem. Phys. Lett.* **2007**, *445*, 51.
- [12] a) A. Bakandritsos, R. G. Kadam, P. Kumar, G. Zoppellaro, M. Medved', J. Tucek, T. Montini, O. Tomanec, P. Andryskova, B. Drahos, R. S. Varma, M. Otyepka, M. B. Gawande, P. Fornasiero, R. Zboril, *Adv. Mater.* **2019**, *31*, 1900323; b) R. Langer, E. Fako, P. Błoński, M. Vavrečka, A. Bakandritsos, M. Otyepka, N. López, *Appl. Mater. Today* **2020**, *18*, 100462; c) M. Blanco, D. Mosconi, C. Tubaro, A. Biffis, D. Badocco, P. Pastore, M. Otyepka, A. Bakandritsos, Z. Liu, W. Ren, S. Agnoli, G. Granozzi, *Green Chem.* **2019**, *21*, 5238.
- [13] a) B. T. Qiao, A. Q. Wang, X. F. Yang, L. F. Allard, Z. Jiang, Y. T. Cui, J. Y. Liu, J. Li, T. Zhang, *Nat. Chem.* **2011**, *3*, 634; b) S. Ji, Y. Chen, X. Wang, Z. Zhang, D. Wang, Y. Li, *Chem. Rev.* **2020**, <https://doi.org/10.1021/acs.chemrev.9b00818>; c) M. B. Gawande, P. Fornasiero, R. Zbořil, *ACS Catal.* **2020**, *10*, 2231; d) D. Grasseschi, W. C. Silva, R. d. Souza Paiva, L. D. Starke, A. S. do Nascimento, *Coord. Chem. Rev.* **2020**, *422*, 213469.
- [14] a) X. Liu, Y. Sui, T. Duan, C. Meng, Y. Han, *Phys. Chem. Chem. Phys.* **2014**, *16*, 23584; b) J. Zhang, Z. Zhao, Z. Xia, L. Dai, *Nat. Nanotechnol.* **2015**, *10*, 444; c) M. Moses-DeBusk, M. Yoon, L. F. Allard, D. R. Mullins, Z. Wu, X. Yang, G. Veith, G. M. Stocks, C. K. Narula, *J. Am. Chem. Soc.* **2013**, *135*, 12634.
- [15] S. Stambula, N. Gauquelin, M. Bugnet, S. Gorantla, S. Turner, S. Sun, J. Liu, G. Zhang, X. Sun, G. A. Botton, *J. Phys. Chem. C* **2014**, *118*, 3890.
- [16] a) M. Yan, F. Zhu, W. Gu, L. Sun, W. Shi, Y. Hua, *RSC Adv.* **2016**, *6*, 61162; b) H. L. Fei, J. C. Dong, M. J. Arellano-Jimenez, G. L. Ye, N. D. Kim, E. L. G. Samuel, Z. W. Peng, Z. Zhu, F. Qin, J. M. Bao, M. J. Yacaman, P. M. Ajayan, D. L. Chen, J. M. Tour, *Nat. Commun.* **2015**, *6*, 8668; c) L. Lin, W. Zhou, R. Gao, S. Yao, X. Zhang, W. Xu, S. Zheng, Z. Jiang, Q. Yu, Y.-W. Li, C. Shi, X.-D. Wen, D. Ma, *Nature* **2017**, *544*, 80.
- [17] a) H. Yan, H. Cheng, H. Yi, Y. Lin, T. Yao, C. Wang, J. Li, S. Wei, J. Lu, *J. Am. Chem. Soc.* **2015**, *137*, 10484; b) R. Nie, M. Miao, W. Du, J. Shi, Y. Liu, Z. Hou, *Appl. Catal., B* **2016**, *180*, 607; c) F. Huang, Y. Deng, Y. Chen, X. Cai, M. Peng, Z. Jia, P. Ren, D. Xiao, X. Wen, N. Wang, H. Liu, D. Ma, *J. Am. Chem. Soc.* **2018**, *140*, 13142; d) F. Huang, Y. Deng, Y. Chen, X. Cai, M. Peng, Z. Jia, J. Xie, D. Xiao, X. Wen, N. Wang, Z. Jiang, H. Liu, D. Ma, *Nat. Commun.* **2019**, *10*, 4431.
- [18] J. Zhang, Y. Deng, X. Cai, Y. Chen, M. Peng, Z. Jia, Z. Jiang, P. Ren, S. Yao, J. Xie, D. Xiao, X. Wen, N. Wang, H. Liu, D. Ma, *ACS Catal.* **2019**, *9*, 5998.
- [19] a) S. N. Ahmed, W. Haider, *Nanotechnology* **2018**, *29*, 342001; b) M. Shahrezaei, S. M. H. Hejazi, Y. Rambabu, M. Vavrečka, A. Bakandritsos, S. Oezkan, R. Zbořil, P. Schmuki, A. Naldoni, Š. Kment, *Catalysts* **2020**, *10*, 717.
- [20] W. Yang, L. Dong, W. Yang, C. Xu, G. Shao, G. Wang, *Small Methods* **2020**, *4*, 1900670.
- [21] Z. Chen, E. Vorobyeva, S. Mitchell, E. Fako, M. A. Ortuño, N. López, S. M. Collins, P. A. Midgley, S. Richard, G. Vilé, J. Pérez-Ramírez, *Nat. Nanotechnol.* **2018**, *13*, 702.
- [22] H. Fei, J. Dong, M. J. Arellano-Jiménez, G. Ye, N. Dong Kim, E. L. G. Samuel, Z. Peng, Z. Zhu, F. Qin, J. Bao, M. J. Yacaman, P. M. Ajayan, D. Chen, J. M. Tour, *Nat. Commun.* **2015**, *6*, 8668.
- [23] a) J. Zhang, Y. Zhao, X. Guo, C. Chen, C.-L. Dong, R.-S. Liu, C.-P. Han, Y. Li, Y. Gogotsi, G. Wang, *Nat. Catal.* **2018**, *1*, 985; b) D. Zhao, Z. Chen, W. Yang, S. Liu, X. Zhang, Y. Yu, W.-C. Cheong, L. Zheng, F. Ren, G. Ying, X. Cao, D. Wang, Q. Peng, G. Wang, C. Chen, *J. Am. Chem. Soc.* **2019**, *141*, 4086.
- [24] G. Liu, A. W. Robertson, M. M.-J. Li, W. C. H. Kuo, M. T. Darby, M. H. Muhieddine, Y.-C. Lin, K. Suenaga, M. Stamatakis, J. H. Warner, S. C. E. Tsang, *Nat. Chem.* **2017**, *9*, 810.
- [25] J. Granatier, M. Dubecký, P. Lazar, M. Otyepka, P. Hobza, *J. Chem. Theory Comput.* **2013**, *9*, 1461.
- [26] a) Y. Zhu, S. Murali, M. D. Stoller, K. J. Ganesh, W. Cai, P. J. Ferreira, A. Pirkle, R. M. Wallace, K. A. Cychoz, M. Thommes, D. Su, E. A. Stach, R. S. Ruoff, *Science* **2011**, *332*, 1537; b) Y. Zhai, Y. Dou, D. Zhao, P. F. Fulvio, R. T. Mayes, S. Dai, *Adv. Mater.* **2011**, *23*, 4828; c) Y. Wang, Z. Shi, Y. Huang, Y. Ma, C. Wang, M. Chen, Y. Chen, *J. Phys. Chem. C* **2009**, *113*, 13103.
- [27] a) T. He, C. Zhang, A. Du, *Chem. Eng. Sci.* **2019**, *194*, 58; b) H. Wang, Q. Wang, Y. Cheng, K. Li, Y. Yao, Q. Zhang, C. Dong, P. Wang, U. Schwingenschlög, W. Yang, X. X. Zhang, *Nano Lett.* **2012**, *12*, 141; c) L. Zhang, Y. Jia, G. Gao, X. Yan, N. Chen, J. Chen, M. T. Soo, B. Wood, D. Yang, A. Du, X. Yao, *Chem* **2018**, *4*, 285; d) Y. Mao, J. Yuan, J. Zhong, *J. Phys.: Condens. Matter* **2008**, *20*, 115209; e) C. Cao, M. Wu, J. Jiang, H.-P. Cheng, *Phys. Rev. B* **2010**, *81*, 205424; f) L. Hu, X. Hu, X. Wu, C. Du, Y. Dai, *J. Deng. Phys. B* **2010**, *405*, 3337; g) H. Valencia, A. Gil, G. Frapper, *J. Phys. Chem. C* **2010**, *114*, 14141; h) K. Nakada, A. Ishii, *Solid State Commun.* **2011**, *151*, 13.
- [28] a) J. P. Perdew, M. Ernzerhof, K. Burke, *J. Chem. Phys.* **1996**, *105*, 9982; b) C. Adamo, V. Barone, *J. Chem. Phys.* **1999**, *110*, 6158; c) A. Schäfer, H. Horn, R. Ahlrichs, *J. Chem. Phys.* **1992**, *97*, 2571; d) A. Schäfer, C. Huber, R. Ahlrichs, *J. Chem. Phys.* **1994**, *100*, 5829.
- [29] M. J. Frisch, G. W. Trucks, H. B. Schlegel, G. E. Scuseria, M. A. Robb, J. R. Cheeseman, G. Scalmani, V. Barone, G. A. Petersson, H. Nakatsuji, X. Li, M. Caricato, A. Marenich, J. Bloino, B. G. Janesko, R. Gomperts, B. Mennucci, H. P. Hratchian, J. V. Ortiz, A. F. Izmaylov, J. L. Sonnenberg, D. Williams-Young, F. Ding, F. Lipparini, F. Egidi, J. Goings, B. Peng, A. Petrone, T. Henderson, D. Ranasinghe, et al., *Gaussian 09*, Gaussian, Inc., Wallingford, CT **2016**.
- [30] A. V. Marenich, C. J. Cramer, D. G. Truhlar, *J. Phys. Chem. B* **2009**, *113*, 6378.
- [31] V. Blum, R. Gehrke, F. Hanke, P. Havu, V. Havu, X. Ren, K. Reuter, M. Scheffler, *Comput. Phys. Commun.* **2009**, *180*, 2175.
- [32] a) C. Choi, S. Back, N.-Y. Kim, J. Lim, Y.-H. Kim, Y. Jung, *ACS Catal.* **2018**, *8*, 7517; b) C. Kittel, *Introduction to Solid State Physics*, John Wiley & Sons, Inc., Hoboken, NJ **2005**.
- [33] D. R. Lide, *CRC Handbook of Chemistry and Physics*, CRC, Boca Raton, FL **2004**.

- [34] a) J. E. Carpenter, *Extension of Lewis Structure Concepts to Open-Shell and Excited-State Molecular Species*, University of Wisconsin, Madison, WI **1987**; b) J. E. Carpenter, F. Weinhold, *J. Mol. Struct.: THEOCHEM* **1988**, 169, 41; c) R. Blümel, U. Smilansky, *The Structure of Small Molecules and Ions*, Plenum Press, New York **1988**; d) A. E. Reed, F. Weinhold, *J. Chem. Phys.* **1985**, 83, 1736; e) A. E. Reed, R. B. Weinstock, F. Weinhold, *J. Chem. Phys.* **1985**, 83, 735; f) A. E. Reed, F. Weinhold, *J. Chem. Phys.* **1983**, 78, 4066;
- g) J. P. Foster, F. Weinhold, *J. Am. Chem. Soc.* **1980**, 102, 7211; h) A. E. Reed, L. A. Curtiss, F. Weinhold, *Chem. Rev.* **1988**, 88, 899.
- [35] a) G. Aullón, S. Alvarez, *Theor. Chem. Acc.* **2009**, 123, 67; b) A. Walsh, A. A. Sokol, J. Buckeridge, D. O. Scanlon, C. R. A. Catlow, *Nat. Mater.* **2018**, 17, 958.
- [36] M. Kubin, M. Guo, T. Kroll, H. Löchel, E. Källman, M. L. Baker, R. Mitzner, S. Gul, J. Kern, A. Föhlich, A. Erko, U. Bergmann, V. Yachandra, J. Yano, M. Lundberg, P. Wernet, *Chem. Sci.* **2018**, 9, 6813.

G

Single Co-atoms as Electrocatalysts
for Efficient Hydrazine Oxidation Reaction

Single Co-Atoms as Electrocatalysts for Efficient Hydrazine Oxidation Reaction

Ravishankar G. Kadam, Tao Zhang, Dagmar Zaoralová, Miroslav Medved', Aristides Bakandritsos, Ondřej Tomanec, Martin Petr, Johnny Zhu Chen, Jeffrey T. Miller, Michal Otyepka, Radek Zbořil,* Tewodros Asefa,* and Manoj B. Gawande*

Single-atom catalysts (SACs) have aroused great attention due to their high atom efficiency and unprecedented catalytic properties. A remaining challenge is to anchor the single atoms individually on support materials via strong interactions. Herein, single atom Co sites have been developed on functionalized graphene by taking advantage of the strong interaction between Co^{2+} ions and the nitrile group of cyanographene. The potential of the material, which is named $\text{G}(\text{CN})\text{-Co}$, as a SAC is demonstrated using the electrocatalytic hydrazine oxidation reaction (HzOR). The material exhibits excellent catalytic activity for HzOR, driving the reaction with low overpotential and high current density while remaining stable during long reaction times. Thus, this material can be a promising alternative to conventional noble metal-based catalysts that are currently widely used in HzOR-based fuel cells. Density functional theory calculations of the reaction mechanism over the material reveal that the $\text{Co}(\text{II})$ sites on $\text{G}(\text{CN})\text{-Co}$ can efficiently interact with hydrazine molecules and promote the N-H bond-dissociation steps involved in the HzOR.

the extensive use of fossil fuels not only causes severe environmental issues but also compromises efforts to attain a sustainable energy future.^[1,2] This has made researchers to investigate cost-effective and non-polluting alternatives to produce energy in a greener manner, through such systems as photovoltaic cells, electrolyzers, and fuel cells. Among them, fuel cells have attracted great attention over the past few years.^[1] These devices can convert the chemical energy in fuels such as hydrogen, alcohols, organic acids, and hydrazine into electricity, with high efficiency and minimal greenhouse gas emissions. Among the fuels used in fuel cells, hydrazine is of particular interest for the following three reasons: 1) It produces only N_2 and H_2O and it does not release the greenhouse gas CO_2 or other harmful byproducts as fossil fuels do; 2) Hydrazine is relatively easy to store and transport

1. Introduction

The rapidly growing global energy demand has led to the consumption of increased amounts of non-renewable fossil fuel resources, including coal, petroleum, and natural gas. However,

with existing infrastructures, as it is liquid at room temperature; and 3) Direct hydrazine fuel cells (DHFCs) have a large theoretical cell voltage (+1.61 V) and higher energy/power density than many other fuel cells (e.g., compared with H_2/O_2 fuel cell, which is considered one of the best fuel cells).^[1] However,

Dr. R. G. Kadam, D. Zaoralová, Dr. M. Medved', Dr. A. Bakandritsos, M. Petr, Dr. M. B. Gawande
Regional Centre of Advanced Technologies and Materials
Palacký University
Olomouc Šlechtitelů 27, Olomouc 783 71, Czech Republic
E-mail: manoj.gawande@upol.cz, mb.gawande@marj.ictmumbai.edu.in

Dr. T. Zhang, Prof. T. Asefa
Department of Chemical and Biochemical Engineering
Rutgers, The State University of New Jersey
98 Brett Road, Piscataway, NJ 08854, USA
E-mail: tasefa@rci.rutgers.edu

O. Tomanec, Prof. M. Otyepka, Prof. R. Zbořil
Regional Centre of Advanced Technologies and Materials
Czech Advanced Technology and Research Institute
Palacký University
Olomouc 779 00, Czech Republic
E-mail: radek.zboril@upol.cz

Dr. A. Bakandritsos, Prof. R. Zbořil
Nanotechnology Centre
CEET
VŠB-Technical University of Ostrava
17. Listopadu 2172/15, Ostrava-Poruba 708 00, Czech Republic

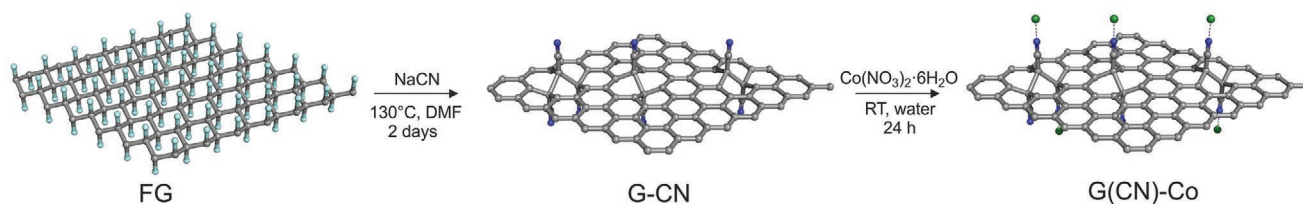
Dr. J. Zhu Chen, Prof. J. T. Miller
Davidson School of Chemical Engineering
Purdue University
480 Stadium Mall Drive, West Lafayette, IN 47906, USA

Prof. T. Asefa
Department of Chemistry and Chemical Biology
Rutgers, The State University of New Jersey
610 Taylor Road, Piscataway, NJ 08854, USA

Prof. M. B. Gawande
Department of Industrial and Engineering Chemistry
Institute of Chemical Technology
Marathwada Campus, Jalna, Mumbai 431203, India

 The ORCID identification number(s) for the author(s) of this article can be found under <https://doi.org/10.1002/smll.202006477>.

DOI: 10.1002/smll.202006477



Scheme 1. Synthesis of G(CN)–Co catalyst. In the structural model, C, F, N, and Co atoms are represented by grey, cyan, blue, and green balls.

in order to enable DHFCs to work effectively and find large-scale practical applications, the rational design and synthesis of advanced, efficient, and sustainable electrocatalysts that can replace noble metal-based electrocatalysts (such as Pt, Pd, Ir, Au, and their alloys), which are currently widely used in them, is required.^[3]

In recent years, single-atom catalysts (SACs) have attracted increased research attention in heterogeneous catalysis since they offer an ultimate atom economy and allow for the full exposure of active sites, resulting in greater catalytic activity in comparison to nanocatalysts.^[4–9] Some SACs have also been reported to catalyze various electrochemical reactions with excellent efficiency. However, there are also challenges when applying SACs in practical systems, due to the tendency of single atoms to cluster and leach during the reactions. One effective strategy to address these challenges entails the use of 2D materials as substrates to anchor the single atoms.^[8,10–20] Graphene, a 2D material, which has large surface area, high electrical conductivity, and good stability, has received significant interest as a support material for making SACs. Graphene is of interest also because of its ability to tune the electronic properties of the guest atoms. Surface-functionalized graphene derivatives, in particular, can render strong interactions with the single atoms, and thereby stabilize SACs and prevent their aggregation and transformation into nanoparticles during catalytic reactions.^[17,19–27]

To this end, herein we present a novel approach to anchor single Co(II) ions on cyanographene (G–CN) sheets to obtain Co-based single atom catalysts (G(CN)–Co SACs). The synthetic process is schematically described in **Scheme 1**. The amounts of Co(II) ions on G–CN could easily be varied by changing the relative amount of Co(II) ions mixed with G–CN. The materials showed efficient electrocatalytic activity toward the hydrazine oxidation reaction (HzOR). Complementary experiments and density functional theory (DFT) calculations corroborated the anchoring of atomically isolated cobalt sites on G–CN. The successful binding of Co(II) ions to G–CN was verified with inductively coupled plasma mass spectrometry, high-resolution transmission electron microscopy (TEM), extended X-ray absorption fine structure (EXAFS) and X-ray absorption near edge structure spectra (XANES). The resulting materials exhibited among the highest electrocatalytic activities for HzOR as well as better activities than many noble metal-based catalytic systems reported in the literature. The stability of the materials was also investigated, and the results suggested that both G–CN and the strong bond between its CN groups and Co(II) ions were crucial in preventing single Co sites from leaching during the electrocatalytic reaction.

2. Results and Discussion

2.1. Synthesis and Structural Characterization of G(CN)–Co Catalyst

The procedure applied to synthesize G(CN)–Co is illustrated in Scheme 1 (see Supporting Information for more details). It follows similar steps as those used to produce various functionalized graphene.^[28] Powder X-ray diffraction pattern (**Figure 1a**; Figure S1, Supporting Information) confirmed the absence of distinctive peaks associated with Co or Co-based inorganic particles. This indirectly suggests the dispersion of Co in isolated forms on the structures of the material. The representative TEM image revealed the presence of G–CN sheets (Figure 1b) without any heavy element-associated inorganic particles. Furthermore, high-angle annular dark-field scanning TEM (HAADF-STEM) (Figure 1c) showed that individual Co atoms are uniformly dispersed on the G–CN sheets. The Co atoms are the bright spots marked with yellow circles in the magnified HAADF-STEM images shown in Figure 1d. In the literature, advance detectors had been used for HAADF-STEM images to probe Co SACs on N-doped carbon.^[25,29,30]

Elemental mapping performed with HAADF-STEM image (Figure 1e–j) confirmed a homogenous dispersion of Co single atoms on the G–CN sheets, besides O, N, and C atoms. However, as precise identification of the lighter elements with HAADF-STEM is challenging,^[31,32] we had to resort to XANES and EXAFS to indirectly determine them (see below).

X-ray photoelectron spectroscopy (XPS) was applied to investigate the chemical composition of G(CN)–Co. The survey spectra (**Figure 2a**) confirmed the presence of C (85.7%), N (8.8%), O (4.8%), and Co (0.7%). The deconvolution of the C 1s spectrum (Figure S2a, Supporting Information) displayed distinct peaks with binding energies (BEs) of 284.82 and 286.01 eV that can be assigned to sp^2 C and sp^3 C atoms bound to –CN groups.^[9,33] Deconvolution of the N 1s spectrum (Figure S2b, Supporting Information) gave three peaks at 398.77, 400.00, and 401.31 eV corresponding to different nitrogen functional groups, respectively (see further details in the Supporting Information). The peak at BE of 781.87 eV (Figure 2b), with the corresponding satellite peaks at 785.19 and 788.77 eV, was assigned to Co^{2+} 2p species.^[34] The charge transfer and the interaction between Co(II) cations and N-atoms in G–CN was analyzed by high-resolution (HR)-XPS of N 1s envelope (Figure S3, Supporting Information).

The oxidation state and coordination environment of cobalt species in G(CN)–Co were further determined by XANES and EXAFS. The pre-edge XANES peak can be used to identify the oxidation state of the catalyst (Figure 2c).^[35] The pre-edge energy of G(CN)–Co SACs (7708.1 eV) was very similar to that

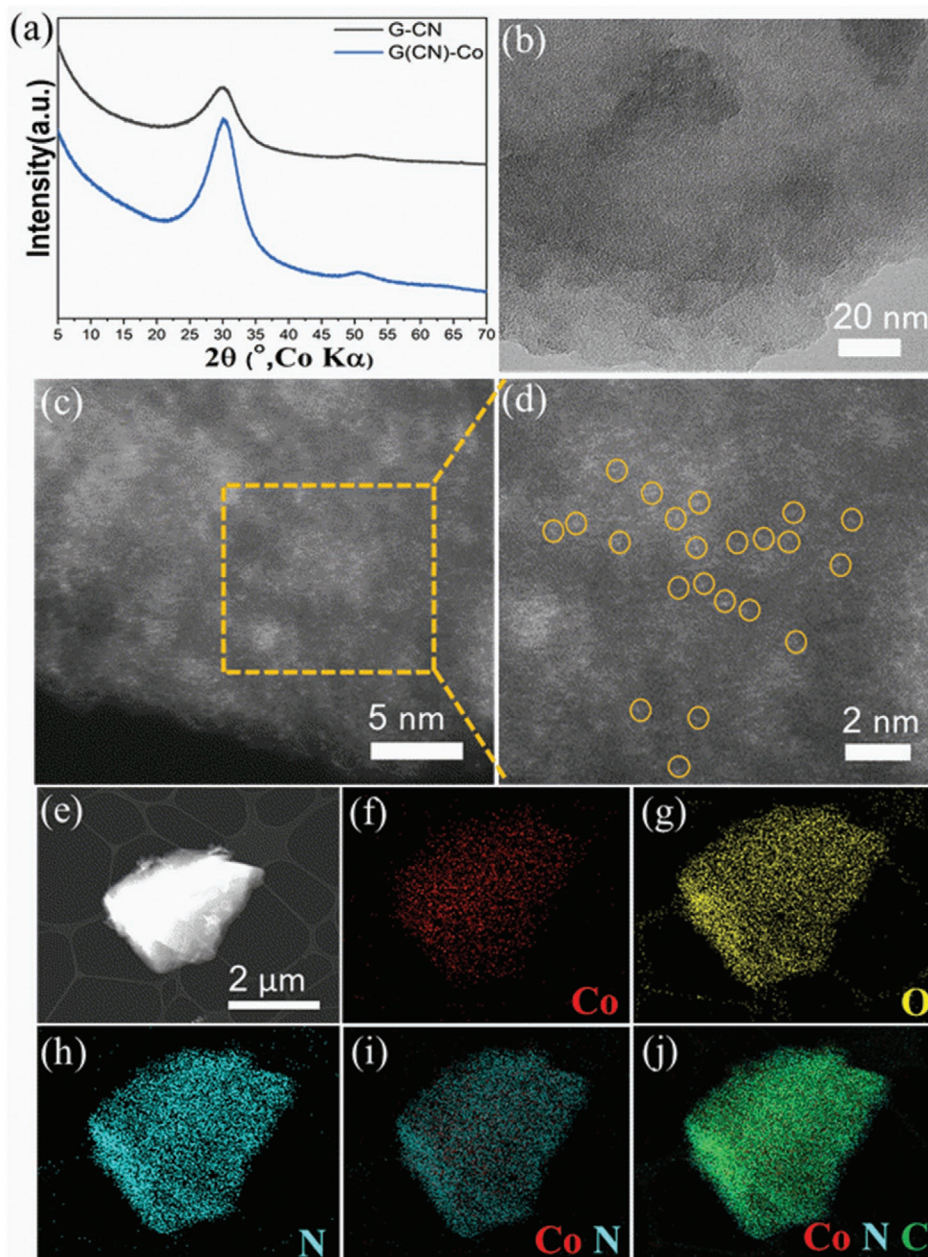


Figure 1. Characterization of G(CN)–Co (3.4 wt%): a) Powder X-ray diffraction (XRD) patterns of G–CN and G(CN)–Co; b) TEM image; c) representative high-angle annular dark-field scanning transmission electron microscopy (HAADF-STEM) image; d) magnified HAADF-STEM image showing the presence of single Co atoms (highlighted by yellow circles); and e) another HAADF image of G(CN)–Co along with the corresponding elemental mapping images of f) Co, g) O, h) N, i) Co and N, and j) Co, N, and C.

of CoO (7708.3 eV) and single site Co(II) on SiO₂. The result we obtained for the latter is similar to one reported before.^[36] The k^2 -weighted magnitude of the first shell peak of EXAFS spectrum for G(CN)–Co (black) and CoO (blue) are very similar to each other (Figure 2d). CoO has 6 Co–O bonds at 2.06 Å (about 1.7 Å phase uncorrected distance in Figure 2d), as can be seen from the fitting results given in Table S1, Supporting Information. In the case of CoO, there is a large second shell peak due to the scattering by Co–(O)–Co at about 2.8 Å. This higher shell peak is characteristic of Co-oxide nanoparticles.

The EXAFS of G(CN)–Co shows only the first shell Co–X scattering, also with 6 Co–N (or O), at 2.07 Å with no scattering from Co atoms at longer distance, which is consistent with single Co²⁺ ions. In EXAFS, the scattering is proportional to the number of electrons; thus, it is not easy to distinguish the type of scattering from C, O, and N atoms. The first shell coordination number of Co/SiO₂ is 4 Co–O at 1.98 Å, which is similar to the result previously reported for this material.^[36] The absence of a higher shell Co–O–Co (in Co/SiO₂) is similar to that of G(CN)–Co, which is a SAC containing Co(II)

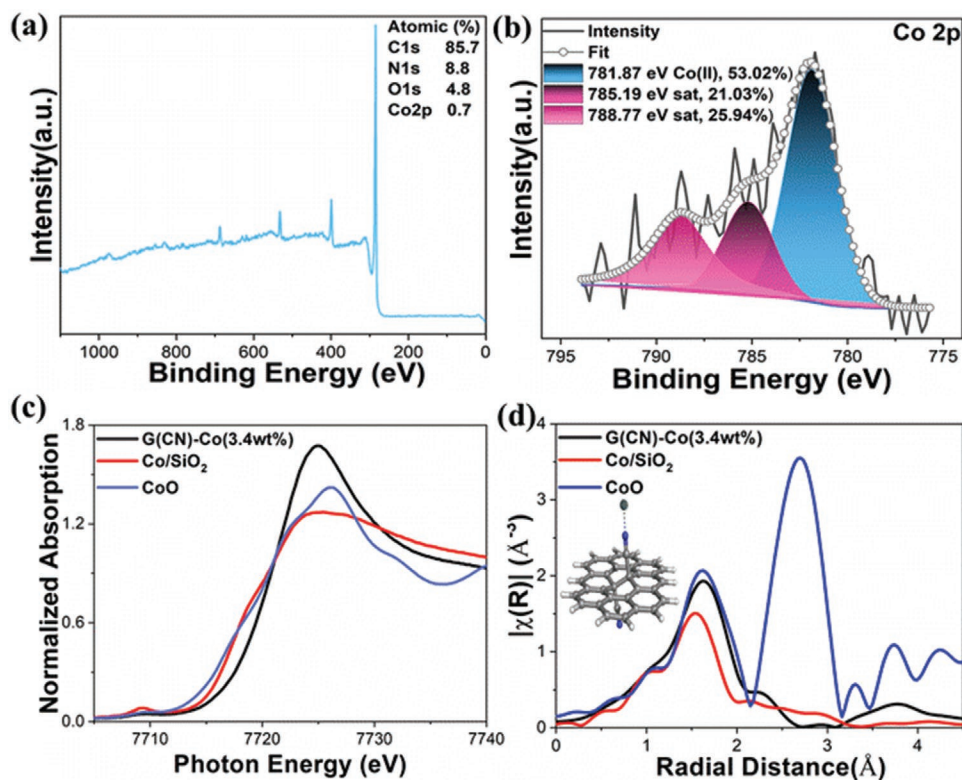


Figure 2. a) Survey X-ray photoelectron spectra of G(CN)–Co. b) High-resolution X-ray photoelectron spectra of G(CN)–Co showing the Co 2p region. X-ray absorption spectra of G(CN)–Co (black curve), CoO reference (blue curve), and Co(II)/SiO₂ (another reference material, which we prepared for comparative study (red curve). c) Co K-edge XANES and d) k^2 weighted magnitude of Fourier transformation of EXAFS (inset: the proposed model for G(CN)–Co).

sites with 6 Co–N (or Co–O) bonds, each with a bond distance of 2.07 Å.

2.2. Electrocatalytic Performance of G(CN)–Co for HzOR

The electrocatalytic performances of the as-prepared materials containing different amounts of Co (i.e., G(CN)–Co (1.2 wt%), G(CN)–Co (1.5 wt%), and G(CN)–Co (3.4 wt%)) for HzOR were studied. First, cyclic voltammetry (CV) curves for the catalysts in the presence of 50 mmol L⁻¹ hydrazine solution in phosphate buffered saline (PBS) (pH 7.4) at a scan rate of 10 mV · s⁻¹ from -0.5 to 0.3 V (vs SCE) were recorded (Figure 3a). The anodic peaks, which were observed in the CV curves of all three catalysts, could be attributed to the oxidation of hydrazine, demonstrating that all samples had catalytic activity toward HzOR. Among the catalysts, G(CN)–Co (3.4 wt%) displayed the best electrocatalytic activity for the reaction, with a relatively large negative onset potential (which means a low overpotential), with a value of ≈ -0.28 V (vs SCE). The corresponding values for G(CN)–Co (1.2 wt%) and G(CN)–Co (1.5 wt%) were -0.25 and -0.26 V, respectively. G(CN)–Co (3.4 wt%) also gave a large negative peak potential of -0.1 V (vs SCE) while the corresponding values for G(CN)–Co (1.2 wt%) and G(CN)–Co (1.5 wt%) were -0.07 and -0.09 V, respectively. Additionally, the peak current density during the HzOR over G(CN)–Co (3.4 wt%) was ≈ 3.5 mA cm⁻², which was higher than those of

G(CN)–Co (1.2 wt%) and G(CN)–Co (1.5 wt%), with values of 2.7 and 3.0 mA cm⁻², respectively. These results showed that G(CN)–Co (3.4 wt%) required a lower overpotential to catalyze HzOR compared with G(CN)–Co (1.2 wt%) and G(CN)–Co (1.5 wt%), indicating that the electrocatalytic activity of these materials increases with the amount of Co. The result also indicated that G(CN)–Co's electrocatalytic activity for HzOR was related to the Co(II) single sites. In addition, the support material, G–CN, showed negligible activity toward HzOR, indirectly corroborating that the anchored Co(II) cations were the active sites. It is also worth adding that the catalytic performance of G(CN)–Co (3.4 wt%) for HzOR was higher than that of many other transition and noble-metal based nanocatalysts that were recently reported (see Table S2, Supporting Information). The mass activities of the three materials for HzOR were compared by normalizing the current densities to the mass of Co atoms in the materials. The results indicated that G(CN)–Co (1.2 wt%) gave the highest catalytic activity for HzOR per mass of Co (Figure 3b). This means, although higher loading of Co could enhance the overall HzOR activity in terms of current density, their relationship was not linear. Therefore, the loading of metals could be optimized to further lower the cost of such catalysts while achieving optimal electrocatalytic activity or current density.

The CV curves of HzOR obtained over G(CN)–Co materials using different concentrations of hydrazine solution (ranging from 10 to 50 mmol L⁻¹) are shown in Figure S4a–c, Supporting

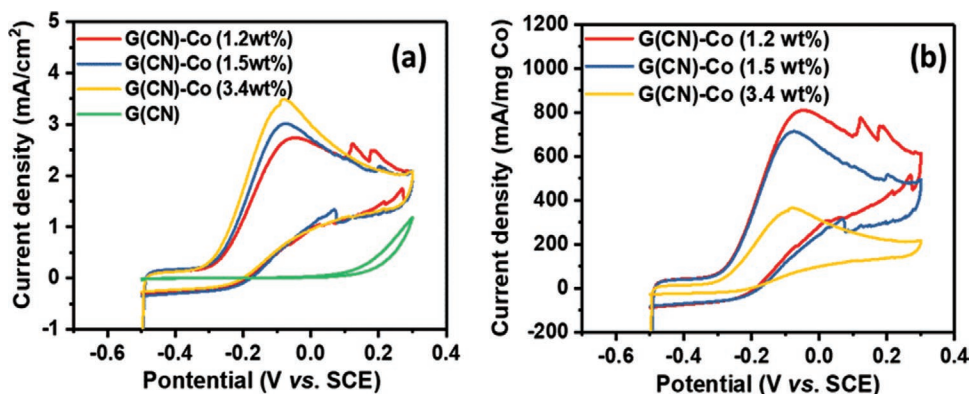


Figure 3. a) Cyclic voltammetry (CV) curves of HzOR obtained over G(CN)–Co (1.2 wt%), G(CN)–Co (1.5 wt%), G(CN)–Co (3.4 wt%), and G(CN) using 50 mmol·L⁻¹ hydrazine in PBS (pH 7.4) at a scan rate of 10 mV·s⁻¹ and b) the corresponding current density normalized to the total mass of Co atoms.

Information. The current density in the CV curves was found to be proportional to the hydrazine concentration (see Figure S4d–f, Supporting Information). The shapes of the CV curves revealed only oxidation peaks and no cathodic peaks during the reverse scans, confirming that the oxidation (or HzOR) over G(CN)–Co was an irreversible process. On the other hand, kinetic studies revealed that increasing electrochemical scan rates resulted in a slight shift toward positive peak potential in the catalytic HzOR (Figure S5a–c, Supporting Information). This is related to the mass diffusion-controlled electrochemical processes involved in HzOR and the occupation of active sites by the reacting species, as reported in our previous works.^[36,39] The oxidation current density was found to be linearly proportional to the square root of scan rate (Figure S5d–f, Supporting Information), once again indicating that the HzOR over the materials was diffusion-controlled.^[1,37–41] The electron transfer number (n) involved in HzOR over the catalysts was determined based on the slope of the current density (I/A) versus square root of the scan rate ($v^{1/2}$) using equation:^[37–41]

$$I/A = 3.01 \times 10^{-5} n [(1-\alpha) n_{\alpha}]^{1/2} c D^{-1/2} v^{1/2} \quad (1)$$

where I is the current produced by the electrocatalytic reaction, A is the surface area of the working electrode ($A = 0.071 \text{ cm}^2$), n is the total number of electrons involved in the HzOR, α is the electron transfer coefficient, n_{α} is the number of electrons involved in the rate-determining step ($n_{\alpha} = 1$), D is the diffusion coefficient, c is the concentration of hydrazine ($c = 50 \text{ mmol L}^{-1}$), and v is the scan rate. The values of α and D are determined based on the linear relationship between the peak potential (E_p) and the natural logarithm of scan rate ($\log v$) (Equation (2)) as well as on the linear correlation between the current density (I/A) and the inverse square root of time ($t^{-1/2}$) as expressed by the Cottrell equation (Equation (3)):

$$E_p = k + [0.03 / \alpha n_{\alpha}] \log v \quad (2)$$

where k is a constant and $n_{\alpha} = 1$

$$I/A = n F C D^{1/2} \pi^{-1/2} t^{-1/2} \quad (3)$$

where F is Faraday constant ($F = 96\,496 \text{ C mol}^{-1}$).

By using Equations (1–3), the total number of electrons involved in the HzOR for the tested catalysts was calculated to be close to 4. This indicated that the reaction would proceed through a 4-electron process to complete the oxidation (Figure S5, Supporting Information), and the net reaction could be written as: $\text{N}_2\text{H}_4 + 4\text{OH}^- \rightarrow \text{N}_2 + 4\text{H}_2\text{O} + 4\text{e}^-$.

The long-term stability of electrocatalysts is important for their practical application in DHFCs. Thus, the stability of the three materials during electrocatalysis was evaluated by monitoring the change in current density near their respective peak potentials in 50 mmol L⁻¹ hydrazine for 10 000 s (Figure S6, Supporting Information). The results showed that there was only a minimal change in the residual current density during the reaction, suggesting that the materials remained reasonably stable during the HzOR. All the above electrochemical results clearly demonstrated that G(CN)–Co materials could serve as efficient noble metal-free electrocatalysts for HzOR. This also means that these materials have a potential to serve as sustainable electrocatalysts at the anode side of DHFC, given their excellent activity as well as good atom economy and non-noble elemental composition.

2.3. Density Functional Theory Studies of the Reaction Mechanism of HzOR on the Catalysts

The mechanism of HzOR over the electrocatalyst was studied step-by-step by geometry optimizations of N_2H_4 , N_2 , and all intermediates with and without G(CN)–Co catalyst using DFT in combination with the implicit solvation model^[42] to account for the aqueous environment. Theoretical models of the G(CN)–Co catalyst were derived from a *trans*-14f,14k-dicyanovalene molecule representing the G–CN substrate by anchoring either a single Co^{2+} cation (model A, Figure S7a, Supporting Information) or a Co^{2+} cation coordinated with five water molecules (model B, Figure S7b, Supporting Information) to one of the cyano groups. The positive binding affinity of Co^{2+} cations to G–CN was recently rationalized in terms of efficient charge transfer from the substrate to metal cations.^[43] The reaction mechanism consists of four deprotonation steps (in basic environment) and four electrochemical oxidation steps (Figure 4). In total, four electrons are released. The HzOR may

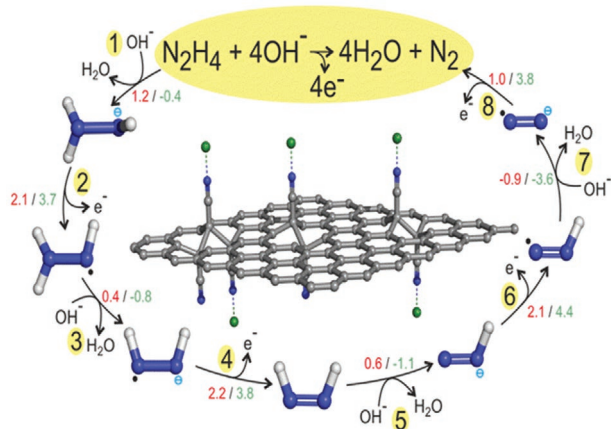


Figure 4. Reaction mechanism of hydrazine oxidation reaction (represented with yellow bubble) with and without the G(CN)–Co catalyst (in the center). The numbers marked in red and green correspond to reaction energies (in eV) obtained without and with the catalyst (model A), respectively.

proceed via two routes differing in steps 3–5 by dissociation of N–H bonds, which are however energetically comparable (see detailed mechanisms in Figures S8 and S9, Supporting Information). Without the catalyst, all reaction steps (except step 7) are energetically demanding (the values marked in red in Figure 4). The presence of G(CN)–Co catalyst significantly promotes the deprotonation steps 1, 3, 5, and 7 (the values marked in green in Figure 4) due to lowering of the N–H bond polarity (see Tables S3 and S4, Supporting Information). In addition, the negatively charged intermediates (i.e., the N–H bond dissociation products) are stabilized owing to charge transfer from N_2H_x ($x = 1–4$) to the catalyst (see q_{tot} values in Tables S3 and S4, Supporting Information), which further decreases the reaction energies of these steps. The electrochemical steps (i.e., electron releasing steps 2, 4, 6, and 8 in Figure 4) are energetically more demanding in the presence of the catalyst.

The coordination of Co^{2+} ion in G(CN)–Co with water molecules lowers the positive charge on Co^{2+} and thus decreases the binding affinity of hydrazine molecule to G(CN)–Co catalyst, from -1.3 to -0.6 eV (step 0 in Figures S8 and S10, Supporting Information). However, the reaction energies and ionization potentials do not substantially change compared to those attained by the simpler model, which does not explicitly take into account water molecules. For example, the reaction energies of steps 1 and 2 decrease from -0.4 to -0.3 eV and from 3.7 to 3.0 eV, respectively (Figures S8 and S10, Supporting Information). Interestingly, a deprotonation step involving coordinatively bound water molecules was also found feasible (path b in Figure S10, Supporting Information). Although, this process can face competition with one involving a direct attack of OH^- on hydrazine, the deprotonation steps appear to be energetically more favorable in the presence of the catalyst.

3. Conclusions

In summary, we have successfully developed Co-based SAC, denoted G(CN)–Co, with well-defined Co(II) sites by a simple

synthetic method. The material showed efficient and selective electrocatalytic activity toward HzOR with low onset/peak potential, high current density, and good stability. The electrocatalytic performances of G(CN)–Co for HzOR were also found to be better than many metal-based catalysts reported in the literature. DFT calculations of the reaction mechanism indicated that single Co active sites would readily interact with the hydrazine molecules and significantly foster the N–H bond dissociation steps. The presented simple synthetic strategy used to produce G(CN)–Co SAC and their efficient catalytic properties can encourage further research into other SACs with improved catalytic activity for HzOR and other reactions.

Supporting Information

Supporting Information is available from the Wiley Online Library or from the author.

Acknowledgements

R.G.K. and T.Z. contributed equally to this work. The authors gratefully acknowledge the support of the Operational Program Research, Development and Education—European Regional Development Fund (ERDF) (project no. CZ.02.1.01/0.0/0.0/16_019/0000754) and the ERDF project “Development of pre-applied research in nanotechnology and biotechnology” (project no. CZ.02.1.01/0.0/0.0/17_048/0007323) of the Ministry of Education, Youth and Sports of the Czech Republic. R.Z. and A.B. acknowledge the support of the Czech Science Foundation, project No. 19-27454X. M.O. acknowledges ERC project (No. 683024) from the European Union’s Horizon 2020. T.A. gratefully acknowledges the financial assistance of the US National Science Foundation (Grant No.: NSF DMR-1508611). Use of the Advanced Photon Source by JTM was supported by the U.S. Department of Energy Office of Basic Energy Sciences under contract no. DE-AC02-06CH11357. MRCAT operations, beamline 10-BM, were supported by the Department of Energy and the MRCAT member institutions.

Conflict of Interest

The authors declare no conflict of interest.

Data Availability Statement

Research data are not shared.

Keywords

electrocatalysis, hydrazine oxidation reaction, renewable energy, single atom catalyst, single Co atom catalyst

Received: October 16, 2020

Revised: February 24, 2021

Published online:

[1] T. Zhang, T. Asefa, *Adv. Mater.* **2019**, *31*, 1804394.

[2] T. Zhang, J. Low, K. Koh, J. Yu, T. Asefa, *ACS Sustainable Chem. Eng.* **2018**, *6*, 531.

- [3] J. Sanabria-Chinchilla, K. Asazawa, T. Sakamoto, K. Yamada, H. Tanaka, P. Strasser, *J. Am. Chem. Soc.* **2011**, *133*, 5425.
- [4] A. Wang, J. Li, T. Zhang, *Nat. Rev. Chem.* **2018**, *2*, 65.
- [5] X. Li, X. Yang, Y. Huang, T. Zhang, B. Liu, *Adv. Mater.* **2019**, *31*, 1902031.
- [6] B. Singh, V. Sharma, R. P. Gaikwad, P. Fornasiero, R. Zbořil, M. B. Gawande, *Small* **2020**, 2006473, <https://doi.org/10.1002/smll.202006473>.
- [7] X. F. Yang, A. Wang, B. Qiao, J. Li, J. Liu, T. Zhang, *Acc. Chem. Res.* **2013**, *46*, 1740.
- [8] M. B. Gawande, P. Fornasiero, R. Zbořil, *ACS Catal.* **2020**, *10*, 2231.
- [9] A. Bakandritsos, R. G. Kadam, P. Kumar, G. Zoppellaro, M. Medved, J. Tuček, T. Montini, O. Tomanec, P. Andryšková, B. Drahoš, R. S. Varma, M. Otyepka, M. B. Gawande, P. Fornasiero, R. Zbořil, *Adv. Mater.* **2019**, *31*, 1900323.
- [10] H. Fei, J. Dong, D. Chen, T. Hu, X. Duan, I. Shakir, Y. Huang, X. Duan, *Chem. Soc. Rev.* **2019**, *48*, 5207.
- [11] Y. Wang, J. Mao, X. Meng, L. Yu, D. Deng, X. Bao, *Chem. Rev.* **2019**, *119*, 1806.
- [12] C. Zhang, J. Sha, H. Fei, M. Liu, S. Yazdi, J. Zhang, Q. Zhong, X. Zou, N. Zhao, H. Yu, Z. Jiang, E. Ringe, B. I. Yakobson, J. Dong, D. Chen, J. M. Tour, *ACS Nano* **2017**, *11*, 6930.
- [13] X. Zhang, J. Guo, P. Guan, C. Liu, H. Huang, F. Xue, X. Dong, S. J. Pennycook, M. F. Chisholm, *Nat. Commun.* **2013**, *4*, 1924.
- [14] K. C. Kwon, J. M. Suh, R. S. Varma, M. Shokouhimehr, H. W. Jang, *Small Methods* **2019**, *3*, 1800492.
- [15] J. Guo, J. Huo, Y. Liu, W. Wu, Y. Wang, M. Wu, H. Liu, G. Wang, *Small Methods* **2019**, *3*, 1900159.
- [16] Y. Cheng, S. Zhao, B. Johannessen, J. P. Veder, M. Saunders, M. R. Rowles, M. Cheng, C. Liu, M. F. Chisholm, R. De Marco, H. M. Cheng, S. Z. Yang, S. P. Jiang, *Adv. Mater.* **2018**, *30*, 1706287.
- [17] Y. Zhu, W. Peng, Y. Li, G. Zhang, F. Zhang, X. Fan, *Small Methods* **2019**, *3*, 1800438.
- [18] W. H. Lai, Z. Miao, Y. X. Wang, J. Z. Wang, S. L. Chou, *Adv. Energy Mater.* **2019**, *9*, 1900722.
- [19] M. D. Hossain, Z. Liu, M. Zhuang, X. Yan, G. L. Xu, C. A. Gadre, A. Tyagi, I. H. Abidi, C. J. Sun, H. Wong, A. Guda, Y. Hao, X. Pan, K. Amine, Z. Luo, *Adv. Energy Mater.* **2019**, *9*, 1803689.
- [20] Y. N. Chen, X. Zhang, Z. Zhou, *Small Methods* **2019**, *3*, 1900050.
- [21] R. R. Amirov, J. Shayimova, Z. Nasirova, A. Solodov, A. M. Dimiev, *Phys. Chem. Chem. Phys.* **2018**, *20*, 2320.
- [22] V. Georgakilas, M. Otyepka, A. B. Bourlinos, V. Chandra, N. Kim, K. C. Kemp, P. Hobza, R. Zbořil, K. S. Kim, *Chem. Rev.* **2012**, *112*, 6156.
- [23] K. Jiang, S. Siahrostami, T. Zheng, Y. Hu, S. Hwang, E. Stavitski, Y. Peng, J. Dynes, M. Gangisetty, D. Su, K. Attenkofer, H. Wang, *Energy Environ. Sci.* **2018**, *11*, 893.
- [24] S. Zhou, L. Shang, Y. Zhao, R. Shi, G. I. N. Waterhouse, Y.-C. Huang, L. Zheng, T. Zhang, *Adv. Mater.* **2019**, *31*, 1900509.
- [25] Z. Du, X. Chen, W. Hu, C. Chuang, S. Xie, A. Hu, W. Yan, X. Kong, X. Wu, H. Ji, L.-J. Wan, *J. Am. Chem. Soc.* **2019**, *141*, 3977.
- [26] H.-J. Qiu, Y. Ito, W. Cong, Y. Tan, P. Liu, A. Hirata, T. Fujita, Z. Tang, M. Chen, *Angew. Chem., Int. Ed.* **2015**, *54*, 14031.
- [27] H. Zhang, J. Li, S. Xi, Y. Du, X. Hai, J. Wang, H. Xu, G. Wu, J. Zhang, J. Lu, J. Wang, *Angew. Chem., Int. Ed.* **2019**, *58*, 14871.
- [28] D. D. Chronopoulos, A. Bakandritsos, M. Pykal, R. Zbořil, M. Otyepka, *Appl. Mater. Today* **2017**, *9*, 60.
- [29] X. Wei, D. Zheng, M. Zhao, H. Chen, X. Fan, B. Gao, L. Gu, Y. Guo, J. Qin, J. Wei, Y. Zhao, G. Zhang, *Angew. Chem., Int. Ed.* **2020**, *59*, 14639.
- [30] Y. Pan, R. Lin, Y. J. Chen, S. J. Liu, W. Zhu, X. Cao, W. X. Chen, K. L. Wu, W. C. Cheong, Y. Wang, L. R. Zheng, J. Luo, Y. Lin, Y. Q. Liu, C. G. Liu, J. Li, Q. Lu, X. Chen, D. S. Wang, Q. Peng, C. Chen, Y. D. Li, *J. Am. Chem. Soc.* **2018**, *140*, 4218.
- [31] H. Yang, L. Shang, Q. Zhang, R. Shi, G. I. N. Waterhouse, L. Gu, T. Zhang, *Nat. Commun.* **2019**, *10*, 4585.
- [32] K. Sohlberg, T. J. Pennycook, W. Zhou, S. J. Pennycook, *Phys. Chem. Chem. Phys.* **2015**, *17*, 3982.
- [33] A. Bakandritsos, M. Pykal, P. Błóński, P. Jakubec, D. D. Chronopoulos, K. Poláková, V. Georgakilas, K. Čépe, O. Tomanec, V. Ranc, A. B. Bourlinos, R. Zbořil, M. Otyepka, *ACS Nano* **2017**, *11*, 2982.
- [34] G. Zhang, C. Huang, X. Wang, *Small* **2015**, *11*, 1215.
- [35] J. P. Krogman, J. R. Gallagher, G. Zhang, A. S. Hock, J. T. Miller, C. M. Thomas, *Dalton Trans.* **2014**, *43*, 13852.
- [36] B. Hu, A. B. Getsoian, N. M. Schweitzer, U. Das, H. Kim, J. Niklas, O. Poluektov, L. A. Curtiss, P. C. Stair, J. T. Miller, A. S. Hock, *J. Catal.* **2015**, *322*, 24.
- [37] T. Zhang, T. Asefa, *Front. Chem. Sci. Eng.* **2018**, *12*, 329.
- [38] B. Dong, B. L. He, J. Huang, G. Y. Gao, Z. Yang, H. L. Li, *J. Power Sources* **2008**, *175*, 266.
- [39] Y. Meng, X. Zou, X. Huang, A. Goswami, Z. Liu, T. Asefa, *Adv. Mater.* **2014**, *26*, 6510.
- [40] A. L. Cazzetta, T. Zhang, T. L. Silva, V. C. Almeida, T. Asefa, *Appl. Catal., B* **2018**, *225*, 30.
- [41] A. C. Martins, X. Huang, A. Goswami, K. Koh, Y. Meng, V. C. Almeida, T. Asefa, *Carbon* **2016**, *102*, 97.
- [42] A. V. Marenich, C. J. Cramer, D. G. Truhlar, *J. Phys. Chem. B* **2009**, *113*, 6378.
- [43] D. Zoralová, R. Mach, P. Lazar, M. Medved, M. Otyepka, *Adv. Mater. Interfaces* **2020**, 2001392.